University of Southampton

Faculty of Engineering and Physical Sciences

National Centre for Advanced Tribology at Southampton

Tribological characterisation of $MoSe_2$ and $MoSe_2$/DLC-W coatings under oil-lubricated sliding conditions

by

Saad Alshammari

ORCID: 0000-0003-4199-5836

Thesis for the degree of Doctor of Philosophy

July 2023

UNIVERSITY OF SOUTHAMPTON

ABSTRACT

FACULTY OF ENGINEERING AND PHYSICAL SCIENCES

Doctor of Philosophy

Tribological characterisation of $MoSe_2$ and $MoSe_2$/DLC-W coatings under oil-lubricated sliding conditions

Saad Alshammari

Reducing frictional losses and wear of the piston rings/cylinder liner tribo-pair in a heavy-duty vehicle's internal combustion engine is a key enabler for minimising fuel consumption, boosting engine efficiency and durability, and minimising hazardous greenhouse gas emissions. One possible approach for reducing friction and improving wear resistance of the piston rings/cylinder liner tribo-pair is to use surface coatings with low coefficients of friction and excellent wear resistance. Molybdenum diselenide ($MoSe_2$) coating can be a promising candidate for the tribo-pair due to its desirable properties such as low coefficient of friction, high load-bearing capacity, high thermal stability, low sensitivity to air humidity, and good wear resistance. For the actual assessment of the potential of $MoSe_2$ coating for the piston rings/cylinder liner tribo-pair, an in-depth investigation and understanding of its tribological performance with oil lubrication are needed because this tribo-pair typically operates under oil-lubricated conditions. However, the entire attention of tribological research conducted on this coating has focused on its tribological performance under dry sliding conditions only, whereas its tribological performance under oil-lubricated sliding conditions has not gained overwhelming attention and remains unexplored. To evaluate its suitability for the piston rings/cylinder liner tribo-pair, it is imperative to have a thorough understanding of its tribological performance in conjunction with oil lubrication. Accordingly, the aim of the present work was to study and investigate the influence of oil lubrication on the tribological performance of $MoSe_2$ coating when used under oil-lubricated sliding conditions.

Using magnetron sputtering, pure $MoSe_2$ coating and layered coating comprising $MoSe_2$ and tungsten-doped diamond-like carbon ($MoSe_2$/DLC-W) were deposited on steel discs and characterised using a variety of experimental techniques. Their tribological properties were evaluated against steel balls using a reciprocating tribometer in polyalphaolefin 4 (PAO4 - the most common synthetic base oil used in industrial and automotive lubricants). Their tribological properties were also evaluated under dry sliding conditions for comparative purposes. Following the tribological tests, different experimental techniques, including profilometry, SEM, EDS, Raman spectroscopy, FIB, and TEM were used for analysing the worn surfaces of coatings and their sliding counterparts to develop a better understanding of the underlying friction and wear mechanisms involved.

When $MoSe_2$ coating was assessed in PAO4-lubricated sliding, it demonstrated a high coefficient of friction (0.101). A crystalline $MoSe_2$ tribolayer with basal planes aligned parallel to the sliding direction, which is known to be crucial for the low-friction mechanism of this type of coatings, was not formed in the coating wear track. Similarly, no beneficial $MoSe_2$ transfer layer was formed on the sliding counterpart. The combined effect of these two factors accounted for this high coefficient of friction. This high friction was accompanied by a low wear rate (15.2×10^{-6} mm^3/N.m) because the oil worked as a sealant and protected the coating from oxidation. In dry sliding, the coating exhibited a low coefficient of friction (0.054). This low friction was attributed to the combined effect of the formation of a lubricous $MoSe_2$ transfer layer on the sliding counterpart and the presence of a crystalline $MoSe_2$ tribolayer in the coating wear track with basal planes aligned parallel to the sliding direction. However, this low friction was accompanied by a high wear rate (20.8×10^{-6} mm^3/N.m), caused by the oxidation of the coating during sliding and the formation of metal oxides that abraded the coating.

When $MoSe_2$ coating was tribologically assessed in PAO4-lubricated sliding at different applied loads and temperatures, it exhibited coefficients of friction in the range 0.067-0.101 and in the range 0.075-0.101, respectively. As the applied load or temperature increased, the coefficient of friction and wear rate of the coating were observed to decrease. Increasing the applied load or temperature was found to enhance the degree of transfer layer formation of the coating on its sliding counterpart, resulting in low friction and wear.

When $MoSe_2$/DLC-W coating was tribologically assessed in PAO4-lubricated sliding at different applied loads, it exhibited high coefficients of friction in the range 0.064-0.12. The oil acted as a barrier between sliding surfaces and significantly hindered the transfer of the coating to its sliding counterpart, making the formation of a beneficial transfer layer impossible. It also prevented the graphitisation of carbon during sliding. These two factors contributed to the observed high friction. Simultaneously, the absence of graphitised carbon and the suppression of coating oxidation contributed to a reduction in the consumption of the coating in PAO4-lubricated sliding, leading to improved wear resistance and low wear rates. In dry sliding, the coating exhibited low coefficients of friction, ranging from 0.025 to 0.085. This low friction was attributed to the graphitisation of carbon and the formation of a uniform and compact coating transfer layer on the sliding counterpart. However, this excellent friction performance was accompanied by poor wear resistance and higher wear rates than those obtained in PAO4-lubricated sliding, caused by the oxidation of the coating during sliding and the formation of soft graphitised carbon.

Table of Contents

List of Figures

List of Tables

Declaration of Authorship

I, Saad Alshammari, declare that the thesis entitled "**Tribological characterisation of $MoSe_2$ and $MoSe_2$/DLC-W coatings under oil-lubricated sliding conditions**" and the work presented in it are my own and has been generated by me as the result of my own original research.

I confirm that:

1. This work was done wholly or mainly while in candidature for a research degree at this University;

2. Where any part of this thesis has previously been submitted for a degree or any other qualification at this University or any other institution, this has been clearly stated;

3. Where I have consulted the published work of others, this is always clearly attributed;

4. Where I have quoted from the work of others, the source is always given. With the exception of such quotations, this thesis is entirely my own work;

5. I have acknowledged all main sources of help;

6. Where the thesis is based on work done by myself jointly with others, I have made clear exactly what was done by others and what I have contributed myself;

7. None of this work has been published before submission.

Signature:

Date:

Acknowledgement

First and foremost, I would like to praise Allah the Almighty, the Most Gracious, and the Most Merciful for His countless blessing and for granting me patience and capability to proceed successfully in completing this thesis.

I would like to express my deepest appreciation and gratitude to my academic supervisors, Dr. Shuncai Wang and Dr. Terry Harvey for their endless support and guidance, constructive feedback, motivation, enthusiasm, constant encouragement, and invaluable advice in all stages of this thesis. I appreciate you so much and value everything I have learned from you. Thank you so much for being such great supervisors and role models, and I will remain forever grateful to you.

Many thanks to Prof. Dan Hewak and Chris Craig (University of Southampton) for supplying $MoSe_2$ coating. Special thanks to Dr. Zabeada Aslam (University of Leeds) for her assistance with FIB and TEM analysis. Special thanks to Dr. Mark Light (University of Southampton) for his assistance with XRD analysis.

Special thanks to my friends Abdulaziz A. Abahussain, Fatih Yanar, Go Tatsumi, Khaled Almoalimi, He Wang, and Mostafa El Laithy for their support, cheering me up, never letting me feel alone, and making my experience in Southampton joyful and exciting. I would like to especially express my deepest appreciation to my friend Deepak Kumar for his tremendous support and help at every stage of this research journey.

My greatest appreciation goes to the Government of the Kingdom of Saudi Arabia and Majmaah University for providing me with the opportunity to pursue my PhD study and for financial sponsorship. I also would like to thank the Saudi Arabian Cultural Bureau in London for their assistance.

Words cannot express my deepest and warmest gratitude to my dear mother Khaznah, my dear brother Menwar, my dear Wife Huda, my dear daughter Rzan, and my dear sons Badr and Salman for their spectacular inspiration, immense support and encouragement, patience, love, and care.

List of abbreviations

a-C	Amorphous carbon
a-C: H	Hydrogenated amorphous carbon
a.u	Arbitrary unit
AW	Antiwear
BFI	Bright field imaging
BSE	Backscattered electrons
DC	Direct current
DFI	Dark field imaging
CFUBMSIP	Closed field unbalanced magnetron sputter ion plating
CVD	Chemical vapour deposition
DLC	Diamond-like carbon
EDS	Energy-dispersive X-ray spectroscopy
EP	Extreme pressure
FIB	Focused ion beam
FM	Friction modifier
GI-XRD	Grazing incidence X-ray diffraction
h-BN	Hexagonal boron nitride
HR-TEM	High-resolution transmission electron microscopy
MoDTC	Molybdenum dithiocarbamate
Mo-S-C	Carbon-doped MoS_2
Mo-Se-C	Carbon-doped $MoSe_2$
Mo-W-C	Molybdenum and tungsten doped carbon-based coating
MSPLD	Magnetron-assisted pulsed laser deposition

PVD	Physical vapour deposition
PACVD	Plasma assisted chemical vapour deposition
PAO	Polyalphaolefin
PEEK	Polyether ether ketone
PTFE	Polytetrafluoroethylene
RF	Radio frequency
RH	Relative humidity
SEM	Scanning electron microscopy
SE	Secondary electrons
TEM	Transmission electron microscopy
TMD	Transition metal dichalcogenide
ta-C	Tetrahedral amorphous carbon
ta-C: H	Hydrogenated tetrahedral amorphous carbon
UHMWPE	Ultra-high-molecular-weight polyethylene
UHV	Ultra-high vacuum
VI	Viscosity index
W-S-C	Carbon-doped WS_2
W-Se-C	Carbon-doped WSe_2
XPS	X-ray photoelectron spectroscopy
XRD	X-ray diffraction
ZDDP	Zinc dialkyldithiophosphate

List of symbols

a	Radius of point contact	m
A_r	Real contact area	m^2
E	Modulus of elasticity	Pa
E'	Reduced modulus	Pa
F	Friction force	N
H	Hardness	Pa
h	Height of ball wear scar	m
h_{min}	Minimum lubricant film thickness	m
h_{gap}	Gap between the undeformed surfaces	m
I_C	Intensity of C peaks in a Raman spectrum	_ _
I_D	Intensity of carbon *D* peak in a Raman spectrum	_ _
I_G	Intensity of carbon *G* peak in a Raman spectrum	_ _
I_{MoSe2}	Intensity of $MoSe_2$ peaks in a Raman spectrum	– –
k	Ellipticity parameter	_ _
L	Total sliding distance	m
m	Radius of ball wear scar	m
μ	Coefficient of friction	_ _
P_m	Mean contact pressure	Pa
P_o	Maximum contact pressure	Pa
R	Radius of sphere	m
R'	Reduced radius of curvature	m
R_a	Surface roughness	nm
R_q	Root-mean square surface roughness	nm

S	Total sliding distance	m
τ	Shear strength	Pa
λ	Lambda ratio	_ _
σ	Composite surface roughness	nm
τ_{max}	Maximum shear stress	Pa
η_0	Dynamic viscosity at atmospheric pressure	Pa/s
α	Pressure-viscosity coefficient	m^2/N
U	Entraining surface velocity	m/s
V	Wear volume	mm^3
V_b	Volume loss of ball	mm^3
v	Poisson's ratio	_ _
W	Normal applied load	N
Z	Wear coefficient	_ _
z	Wear rate	$mm^3/N.m$

Chapter 1: Introduction

1.1 Background

According to the United States Environmental Protection Agency (EPA), CO_2 is the major greenhouse gas generated by human activities and is considered the main contributor to climate change [1]. Approximately 22% of the UK's total greenhouse gas emissions are attributed to road transport, with heavy-duty vehicles accounting for 18% of those emissions [2]. Heavy-duty vehicles, which comprise trucks and buses, globally contribute to 7% of the total greenhouse gas emissions [3]. In terms of global energy consumption, they are ranked second, as shown in **Figure 1.1**, accounting for 21% of global road transport fuel consumption [4]. Global awareness of the need for more fuel-efficient and environmentally friendly heavy-duty vehicles has grown dramatically over the last two decades, owing primarily to limited petroleum reserves and tighter government controls on greenhouse gas emissions. In 2019, the UK government set a binding target to decrease carbon emissions from new heavy-duty vehicles by 15% in 2025 and by 30% in 2030 [5,6]. The government also set an ambitious target of achieving net zero emissions by 2050 as part of the international effort to combat climate change [7]. Accordingly, scientists have been exploring new strategies to improve the fuel efficiency and environmental compatibility of future heavy-duty vehicles.

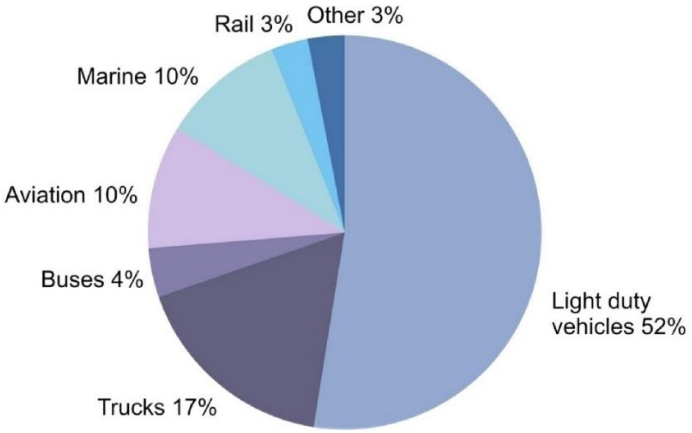

Figure 1.1: Breakdown of global transportation energy consumption [8].

Conventional heavy-duty vehicles rely heavily on internal combustion engines, which burn fossil fuels such as diesel and result in significant environment consequences, particularly the release of high amounts of CO_2 gas into the atmosphere [9]. Electric powertrains are considered zero emission at the point of use and have the potential to contribute to a portion of the overall CO_2 emission reduction. For example, distribution trucks that travel short distances every day or city buses that stop frequently may have the opportunity to recharge their batteries during their stops. However, using electric powertrains in long-haul heavy-duty vehicles is not feasible due to the high energy consumption and long estimated daily travel range. This would need the use of very large and heavy battery packs and restrict the available payload [10,11]. With current energy densities, the battery capacity necessary for an 800 km range would be roughly 1000 kWh of energy, which would require at least 5500 kg dedicated to the battery [10]. The need for large parking spaces and the availability of limited charging infrastructure are another significant roadblocks to a smooth transition to electric powertrains [11]. The time required for battery recharging is another challenge [12]. In comparison to filling a fuel tank in a few minutes, charging a huge battery would take between 5 and 12 hours [13]. These are some of the indicators that the internal combustion engine powered by diesel or alternative fuels will remain as the primary source of energy for heavy-duty vehicles for the foreseeable future. It is therefore critical to continue to make efforts to increase the efficiency of the internal combustion engine in order to meet the UK's CO_2 emissions reduction targets mentioned above in the coming years.

Frictional losses in an internal combustion engine contribute considerably to the fuel consumption of a heavy-duty vehicle. According to Holmberg et al. [4], heavy-duty vehicles consume 180 billion litres of fuel annually to overcome friction. Frictional losses in the engine typically account for 20% to 30% of the fuel consumption [14]. The piston rings/cylinder liner tribo-pair accounts for 75% of the losses, with the piston rings accounting for more than half of those losses [15,16]. Therefore, improving the tribological properties of the piston rings/cylinder liner tribo-pair offers a significant opportunity for minimising frictional losses and reducing fuel consumption and harmful emissions. By implementing advanced tribological technologies for friction reduction in heavy duty vehicles, frictional losses might be decreased by 14% in the short term (4 to 8 years) and by 37% in the long term (8 to 12 years) [4,17]. This would also result in yearly savings of 75,000 million litres of fuel and a reduction of 200 million

tonnes of CO_2 emissions in the short term. In the long term, the yearly benefit would be 200,000 million litres of fuel saved and 530 million tonnes of CO_2 emissions avoided [4,17].

One modern strategy for achieving reduced friction in the piston rings/cylinder liner tribo-pair has been to cover traditional engineering materials such as steel with thin layers of ceramics or composite materials that possess very low coefficients of friction and high wear resistance. Adding a thin layer that is often just a few micrometres thick does not modify the component's shape, but it helps reduce friction and enhance wear resistance [18]. Sophisticated deposition techniques such as physical vapour deposition (PVD), chemical vapour deposition (CVD), and thermal spraying technologies have made it possible to coat engine components with materials that reduce friction and improve wear resistance in a cost-effective and reliable manner. In modern engines, it has become increasingly common to deposit diamond-like carbon (DLC) coatings on piston rings and other engine components such as tappets and camshafts [19-22]. DLC coatings are in growing demand in the automotive industry. Every year, the automotive industry receives about 30 million DLC-coated components, with a rise of almost 50% on an annual basis [23,24]. This is due to a unique combination of mechanical and tribological properties such as high hardness and elastic modulus, low coefficient of friction, and excellent wear resistance [19,20,24]. However, DLC coatings suffer from different challenges. Many recent research studies have reported that the reactivity of DLC coatings with conventional oils and oil additives is limited due to their chemical inertness and low surface energies, making the formation of beneficial tribofilms that reduce friction and wear low and difficult to control [25-36]. Another major drawback of DLC coatings is their high internal residual stresses [37-39]. These residual stresses can lead to serious problems such as poor adhesion to substrates and delamination, making the deposition of well-adhering DLC coatings difficult. Moreover, it is challenging to deposit thick DLC coatings due to the proportional increase in residual stresses with coating thickness [40,41]. All these challenges necessitate the search for viable low-friction coating alternatives to the currently used DLC coatings.

Recently, there has been significant interest in another class of low-friction coatings known as transition metal dichalcogenides (TMDs). These materials are of the form MX_2, where M is a transition metal (Mo, W, Nb), and X is a chalcogen (Se, Te, S) [42]. TMD coatings are

recognised as intrinsic solid lubricants capable of forming low-shear strength tribofilms at sliding interfaces under dry air or vacuum conditions, resulting in extremely low coefficients of friction [42,43]. MoS_2 is the most intensively studied member of the aforementioned class and has found widespread applications in the space industry as a solid lubricant coating because of its extremely low coefficient of friction in dry air and vacuum [44]. Despite its mature application in the space industry, the attempts to apply MoS_2 coating in humid air have largely been unsuccessful. This is because of its high susceptibility to oxidation in humid air, resulting in degradation of its tribological properties with increasing coefficient of friction and wear [42,43]. To overcome this drawback, the coating has been doped with other elements, such as Ti [45,46], Al [47], Pb [48], C [49], Cr [50], and N [51,52] to act as oxygen sinks. From a commercial perspective, titanium is the most successful doping element and finds a place in a number of industrial applications [45,53-55]. Although doping with other elements generally leads to an improvement in the mechanical properties of MoS_2 coating, the detrimental effect of air humidity on its frictional behaviour is still not overcome and remains a challenge.

While MoS_2 coating has received extensive research, only a small amount of attention has been directed towards $MoSe_2$ coating with the aim of achieving less sensitivity to air humidity and better tribological performance in humid air. Nonetheless, studies with $MoSe_2$ coating have demonstrated that it can be a good alternative to MoS_2 coating, with the advantage of being more resistant to the adverse effect of air humidity and having higher thermal stability [43,56-59]. Kubart et al. [56] compared the tribological properties of MoS_2 and $MoSe_2$ coatings under different levels of air humidity. $MoSe_2$ coating outperformed MoS_2 coating with lower coefficients of friction and better wear resistance. The coefficient of friction of $MoSe_2$ coating was found to be almost independent of air humidity. In another study, Polcar et al. [43] investigated the tribological performance of several carbon-doped diselenides and disulphides of Mo and W. The coatings with diselenides demonstrated lower friction in humid air and better wear resistance than the corresponding disulphide coatings. All these results clearly demonstrate the great promise of $MoSe_2$ coating for tribological applications.

The use of $MoSe_2$ coating can be one of the potential solutions for the automotive industry to reduce friction and improve the wear resistance of the piston rings/cylinder liner tribo-pair in

heavy-duty vehicles. If the suitability of $MoSe_2$ coating is to be evaluated for this tribo-pair, an in-depth investigation and understanding of its tribological performance with oil lubrication are needed since this tribo-pair typically operates under oil-lubricated sliding conditions. However, a thorough examination of the literature leads to the fact that the research work in the field of $MoSe_2$ coating has been focused on the evaluation of its tribological performance under dry sliding conditions only, whereas its tribological performance under oil-lubricated sliding conditions yet remains unexplored. The tribological response of the coating in oil-lubricated contacts may significantly differ from that in dry contacts because of the effects arising from interacting with oil lubrication. The major question is whether these interactions with oil lubrication are synergistic, destructive, or have no influence on the tribofilm formation of this coating. This question will be addressed in this research project. The findings of this research will bridge the existing gap in the literature, provide new insights into the friction and wear behaviour of $MoSe_2$ coating, underpin its development, and assess its potential for use in mechanical components operating under oil-lubricated sliding conditions.

1.2 Aim and objectives

The overall aim of this research project is to study and investigate the influence of oil lubrication on the tribofilm formation of $MoSe_2$ coating when operating under oil-lubricated sliding conditions. The specific objectives that need to be accomplished in order to achieve this aim are:

1. To examine the effect of base oils on the friction and wear performance of $MoSe_2$ coating under oil-lubricated sliding conditions.

2. To obtain a deeper understanding of the underlying friction and wear mechanisms of $MoSe_2$ coating under oil-lubricated sliding conditions and compare them to those under dry sliding conditions.

3. To study the effect of contact load on the friction and wear performance of $MoSe_2$ coating under oil-lubricated sliding conditions.

4. To study the effect of operating temperature on the friction and wear performance of $MoSe_2$ coating under oil-lubricated sliding conditions.

5. To examine the effect of base oils on the friction and wear performance of layered $MoSe_2$/DLC-W coating under oil-lubricated sliding conditions. The core idea behind this coating design is to combine the excellent mechanical properties of DLC-W coating with the excellent tribological properties of $MoSe_2$ coating.

1.3 Thesis outline

The thesis is divided into six chapters summarised as follows:

Chapter 1 gives a broad background on the research field, details the research's aim and objectives, and provides an outline of the thesis structure.

Chapter 2 presents background information on the fundamentals of tribology, including friction, wear, and lubrication. It then reviews the current state of knowledge and scientific literature on the mechanical properties of TMD and DLC coatings and their tribological properties under dry and oil-lubricated sliding conditions. At the end of this chapter, the methods used for the deposition of the coatings are discussed.

Chapter 3 provides a description of the materials used, sample preparation, and deposition procedures of $MoSe_2$ and $MoSe_2$/DLC-W coatings. It also describes the experimental procedures and techniques used to characterise the thickness, chemical composition, crystalline structure, mechanical properties, and tribological performance of the deposited coatings.

Chapter 4 presents the results of the experimental work carried out to examine the tribological properties of $MoSe_2$ coating under dry and PAO4-lubricated sliding conditions. It also presents the results of the tribological study undertaken to investigate the influence of contact load and operating temperature on its tribological properties under PAO4-lubricated sliding conditions.

Chapter 5 presents the results of the experimental work carried out to examine the tribological properties of $MoSe_2$/DLC-W coating under dry and PAO4-lubricated sliding conditions.

Chapter 6 is the concluding chapter, which provides a summary of the main findings of the thesis and gives some recommendations for potential future research.

Chapter 2: Literature review

This chapter presents background information on the fundamentals of tribology, including friction, wear, and lubrication. It then reviews the current state of knowledge and scientific literature on the mechanical properties of TMD and DLC coatings and their tribological properties under dry and oil-lubricated sliding conditions. At the end of this chapter, the methods used for the deposition of the coatings are discussed.

2.1 Tribology

Tribology is the field of science and technology dealing with surfaces in relative motion, which means that it deals with the phenomena of friction, wear, and lubrication [60]. Although the term "tribology" was only introduced into the English literature in 1966 and offered as a new field of research, the practice of tribological applications predates recorded history [61]. The Palaeolithic method of igniting a fire by using a rotating stick and the invention of the wheel are both examples of early practical applications of tribology. Another earliest evidence of the usage of tribological concepts is the Egyptian method of moving large stone statues, depicted in a painting dated to around 1880 B.C. and discovered in a grotto at El-Bershed [62], as shown in **Figure 2.1**. It shows a man standing at the front of a pedestal and pouring a lubricant from a jar in front of a sledge used to transport a large stone statue.

Whenever two surfaces move relatively to each other, there is always some resistance to movement, and the resisting force is called friction. If there is only a small amount of friction between the two surfaces, the mechanical movement is smooth and requires less force. On the contrary, if the friction is high, the movement becomes difficult, producing a lot of heat energy that can damage the mechanical components. This loss of energy as heat leads to an overall reduction in the efficiency of machines. Friction not only contributes negatively to the dissipation of energy but also to the emission of harmful CO_2 gas into the atmosphere. Wear is defined as the surface damage or material removal of interacting surfaces in relative motion.

In most cases, wear is detrimental, leading to increased clearances between moving components, loss of precision, vibrations, and sometimes complete failure. Due to wear, huge amounts of money are spent annually on repairing or replacing mechanical components. One of the most effective approaches to reduce friction and wear is using proper lubricants, and the study of lubrication is very closely related to the study of friction and wear.

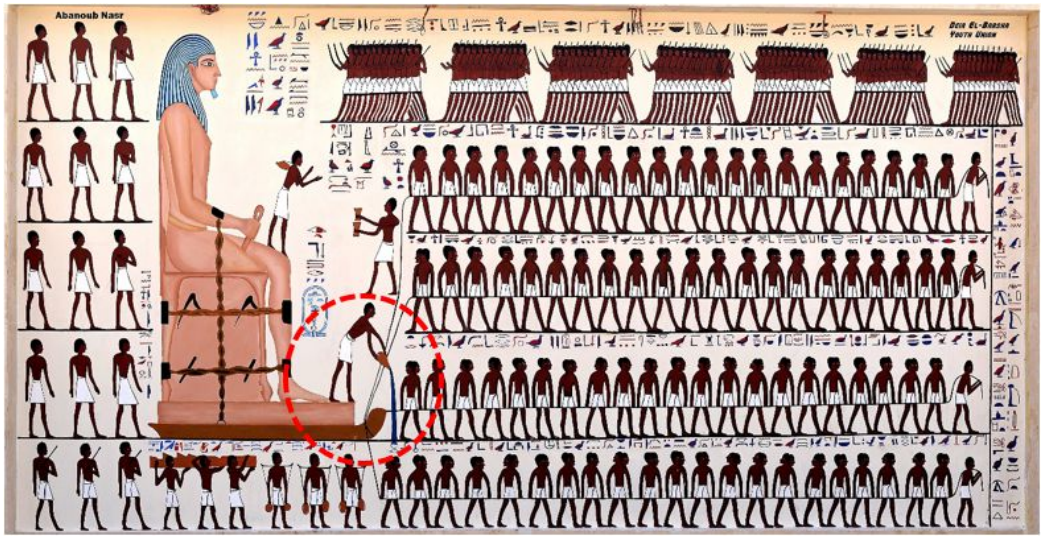

Figure 2.1: Painting found in a grotto at El-Bershed shows a man pouring a lubricant onto the ground in front of a sledge used to transport an Egyptian statue [62].

2.2 Contact Mechanics

When two bodies with curved surfaces are brought into contact with each other, they either touch at a single point or along a line. Under the application of the slightest load, localised elastic deformation takes place, and the contact point is transformed into a finite area, which is relatively small compared to the dimensions of the two bodies. In 1881, Heinrich Hertz first ly described a method for determining the size of this finite area and calculating the contact pressure [63]. His method was based on the following assumptions:

1. The size of the contact area is small compared to the dimensions of the curved surfaces.
2. Both curved surfaces are smooth and frictionless.
3. The gap h_{gap} between the undeformed surfaces may be approximated by an expression of the form:

$$h_{gap} = Ax^2 + By^2 \quad (2.1)$$

where A and B are constants. x and y are orthogonal coordinates lying in the common tangent plane to the two surfaces.

4. The deformation is elastic and can be calculated by treating each body as an elastic half space.

When two spheres of radii R_1 and R_2 are pressed against each other under a normal load W, the contact will occur over a circular area of a radius a, as schematically shown in **Figure 2.2**. Such contact is commonly referred to as a point contact. The radius of the contact area a can be calculated as [63-65]:

$$a^3 = \sqrt{\frac{3WR'}{4E'}} \quad (2.2)$$

where R' is the reduced radius of curvature and is defined in terms of the radii of the two spheres R_1 and R_2 as follows:

$$\frac{1}{R'} = \frac{1}{R_1} + \frac{1}{R_2} \quad (2.3)$$

E' is the reduced modulus and is defined as:

$$\frac{1}{E'} = \frac{1 - {v_1}^2}{E_1} + \frac{1 - {v_2}^2}{E_2} \quad (2.4)$$

where v_1 and v_2 are the Poisson's ratios of the two spheres, and E_1 and E_2 are their Young's moduli. The maximum pressure P_o (also called the Hertzian pressure) is given by:

$$P_o = \frac{3W}{2\pi a^2} \quad (2.5)$$

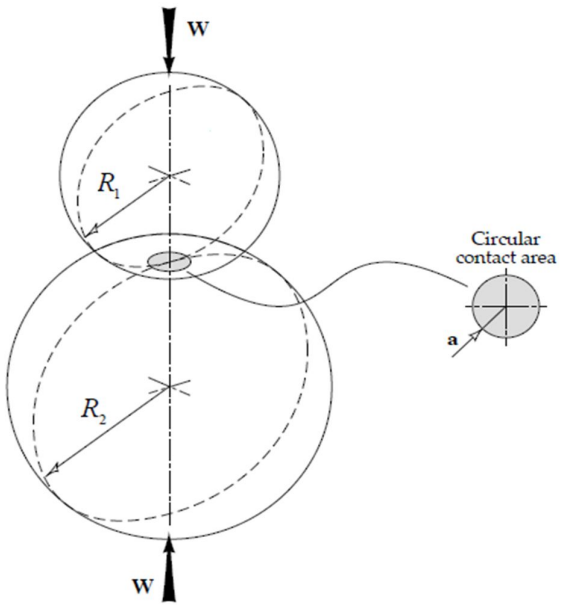

Figure 2.2: Schematic illustration of two spheres pressed against each other under a normal load W, forming a circular contact area with a radius a [63].

2.3 Friction

Friction is a tangentially acting force that resists and opposes the relative motion between two contacting bodies. The classic laws of friction in tribology are referred to as Amonton's laws of friction and state the following [66]:

1. The frictional force is proportional to the load exerted by one surface on the other.
2. The frictional force is independent of the apparent contact area between the contacting bodies.

The first law is mathematically expressed as [66]:

$$F = \mu \times W \tag{2.6}$$

where μ is the coefficient of friction, F is the friction force, and W is the normal applied load. Friction is classified into two main types depending on the status of relative motion: static friction and dynamic friction [67]. Static friction occurs between two objects that are at rest and not moving relatively to each other. If two objects are in contact and moving relatively to each other, then the friction between them is called dynamic friction.

There are two main sources of friction: adhesion and deformation [68]. Since surfaces are never completely smooth at the microscopic level, they always have some degree of surface roughness. This roughness is usually described in terms of surface asperities relative to a reference plane [66]. When two surfaces are brought into contact under an applied load, the contact initially takes place at a small number of asperity tips, as illustrated in **Figure 2.3**. The applied load is entirely carried by these few asperity tips, resulting in high local contact pressures. These asperities can be squeezed against the surfaces and even welded together by these high contact pressures. If this happens, an additional force will be required to overcome the interfacial adhesive forces formed between the interacting asperities.

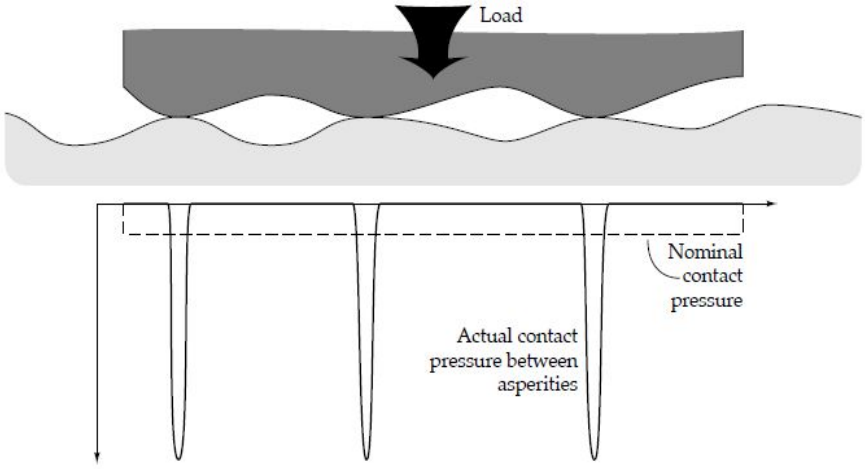

Figure 2.3: Schematic illustration of two solid surfaces in contact [64].

The second mechanism for the generation of friction is the plastic deformation of one or two surfaces in relative motion. During the contact of two surfaces, the resulting surface deformation is either elastic (reversible) or plastic (irreversible). If a sliding surface undergoes elastic deformation, the energy of deformation will be recovered when the surface resumes its original shape. As a result, there is no energy loss due to elastic deformation, and hence no frictional losses [68]. When a harder material rubs against a softer one, the asperities of the harder surface are pressed and embedded into the asperities of the softer surface, causing plastic deformation and a permanent change in the shape of the softer surface.

Bowden and Tabor examined the influence of the contact area on the friction between two metal surfaces and found that the friction force was highly dependent on the actual contact area, contradicting the Amonton's second law of friction [63,69]. They assumed that when the metal surfaces were brought into contact with each other, the asperity tips of the softer metal deformed and flowed plastically due to high local contact pressures, causing the real contact area and the friction force to increase. According to them, the friction force may be written as [63,70]:

$$F = F_{adh} + F_{def} = A_r \,.\, \tau + A_p \,.\, p \tag{2.7}$$

where τ is the shear strength of the junctions formed in the region of contact, and A_r is the real contact area in which the shear occurs. The product of these represents the frictional force due to adhesion F_{adh}. A_p is the cross-sectional area of the scratches formed by ploughing asperities, and p is the pressure needed to cause flow of the ploughed material. The product of these two quantities represents the frictional force due to deformation F_{def}.Therefore, achieving low friction is a matter of decreasing any component in the equation above and can be summarised as:

1. Minimising the interfacial shear strength in the contacting asperities.
2. Minimising the real contact area in order to keep the sheared area as small as possible.
3. Keeping abrasion to a minimum by ensuring the harder surface is smooth and has low and flat asperities.

2.4 Wear

Wear occurs when the relative motion of two moving solid components results in material loss or surface damage to one or both components. Wear is not a material property, but rather a complex response of a tribological system. Surface interactions on the asperity scale, operating conditions, system design, and contacting surface materials are the factors that influence material wear [64,70,71]. The most widely used equation to quantify wear was formulated by Archard and quantities wear as follows [72]:

$$\frac{V}{L} = Z\frac{W}{H} \tag{2.8}$$

where V represents the total volume of material removed, L is the total sliding distance, W is the normal applied load, and H is the hardness of the affected material. Z is a dimensionless constant usually known as the wear coefficient. Z/H is usually replaced by z, which is the wear rate and is expressed as [72]:

$$z = \frac{V}{WL} \tag{2.9}$$

z is commonly quoted in units of mm^3/N.m. Depending on the mode of surface damage observed on worn surfaces, wear is classified into different types such as adhesive wear, abrasive wear, fatigue wear, and delamination wear.

2.4.1 Adhesive wear

Adhesive wear is characterised by the appearance of asperity junctions at the contact area of surfaces in relative motion. When these junctions are weak, shear occurs at the interface of the two surfaces, and there is no wear. However, when these junctions are strong, the softer material may be pulled off during sliding and adhere to the harder surface [64], as shown in **Figure 2.4**. Adhesive wear is associated with a high wear rate and severe degradation of sliding surfaces, as shown in the example in **Figure 2.5**.

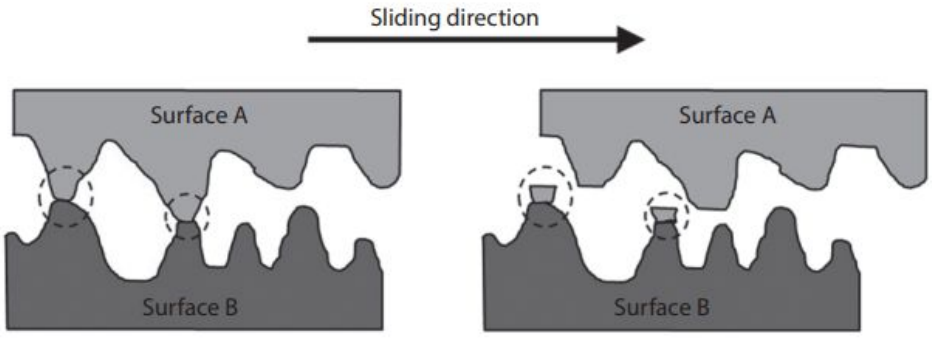

Figure 2.4: Schematic illustration of adhesive wear mechanism shows material transfer from one surface to another [73].

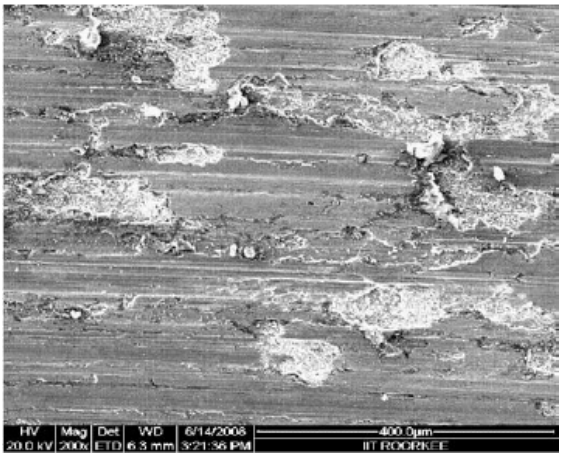

Figure 2.5: SEM image of Al-Si alloy surface experiencing adhesive wear [74].

2.4.2 Abrasive wear

Abrasive wear is commonly categorised into two types: two-body and three-body abrasion [75]. When the asperities of a hard surface plough or cut through a softer one, this is referred to as two-body abrasion. Three-body abrasion is caused by hard particles sliding and rolling freely between two contacting surfaces. An illustration of the difference between the two types is shown in **Figure 2.6**. In two-body abrasive wear, wear grooves are usually found on one or both contacting surfaces along the direction of sliding. Three-body abrasion usually results in a surface topography dominated by multiple indentations. **Figure 2.7** depicts steel surfaces subjected to two-body and three-body abrasive wear.

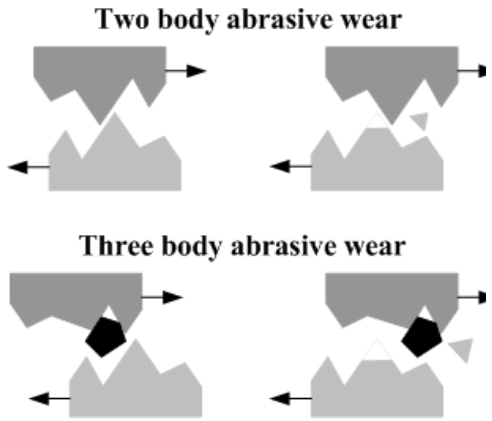

Figure 2.6: Two and three-body modes of abrasive wear [75].

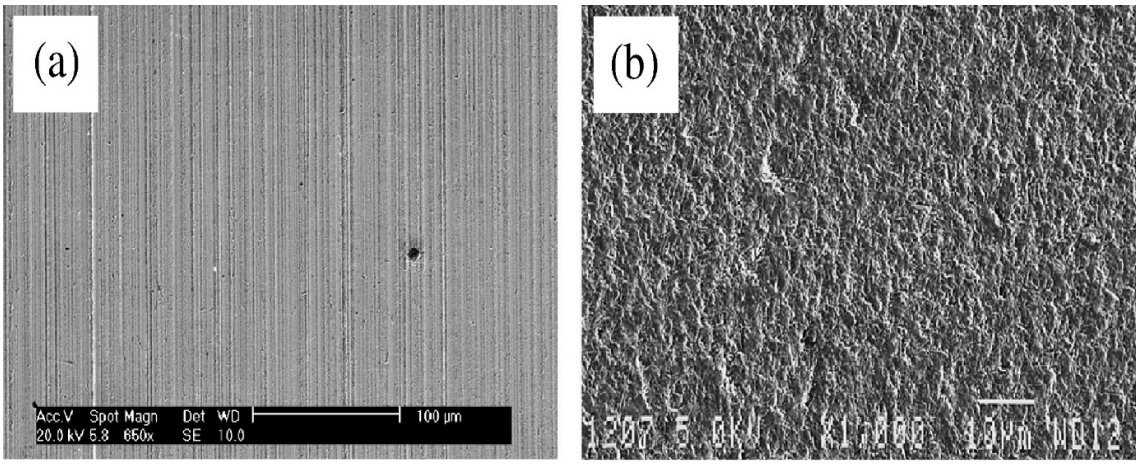

Figure 2.7: SEM images of steel surfaces subjected to: (a) two-body abrasion [76] and (b) three-body abrasion [77].

2.4.3 Fatigue wear

Fatigue wear occurs when a material is subjected to cyclic loading. This loading causes surface or subsurface cracks to emerge, as shown in **Figure 2.8**, which propagate and connect to each other, resulting in a huge crack network [73]. This eventually leads the material to suddenly break apart, forming large wear debris. An example of this wear type is shown in **Figure 2.9**.

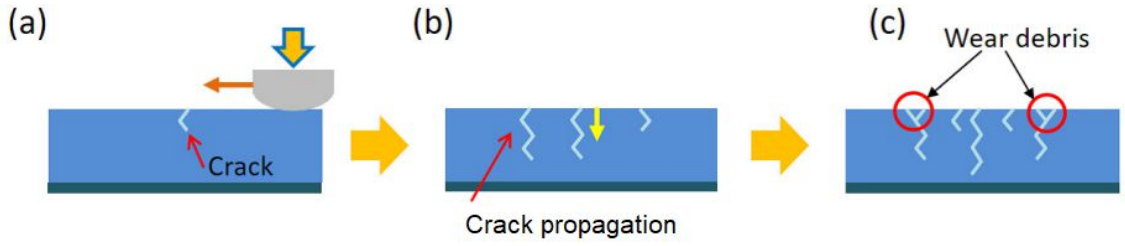

Figure 2.8: Stages of fatigue wear [78].

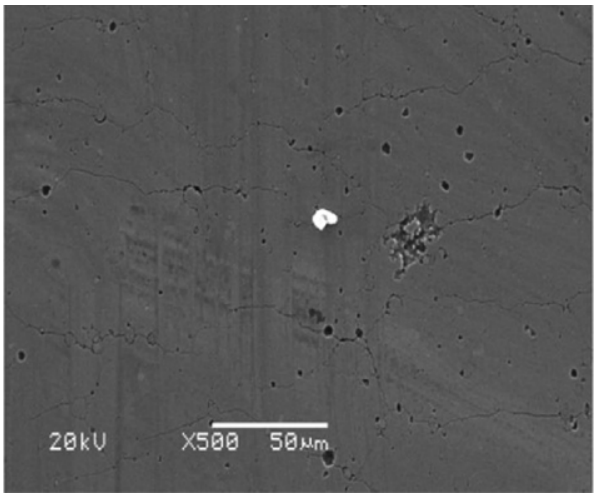

Figure 2.9: SEM image of CrN coating experiencing fatigue wear [79].

2.4.4 Delamination wear

Delamination wear occurs when subsurface cracks form and propagate parallel to the surface of a material, eventually causing the material to flake off in sheet-like wear particles [64]. This type of wear is somewhat similar to fatigue wear in that both occur from subsurface cracks and do not involve the transfer of material from one surface to another. However, cyclic loading is the main cause of fatigue wear, whereas a combination of cyclic loading and high applied loads causes subsurface cracking in delamination wear [80]. **Figure 2.10** shows an example of delamination wear.

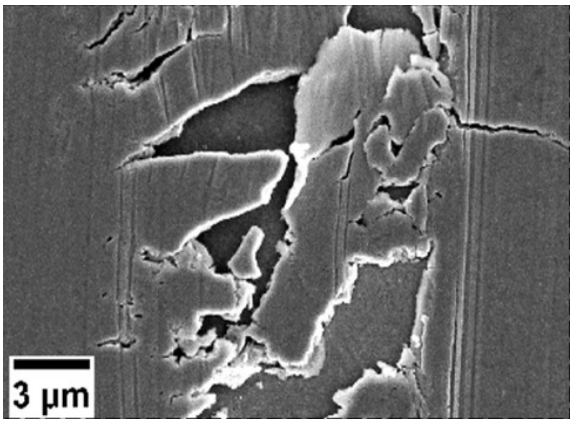

Figure 2.10: SEM image of Ni-doped MoS_2 coating experiencing delamination wear [81].

2.5 Lubrication

Lubrication is the control of friction and wear by the introduction of a material between surfaces that are moving against each other. Two types of lubrication are discussed in the present work: oil lubrication and solid lubrication.

2.5.1 Oil lubrication

In addition to controlling friction, oil lubrication plays other fundamental roles. When two surfaces come into contact, frictional heat is generated, resulting in unfavourable consequences such as changing the microstructure and mechanical properties of the surface materials. In worst-case scenarios, excessive heating might result in material softening or even melting. Therefore, a successful operation requires rapid heat dissipation. This is where oil lubricants come into the picture. The excellent thermal conductivity of oil lubricants allows them to effectively dissipate the generated heat between contacting surfaces [82]. Most mechanical components deteriorate over time, causing the formation of wear debris that adversely affect the tribological properties of contacting surfaces by rapidly increasing friction and abrasion. Oil lubricants can transport wear debris to filters for removal [67,82]. Oil lubricants often contain additives intentionally added to form chemical bonds with metal surfaces and reduce oxidation, thereby avoiding corrosion of contacting surfaces [83,84]. Oil lubricants are useful for machines with moving components such as pistons and shafts. They can function as sealants by occupying clearances between contacting surfaces. This favourably helps in maintaining internal forces, preventing gas leakages, and avoiding the invasion of external foreign materials [85].

2.5.1.1 Physical properties of lubricating oils

The viscosity, viscosity index, pour point, flash point, oxidation resistance, thermal stability, and cloud point are all fundamental properties and are often indicated in the technical details and specifications of lubricating oils. Knowing about these properties is important in determining the suitability of an oil for a particular application. The main physical properties of some lubricating oils are summarised in **Table 2.1**.

Table 2.1: Physical properties of some lubricating oils [61,64,86-91].

Lubricants	Kinematic viscosity at 40 ºC (cSt)	Kinematic viscosity at 100 ºC (cSt)	Viscosity index	Thermal stability (ºC)	Flash point (ºC)	Cloud point (ºC)
Mineral oils	19	5.5	100	135	105	-57
Polyalphaoleins (PAOs)						
PAO4	16.4	4.1	126	-	220	-66
PAO6	31	5.8	138	-	246	-57
PAO8	41	8	139	-	260	-48
PAO10	66	10	137	-	266	-48
Esters						
Phosphate esters	11	4	-	240	180	-57
Silicate esters	12	4	-	250	185	-65
Neopentyl polyol esters	15	4.5	-	230	250	-62
Silicones						
Phenyl methyl	74	25	-	280	260	-70
Fluoro	190	30	-	260	290	-50
Bio-based oils						
Castor oil	209	18.8	87	-	305	-27
Soy oil	31	8	-	-	314	-16

2.5.1.1.1 Oil viscosity

One of the most important characteristics of a lubricating oil is its viscosity. It is a measure of its internal resistance and how its molecules interact with each other in response to relative shearing motion [92]. A low viscosity oil is required for applications involving low loads, low temperatures, and high speeds. On the other hand, applications with high temperatures, low speeds, and high loads require a high viscosity oil. The most common unit of measurement for

the viscosity is kinematic viscosity, which is defined as an oil's resistance to flow and shear under the force of gravity [92]. The kinematic viscosity is usually quoted in technical data sheets of oil lubricants at temperatures of 40 °C and 100 °C. The most commonly used kinematic viscosity unit is centistokes (1 cSt = 10^{-6} m^2/s) [64].

2.5.1.1.2 Viscosity index

The viscosity of a lubricating oil is highly temperature-dependent. It decreases dramatically as the temperature increases, and the rate of change varies according to the type of oil. The viscosity index (VI) is a method of numerical determination of this rate of change. A lubricating oil with a high viscosity index has a relatively low rate of change of viscosity with temperature, whereas an oil with a low viscosity index has a relatively high rate of change of viscosity with temperature. For many applications, it is desirable to have a lubricating oil whose viscosity remains constant for a wide range of operating temperatures, i.e. a high VI [61].

2.5.1.1.3 Pour point

At low temperatures, one of the disadvantages of most lubricating oils is their tendency to transform into a semifluid or a solid immovable mass. The pour point is the temperature at which a lubricating oil gets so thick that it can no longer retain its flow characteristics. It is an important physical feature of lubricating oils, especially for low-temperature applications. When the operational temperature of a lubricating oil falls below its pour point, the oil loses its fluidity and is unable to be circulated, a phenomenon known as oil starvation [93].

2.5.1.1.4 Flash point

The flash point of a lubricating oil is the lowest temperature at which the oil gives off an ignitable vapour mixture when heated in air. The higher the flash point, the more difficult it is to ignite the oil. To eliminate ignition and fire hazards in a mechanical system, a lubricating oil must have a high flash point [94].

2.5.1.1.5 Oxidation resistance

When a lubricating oil is exposed to air, it undergoes an oxidative degradation. Acidic chemicals, sludge, and lacquers can be formed as a result of this oxidation [61,95]. These compounds cause the oil to thicken and become more viscous, resulting in poor lubrication, increased acidity, and, most importantly, a shorter oil service life. Antioxidants are commonly added to lubricating oils in concentrations ranging from 0.1% to 0.5%, and their purpose is to extend the life of these oils by improving their oxidative resistance at high temperatures [96-98].

2.5.1.1.6 Thermal stability

The thermal stability of a lubricating oil refers to the resistance of oil molecules to thermal degradation at high temperatures [99]. Each lubricating oil has a particular working temperature range. At a high temperature, well above the normal operating temperature, oil molecules start to decompose and break down. This thermal degradation results in a considerable loss in oil viscosity and poor lubricating capabilities.

2.5.1.1.7 Cloud point

The cloud point of a lubricating oil is the temperature at which paraffin wax begins to precipitate in the oil and causes it to appear cloudy. When wax begins to solidify and accumulate, especially under low-temperature working conditions, it thickens the oil and impairs its flow properties. If left untreated, wax build-up may significantly increase the viscosity of the oil and eventually cause the oil lubrication system to fail completely [100].

2.5.1.2 Lubrication regimes

Lubrication regimes specify the type of lubrication that is formed under specific operating conditions. There are primarily three main lubrication regimes: boundary lubrication, mixed lubrication, and full-film lubrication [63]. The lambda ratio (λ) is a commonly used parameter for determining the lubrication regime in an operational contact. It is defined as the ratio of the

calculated minimum film thickness h_{min} and the composite surface roughness σ, as expressed in equation (2.10):

$$\lambda = \frac{h_{min}}{\sigma} = \frac{h_{min}}{\sqrt{({R_{q_1}}^2 + {R_{q_2}}^2)}} \tag{2.10}$$

where R_{q_1} and R_{q_2} are the root-mean-square surface roughness values for the two contacting surfaces. Hamrock and Dowson presented the following correlation for the estimation of h_{min} [101,102]:

$$\frac{h_{min}}{R_x} = 3.63 \left(\frac{U\eta_0}{E'R'_x}\right)^{0.68} (\alpha E')^{0.49} \left(\frac{W}{E'{R'_x}^2}\right)^{-0.073} (1 - \mathrm{e}^{-0.68k}) \tag{2.11}$$

where:

U is the entraining surface velocity, i.e. $U = (U_A + U_B)/2$, where subscripts 'A' and 'B' refer to the velocities of bodies 'A' and 'B', respectively.

η_0 is the dynamic viscosity of oil lubricant at atmospheric pressure.

E' is the reduced Young's modulus.

R'_x is the reduced radius of curvature in the direction of motion.

W is the contact load.

k is the ellipticity parameter and is defined as $k = a/b$, where 'a' is the semiaxis of the contact ellipse in the transverse direction, and 'b' is the semiaxis in the direction of motion.

α is the pressure-viscosity coefficient and is defined as $\alpha = (0.965 \log_{10}(v) + 0.6) . 10^{-8}$ where v is the kinematic viscosity. The lubrication regimes as a function of λ are depicted in **Figure 2.11**.

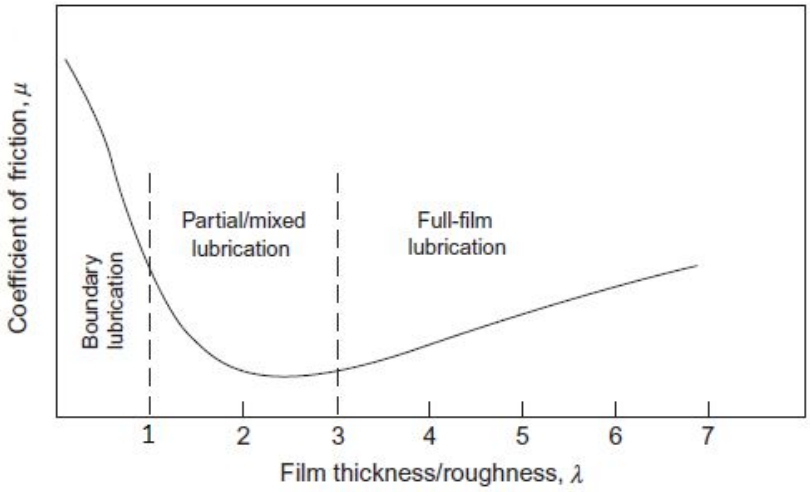

Figure 2.11: Lubrication regimes as a function of λ [63].

2.5.1.2.1 Boundary lubrication (λ <1)

The boundary lubrication regime occurs under conditions of high load or low speed in which the applied load is totally supported by contacting asperities rather than an oil film. This results in higher frictional losses and wear in comparison to the other lubrication regimes. The severity of friction and wear can be mitigated by using oil additives such as anti-wear additives, which interact with surfaces and form easily sheared protective films [64].

2.5.1.2.2 Mixed lubrication (1< λ <3)

The mixed lubrication regime occurs when there is an appreciable contact between the asperities of contacting surfaces despite the presence of an oil film. In this regime, the applied load is divided between the oil film and the contacting surface asperities. For this reason, this regime is considered a combination of boundary and full-film lubrication regimes. It generally occurs under conditions of high load, low speed, or low oil viscosity [61].

2.5.1.2.3 Full-film lubrication (λ >3)

Full-film lubrication is the lubrication regime in which surfaces are completely separated by a relatively thick oil film, and no contact occurs. In this regime, the applied load is entirely

carried by the oil film. Since there is no direct contact between the surfaces, there is little wear [63].

2.5.1.3 Types of lubricating oils

Lubricating oils consist of two primary components: base oils and additives. Mineral oils, synthetic oils, and bio-based oils are the three major types of base oils. Mineral oils are derived from petroleum and include hydrocarbons with varying carbon atoms, depending on the crude oil used. Paraffinic, naphthenic, and aromatic oils are the three major hydrocarbon families found in mineral oils. Mineral oils, in addition to carbon and hydrogen, also contain small amounts of other elements such as oxygen and sulphur. Mineral oils are the most extensively used base oils due to their abundance, low cost, wide range of viscosity, and improved solubility with oil additives [67,99]. On the downside, they have poorer lubrication performance compared to synthetic oils and are environmentally more hazardous [103].

Synthetic oils are made up of artificially made chemical compounds and can provide superior performance to mineral oils. They also provide customised solutions to meet the rising demands of industrial applications. Synthetic oils are classified into several types, including polyalphaolefins (PAOs), di-esters, polyol esters, phosphate esters, polyglycols, and silicones. PAOs are the most widely used class of synthetic oils and are made by polymerising hydrocarbon molecules (alphaolefins). Because of their great thermal and oxidative stability, superior flow characteristics at low temperatures, and low toxicity, PAOs have emerged as key components in many industrial and automotive lubricants [104].

Growing awareness of the possible environmental implications of both mineral and synthetic base oils has led to the development of bio-based oils in recent years. The most significant benefit of these oils is that they are easily biodegradable when compared to mineral oils and the majority of synthetic oils. They are already used in a number of applications, most notably in the machinery used in forests, agriculture, and mining [105,106]. They are also used in the food and pharmaceutical industries, where the risk of contamination must be reduced to a minimum [107]. The most evident drawbacks of bio-based oils are their low oxidation

resistance and poor cold flow behaviour [108,109]. In terms of economic considerations, they are two or three times more expensive than mineral oils [110].

2.5.1.4 Oil additives

Base oils are insufficient in terms of engine cleanliness, corrosion prevention, oxidation stability, and friction and wear protection. Therefore, several chemicals are deliberately added to base oils to improve their overall performance, commonly known as additives. Some additives impart new and useful properties to lubricating oils, while others enhance their existing properties. Commercially available lubricating oils include between 80% and 95% base oil, with the remaining being additives [111]. There are ten major classes of additives, categorised according to their functions, as shown in **Table 2.2**.

Table 2.2: Oil additives and their main functions [112-114].

Additive type	Function
Antioxidant	Prevents oil decomposition
VI improver	Makes oil viscosity higher at elevated temperatures
Corrosion inhibitor	Protects metallic surfaces against corrosion
Detergent	Prevents formation of sludges and varnishes
Extreme pressure additive	Protects surfaces against friction and wear at high contact pressures
Foam inhibiter	Reduces and hinders formation of foams
Friction modifier	Enhances lubricity between contacting surfaces
Pour point depressant	Improves oil's ability to flow at lower temperatures
Anti-wear additive	Protects surfaces against wear by forming a protective thin film
Dispersant	Keeps insoluble deposition products in suspension

2.5.2 Solid lubrication

Solid lubricants are materials that, despite their solid state, are able to decrease friction without the need for an external supply of liquid lubricants. Solid lubrication can address some of the drawbacks of oil lubrication. Oil lubricants are not stable at high temperatures because they break down and oxidise easily. This makes the oil thicker and more viscous, causing oil starvation. At low temperatures, oil lubricants can solidify or become highly viscous. In contrast, solid lubricants have high thermal stability and allow mechanical systems to operate at higher temperatures while maintaining low coefficients of friction [115,116]. Because of their high volatility, most oil lubricants are not particularly popular in applications operated under high vacuum conditions such as space. Solid lubricants are less volatile, making them the preferred lubricating materials for high vacuum applications [116]. For equipment immersed in liquids, such as immersion pumps, solid lubricants have an advantage over oil lubricants since they cannot be washed away or readily removed from surfaces, allowing them to remain in place for extended periods of time [117]. Solid lubricants simplify the design of mechanical systems since they eliminate the need for mechanical seals, oil reservoirs, and oil circulating systems. They are very useful for providing in-place lubrication for mechanical parts such as locks and pivots in situations where the use of oil lubricants is not practical.

2.5.2.1 Types of solid lubricants

Solid lubricants are divided into four main categories: lamellar solids, soft metals, polymers, and lubricious fluorides, oxides, and sulphates. Each category has a different lubricating mechanism as discussed below.

2.5.2.1.1 Lamellar solids

Lamellar solid lubricants are the most extensively researched type of solid lubricants and are widely used in industry. Typical examples are graphite, hexagonal boron nitride (h-BN), boric acid, calcium fluoride, and transition metal dichalcogenides (TMDs) such as MoS_2. The crystal lattice of these materials consists of hexagonal rings forming thin parallel planes on top of each other. Atoms in each plane are held together by strong covalent bonds, whereas the planes themselves are bonded to each other by weak Van der Waals forces [118]. When applied to a

sliding surface, the weak bonding facilitates easy movement of the planes over one another at a low shear strength, resulting in low friction. This mechanism of lubrication is schematically shown in **Figure 2.12**. Lamellar solids are commonly applied to tribological surfaces as thin coatings or fine powders.

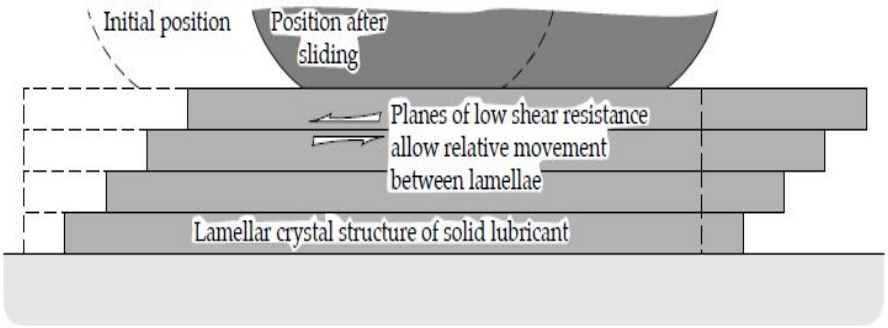

Figure 2.12: Schematic representation of solid lubrication provided by lamellar solids [64].

2.5.2.1.2 Soft metals

Soft metals such as lead, platinum, indium, tin, silver, and gold can be used as solid lubricants owing to their low shear strengths and high plasticity [119]. The applications of soft metals are limited by their physical properties. Lead, indium, and tin are prone to oxidation and melting when used in applications involving high temperatures [120]. For this reason, gold and silver are commonly used in high-temperature applications because they offer excellent oxidative stability and have high melting points [120]. Soft metals are commonly applied to tribological surfaces as thin coatings by various deposition techniques such as electroplating, magnetron sputtering, and ion plating [119].

2.5.2.1.3 Polymers

Polymers are used in a wide variety of tribological applications due to their lightweight nature, resistance to corrosion and chemicals, low cost, and ease of fabrication. Certain polymers such as polytetrafluoroethylene (PTFE), polyetheretherketones (PEEK), ultra-high-molecular-weight polyethylene (UHMWPE), and polyimide have self-lubricating properties due to their weak molecular bonds [120,121]. They can be applied to tribological surfaces by spraying their

powders and then curing them at high temperatures [122]. Some polymers such as PTFE can be used as additives in oils and greases [123,124].

2.5.2.1.4 Lubricious fluorides, oxides, and sulphates

Certain fluorides (calcium fluoride, barium fluoride, and magnesium fluoride), oxides (lead monoxide, molybdenum trioxide, and rhenium oxide), and sulphates (calcium sulphate, barium sulphate, and strontium sulphate) can be used as solid lubricants for high-temperature applications because they become soft and shear easily at high temperatures [122]. However, they cannot be used to provide lubrication under normal ambient conditions due to their brittleness [115,125]. They are commonly applied to tribological surfaces as surface coatings by various deposition techniques such as plasma spraying and fusion bonding [125]. They can also be blended with other solid lubricants to provide lubrication over considerably larger temperature ranges [115].

2.6 Transition metal dichalcogenides (TMDs)

2.6.1 Overview

TMDs are a class of layered materials that have attracted enormous research interest owing to a unique combination of structural and physical properties. These properties result from the existence of non-bonding *d* bands and the degree to which the bands are filled with electrons [126,127]. TMDs have the chemical formula MX_2, where M is a transition metal from groups 4-10 of the periodic table (such as Mo, W, and V), and X is a chalcogen element (S, Se, and Te). **Figure 2.13** depicts the periodic table of elements, with transition metals and chalcogens forming layered structures highlighted. Metals that form layered structures with some chalcogens but not with others are partially highlighted. Depending on their chemical compositions and structural configurations, TMDs can be divided into insulators (e.g. HfS_2), semiconductors (e.g. MoS_2 and WS_2), semimetals (e.g. WTe_2 and $TiSe_2$), and superconductors (e.g. NbS_2 and VSe_2) [126].

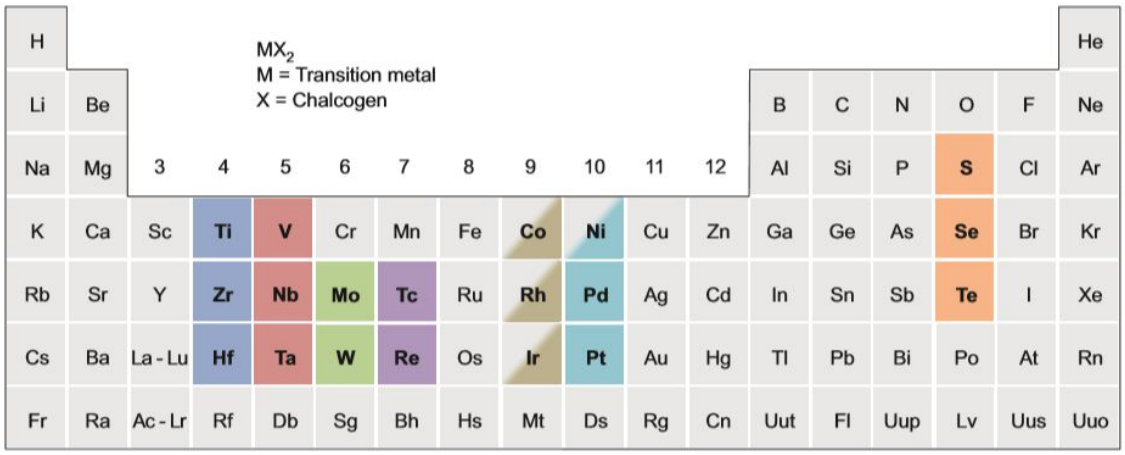

Figure 2.13: The transition metals and the three chalcogen elements that crystallise into layered structures are highlighted in the Periodic Table. The transition metals that crystallise into layered structures with some chalcogens but not with others are partially highlighted [126].

Transition metal disulphides (MS_2) are the most investigated TMDs, with MoS_2 accounting for more than half of all TMD publications. The wide range of accessible TMDs and their useful properties make them attractive for a broad array of applications such as electronics [128,129], optoelectronics [130,131], chemical sensing [132,133], energy storage [134-136], and tribological applications [42,43,57]. Among different TMDs, only disulphides and diselenides of molybdenum and tungsten have favourable tribological properties and are typically used as oil additives [137-139] or surface coatings [43,45,53,59]. The latter can be fabricated as thick coatings prepared by, for example, burnishing [140,141] or electrochemical processes [142-144] or as thin coatings predominantly deposited by PVD. TMDs can also form on tribological surfaces as low-friction tribofilms by tribo-chemical reactions [145-148].

2.6.2 Crystal structure of TMDs

The crystal structure of TMDs can be hexagonal or rhombohedral. We will discuss only the hexagonal structure in this section because it is the most used structure in tribological applications. It results from the stacking of layers of hexagonally packed atoms with two consecutive chalcogen atom planes separated by a plane of metal atoms [149], as shown in

Figure 2.14. Atoms forming this three-layer configuration are connected by strong covalent bonds. The layers themselves are held together by weak Van der Waals bonds.

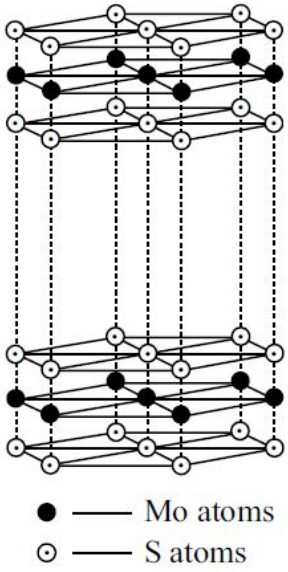

Figure 2.14: Schematic representation of the crystal structure of MoS_2 [116].

2.6.3 Lubrication mechanism of TMDs

The excellent self-lubricating behaviour of TMD coatings stems from their highly anisotropic crystal structure. When a nanocrystalline or amorphous TMD structure is present on a hard surface and subjected to shear deformation during tribological contact, it rearranges to produce a crystalline tribofilm. The topmost atomic layers of this tribofilm become horizontally aligned and parallel to the sliding direction, as shown in **Figure 2.15 (a)**. As a result, the shear strength is minimised at the contact interface, resulting in a very low coefficient of friction [48,150-153]. As sliding progresses, some of the coating material detaches from the coating surface and adheres to the sliding counterpart, resulting in the formation of a transfer film. The composition and structure of this transfer film are similar to those of the original coating. The topmost layers of this transfer film also align parallel to the sliding direction. The formation of a transfer film with easily sheared layers plays a vital role in the low-friction mechanism of TMD coatings since it results in predominantly TMD/TMD interfacial sliding and prevents the direct contact between sliding surfaces [151,154-158]. The ability of TMD coatings to form transfer films on

their sliding counterparts implies that it is not necessary to coat both sliding surfaces since coating one of them is enough to provide low friction.

When a TMD tribofilm is mechanically removed during sliding, the coefficient of friction and coating wear both rise dramatically. Consequently, active tribofilm regeneration is required to protect the underlying coating and avoid a rapid rise in friction and wear. TMD tribofilms can repair themselves autonomously and continuously to replenish the consumed lubricous layers, thereby recovering their functionality [151,159,160]. When a TMD tribofilm is formed during sliding, its total thickness is typically in the range 100-1000 nm, with the topmost part having a thickness between 5 nm and 50 nm and exhibiting a desirable alignment parallel to the sliding direction [151,161], as shown in **Figure 2.15 (b)**.

In summary, the low-friction mechanism of TMD coatings is governed by: (a) the shear-induced orientation of TMD basal planes parallel to the sliding direction to facilitate interlamellar slip with minimal frictional resistance to motion and (b) the formation of a transfer film on the sliding counterpart to prevent direct contact between the surfaces and accommodate interfacial shear.

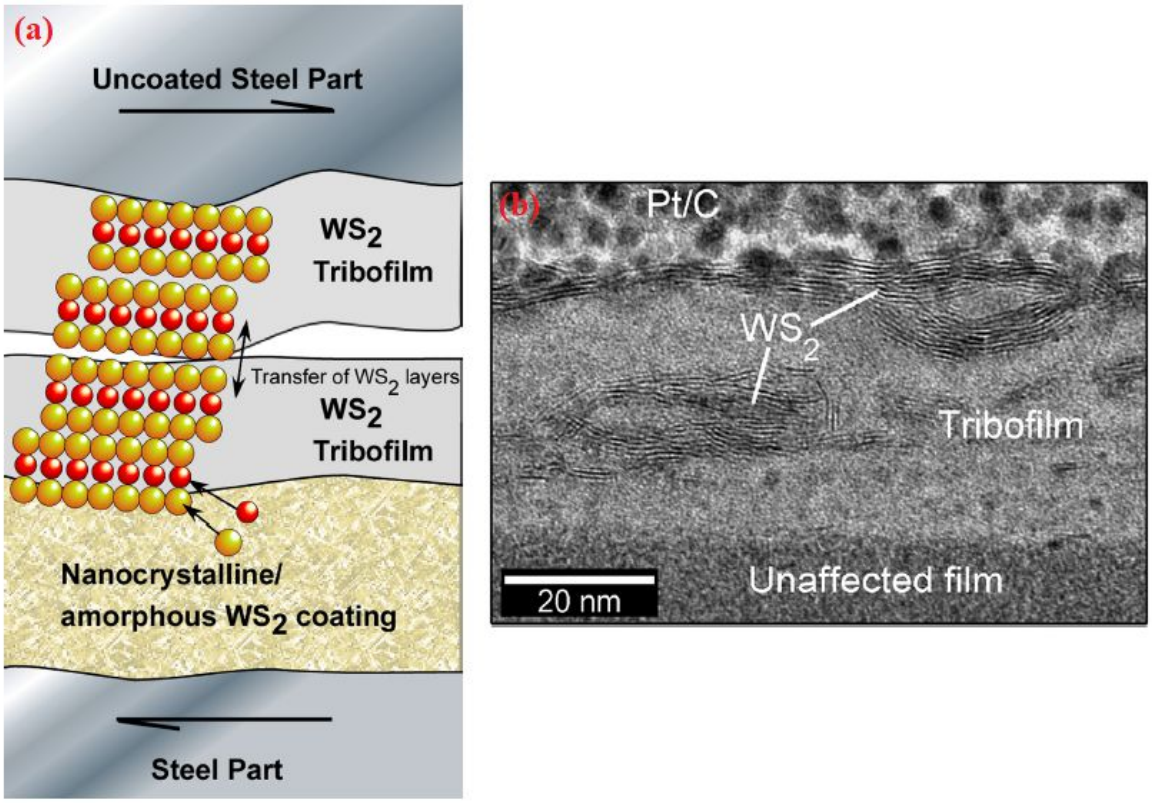

Figure 2.15: (a) WS_2 coating becomes crystallised during sliding, and a few of the topmost atomic layers become aligned with the basal planes parallel to the sliding direction. This mechanism is accompanied by the transfer of some coating material to the counterpart [151]. (b) TEM image shows horizontally aligned WS_2 planes on the top surface of a wear track and within the amorphous tribofilm [162].

2.6.4 TMD coatings

2.6.4.1 Molybdenum disulphide (MoS_2)

Among several TMDs, MoS_2 is the predominant material used as a solid lubricant. Ball bearings, gears, slip rings, pointing mechanisms, actuators, and release mechanisms are some examples of components in space applications that currently use MoS_2 coating [163-165]. Its most notable early application was on the Apollo Lunar Module's extendible legs in 1969 [166]. For space-related technologies, MoS_2 has been generally used in three types: burnished, bonded, and sputtered. Burnishing of MoS_2 powder onto a metal surface often results in surface coatings with a thickness ranging from 0.1 μm to 10 μm [165]. The resulting coating thickness

and adhesion are highly dependent on the substrate preparation and burnishing method, both of which are difficult to control and replicate. As a result of their weak adhesion, burnished MoS_2 coatings have low endurance when compared to other preparation procedures [166]. Bonded MoS_2 coatings are made from a mixture of MoS_2 powder and an adhesive binder. In comparison to the burnished ones, they have better adhesion to substrates because of the use of the binder, resulting in a higher load-bearing capacity. However, they often have a thickness ranging from 5 μm to 25 μm, which is difficult to control and dimensionally inappropriate (too thick) for high-precision components [165]. In addition, the presence of the binder causes coefficients of friction to be higher than they would be without the binder. MoS_2 coatings made using sputtering have a precisely controlled thickness in the range 0.2-2 μm and outperform the burnished and bonded ones in terms of purity, density, and adhesion [165]. Roberts et al. [167] tested the tribological performance of MoS_2 coatings produced by the three methods mentioned above in a pin-on-disk tribometer under high vacuum conditions, as shown in **Figure 2.16**. The one produced by sputtering showed the best tribological properties, with the lowest coefficient of friction and longest endurance life. Such excellent tribological behaviour of the sputtered MoS_2 coating was attributed to better adhesion, higher purity (due to the vacuum deposition technique), and higher density compared to those made by burnishing and bonding.

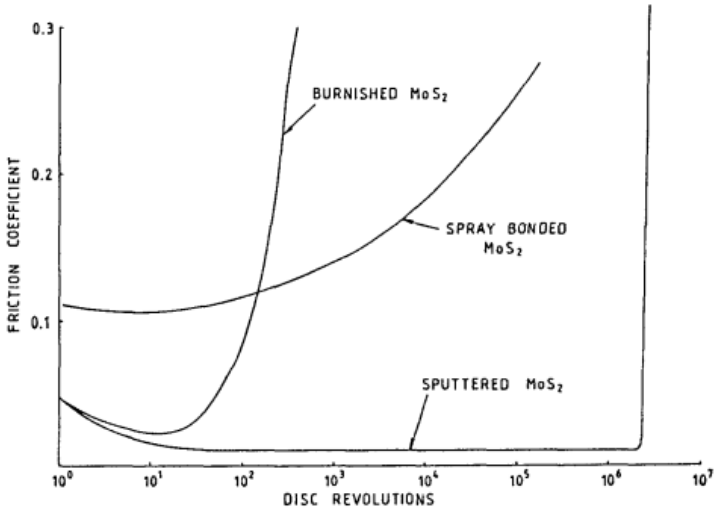

Figure 2.16: Coefficients of friction of MoS_2 coatings prepared by burnishing, bonding, and sputtering under high vacuum conditions. (Test conditions: counterparts: 52100 steel balls; normal load: 50 N) [167].

MoS_2 coating is intrinsically triboactive. It displays exceptional self-lubricating performance without relying on additives. This is different from other solid lubricants such as graphite, which require the presence of contaminants such as water vapour to provide lubrication [168]. For this reason, MoS_2 coating can provide a very low coefficient of friction when operating in vacuum or inert atmospheres. The coefficients of friction of sputtered MoS_2 coating evaluated in vacuum are typically in the range 0.01-0.04, with extremely low wear and endurance lifetimes of several million cycles [169]. It also exhibits superlubricity, with coefficients of friction between 0.001 and 0.003 when sliding under ultra-high vacuum (UHV) conditions [170,171]. This extremely low friction was caused by two factors: (a) the orientation of MoS_2 basal planes parallel to the sliding direction and (b) the absence of any contaminants on sliding surfaces [170,171]. Another advantage of MoS_2 coating as a lubricant is its high thermal stability and ability to maintain favourable tribological properties at high temperatures. In vacuum, the maximum operating temperature at which MoS_2 coating provides effective lubrication is 650 °C [172].

The outstanding tribological properties of MoS_2 coating in vacuum and at a wide range of temperatures make it an obvious candidate as a solid lubricant for use in space applications. However, its lubricity rapidly degrades in humid air due to its high sensitivity to air humidity, which represents a substantial barrier to its widespread usage in high-demanding terrestrial applications. Vierneusel et al. [173] examined the tribological behaviour of MoS_2 coating in vacuum and humid air, as shown in **Figure 2.17**. In vacuum, the coating showed a very low coefficient of friction of 0.022 and did not fail. In humid air, it showed a high coefficient of friction of 0.112, which was five times higher than the one obtained in vacuum. It also showed very poor wear resistance and failed after 360 m of sliding.

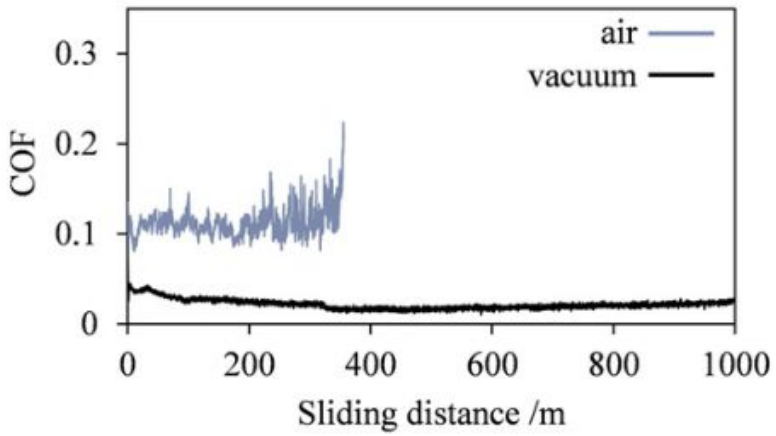

Figure 2.17: Coefficients of friction of MoS_2 coating in vacuum and humid air (RH: 40%). (Test conditions: counterparts: 100Cr6 steel balls; normal load: 10 N; temperature: 23 °C) [173].

Donnet et al. [170] tribologically tested sputtered MoS_2 coating in UHV, HV, dry nitrogen, and ambient air. The lowest coefficient of friction of 0.004 was measured in UHV, whereas the highest coefficient of friction of 0.2 was measured in ambient air. In another study, MoS_2 coating exhibited low coefficients of friction in the range 0.005-0.05 and a wear rate of the order of 10^{-8} $mm^3/N.m$ under vacuum conditions [174]. Under humid air conditions, it exhibited higher coefficients of friction in the range 0.15-0.30, and the wear resistance decreased by a factor of 10 to 1000 when compared to those obtained under vacuum conditions [174].

Recent advancements in the field of coating technology, particularly the use of closed field unbalanced magnetron sputter ion plating (CFUBMSIP) to dope MoS_2 coating with titanium, have resulted in coatings with improved resistance to air humidity [45,53,54]. These advancements allowed MoS_2-based coatings to be used successfully in dry machining operations such as forming and cutting [54]. Despite these improvements, it is anticipated that for the foreseeable future, MoS_2 coating will continue to be used primarily in space applications, with ongoing research aiming at tailoring its tribological properties for a wide range of operating conditions.

2.6.4.2 Molybdenum diselenide ($MoSe_2$)

$MoSe_2$ is similar to MoS_2 in terms of sandwich microstructure, lattice constant, and excellent lubricity. However, it has been less explored than MoS_2 coating for tribological purposes. In vacuum and dry air, $MoSe_2$ coating has a higher wear rate than MoS_2 coating [56,58], which is one of the reasons contributing to its low exploration. Another reason is that, in contrast to MoS_2 coating, it is not readily available as a natural material. Similarly, sulphur is found in greater abundance in nature than selenium. This adds to the financial burden of $MoSe_2$ from a cost perspective. Nevertheless, tribological studies with $MoSe_2$ coating have demonstrated that it can be a good alternative to MoS_2 coating, with the advantage of being more resistant to the adverse effects of humidity, although the underlying reason behind this is still unknown [43,56-58].

Another advantage of $MoSe_2$ coating is the small atomic mass difference between its chemical elements when compared to MoS_2 and WS_2 coatings [175]. This is important for the deposition of the coating via magnetron sputtering since the scattering behaviour of the sputtered atoms travelling from the target to the substrates will be comparable, allowing for an easily regulated Se/Mo ratio that determines the resulting properties and structure of the coating. Furthermore, the preferential re-sputtering of Se atoms from the growing film as a result of bombardment with energetic species is minimised [176,177]. $MoSe_2$ coating is more thermally stable than MoS_2 coating and can provide satisfactory lubrication up to 980 °C under vacuum conditions [58]. In humid air, $MoSe_2$ coating starts to oxidise at higher temperatures than MoS_2 coating [56]. However, they both oxidise at the same rate at a temperature of 450 °C [178].

2.6.4.3 Tungsten disulphide (WS_2)

Although MoS_2 coating was extensively explored during the earliest phase of research on TMDs, WS_2 coating eventually emerged as the primary study focus owing to its extraordinary features. Compared with MoS_2, the load-bearing capacity of WS_2 is impressive, being almost three times more than that of MoS_2 [179]. It also has higher thermal stability than MoS_2, making it suitable for use under harsh conditions of temperature. It can be satisfactorily used in air at temperatures ranging from 270 °C to 650 °C and in vacuum at temperatures ranging from 188

°C to 1316 °C [172,180,181]. It is also more stable and resistant to oxidation [182]. In air, it starts to oxide at a temperature of 400 °C, whereas MoS_2 starts to oxidise at a temperature of 300 °C [58,172]. The oxidation of WS_2 results in the formation of a compact WO_3 protective layer, which can prevent further oxidation of the material [172]. In addition, WO_3 provides a lower coefficient of friction than the corresponding MoO_3. The coefficient of friction of WO_3 is in the range 0.2-0.3, whereas MoO_3 has a coefficient of friction ranging from 0.5 to 0.6 [183]. However, the cost of WS_2 is relatively high, being almost three times more than that of MoS_2 [116].

WS_2 coating exhibits a very low coefficient of friction when operating in vacuum or inert atmospheres. **Figure 2.18** shows the friction behaviour of WS_2 coating when tested in dry nitrogen and humid air. In dry nitrogen, the coating produced a smooth friction curve with a very low coefficient of friction of 0.04, whereas humid air increased the coefficient of friction to 0.15 [184]. In another study, WS_2 coating was tested in vacuum against a steel ball at a normal load of 2 N and showed a very low coefficient of friction of 0.03 [185].

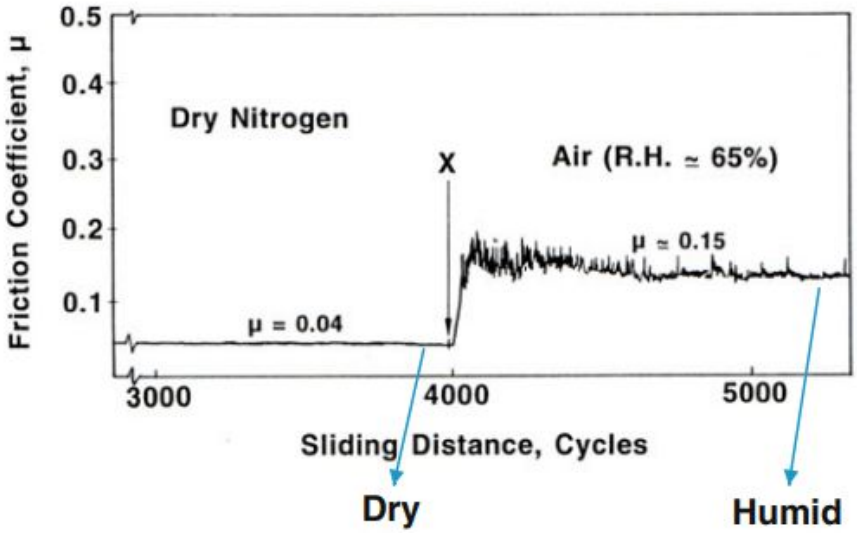

Figure 2.18: Transition in the coefficient of friction of WS_2 coating from dry nitrogen to humid air (RH: 65%). (Test conditions: counterpart: 440C stainless steel ball; normal load: 1 N; temperature: room temperature) [184].

2.6.4.4 Tungsten diselenide (WSe_2)

While WS_2 coating has been studied quite intensively, a rather small amount of attention has been paid so far to WSe_2 coating. WSe_2 coating has similar physical and chemical properties and a layered crystal structure to that of WS_2 coating [186]. Nevertheless, a number of studies have demonstrated that WSe_2 coating can be a viable alternative to MoS_2 and WS_2 coatings as a solid lubricant in a variety of tribological applications operating in vacuum or humid air due to its higher chemical stability and lower humidity sensitivity [186-190].

Simmonds et al. [191] evaluated the tribological properties of MoS_2 coatings doped with WSe_2, Au, Cr, and Ti. WSe_2 was found to be the best dopant for improving the tribological performance of the coatings owing to its lower sensitivity to air humidity and excellent wear resistance. Meister et al. [187] evaluated the tribological performance of MoS_2 and WSe_2 coatings against steel balls in ambient air and dry nitrogen at a normal load of 2 N. WSe_2 coating showed better friction results in both testing environments. In humid air, it exhibited a coefficient of friction of 0.08, which was significantly lower than 0.19 exhibited by MoS_2 coating [187]. In dry nitrogen, WSe_2 coating showed a very low coefficient of friction of 0.02 compared to a coefficient of friction of 0.06 exhibited by MoS_2 coating [187]. In another study, Meister et al. [189] examined the tribological properties of WSe_2 coating in ambient air (1 x 10^3 mbar) and two HV pressures (4 x 10^{-7} mbar and 3.5 x 10^{-8} mbar), HV-1 and HV-2, respectively, as shown in **Figure 2.19**. All the coefficients of friction were found to be below 0.1. The lowest coefficient of friction of 0.04 was achieved at HV-1, whereas the highest coefficient of friction of 0.08 was obtained in ambient air [189].

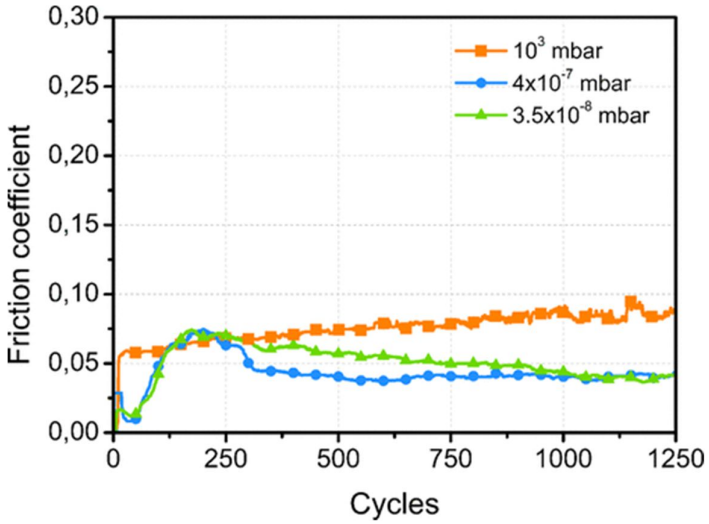

Figure 2.19: Coefficients of friction of WSe_2 coating tested in ambient air (1 x 10^3 mbar), HV-1 (4 x 10^{-7} mbar), and HV-2 (3.5 x 10^{-8} mbar). (Test conditions: counterparts: 100Cr6 steel balls; normal load: 1 N; temperature: room temperature) [189].

2.6.5 Drawbacks of TMD coatings

Despite their excellent tribological performance, TMD coatings have several drawbacks that prevent them from being widely used as solid lubricant coatings as follows:

1. They are extremely sensitive to environmental attacks. When sliding in humid air, the presence of humidity negatively influences their tribological performance by increasing their coefficients of friction and wear rates [42,43,192-194]. For this reason, they exhibit very low coefficients of friction, excellent wear resistance, and extended lifetimes only in dry air or vacuum.

2. They are commonly deposited by magnetron sputtering, which inevitably results in the formation of characteristic columnar morphologies perpendicular to substrates with high levels of porosity [43,195-199], as shown in the example in **Figure 2.20**. Consequently, the adhesion of the coatings to substrates and their load-bearing capacity are very low, causing them to flake off during sliding [43,195]. On the other hand, the high porosity allows high reactivity of the coatings and easily facilitates the penetration

of oxygen and reactive species in humid air, leading to deteriorated tribological properties. It also makes storing the coatings in an open environment difficult.

3. Compared with other competitive low-friction coatings such as DLC coatings, TMD coatings generally exhibit low hardness, typically in the range 0.3-2 GPa, depending on the deposition parameters and subsequent surface morphology achieved [43].

4. Tribological materials are frequently subjected to high temperatures owing to frictional heating. Because of their poor thermal conductivity, TMD coatings are incapable of effectively dissipating the frictional heat generated at sliding contacts [44,165,200-203]. This is another constraint on their widespread usage, particularly in situations where high heat generation is intolerable.

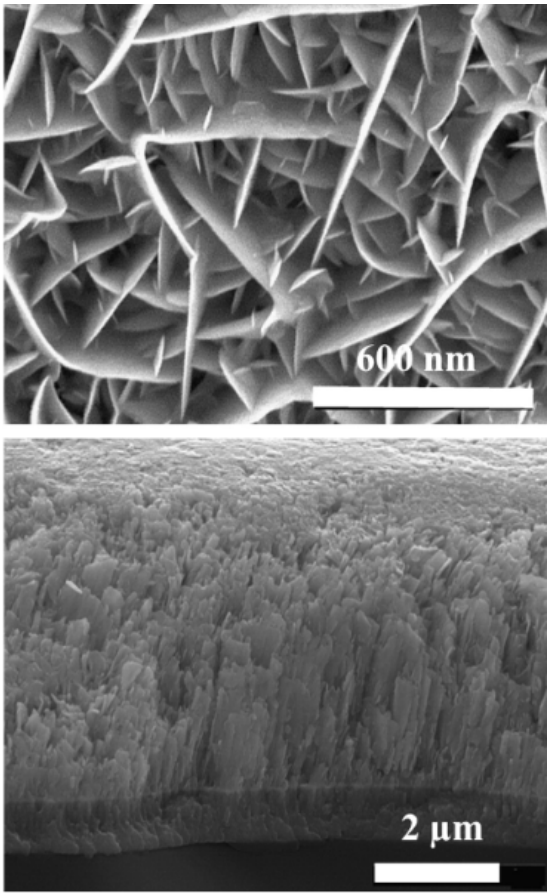

Figure 2.20: SEM images of purely sputtered WS_2 coating show its porous and columnar morphology [43].

2.6.6 Effect of operating parameters on the tribological properties of TMD coatings

The tribological behaviour of TMD coatings is not only dependent on intrinsic conditions such as the microstructure but also on various extrinsic conditions such as air humidity, operating temperature, and applied load.

2.6.6.1 Effect of air humidity

When sliding occurs in humid air, dangling or unsaturated bonds on the edges of TMD basal planes react with oxygen and moisture in the environment to form tribo-oxidation products such as MoO_3 and WO_3 [184,204-206]. The formation of these oxides is very detrimental to the self-lubricating performance of TMD coatings. They act as contaminants in the hexagonal structure of the coating, causing strong interplanar bonding and, consequently, a high interfacial shear strength [55,150,184,206,207]. As a result, the coating loses its self-lubricating properties and exhibits an increased coefficient of friction. This also leads to reduced wear resistance, diminishing the coating lifetime. Zhao et al. [208] studied the tribological behaviour of MoS_2 coating under different levels of relative humidity (RH), as shown in **Figure 2.21**. The coefficient of friction was observed to increase with increasing air humidity. The lowest coefficient of friction of 0.04 was obtained at the lowest RH of 10%, and the highest coefficient of friction of 0.25 was obtained at the highest RH of 70%. The coating wear rate was also observed to increase with increasing air humidity. In another study, Nabot et al. [209] found that increasing RH from 5% to 60% caused an increase in the coefficient of friction of MoS_2 coating from 0.05 to 0.27. A similar behaviour was also observed by Zhang et al. [210] in which the coefficient of friction of MoS_2 coating was 0.06 at 10% RH, but it increased to 0.14 at 90% RH.

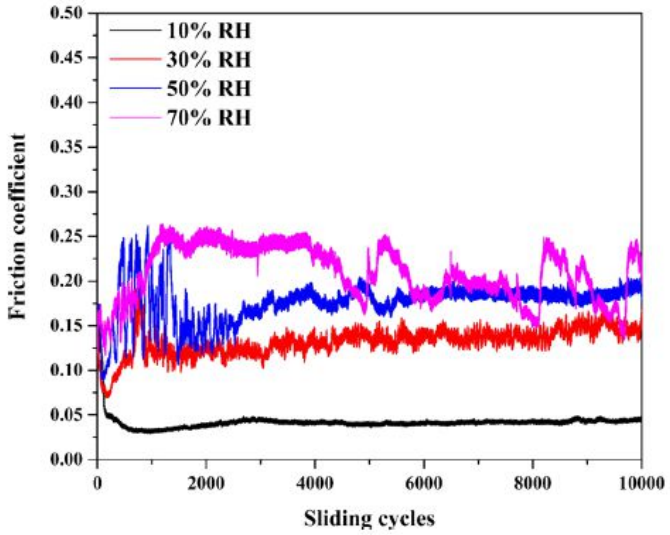

Figure 2.21: Coefficients of friction of MoS_2 coating tested under different levels of RH. (Test conditions: counterparts: GCr15 steel balls; normal load: 2 N; temperature: room temperature) [208].

Despite sharing the common sensitivity characteristics to humid air, TMD coatings have different tribological responses to air humidity. WS_2 and WSe_2 coatings have a clear advantage over MoS_2 coatings in terms of oxidation resistance. The reason for this is the formation of WO_3, which is more protective against further oxidation and provides a lower coefficient of friction than the corresponding MoO_3 [186,187,211-215]. When comparing the friction performance of MoS_2 and $MoSe_2$ coatings, the latter is less sensitive to air humidity and provides better lubrication. Kubart et al. [56] conducted a comparative study on the tribological properties of MoS_2 and $MoSe_2$ coatings under different levels of RH, as shown in **Figure 2.22**. $MoSe_2$ coating was observed to outperform MoS_2 coating because it was less sensitive to air humidity and had lower coefficients of friction than MoS_2 coating. It was also observed that the coefficient of friction of $MoSe_2$ coating was almost independent of air humidity [56]. This clearly shows that $MoSe_2$ coating has a lot of potential as a good alternative to MoS_2 coating for mechanical components used in humid air.

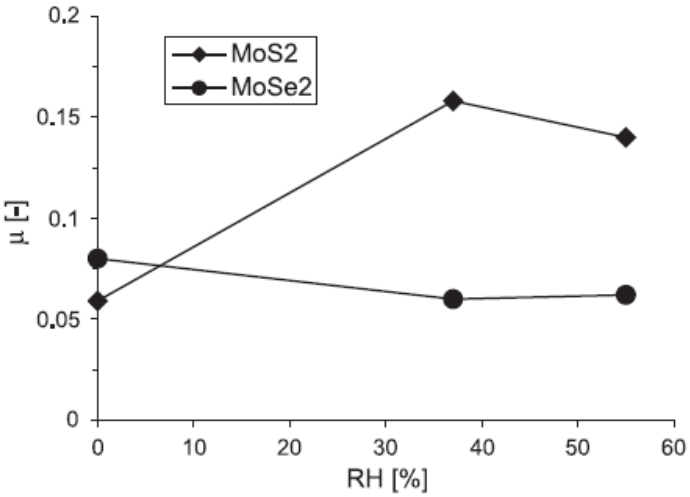

Figure 2.22: Coefficients of friction of MoS_2 and $MoSe_2$ coatings tested under different levels of RH. (Test conditions: counterparts: 100Cr6 steel balls; normal load: 5 N; temperature: room temperature) [56].

2.6.6.2 Effect of operating temperature

The operating temperature of TMD coatings also has a considerable impact on their tribological performance. Their self-lubricating properties in humid air generally degrade with increasing temperature because of increased oxidation [150,166,216-220]. The transition temperature for MoS_2 coating, at which the oxidation rate drastically rises, has been reported to be in the range 100-400 °C, depending on the method used for coating preparation [56,178,221-223]. Meng et al. [224] studied the tribological performance of MoS_2 coating at temperatures ranging from 25 °C to 500 °C, as shown in **Figure 2.23**. The coefficient of friction started to show a significant increase beyond 350 °C. At temperatures less than 350 °C, the coefficients of friction were stable and had values smaller than that observed at room temperature.

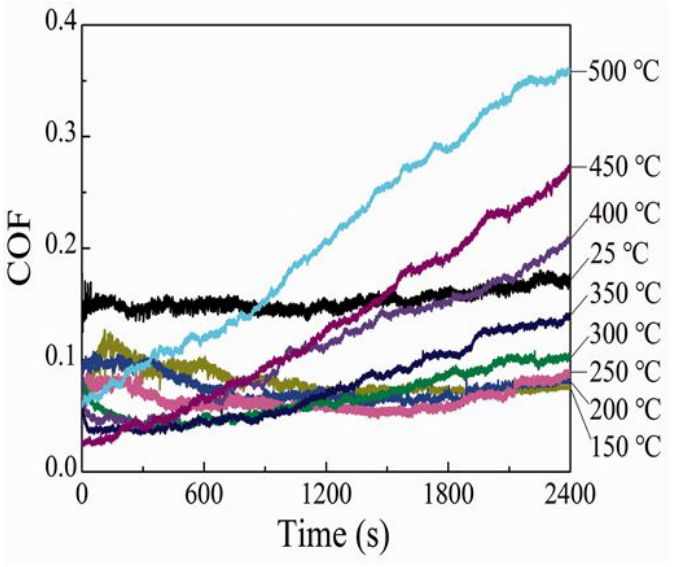

Figure 2.23: Friction curves of MoS_2 coating tested at different temperatures. (Test conditions: counterparts: GCr15 steel balls; normal load: 10 N) [224].

WS_2 coating offers improved thermal stability and a 100 °C increase in the maximum operating temperature when compared to MoS_2 coating, making it more suitable for high-temperature applications [172]. Similarly, $MoSe_2$ coating is more thermally stable than MoS_2 coating and has less temperature-sensitive oxidation [56,57,225]. Kubart et al. [56] investigated the effect of operating temperature on the tribological properties of MoS_2 and $MoSe_2$ coatings, as shown in **Figure 2.24**. The coefficient of friction of MoS_2 coating dropped from 0.14 to 0.05 as the temperature increased from room temperature to 100 °C. The decrease in friction was attributed to a decrease in relative humidity in the atmosphere surrounding the heated coating sample. In contrast, the coefficient of friction of $MoSe_2$ coating was stable at about 0.06 up to 200 °C. At higher temperatures, the coefficient of friction of both coatings increased owing to a higher degree of coating oxidation at elevated temperatures [56].

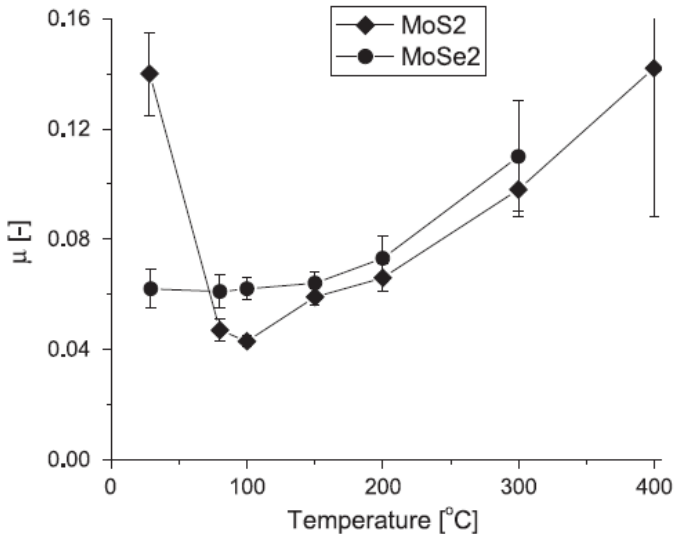

Figure 2.24: Coefficients of friction of MoS_2 and $MoSe_2$ coatings tested at different temperatures. The error lines correspond to the standard deviation of the mean value. (Test conditions: counterparts: 100Cr6 steel balls; normal load: 5 N; relative humidity: 50%) [56].

2.6.6.3 Effect of applied load

TMD coatings typically exhibit a reduction in the coefficient of friction with increasing load, making them suitable for highly loaded mechanical components [224,226-228]. Such behaviour contrasts with Amontons' first law of friction, which states that there is a direct proportional relationship between frictional force and applied load [229]. This load-dependent friction behaviour of TMD coatings is not fully understood and has been investigated by several research groups. According to Midgley [230] and Gansheimer [231], the decrease in the coefficient of friction displayed by TMD coatings with increasing load is due to frictional heating at the sliding interface, which causes the drying of air humidity. According to several studies, higher loads facilitate the formation of TMD tribofilms and result in a higher degree of parallel alignment of basal planes, leading to lower interfacial shear strengths and, thus, lower coefficients of friction [204,226,232].

Meng et al. [224] studied the tribological performance of MoS_2 coating at different applied loads, as shown in **Figure 2.25**. The coefficient of friction was found to decrease with

increasing load. The lowest coefficient of friction of 0.013 was obtained at the highest applied load of 50 N. The transfer of the coating material to the counterpart surface was reported to be proportional to the applied load. This promoted the formation of compact and continuous transfer films on the sliding counterparts, resulting in lower coefficients of friction at higher loads.

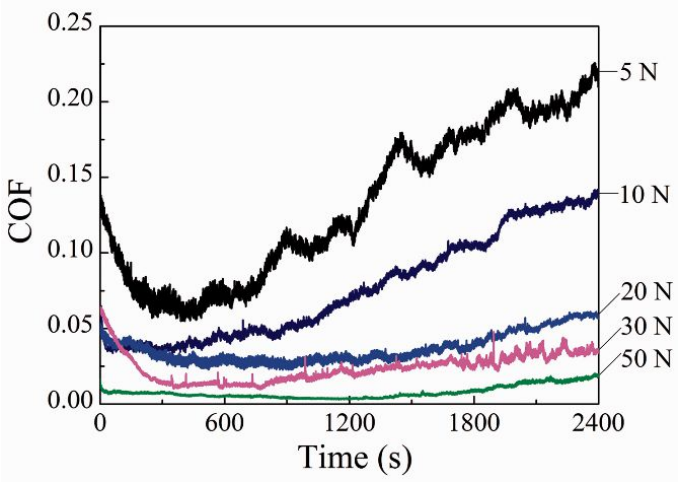

Figure 2.25: Friction curves of MoS_2 coating tested at different applied loads. (Test conditions: counterparts: GCr15 steel balls; temperature: 350 °C) [224].

2.6.7 Metal-alloying of TMD coatings

As previously discussed, the main drawbacks of TMD coatings limiting their extensive applications are low hardness, porous and columnar nature, low load-bearing capacity, and high reactivity with oxygen in humid air. Significant research efforts have been directed towards addressing these drawbacks using two primary approaches. The first approach is based on changing the method of deposition and controlling the deposition parameters. This approach can improve the microstructural properties of TMD coatings by: (a) changing the method of deposition such as by using ion-beam-assisted deposition [233-236], high-power impulse magnetron sputtering [237], N_2-spray deposition [238], unbalanced magnetron sputtering [173,193,239] or pulsed magnetron sputtering [240], (b) minimising the oxygen content in the coating by reducing residual oxygen and any water vapour present in the deposition chamber [241,242], and (c) adjusting sputtering parameters during coating deposition such as reducing sputtering gas pressure and substrate temperature to achieve a compact microstructure with the

lowest possible density of defects [206,210,243-248]. This approach can improve the resistance of TMD coatings to environmental attacks, but it has no major effect on their mechanical properties.

The second approach, which has been used since 1970 [249], is based on the incorporation of a small amount of metallic elements into TMD coatings during deposition. The main goal of this approach is to make TMD microstructures denser so that their typical porosity can be reduced, adhesion to substrates can be improved, and wear resistance in humid air can be made better. In general, this approach has been successful in meeting its goal. **Table 2.3** lists different metal-alloyed TMD coatings and their hardness and coefficients of friction. Ti has received the greatest attention and has been found to be the most successful alloying metal from a commercial perspective. The incorporation of Ti into MoS_2 coating has been introduced to the market with the tradename 'MoST' by Teer Coatings Ltd [250].

Although alloying TMD coatings with metals generally results in an improvement in their mechanical properties and wear resistance, they still exhibit high coefficients of friction when exposed to humid air. This is because alloying metals can impede the formation of effective tribofilms [251-253]. Furthermore, some metals such as Ti tend to oxide during sliding because of their low thermal stability, which results in the formation of abrasive oxide particles [251,254-257]. If these newly formed particles become trapped at the sliding interface, they can cause severe wear of sliding surfaces and, in some cases, complete coating failure. Apart from that, low alloying concentrations for certain metals such as Cr and Ti are recommended in the literature [45,258,259]. Consequently, the benefit obtained from this alloying with low metal concentrations will be negligible on the porous and columnar nature of TMD coatings. Metal-alloying of TMDs is generally unfavourable for industrial applications because: (a) operational costs can rise dramatically such as in the case of Au, (b) some metals have low deposition rates, and some are difficult to deposit, and (c) PVD systems must be equipped with at least two targets, one for the alloying metal and the other for TMD, resulting in higher processing and development costs.

TMD coatings have also been alloyed with several compounds such as TiB_2 [260-262], ZnO [263-265], PbO [266,267], B_2O_3 [268], Sb_2O_3 [269-273], TiN [274], and CaF_2 [275]. However, the benefit of alloying with such compounds was found to be insignificant compared to that of metals.

Table 2.3: Hardness, tribological testing parameters, and coefficients of friction of different metal-alloyed TMD coatings.

Coating system	Metal content (at.%)	Hardness (GPa)	Applied load (N)	Sliding counterpart	Relative humidity (%)	Coefficients of friction
Mo-S-Ti [276]	16	7.9	2	AISI 52100 steel	45-50	0.14
Mo-S-Ti [45]	5-20	9.8-16.4	2-80	WC	40-50	0.04-0.1
Mo-S-Ti [55]	5-15	15-21	10-80	Stainless steel 316L	41	0.02-0.1
Mo-S-Ti [277]	10-30	7.2-8.4	20	Alumina	8-98	0.005-0.65
Mo-S-Ti [259]	5.5	13.4	5	WC	30	0.1
Mo-S-Ti [251]	12-31	-	10	440C steel	45-55	0.05-0.08
Mo-S-Ti [278]	20	-	5	WC	50	0.09
Mo-S-Ti [250]	-	4	10-80	WC/Co	40	0.025-0.5
Mo-S-Ti [279]	-	-	5	AISI 52100 steel	50	0.2-0.65
W-S-Ti [206]	2-35	-	1	Si_3N_4	40	0.1-0.2
Mo-S-Cu [280]	15.9	3.14	2	AISI 52100 steel	45	0.07
Mo-S-Cu [257]	7.8-47.99	-	10	GCr15 steel	60	0.05-0.6
Mo-S-Zr [45]	5-30	7.9-8.9	2-80	WC	40-50	0.03-0.12
Mo-S-Cr [45]	5-20	9.4-15.8	2-80	WC	40-50	0.03-0.15
Mo-S-Cr [277]	10-33	6.1-7.5	20	Alumina	8-98	0.005-0.85
Mo-S-Cr [258]	5-13	7.28-8.29	10	AISI 52100 steel	45-55	0.09-0.17
Mo-S-Si [281]	3.5-17.3	6.3-7.2	10	GCr15 steel	50	0.08-0.11
Mo-S-W [45]	5-20	5.6-6.4	2-80	WC	40-50	0.02-0.04
Mo-S-W [282]	1.7-10.8	6.4-7.7	5	GCr15 steel	33	0.04-0.08
Mo-S-Au [283]	5	5.2	40	WC/Co	45	0.05
Mo-S-Au [284]	32-80	-	5	440C steel	1	0.05-0.12

Mo-S-Au [266]	-	-	1	100Cr6 steel	50	0.15
Mo-S-Au [285]	42-89	-	5	440C steel	1	0.03-0.04
Mo-S-Pb [286]	2.3-14.8	3.8-7.2	5	GCr15 steel	13-75	0.04-0.2
Mo-S-Pb [287]	4-26	-	9.8	AISI 52100 steel	2	0.007-0.02
Mo-S-Y [288]	-	7.5	5	GCr15 steel	75-80	0.13
Mo-S-Al [289]	4-15	1.2-1.5	1	M-50 steel	10-40	0.06-0.14
Mo-S-Pb [279]	-	-	5	AISI 52100 steel	50	0.1-0.6
Mo-S-Nb [290]	10.8	5.3	5	AISI 52100 steel	45-55	0.08
Mo-S-Ni [266]	-	-	1	100Cr6 steel	50	0.27
Mo-S-Ni [272]	5	-	5	AISI 52100 steel	45	0.084

2.6.8 Carbon-alloying of TMD coatings

Besides the two approaches discussed in the previous section, another approach finds its presence in the literature. This approach is based on the incorporation of carbon into TMD coatings. It has been one of the most successful and dominant ways of achieving good improvements in both the mechanical and tribological properties of TMD coatings in humid air. Unlike alloying with metals, an obvious advantage of this approach is that the resulting oxides are gaseous and easily escape the coatings without adversely affecting their self-lubricating properties [43,291-294]. When TMD coatings are alloyed with carbon, there is always a possibility that the carbon atoms react with the atoms of transition metals, resulting in composite coatings with higher non-TMD contents [43,175,295,296]. A typical example is the formation of tungsten carbides [214,297,298]. These carbides act as hard phases, which is beneficial for improving the mechanical properties and wear resistance [214,215,299,300]. In this section, different TMD coatings alloyed with different carbon contents are discussed in detail with respect to their mechanical properties and tribological performance.

2.6.8.1 Mo-S-C coatings

In the late 1990s, a new concept in coatings based on the alloying of MoS_2 coatings with carbon started to attract the attention of many researchers. The original idea was to combine the

excellent self-lubricity of MoS_2 coatings in vacuum and dry air with the excellent mechanical properties of DLC coatings. Carbon-alloyed MoS_2 (Mo-S-C) coatings deposited by magnetron sputtering are usually amorphous or consist of MoS_2 crystals embedded in an amorphous carbon matrix [42,43,291,293]. They generally exhibit good lubrication properties and are denser and harder than pure MoS_2 coatings. **Table 2.4** lists different Mo-S-C coatings and their hardness and coefficients of friction.

Table 2.4: Hardness, tribological testing parameters, and coefficients of friction of different Mo-S-C coatings.

Coating system	Carbon content (at.%)	Hardness (GPa)	Applied load (N)	Sliding counterpart	Relative humidity (%)	Coefficients of friction
Mo-S-C [291]	18-55	0.7-4	5-30	100Cr6 steel	30	0.04-0.36
Mo-S-C [293]	40.9-73.1	7-10.8	5	GCr15 steel	50	0.08-0.095
Mo-S-C [292]	25-40	0.3-2.3	3	GCr15 steel	35	0.05-0.25
Mo-S-C [301]	19	1.96	3	GCr15 steel	25	0.08
Mo-S-C [296]	40	5	5	GCr15 steel	78	0.24
Mo-S-C [302]	-	6.5-14	5	440C steel	30-45	0.025-0.17
Mo-S-C [303]	74	-	2	SiC	vacuum	0.8
Mo-S-C [304]	-	1.3-2.8	5	GCr6 steel	45	0.056
Mo-S-C [305]	-	1.37	3	GCr15 steel	35	0.08
Mo-S-C [306]	44.73-84.33	7-8.7	10	GCr15 steel	35	0.05-0.1
Mo-S-C [307]	-	3.55	5	GCr6 steel	vacuum	0.04
Mo-S-C [308]	38-75	-	1	100Cr6 steel	50	0.2-0.6

Pimentel et al. [291] deposited a series of Mo-S-C coatings by radio frequency (RF) magnetron sputtering from two targets: MoS_2 and graphite. The power ratio of the targets was varied to prepare coatings with different carbon contents in the range 18-55 at.%. The hardness of the coatings increased linearly from 0.7 GPa to 4 GPa with the increase in the carbon content. The coatings were harder than the reference pure MoS_2 coating deposited by the same equipment, which showed a hardness value of 0.3 GPa. This enhancement in the hardness was attributed

to an increase in the density of the coating, reduction of porosity, and elimination of undesirable columnar morphology. The tribological properties of the coatings were evaluated at different loads in humid air, as shown in **Figure 2.26**. The coating with the highest carbon content of 55 at.% showed the best tribological properties with the lowest coefficient of friction and the lowest wear rate. The coefficient of friction was observed to decrease with increasing applied load.

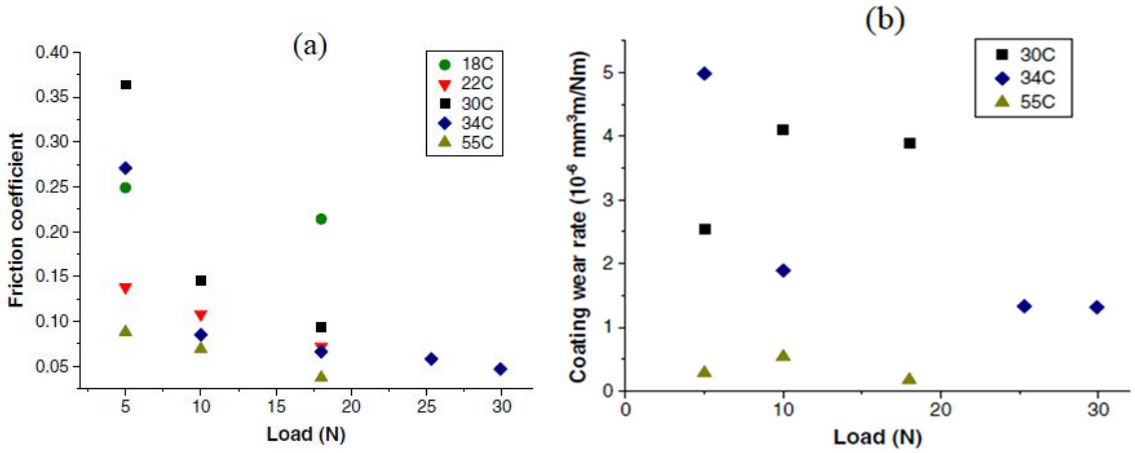

Figure 2.26: (a) Coefficients of friction and (b) wear rates of Mo-S-C coatings tested at different applied loads. (Test conditions: counterparts: 100Cr6 steel balls; relative humidity: 30%; temperature: room temperature) [291].

In another study, Gu et al. [293] prepared MoS_2 coatings with different carbon contents in the range 40.9-73.1 at.% by direct current (DC) magnetron sputtering. **Figure 2.27 (a)** shows the mechanical properties of the deposited coatings. With increasing carbon content, the hardness increased from 7 GPa to 10.8 GPa. Such enhancement in the mechanical properties was ascribed to an increase in the amorphous content of the coating with increasing carbon content. **Figure 2.27 (b)** displays the coefficients of friction and wear rates of the coatings tested in humid air. All the coatings exhibited low coefficients of friction (less than 0.1). A slight reduction in the coefficient of friction was observed with increasing carbon content. Low wear rates in the order level of 10^{-7} m^3/N.m were obtained for all the coatings, and the one with the lowest carbon content of 40.9 at.% offered the best wear resistance. The excellent friction performance exhibited by the coatings was attributed to the composite structure, which protected MoS_2 from oxidation and enhanced the mechanical properties of the coatings [293].

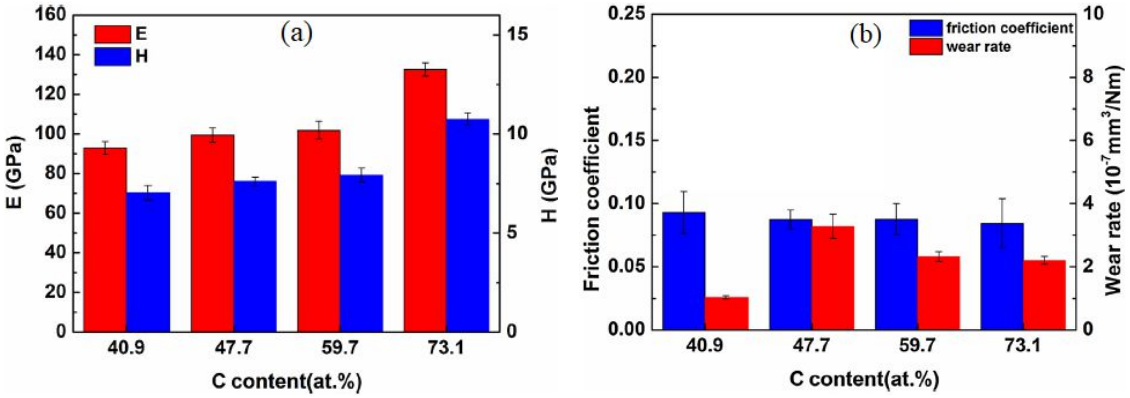

Figure 2.27: (a) Hardness *H* and elastic modulus *E* of Mo-S-C coatings alloyed with different carbon contents and (b) their coefficients of friction and wear rates. (Test conditions: counterparts: GCr15 steel balls; normal load: 5 N; relative humidity: 50%; temperature: room temperature) [293].

2.6.8.2 W-S-C coatings

The alloying of WS_2 coating with carbon was first introduced by Voevodin et al. [265]. They prepared WC/WS_2/DLC coatings consisting of hard WC and WS_2 phases embedded into a non-hydrogenated DLC matrix. In environmental cycling tests, the coatings exhibited excellent tribological properties with a very low coefficient of friction of 0.02 during dry air cycles and a high coefficient of friction of 0.2 during humid air cycles. In another study, they fabricated WC/WS_2/DLC composite coatings and measured their coefficients of friction in dry and humid atmospheres [299]. The coatings showed a very low coefficient of friction of 0.02 in dry air. In humid air, however, the coefficient of friction increased to 0.15. They observed that during dry/humid air environmental cycling, the coefficient of friction dropped in dry air, increased in humid air, and then dropped again in dry air. This interesting observation was termed as "chameleon behaviour" where the coatings adapt their frictional properties depending on the environmental conditions [299]. It was suggested that WS_2 was responsible for lowering friction in dry air, whereas DLC was responsible for lowering friction in humid air. Recent studies, however, do not support this hypothesis. Polcar et al. [309] prepared carbon-alloyed WS_2 (W-S-C) coatings with 42 at.% C and tested their tribological behaviour under dry and humid air conditions. They reported that the reason for the chameleon behaviour was the formation of a tribofilm consisting exclusively of WS_2. It was also reported that carbon did not play a significant role in the sliding process, but it did contribute to improving the hardness of

the coatings, resulting in a high hardness value of 9.7 GPa. **Table 2.5** lists different W-S-C coatings and their hardness and coefficients of friction.

Table 2.5: Hardness, tribological testing parameters, and coefficients of friction of W-S-C coatings.

Coating system	Carbon content (at.%)	Hardness (GPa)	Applied load (N)	Sliding counterpart	Relative humidity (%)	Coefficients of friction
W-S-C [213]	15-62	2-5.5	10	100Cr6 steel	-	0.18-0.23
W-S-C [214]	13-64	0.8-5.4	5-10	100Cr6 steel	60	0.07-0.22
W-S-C [215]	50	5.4	10	100Cr6 steel	60	0.2
W-S-C [302]	-	11-17	5	440C steel	30	0.05-0.15
W-S-C [310]	15-72	0.5-13	10	100Cr6 steel	40	0.1-0.3
W-S-C [310]	34-63	3-7	10	100Cr6 steel	40	0.1-0.4
W-S-C [311]	29-70	4-10	5	100Cr6 steel	30	0.2-0.3
W-S-C [312]	26-70	4-10	5-47	100Cr6 steel	30	0.05-0.23
W-S-C [294]	29-70	4-10	5	100Cr6 steel	5-70	0.03-0.3
W-S-C [309]	42	9.7	20-1000	100Cr6 steel	40	0.04-0.15
W-S-C [313]	42	4.9	1-15	100Cr6 steel	34	0.07-0.26
W-S-C [314]	39	9	1-50.8	100Cr6 steel	30	0.04-0.2
W-S-C [315]	16-32	4.1-6.8	5	100Cr6 steel	5	0.02-0.03
W-S-C [162]	18-41	-	5	100Cr6 steel	50	0.1-0.15
W-S-C [316]	14-69	-	0.2	-	40	0.2-0.4
W-S-C [317]	29-66	5.7-7.1	5	100Cr6 steel	5-90	0.03-0.3
W-S-C [318]	17-64	5.4-10.5	5	100Cr6 steel	55	0.1-0.17
W-S-C [152]	16	-	5	100Cr6 steel	55	0.1
W-S-C [319]	16-27	5.4-12	5	100Cr6 steel	5	0.02-0.15

Polcar et al. [312] used RF magnetron sputtering to deposit W-S-C coatings with different carbon contents in the range 26-70 at.% from a carbon target partly covered by WS_2 pellets. **Figure 2.28** shows the evolution of the hardness of the coating as a function of the carbon

content. Initially, the hardness increased with increasing carbon content, reaching a maximum value of 10 GPa at 40 at.% C. This improvement was attributed to an increase in the compactness of the coatings with increasing carbon content and the possibility of the formation of nano-sized carbide phases, which are intrinsically harder than WS_2 [312]. As the carbon content increased beyond 40 at.%, the hardness started to decrease. The lack of available W to establish W-C bonds at higher carbon contents was reported to cause this drop in the hardness. Some of the coatings were tribologically tested on a pin-on-disk tribometer against steel balls at different loads with 500 and 5000 laps, as shown in **Figure 2.29**. The coatings exhibited a decreasing friction trend with increasing contact load. It was noticed that the coefficients of friction corresponding to 5000 laps were generally lower than those of 500 laps. After conducting a thorough investigation of worn surfaces, it was found that increasing the number of laps to 5000 enhanced the formation of a WS_2 tribofilm at the siding interface, resulting in lower coefficients of friction than those of 500 laps [312].

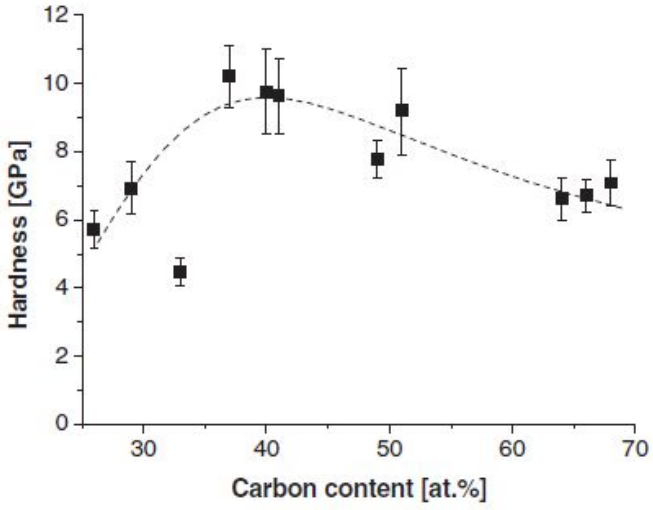

Figure 2.28: Evolution of the hardness of W-S-C coatings with the carbon content [312].

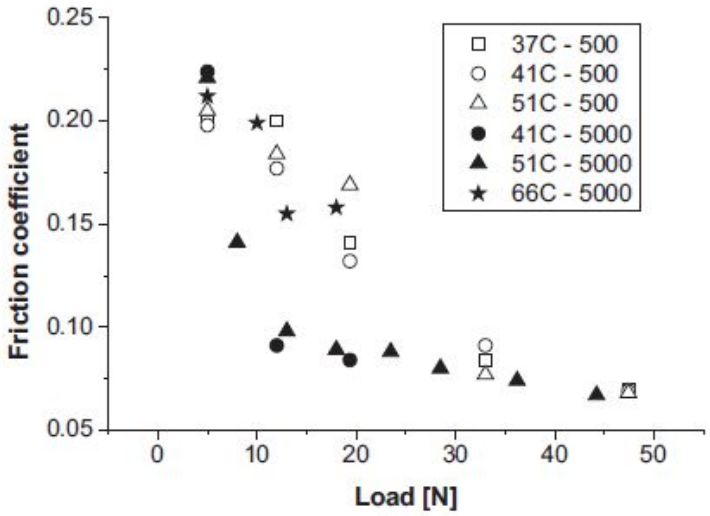

Figure 2.29: Coefficients of friction of W-S-C coatings tested at different applied loads. Note the different number of laps. (Test conditions: counterparts: 100Cr6 steel balls; relative humidity: 30%; temperature: room temperature) [312].

In another work, W-S-C coatings were deposited using RF magnetron sputtering from a carbon target containing several WS_2 pellets to obtain final carbon contents in the range 29-66 at.% [317]. The tribological behaviour was evaluated on a pin-on-disc tribometer at different RH levels, as shown in **Figure 2.30**. When evaluated at 5% RH, all the coatings exhibited very low coefficients of friction in the range 0.03-0.06. As RH increased further up to 40%, the coefficients of friction increased, reaching a maximum value of 0.2. Beyond 40% RH, different friction trends were observed. The coatings with the highest carbon contents were less susceptible to high humidity levels, with even a minor drop in their coefficients of friction. The coefficients of friction increased with increasing RH levels for the other carbon contents. In contrast to the friction results, the wear rates showed no significant dependence on RH levels. The best wear resistance was exhibited by the coatings with 33 at.% and 37 at.% C. The coating with the highest carbon content of 66 at.% exhibited the highest wear rate at 5% RH. This unexpectedly high wear rate was further investigated. The coating was found to have a very high coefficient of friction for the first 25 laps of tribological testing before dramatically decreasing to a steady-state level at the lowest stabilised value. Similarly, it exhibited the highest wear only in the first couple of laps. It was reported that there was insufficient self-lubricating WS_2 material to form a beneficial tribolayer at the beginning of the tribological

testing, consequently resulting in a high coefficient of friction and significant surface damage to the coating surface [317].

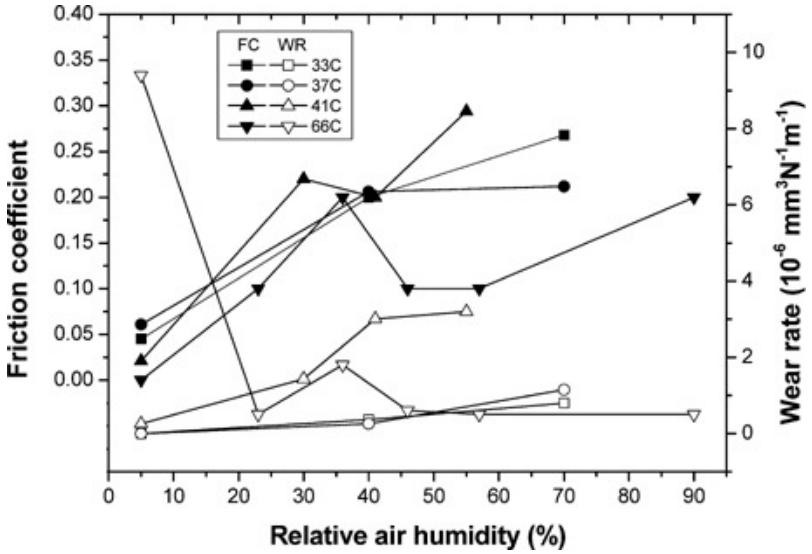

Figure 2.30: Coefficients of friction (full symbols) and wear rates (open symbols) of W-S-C coatings tested under different levels of RH. (Test conditions: counterparts: 100Cr6 steel balls; normal load: 5 N; temperature: room temperature) [317].

2.6.8.3 Mo-Se-C coatings

Although carbon-alloyed $MoSe_2$ (Mo-Se-C) coatings are a less explored subset of carbon-alloyed TMD coatings, they are a promising candidate for use as solid lubricant coatings in diverse environments owing to their low coefficients of friction, high load-bearing capacity, good wear resistance, and excellent oxidative stability. In a recent study, Yaqub et al. [320] tested the tribological properties of Mo-Se-C coatings against steel balls at a normal load of 5 N under vacuum and ambient air conditions. By varying the sliding conditions, no significant differences in performance were observed. The coatings exhibited very similar low coefficients of friction in the range 0.02-0.06 and low wear rates ranging from 2×10^{-7} mm^3/N.m to 6×10^{-7} mm^3/N.m under both ambient air and vacuum conditions. This makes the coatings suitable as low-friction coatings for terrestrial and aerospace applications. **Table 2.6** lists different Mo-Se-C coatings and their hardness and coefficients of friction.

Table 2.6: Hardness, tribological testing parameters, and coefficients of friction of Mo-Se-C coatings.

Coating system	Carbon content (at.%)	Hardness (GPa)	Applied load (N)	Sliding counterpart	Relative humidity (%)	Coefficients of friction
Mo-Se-C [309]	50	3	20-120	100Cr6 steel	30-40	0.045-0.195
Mo-Se-C [321]	47	2.1	2-10	100Cr6 steel	55	0.095-0.1
Mo-Se-C [321]	61	3.2	2-10	100Cr6 steel	55	0.05-0.095
Mo-Se-C [232]	29-68	0.6-4.1	5	100Cr6 steel	5-70	0.02-0.16
Mo-Se-C [322]	36.85-60.66	1-5.5	0.004	diamond	-	0.06-0.17
Mo-Se-C [320]	18-25	-	5	100Cr6 steel	35-45	0.03-0.06
Mo-Se-C [43]	51	2.9	5-100	100Cr6 steel	50	0.04-0.19
Mo-Se-C [320]	18-25	-	5	100Cr6 steel	vacuum	0.02-0.06

Polcar et al. [232] deposited Mo-Se-C coatings by RF magnetron sputtering from a graphite target partially covered with pellets of $MoSe_2$ in order to achieve final carbon contents in the range 29-68 at.%. Due to the enhanced densification of the coatings and the removal of pores with increasing carbon content, the hardness of the coatings linearly increased from 0.6 GPa to 4.1 GPa. The tribological performance of the coatings was evaluated using a pin-on-disc tribometer at different applied loads, as shown in **Figure 2.31**. The coefficients of friction and wear rates decreased with increasing applied load. Analyses of worn surfaces revealed that the excellent tribological performance of Mo-Se-C coatings was due to the formation of a crystalline $MoSe_2$ tribofilm in the topmost parts of the wear tracks, as shown in **Figure 2.32**. It was reported that carbon was progressively removed from the wear tracks during sliding and had only a limited influence on the sliding process. However, it significantly contributed to the improvement of the mechanical properties of the coatings and their wear resistance [232].

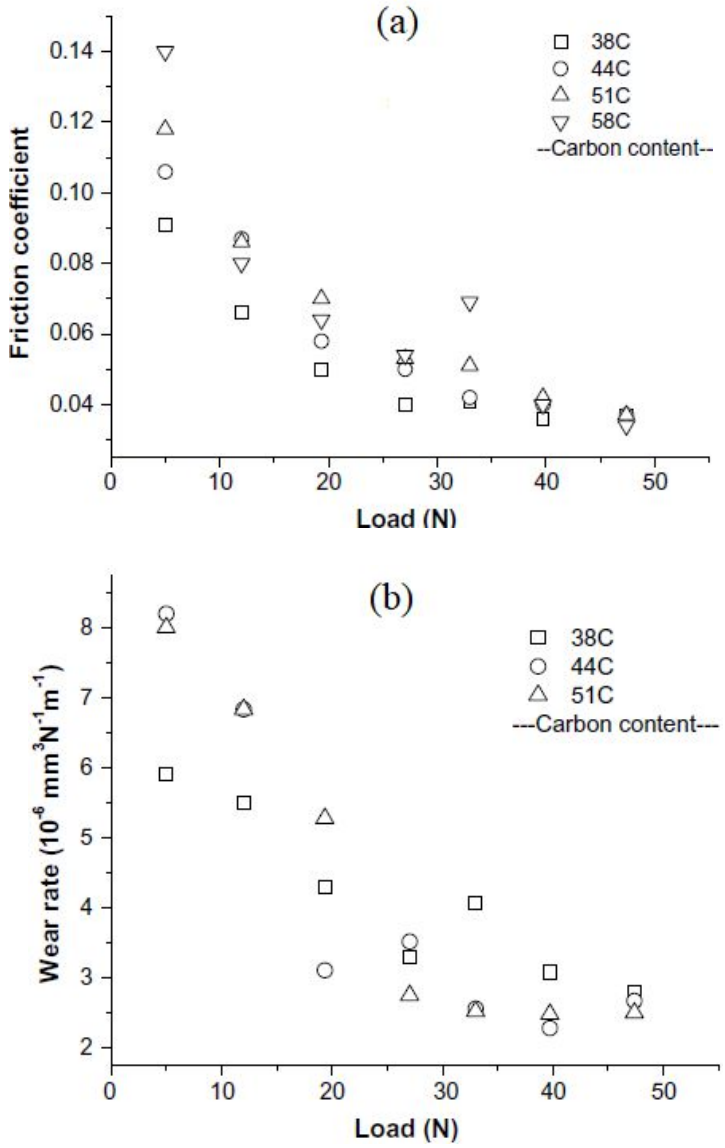

Figure 2.31: (a) Coefficients of friction and (b) wear rates of Mo-Se-C coatings tested at different loads. (Test conditions: counterparts: 100Cr6 steel balls; relative humidity: 35%; temperature: room temperature) [232].

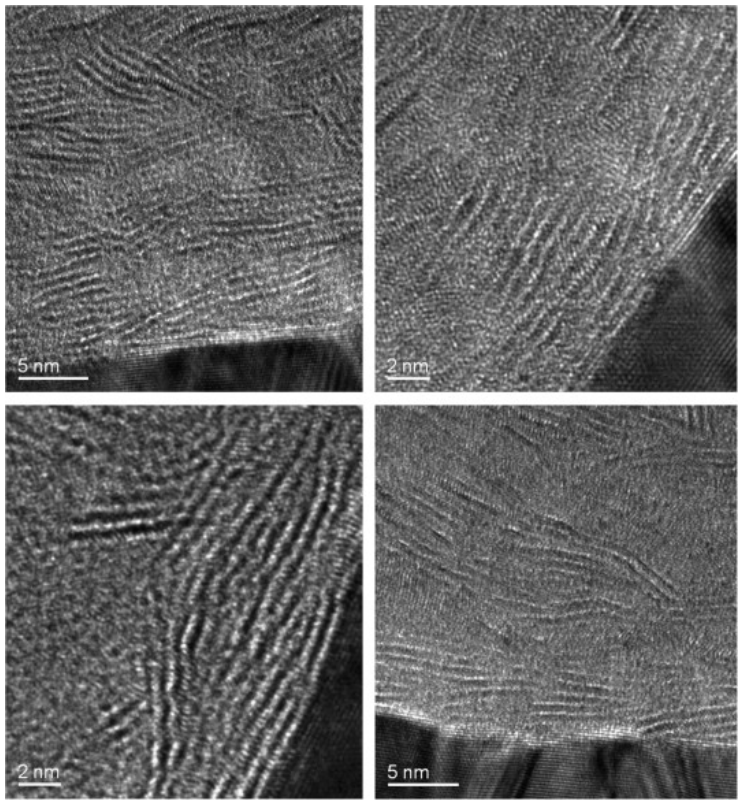

Figure 2.32: TEM images of cross-sections taken from the wear track of Mo-Se-C coating with 51 at.% C tested at a normal load of 33 N. The dark part of images corresponds to the sputtered gold covering the wear track [232].

Figure 2.33 shows the friction curves of Mo-Se-C coating containing 44 at.% C as a function of the applied load [232]. For loads up to 20 N, the running-in period was long as the coefficient of friction monotonically decreased until it reached a steady-state level. For higher loads, the running-in period was extremely short, and the friction was less noisy and reached a steady-state level faster. It was reported that when the contact pressure was high, the initial wear of the coating was higher, and the formation of the desirable $MoSe_2$ tribofilm was faster, leading to a short running-in period and quick stabilisation of the coefficient of friction [232].

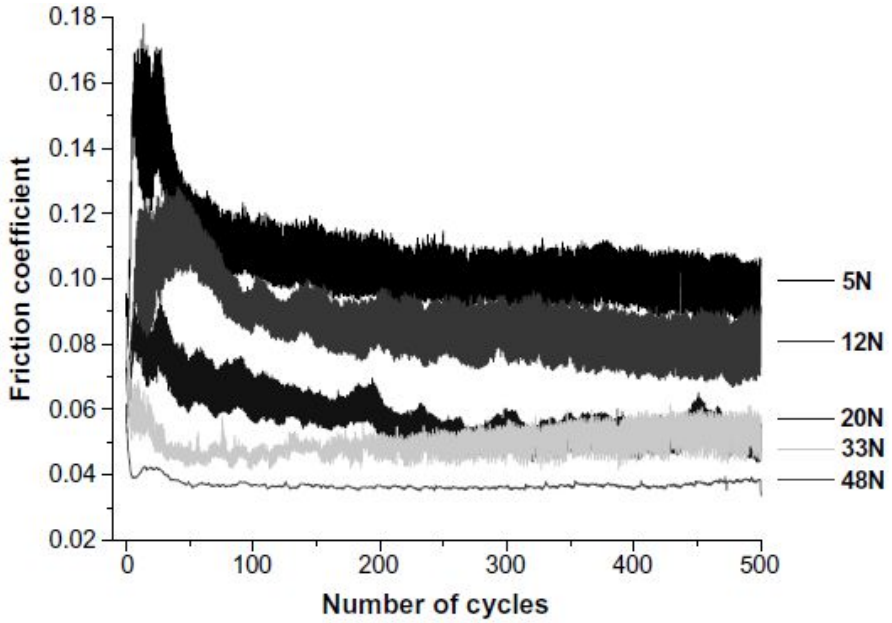

Figure 2.33: Friction curves of Mo-Se-C coating with 44 at.% C tested at different loads. (Test conditions: counterparts: 100Cr6 steel balls; relative humidity: 35%; temperature: room temperature) [232].

2.6.8.4 W-Se-C coatings

Carbon-alloyed WSe_2 (W-Se-C) coatings are the least investigated of the carbon-alloyed TMD coatings. Evaristo et al. [323] deposited W-Se-C coatings with carbon contents ranging from 7 at.% to 70 at.% by RF magnetron sputtering from WSe_2 and C targets. The hardness of the coatings was observed to increase with increasing carbon content, with values ranging from 3.8 GPa to 5.6 GPa. The tribological properties of W-Se-C coating with 56 at.% C were evaluated using a pin-on-disc tribometer at different applied loads, as displayed in **Figure 2.34**. At all the applied loads, the coefficient of friction decreased after a few laps to its smallest value and then gradually increased with increasing number of laps. The highest applied load of 27 N resulted in rapid destruction of the coating due to its poor adhesion to the substrate [323].

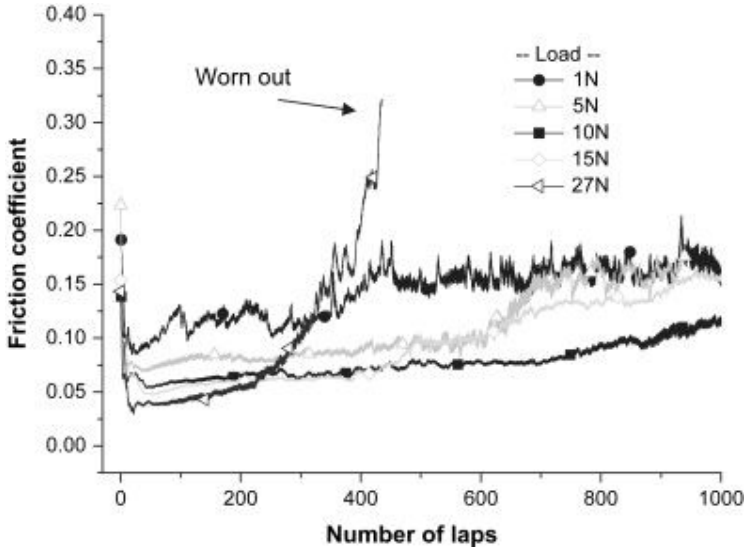

Figure 2.34: Friction curves of W-Se-C coating with 56 at.% C tested at different loads. (Test conditions: counterparts: 100Cr6 steel balls; temperature: room temperature) [323].

2.6.9 Layered TMD coatings

Fabricating layered structures is another approach to improve the performance of TMD coatings in humid air [212,324-331]. By depositing several layers with various properties on each other, the multi-interfaces between these layers can suppress and deflect the crack initiation and propagation and inhibit the porous layer growth of TMD coating, which is beneficial to the improvement of the mechanical and tribological properties of the coating system [326,328,331].

Zhao et al. [324] used unbalanced magnetron sputtering to prepare a series of DLC/MoS_2 coatings and a single layer of MoS_2 coating as a reference sample. **Table 2.7** depicts the design parameters of these fabricated coatings. The mechanical properties of the coatings are shown in **Figure 2.35**. As discussed in section 2.7.5, pure TMD coatings exhibit low hardness, typically in the range 0.3-2 GPa [43], which is much lower than that of DLC coatings. However, the hardness of MoS_2 coating in this study was 7.9 GPa, which was much higher than that of traditional MoS_2 coating. It was reported that this high hardness of MoS_2 coating was caused by a dense and compact coating structure [324]. The combination of DLC and MoS_2 showed a

weak influence on the mechanical properties. The hardness of the layered coatings varied from 7.9 GPa to 8.6 GPa, and their elastic modulus was in the range 97-114 GPa [324].

Table 2.7: Design parameters of DLC/MoS_2 and MoS_2 coatings [324].

Sample	Modulation ratio	DLC deposition time (s)	DLC thickness (nm)	MoS_2 deposition time (s)	MoS_2 thickness (nm)	Total thickness (nm)
S3	1:3	296	25	805	75	1000
S5	1:5	197	16.7	894	83.3	1000
S7	1:7	148	12.5	939	87.5	1000
S9	1:9	118	10	966	90	1000
MoS_2	-	-	-	10730	1000	1000

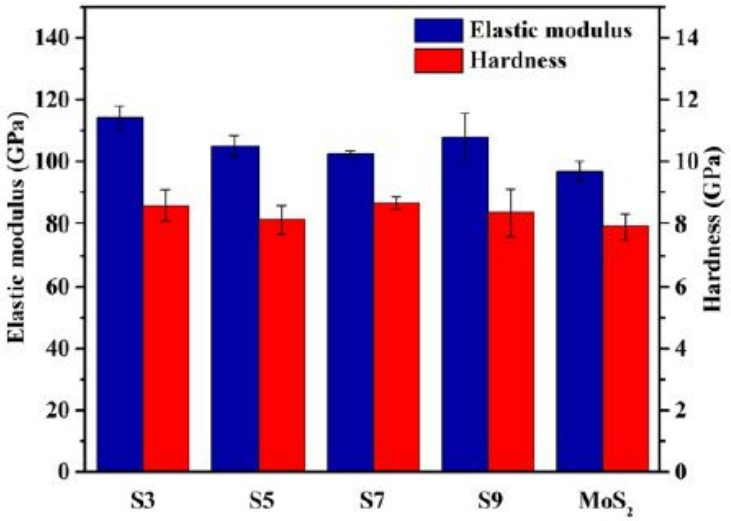

Figure 2.35: Mechanical properties of DLC/MoS_2 and MoS_2 coatings [324].

Figure 2.36 shows the tribological properties of the coatings. MoS_2 coating showed the highest wear rate. The addition of the DLC layers was beneficial to reduce wear. Increasing the thickness of the DLC layer reduced the wear rate and kept the coefficient of friction low and steady. This improvement in the wear resistance was attributed to the presence of carbon, which reacted with oxygen in the surrounding environment during tribological testing and inhibited the formation of abrasive MoO_3 particles [324].

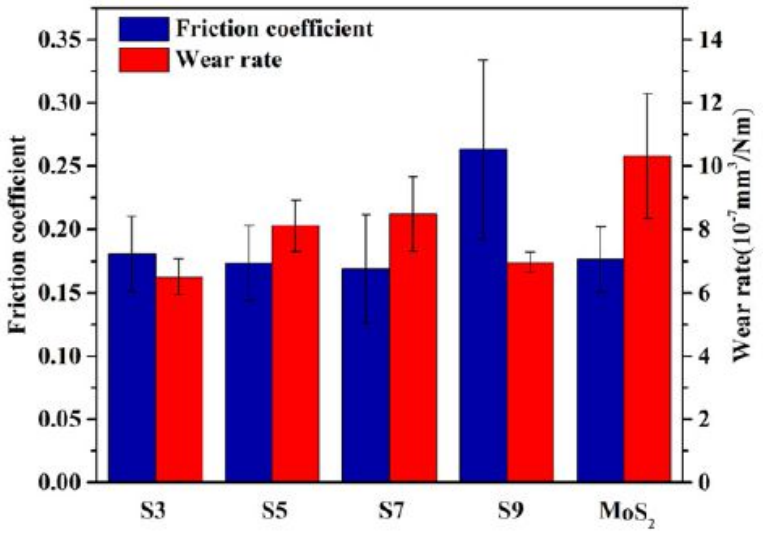

Figure 2.36: Coefficients of friction and wear rates of DLC/MoS_2 and MoS_2 coatings. (Test conditions: counterparts: GCr15 steel balls; normal load: 2 N; relative humidity: 90%; temperature: room temperature) [324].

In another study, Watanabe et al. [212] prepared layered WS_2/MoS_2 coatings and single layers of WS_2 and MoS_2 using RF magnetron sputtering. The single-layer WS_2 coating showed a hardness value of 0.6 GPa, whereas the single-layer MoS_2 coating showed a hardness value of 0.5 GPa. The hardness of the layered coating was 3.1 GPa. This enhancement in the hardness of the layered coating was attributed to the restricted dislocation movement within and between its two layers, which made the coating more resistant to plastic deformation [212]. **Figure 2.37** shows the coefficients of friction of the coatings. The coefficients of friction of the two single-layer coatings peaked suddenly before 10000 revolutions, indicating coating failure. In contrast, the layered coating exhibited a low and stable coefficient of friction up to 65000 revolutions. **Figure 2.38** shows the wear rates of the coatings after 3000 revolutions of tribological testing. When compared to the single-layer coatings, the layered one exhibited the lowest wear rate owing to its higher hardness and improved wear resistance [212].

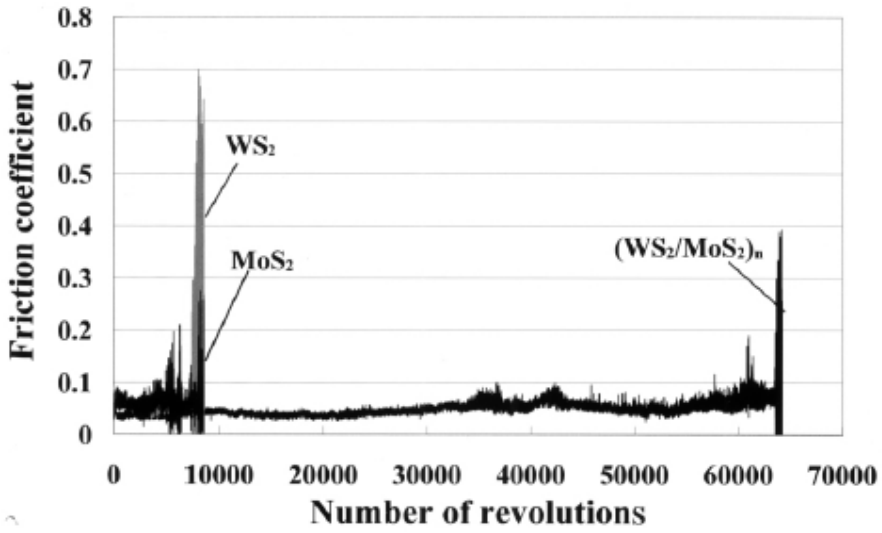

Figure 2.37: Coefficients of friction of single layers of MoS_2 and WS_2 coatings and layered WS_2/MoS_2 coating. (Test conditions: counterparts: AISI 440C steel balls; normal load: 1 N; relative humidity: 30-45%; temperature: room temperature) [212].

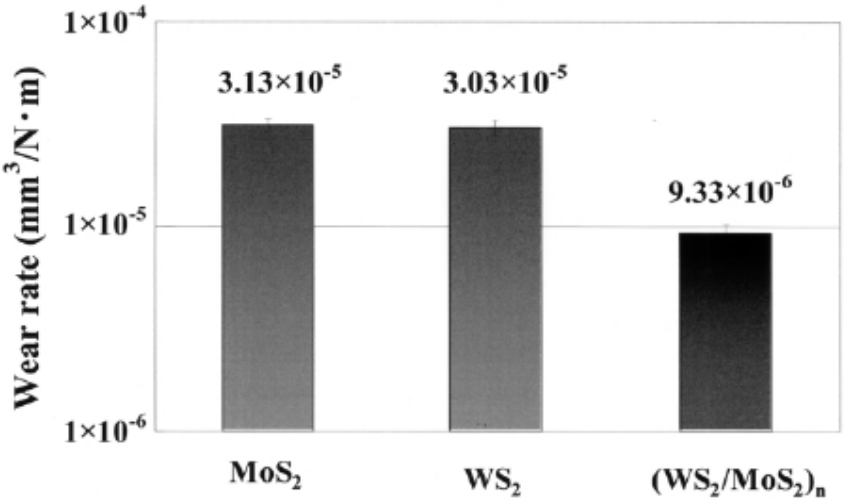

Figure 2.38: Wear rates of single layers of MoS_2 and WS_2 coatings and layered WS_2/MoS_2 coating at 3000 revolutions [212].

2.6.10 Tribological properties of TMD coatings under oil-lubricated sliding conditions

There are two ways in which TMDs are used in tribological applications: either as surface coatings for dry lubrication [42,43,166,332] or as nanoparticles incorporated into lubricating oils [333-336]. The use of TMD nanoparticles as oil additives has gained popularity in recent years because of their great ability to improve the tribological properties of surfaces in relative motion [335-340]. For example, it was found that the addition of 1 wt% of WS_2 nanoparticles to PAO oil significantly reduced the coefficient of friction from 0.1 to 0.04 and resulted in extremely low wear [340]. In another study, the lubrication effects of mineral oil were greatly enhanced with the addition of $MoSe_2$ nanoparticles at a concentration of 0.75 wt%, as the coefficient of friction and wear rate were reduced by 43% and 87%, respectively [341].

Despite the positive findings reported for TMD nanoparticles as oil additives, several limitations hinder them from being employed in a wide variety of applications. One of which is their low solubility and tendency to agglomerate in base oils [333,342,343]. In order to reduce their agglomeration, they need to be dispersed with chemicals known as dispersant agents. The majority of dispersive agents are corrosive and may cause damage to contacting surfaces [138,344]. On the other hand, even if the dispersive agent is completely safe for the surfaces, it is necessary to guarantee that it is compatible with other oil additives, which further complicates the situation. Furthermore, concerns have been raised about the safety of these nanoparticles for human health and the environment [345-347].

Surprisingly, there have been very few attempts to introduce TMDs into oil-lubricated contacts as surface coatings. Rodrigues et al. [348] deposited WS_2 coatings with different carbon and fluorine contents, and tribologically tested them against steel balls under both dry and PAO8-lubricated sliding conditions. The tribological test carried out in dry sliding resulted in a low coefficient of friction of 0.03. This low friction was attributed to the formation of a tribologically beneficial WS_2 tribofilm on sliding surfaces. The coefficient of friction measured in PAO8-lubricated sliding was 0.07, which was higher than the one measured in dry sliding. It was reported that the uneven spreading of the oil on the sliding surfaces led to this higher coefficient of friction. In contrast to the friction results, the coating showed a wear rate of 0.49

x 10^{-6} mm^3/N.m in PAO8-lubricated sliding, which was lower than 1.1 x 10^{-6} mm^3/N.m obtained in dry sliding [348]. In another study, Hovsepian et al. [349] investigated the tribological performance of molybdenum and tungsten doped carbon-based coating (Mo-W-C) against steel balls under oil-lubricated sliding conditions using a commercially available engine oil. The coating showed a very low coefficient of friction of 0.033. Although this low friction was attributed to the *in-situ* formation of a tribofim containing particles of WS_2 and MoS_2 on sliding surfaces, the lubricating oil used was a fully formulated engine oil, thus making it difficult to determine whether the coating itself formed the tribofilm independently without any synergistic or antagonistic influence of oil additives. Gustavsson et al. [146] compared the tribological performance of different coatings based on DLC, inorganic fullerene-like IF-WS_2, C-doped $MoSe_2$, and Ti-doped MoS_2 in five commercially available fuels using a reciprocating pin-on-flat tribometer. The three TMD coatings showed very promising friction results in several fuels such as diesel, as shown in **Figure 2.39**. However, the underlying mechanisms contributing to these low friction results were not elucidated. Apart from that, the tests were conducted with fuels intended for combustion engines rather than lubrication of tribological surfaces.

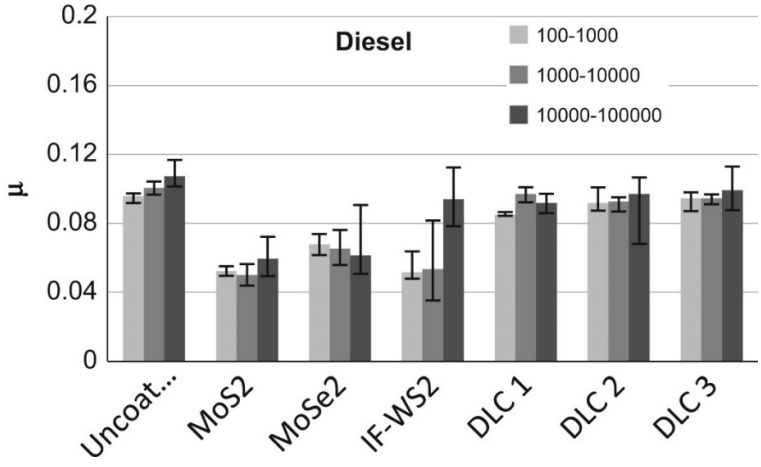

Figure 2.39: Coefficient of friction of different coatings based on DLC, inorganic fullerene-like IF-WS_2, C-doped $MoSe_2$, and Ti-doped MoS_2 tested under diesel-lubricated sliding conditions. Note average values over different stroke intervals. (Test conditions: counterparts: 100Cr6 steel balls; normal load: 10 N; temperature: room temperature) [146].

2.7 Diamond-like carbon (DLC) coatings

DLC coatings are a class of solid lubricants having mechanical, optical, electrical, and chemical properties similar to natural diamond, but without a crystalline lattice structure [350]. They generally exhibit high hardness and elastic modulus, low coefficients of friction, and high wear resistance. Owing to this unique combination of attractive mechanical and tribological properties, they are currently used in a wide variety of industrial applications, including the automotive industry (e.g. piston rings, camshafts, and tappets) [20-22,351], optics [352,353], injection moulding [354,355], cutting tools [356-358], and biomedical fields [359-362].

Aside from all those great mechanical and tribological properties, DLC coatings suffer from different challenges. Because of their low surface energies and chemical inertness, these coatings cannot react effectively with conventional oils and oil additives, making the formation of self-lubricating tribofilms low and difficult to control [25-36]. Another major drawback is their high internal residual stresses [37-39]. These residual stresses can lead to serious problems such as poor adhesion to substrates and delamination. In addition, they make the deposition of thick DLC coatings difficult since they increase proportionately with increasing coating thickness [40,41].

2.7.1 Structural and mechanical properties of DLC coatings

Carbon can exist in three types of hybridisations: sp^3, sp^2, and sp^1, as shown in **Figure 2.40**. In sp^3 hybridisation, each carbon atom is bonded to four other carbon atoms by very strong covalent bonds. The high hardness of diamond originates from these strong covalently bonded carbon atoms. In sp^2 hybridisation, such as in graphite, each carbon atom is bonded to three other carbon atoms in the same plane by strong covalent bonds. The hybridised carbon atoms are stacked in layers with weak Van der Waals bonds between them. This weak bonding allows the layers to slide over one another with relative ease [363]. DLC coatings are amorphous and consist of a mixture of sp^2 (graphite-like) and sp^3 (diamond-like) hybridisations [364].

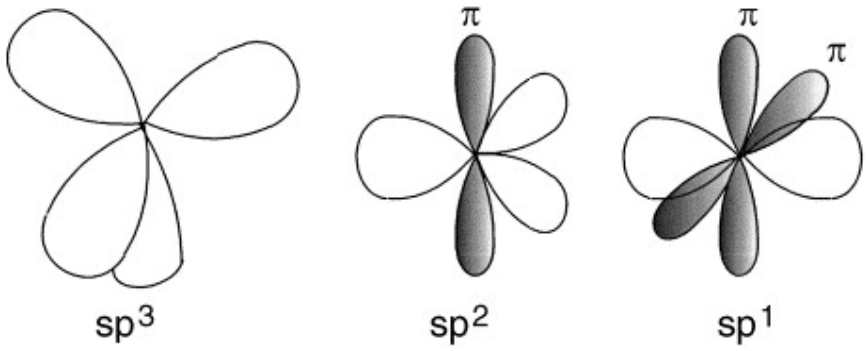

Figure 2.40: Schematic illustration of sp^1, sp^2, and sp^3 hybridisations in carbon [365].

DLC coatings are divided into four main categories: amorphous carbon (a-C), hydrogenated amorphous carbon (a-C:H) with a majority of sp^2 bonds, tetrahedral amorphous carbon (ta-C), and hydrogenated tetrahedral amorphous carbon (ta-C:H) with a majority of sp^3 bonds [366]. Non-hydrogenated DLC coatings have a hydrogen content as low as 1%, while hydrogenated DLC coatings have a hydrogen content as high as 60% [367]. The amount of hydrogen has a significant influence on the mechanical properties of DLC coatings and is also important for the development of favourable frictional properties. Robertson and Ferrari proposed a ternary diagram, as shown in **Figure 2.41**, for classifying DLC coatings based on the proportions of sp^3 and sp^2 bonds and the hydrogen content [365]. DLC coatings offer a diverse spectrum of structural and mechanical properties, allowing them to be tailored to a variety of applications demanding high hardness, low friction, and excellent wear resistance. **Table 2.8** lists the sp^3 hybridisation content, hydrogen content and mechanical properties of each category of DLC coatings, as well as diamond and graphite for comparison.

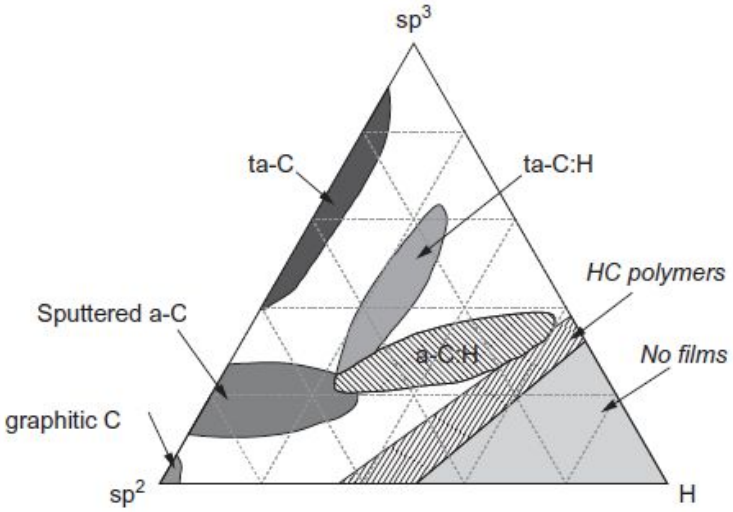

Figure 2.41: Ternary phase diagram for different DLC coatings with respect to their sp^3, sp^2, and hydrogen content [368].

Table 2.8: Properties of different DLC coatings and other carbon-based materials [19,365].

	sp^3 content (%)	**Hydrogen content (%)**	**Hardness (GPa)**	**Young's modulus (GPa)**
Graphite	0	0	0.2-2	10
Diamond	100	0	100	1000
a-C	0-5	0	10-20	100-200
a-C:H soft	60	40-60	<10	100-300
a-C:H hard	40	20-40	10-30	100-300
ta-C	80-88	0	50-80	300-500
ta-C:H	70	25-30	<50	<300

2.7.2 Tribological properties of DLC coatings under dry sliding conditions

DLC coatings have different tribological properties under dry sliding conditions. This variation is primarily attributable to differences in the chemical composition, ratio of sp^2/sp^3 bonds, hydrogen content, doping elements, and operating parameters.

The hydrogen content has the greatest effect on the tribological performance of DLC coatings. **Figure 2.42** shows a schematic representation of the friction performance of hydrogenated and hydrogen-free DLC coatings. In dry air, hydrogen-free DLC coatings exhibit high coefficients of friction (> 0.4) because of strong covalent bond interactions between carbon atoms on contacting surfaces [369-371]. In contrast, hydrogenated DLC coatings exhibit much lower coefficients of friction in the range 0.001-0.02 in dry air [369,372]. This low friction of hydrogenated DLC coatings in dry air is attributed to the hydrogen-terminated covalent bonds with weak Van der Waals bonds acting between contacting surfaces [369-372]. In humid air, the adsorption of water vapour molecules on contacting surfaces results in increased coefficients of friction of hydrogenated DLC coatings, typically in the range 0.05-0.2 [369-372]. However, the friction of hydrogen-free DLC coatings decreases as the humidity increases and can reach the same range as that of hydrogenated DLC coatings because of the termination of covalent bonds by water molecules [369,370].

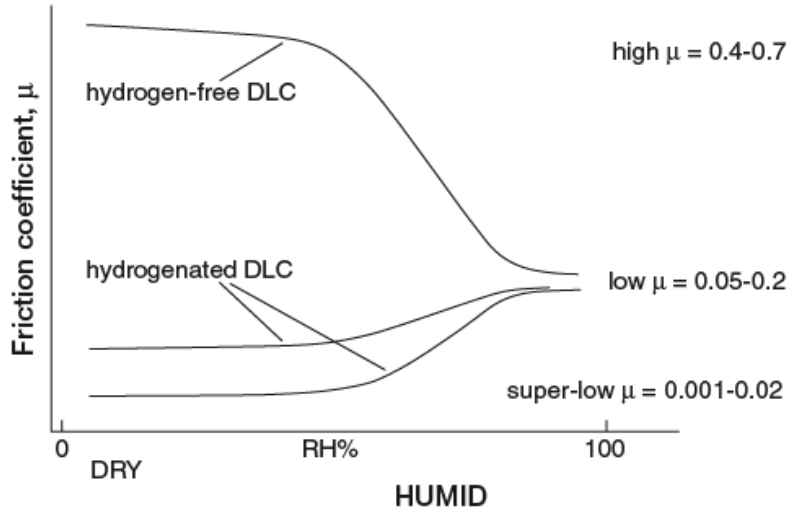

Figure 2.42: Friction performance of hydrogenated and hydrogen-free DLC coatings [369].

Under dry sliding conditions, the graphitisation of DLC coatings has a significant impact on their frictional properties. Graphitisation is defined as the transformation of a molecule structure from a diamond-like sp^3 structure to a graphite-like sp^2 structure at a temperature higher than 300 °C [373,374]. The temperature rise at the contacting asperities during sliding can induce graphitisation of the DLC coating, resulting in the formation of soft graphite-like carbon, which can then transfer to the sliding counterpart of the DLC coating, forming a transfer layer. The formation of this graphite-like carbon and its transfer to the sliding counterpart cause an easy slip between the sliding surfaces, resulting in low friction [373-376]. Raman spectroscopy is commonly used to analyse the graphitisation of DLC coatings [154,377,378]. An example is shown in **Figure 2.43** in which Raman spectroscopy was used to analyse the structure of hydrogenated DLC coating before and after tribological testing. The Raman spectrum of the as-deposited coating shows two broad peaks located at wavenumbers 1350 cm^{-1} and 1550 cm^{-1}. The peak at 1350 cm^{-1} is called the *D* peak and arises from the breathing modes of sp^2 atoms only in aromatic rings, whereas the peak at 1550 cm^{-1} is called the *G* peak and arises from the bond stretching modes of sp^2 atoms in both aromatic rings and chains [379,380]. According to Ferrari and Robertson [380], a change in the intensity ratio (I_D /I_G) of the *D* and *G* peaks and the *G* peak position can indirectly reflect the relative change of sp^2 and sp^3 bonds. They pointed out that the shift of the *G* peak position to a higher wavenumber and the increase in the (I_D /I_G) ratio are associated with a decreased sp^3 content and an increased sp^2 content. In **Figure 2.43**, the Raman spectrum acquired from the wear track of the coating shows an upward shift of the *G* peak position and an increase in the (I_D /I_G) ratio, indicating tribo-induced graphitisation of the coating during sliding [381].

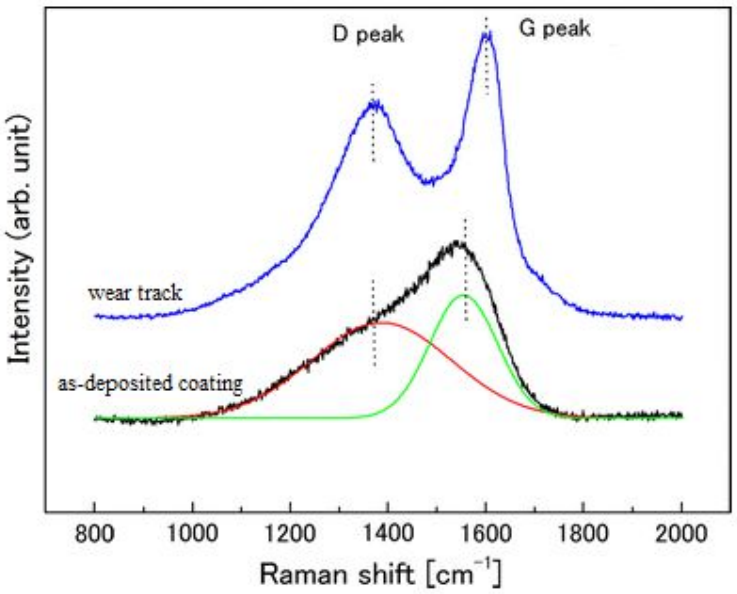

Figure 2.43: Raman spectra acquired from the as-deposited hydrogenated DLC coating and its wear track when tested at a normal load of 10 N under dry sliding conditions. The spectrum acquired from the wear track (blue line) indicates tribo-induced graphitisation of the coating during sliding [381].

There is a large diversity in the effect of dopants on the tribological properties of DLC coatings. Kim et al. [382] examined the tribological properties of silicon-doped a-C:H (Si) coatings, as shown in **Figure 2.44**. The coefficient of friction was observed to decrease with increasing silicon concentration. The lowest coefficient of friction of 0.06 was observed at the highest silicon concentration of 9.5 at.%. A major decrease in the coefficient of friction was observed with silicon concentrations ranging from 0.5 at.% to 3.2 at.%, indicating that a small amount of silicon can significantly affect the tribological performance of the coatings. The low-friction behaviour exhibited by the coatings was attributed to the formation of silicon-rich oxide debris covering both the coatings and their sliding counterparts. This formation was found to be enhanced with increasing silicon concentration [382].

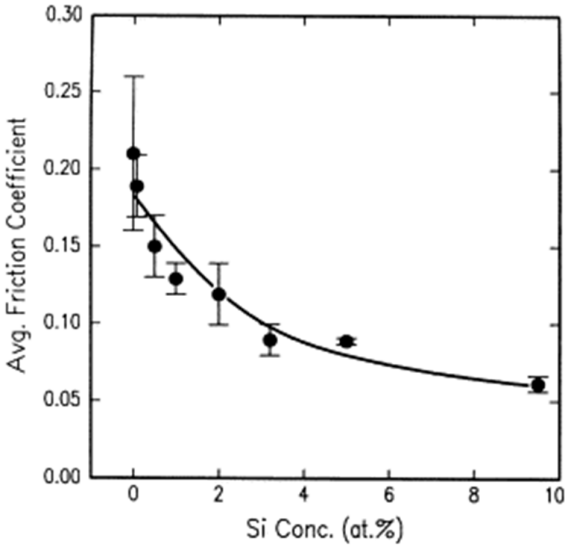

Figure 2.44: Average coefficients of friction of a-C:H (Si) coatings as a function of Si concentration. (Test conditions: counterparts: AISI 52100 balls; normal load: 5.9 N; relative humidity: 50-60%; temperature: room temperature) [382].

In another study, Zhao et al. [350] investigated the tribological performance of undoped and Ti-doped DLC coatings, as shown in **Figure 2.45**. The undoped coating showed a coefficient of friction of 0.03 and failed quickly, whereas the Ti-doped one showed a very stable and lower coefficient of friction of 0.08 and was able to reach 20,000 laps without failure. The excellent lubrication performance of Ti-doped DLC coating was ascribed to the combined effect of its excellent physical properties, such as high hardness and excellent toughness, and the friction-induced graphitisation of carbon.

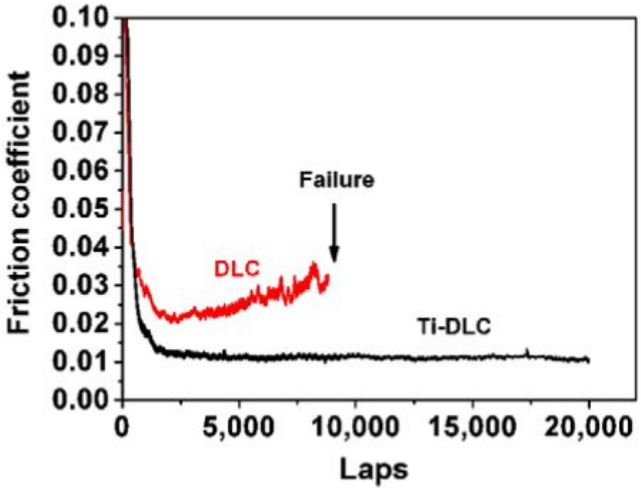

Figure 2.45: Coefficients of friction of undoped and Ti-doped DLC coatings. (Test conditions: counterparts: Si3N4 balls; normal load: 20 N; relative humidity: 56%; temperature: room temperature) [350].

Manninen et al. [383] investigated the tribological performance of undoped DLC coating and three Ag-doped DLC coatings having different Ag contents: Ag1 (1.3 at.%), Ag6 (6.1 at.%), and Ag13 (13.1 at.%), as shown in **Figure 2.46**. The undoped coating showed the lowest coefficient of friction of 0.1. Doping the coatings with Ag was found to have a negative influence on their frictional performance. The coefficient of friction was observed to increase with increasing Ag content, reaching the highest value of 0.2 at the highest Ag content of 13.1 at.%. It was found that this increase in the coefficient of friction with increasing Ag content was caused by the strong adhesion between the Ag aggregates that formed in the coating wear tracks and the Ag-rich transfer layers on their sliding counterparts.

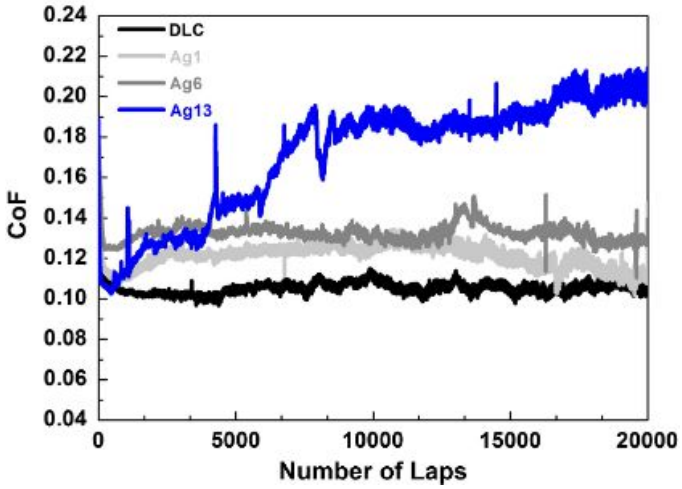

Figure 2.46: Coefficients of friction of undoped DLC coating and three Ag-doped DLC coatings having different Ag contents. (Test conditions: counterparts: zirconia balls; normal load: 10 N; relative humidity: 40%; temperature: room temperature) [383].

Silva et al. [384] investigated the tribological properties of a-C coating and tungsten-doped a-C:H (W) coatings having different tungsten contents in the range 6-12 at.% against steel balls at a normal load of 5 N. a-C:H (W) coatings showed low coefficients of friction ranging from 0.05 to 0.12, whereas a-C coating showed the highest coefficient of friction of 0.2. The presence of moisture and the passivation of covalent bonds caused by the addition of tungsten were reported to be both responsible for the observed better frictional performance of a-C:H (W) coatings compared to a-C coating. In another study, coefficients of friction in the range 0.12-0.25 were reported for a-C:H (W) coatings when tested against steel balls at a normal load of 30 N [385].

2.7.3 Tribological properties of DLC coatings under oil-lubricated sliding conditions

The tribological properties of DLC coatings under dry sliding conditions can also be beneficial under oil-lubricated conditions. As discussed in the previous section, the formation of a soft graphite-like carbon layer on the DLC coating surface and the formation of a transfer layer on its sliding counterpart play a key role in determining the tribological performance of DLC coatings under dry sliding conditions. The formation of these beneficial layers under oil-

lubricated conditions is highly impacted by the type of base oil used and chemically active oil additives [19,369]. It is also affected by the microstructure of the coatings and any doping elements [369,376].

When used with right base oils and oil additives, DLC coatings can display low friction and high wear resistance. **Figure 2.47** shows the tribological properties of uncoated steel disc and coatings of ta-C, a-C:H, and titanium-doped a-C:H (Ti) tested under dry and oil-lubricated sliding conditions with and without the presence of extreme pressure (EP) additives. In dry sliding, the uncoated disc exhibited the highest coefficient of friction of 0.64. The coefficients of friction of ta-C and a-C:H coatings were much lower in the range 0.15-0.22. a-C:H (Ti) coating showed the best friction performance with a coefficient of friction of 0.10. The steel pin sliding against the uncoated disc suffered from severe wear, and the pin material transferred to the disc surface. However, there was no measurable wear on the disc surface. ta-C coating showed the best wear resistance in dry sliding, but the wear of its steel counterpart was significantly higher than those obtained for ta-C and a-C:H (Ti) coatings. For the oil-lubricated tests, the base oil without oil additives reduced the coefficients of friction of both ta-C and a-C:H coatings by 10%, while slightly increasing the coefficient of friction of a-C:H (Ti) coating [386]. When the coatings were lubricated with the base oil containing EP additives, the coefficient of friction decreased by 10% to 40% for ta-C and a-C:H coatings, but it slightly increased for a-C:H (Ti) coating. ta-C coating exhibited the lowest coefficient of friction of 0.08. It was reported that a transfer layer formed on the steel pins in dry sliding and favourably influenced the friction and wear performance of the coatings. However, under oil-lubricated conditions, the formation of this transfer layer was prohibited for ta-C and a-C:H coatings, while it was observed to be formed for a-C:H (Ti) coating. The low friction exhibited by ta-C and a-C:H coatings was attributed to a normal boundary lubrication mechanism in which a chemical reaction layer formed on the steel pins. This layer resulted in low friction and improved the wear resistance of the coatings, especially when the oil containing EP additives was used [386].

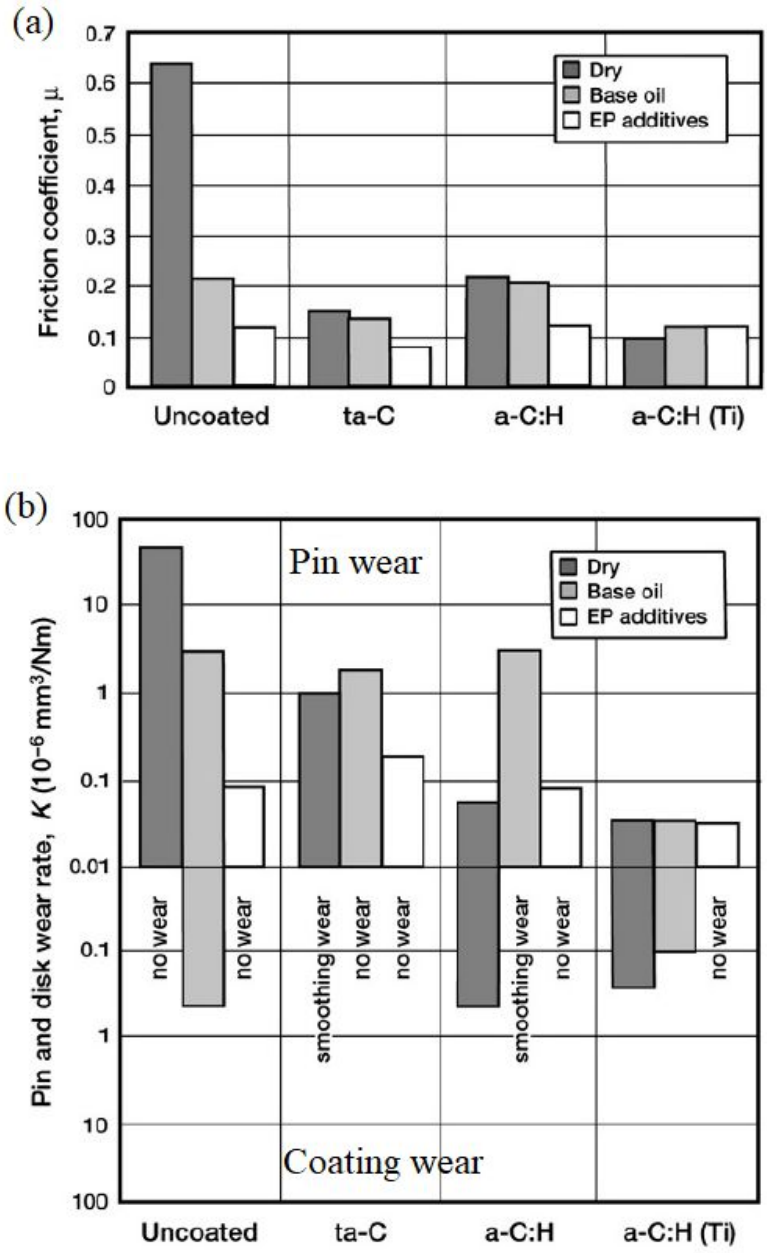

Figure 2.47: (a) Coefficients of friction and (b) wear rates of uncoated steel disc and coatings of ta-C, a-C:H, and a-C:H (Ti) tested in dry and oil-lubricated sliding with and without EP additives. (Test conditions: counterparts: AISI 52100 steel balls; normal load: 10 N; relative humidity: 50%; temperature: 22 °C) [386].

Zinc dialkyldithiophosphate (ZDDP) and molybdenum dithiocarbamate (MoDTC) are the most used anti-wear and friction modifier additives, respectively, designed to work effectively with

ferrous surfaces. MoDTC works by forming a low-friction tribofilm of MoS_2 on contacting surfaces [112,387]. ZDDP works by forming tribofilms of sulphides and phosphates to provide contacting surfaces with enough protection against wear [113,388,389]. The effect of these oil additives on the tribological properties of DLC coatings varies. Bouchet et al. [390] investigated the tribological properties of various types of DLC coatings, including a-C:H, titanium-doped Ti-C:H, and a-C under oil-lubricated sliding conditions, as shown in **Figure 2.48**. Pure PAO and PAO blended with ZDDP and MoDTC were used. In pure PAO, the coatings exhibited coefficients of friction in the range 0.08-0.1, which were much lower than 0.2 measured for the uncoated steel. The tests performed with MoDTC and ZDDP revealed decreased friction for a-C:H and Ti-C:H coatings, with coefficients of friction of 0.05 and 0.06, respectively. a-C coating exhibited the highest coefficient of friction of 0.08 and the highest wear rate. It was reported that a-C:H and Ti-C:H coatings had less friction than a-C coating because of the formation of low-friction MoS_2 tribofilms derived from MoDTC. ZDDP was observed to have no significant influence on the wear performance of all the tested coatings since they showed similar wear rates in the pure PAO and the PAO with MoDTC and ZDDP [390].

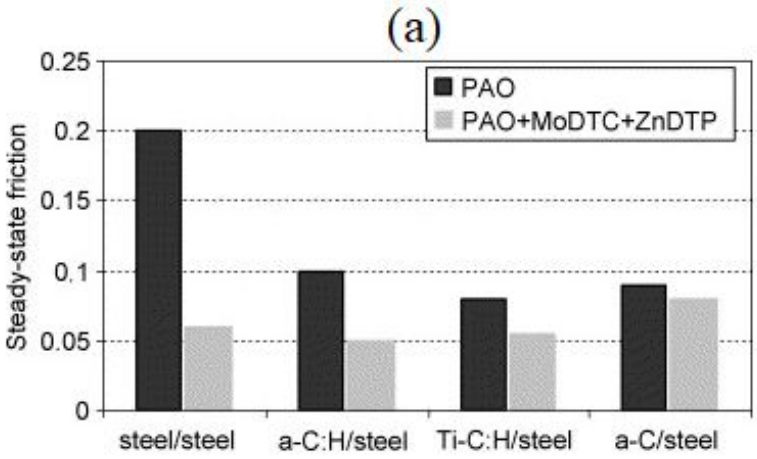

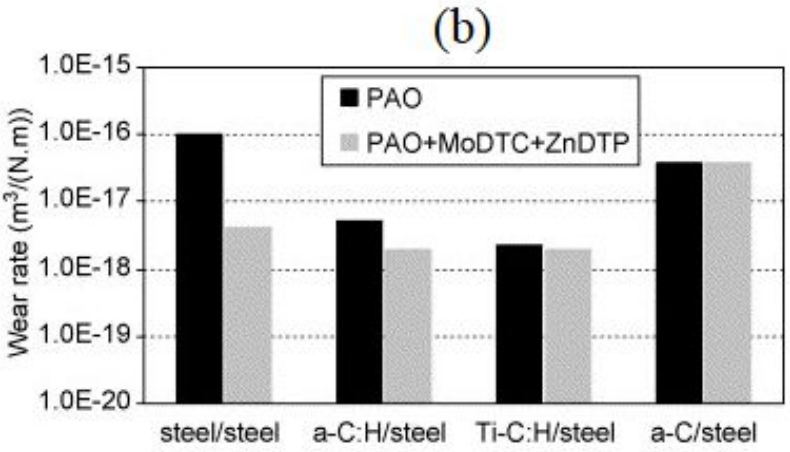

Figure 2.48: (a) Steady-state coefficients of friction and (b) wear rates of uncoated steel and a-C:H, Ti-C:H, and a-C coatings tested in pure PAO and PAO with MoDTC and ZDDP. (Test conditions: counterparts: AISI 52100 steel cylinders; normal load: 350 N; temperature: 100 °C) [390].

Podgornik et al. [145] examined the tribological performance of a-C:H (W) and a-C coatings in pure PAO and PAO mixed with sulphur-based extreme pressure (EP) or phosphorus-based anti-wear (AW) additives, as shown in **Figure 2.49**. In general, the coefficients of friction of a-C:H (W) coating were lower than those of the uncoated steel and a-C coatings. In pure PAO, a-C:H (W) coating exhibited the lowest coefficient of friction of 0.22 compared to 0.42 and 0.26 exhibited by the uncoated steel and a-C coating, respectively. The low friction of a-C:H (W) coating was attributed to the formation of a transfer layer containing WC particles on the steel counterpart surface. The highest EP additive concentration of 10% and the phosphorus-based AW additive resulted in increased friction, which was caused by the formation of the same sulphur-rich and phosphorus-rich tribofilms observed in the steel/steel tribological contacts. When the EP additive was used in concentrations between 0.1% and 5%, tungsten was found to transfer from a-C:H (W) coating and interact with the sulphur in the EP additive. This caused a WS_2 tribofilm to form on the steel counterpart surface. This newly formed tribofilm led to a reduction in the friction and wear of a-C:H (W) coating.

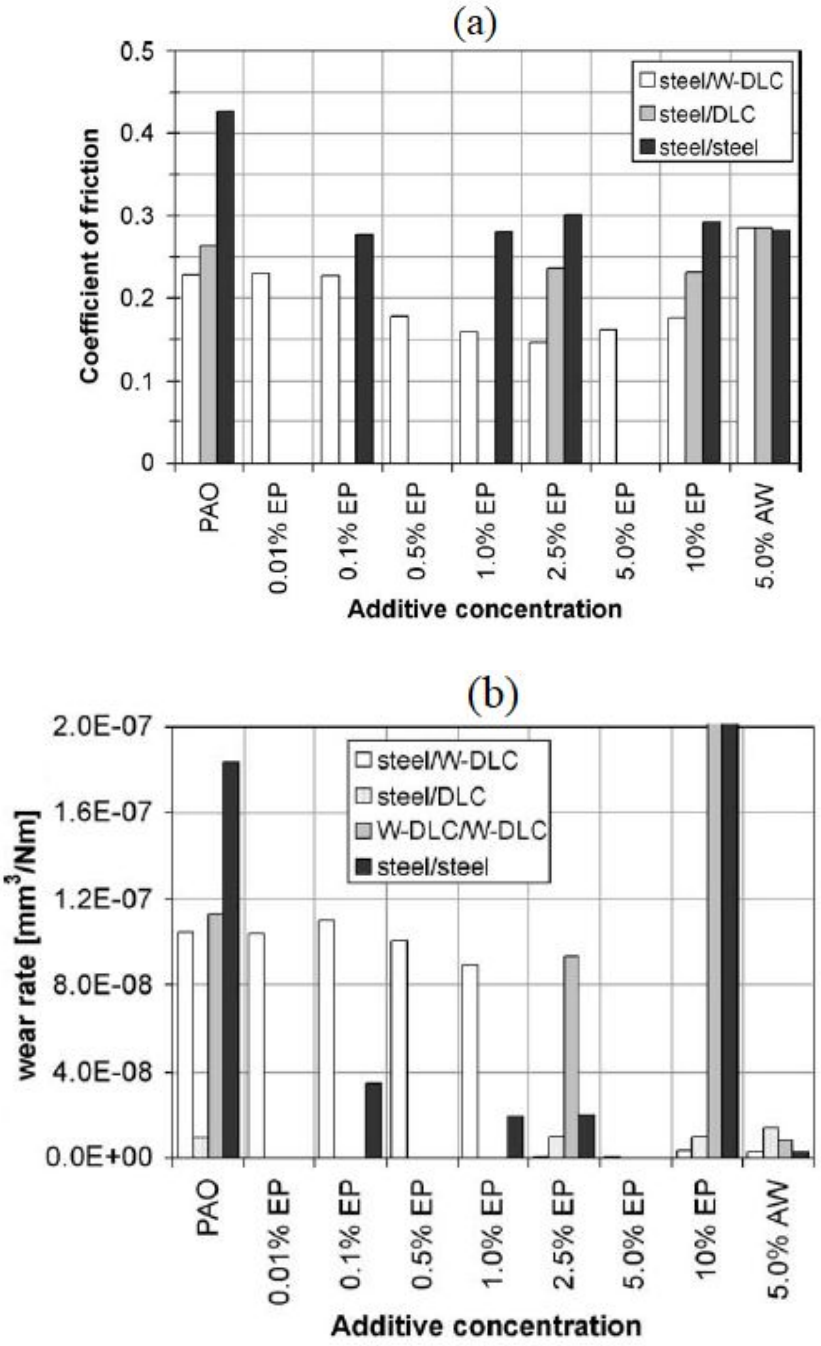

Figure 2.49: (a) Steady-state coefficients of friction and (b) wear rates of a-C:H (W) and a-C coatings and uncoated steel tested in pure PAO and PAO mixed with sulphur-based extreme pressure (EP) or phosphorus-based anti-wear (AW) additives. (Test conditions: counterparts: steel balls; normal load: 33 N; temperature: 50 °C) [145].

2.8 Deposition of TMD and DLC coatings

TMD coatings for tribological applications are mostly prepared by physical vapour deposition (PVD) techniques. PVD refers to a class of thin film deposition techniques in which a solid material is vaporised and then condensed onto a substrate as a thin layer. Magnetron sputtering is the most used PVD technique to prepare TMD coatings. The microstructure and properties of sputtered TMD coatings can be tailored by tuning deposition parameters such as the target-to-substrate distance, target temperature, substrate bias voltage, substrate temperature, and working pressure [175,391]. Typical sputtered TMD coatings exhibit a columnar morphology with high levels of porosity and a mixture of phase orientations [43,195-199]. Regarding the chemical composition, the coatings are metal-rich due to the preferential re-sputtering of chalcogenide atoms from the growing coatings and the chemical reaction of chalcogenide atoms with residual atmosphere during coating deposition [175,226,391,392].

DLC coatings are commonly fabricated using PVD and chemical vapour deposition (CVD) techniques. CVD is a technique in which a solid material is deposited onto a heated substrate surface as a result of a chemical reaction in the vapour phase. The deposition technique is chosen depending on the type of DLC coatings. Magnetron sputtering is commonly used for producing a-C coatings, where carbon is obtained from a solid graphite target [37,393]. a-C:H coatings are commonly produced by plasma enhanced chemical vapour deposition (PECVD) and reactive sputtering [372,393-395]. ta-C coatings are commonly produced by filtered cathodic vacuum arc (FCVA) [372,396,397], whereas ta-C:H coatings are commonly produced by PECVD [19,398,399]. The commonly used deposition techniques for TMD and DLC coatings are briefly discussed below.

2.8.1 Magnetron sputtering

Magnetron sputtering is a highly versatile PVD technique that uses magnets to confine charged plasma ions close to the surface of the sputtering target by creating high electric and magnetic fields around them. A schematic illustration of magnetron sputtering is shown in **Figure 2.50**. It basically involves four steps: ionisation, collision of atoms, transportation, and deposition [400]. The material to be deposited is initially put as a solid target within a vacuum chamber

filled with an inert gas (usually argon) at a pressure ranging from 0.5 Pa to 10 Pa [401]. An electric field is then used to create a gaseous plasma, which ionises and accelerates the inert gas atoms towards the target. The positively charged and highly energetic gas ions are drawn to a negatively charged cathode positioned behind the solid target, causing the target material to erode. The target atoms are then ejected with high energy in the vacuum chamber, where they reach the substrate and eventually adhere to its surface, forming a coating layer. Strong magnets are required to keep a high plasma density near the target surface by trapping secondary electrons. This significantly improves the efficiency of ionisation of gas atoms and results in higher deposition rates. These magnets are arranged perpendicular to the electric field behind the target. The electric field is generated by either radio frequency (RF) or (DC) power sources [402]. DC magnetron sputtering is widely used for the deposition of coating materials with high electrical conductivity since the positively charged gas ions can be easily accelerated to the target surface. RF magnetron sputtering is preferred for non-conducting and insulating materials because it inhibits the build-up of positive charges on the target by alternating the applied electric current at radio frequencies [403]. Magnetron sputtering is usually done in a high vacuum, with a pressure between 10^{-5} Pa and 10^{-3} Pa [401]. This makes the coating microstructure more compact and improves the adhesion to substrates.

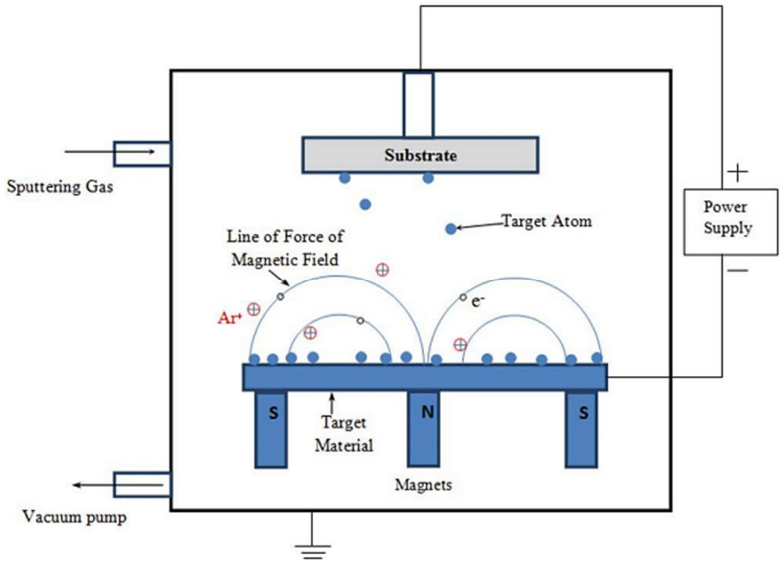

Figure 2.50: Schematic illustration of a magnetron sputtering system [402].

2.8.2 Reactive sputtering

Although sputtering techniques allow the use of one or multiple target materials in the vacuum chamber, achieving the desired coating composition is not always possible. An alternative method to get around this problem is to introduce a reactive gas or a mixture of gases into the sputtering chamber, a technique known as reactive sputtering. A schematic illustration of this technique is shown in **Figure 2.51**. In this technique, a gas that is inert under ambient conditions undergoes a chemical reaction with the target material in the presence of gas plasma, producing a chemical composition that differs from the target material [404]. Oxygen, nitrogen, acetylene, and methane are the most commonly used reactive gases [405].

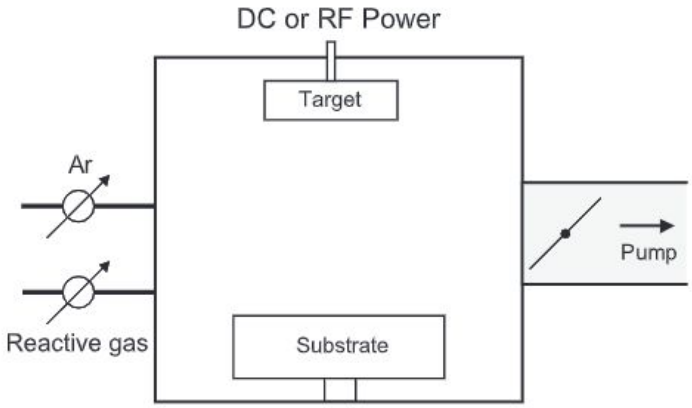

Figure 2.51: Schematic illustration of a reactive sputtering system [404].

2.8.3 CVD and PECVD

Unlike PVD techniques, which evaporate atoms from solid materials into gaseous vapour, CVD technique uses one or more volatile precursors, which chemically react on the substrate surface to make the desired coating. A typical CVD system is shown in **Figure 2.52**. The properties and microstructure of the CVD-deposited coating are highly dependent on the substrate's temperature [403]. A low temperature can cause a poor coating microstructure and a high level of impurity contamination. As a result, the technique is usually carried out at high temperatures in the range 600-800 °C [406]. This, however, limits the substrate material selection to those capable of withstanding high temperatures. PECVD overcomes this limitation by allowing deposition at lower temperatures ranging from room temperature to 350 °C [406]. In PECVD, reactant gases are excited into a plasma by applying a high electric field.

This excitation induces a chemical reaction, and the product of this reaction is then deposited onto a substrate as a coating layer. A typical PECVD system is shown in **Figure 2.53**.

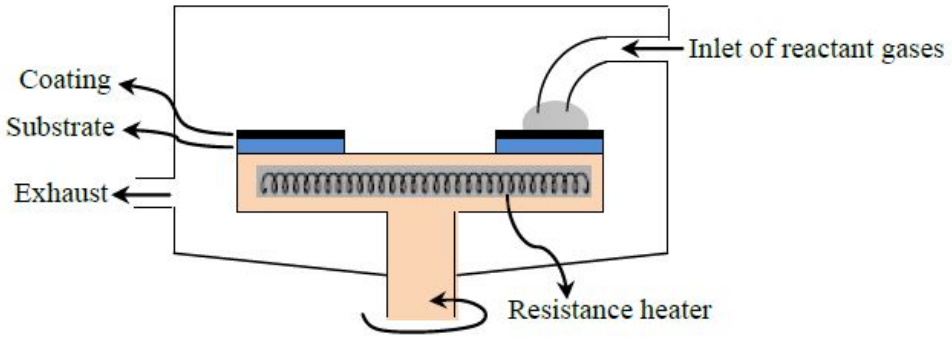

Figure 2.52: Schematic illustration of a CVD system [407].

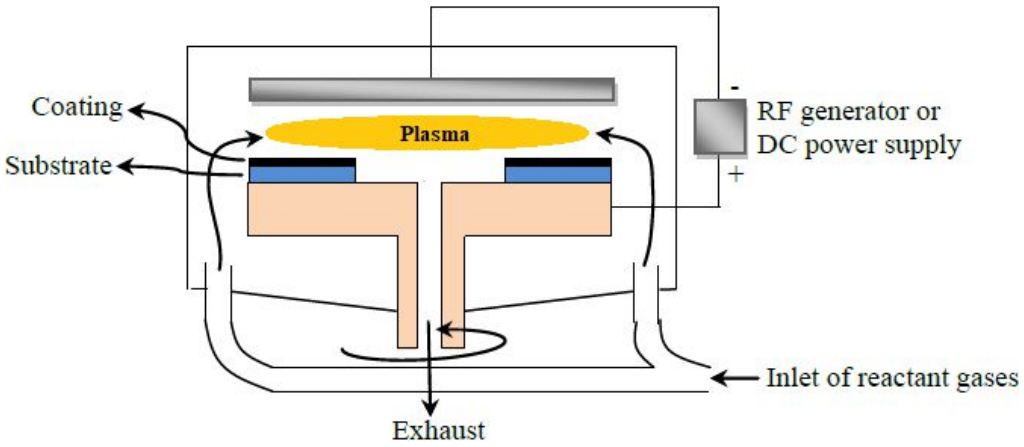

Figure 2.53: Schematic illustration of a PECVD system [407].

2.8.4 FCVA

FCVA is a PVD technique that vaporises the material to be deposited from a cathodic target using an electric arc. When the cathodic target is touched with a small striker electrode in a high vacuum, the electric arc is initiated and produces highly ionised plasma. It also produces unwanted droplets and debris particles from the cathodic target with a size ranging from 0.1 μm to 10 μm, which are commonly referred to as macroparticles due to their larger size compared to the ionised plasma [408,409]. These macroparticles can easily reach the substrate and cause contamination of the growing coating layer. Therefore, the plasma is guided into a

curved magnetic filter for the removal of the macroparticles before reaching the substrate [409]. A schematic illustration of FCVA is shown in **Figure 2.54**.

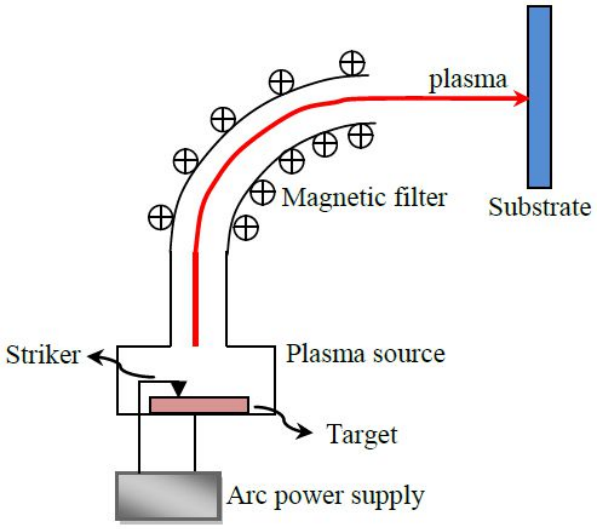

Figure 2.54: Schematic illustration of a FCVA system [407].

2.9 Summary

Despite significant advances in the field of tribology, friction continues to contribute to large energy losses that impair the efficiency and durability of mechanical systems. One approach for tackling this issue is by covering tribological surfaces with coatings possessing low coefficients of friction. Among different low-friction coatings, TMDs are well known for their excellent self-lubricating properties, which are attributed to (a) the formation of a crystalline tribolayer in the topmost coating surface with TMD basal planes aligned parallel to the sliding direction and (b) the formation of a sliding-induced transfer layer on the coating's counterpart.

Among different TMD coatings, $MoSe_2$ has a great promise for many tribological applications due to its desirable properties such as low coefficient of friction, high thermal stability, low sensitivity to air humidity, and good wear resistance. For the actual assessment of the potential of $MoSe_2$ coating for tribological applications, an in-depth investigation and understanding of its tribological performance with oil lubrication are needed since most mechanical components are typically used under oil-lubricated conditions. However, upon exploration of the available

literature, it was realised that no single study exists that evaluates the tribological performance of $MoSe_2$ coating under oil-lubricated sliding conditions. The entire attention of previously conducted tribological studies has focused on evaluating its tribological performance in environments such as humid air, vacuum, and different gas atmospheres under dry sliding conditions only, whereas its tribological performance under oil-lubricated sliding conditions has not yet been experimentally studied and remains unexplored. The tribological response of $MoSe_2$ coating in oil-lubricated contacts may significantly differ from that in dry contacts because of the effects arising from interacting with oil lubrication. These interactions may have a synergistic, detrimental, or neutral effect on its self-lubricating properties. The current study will bridge the existing knowledge gap in the tribology of $MoSe_2$ coating by deeply investigating its tribological performance under oil-lubricated sliding conditions. The results of the study will create new knowledge about the tribology of the coating and allow for the determination of its potential for usage in mechanical components operating under oil-lubricated conditions.

Chapter 3: Materials, procedures, and experimental techniques

This chapter provides a description of the materials used, sample preparation, and deposition procedures of $MoSe_2$ and $MoSe_2$/DLC-W coatings. It also describes the experimental procedures and techniques used to characterise the thickness, chemical composition, crystalline structure, mechanical properties, and tribological performance of the deposited coatings.

3.1 Materials and coating preparation

3.1.1 Substrates

Discs of 100Cr6 steel were used as substrates for the deposition of $MoSe_2$ and $MoSe_2$/DLC-W coatings in the present work. The discs have a diameter of 50 mm and a thickness of 5 mm. They also have a small hole drilled in the middle to facilitate mounting on sample holders. The chemical composition of 100Cr6 steel is shown in **Table 3.1**. The discs were first ground using P120, P500, P1200, and P4000 SiC grit papers, and subsequently polished using 3 μm and 1 μm diamond suspensions to achieve a mirror-like surface finish. Polishing resulted in a surface roughness R_a of 0.03 ± 0.004 μm measured by the Alicona 3D optical profilometer.

Table 3.1: Chemical composition of 100Cr6 steel in wt% [410].

C	Cr	Mn	P	S	Cu	Si	Fe
0.96	1.38	0.23	0.003	0.001	0.05	0.30	balance

3.1.2 $MoSe_2$ coating

$MoSe_2$ coating was deposited on the 100Cr6 steel discs. It was also deposited on a wafer of polished borosilicate glass to determine its thickness. The discs were first ultrasonically cleaned in acetone for 60 minutes, washed with distilled water, and then baked in an oven at a

temperature of 120 °C for 30 minutes to remove residual water molecules. They were then plasma etched with oxygen using a microwave plasma etching system (Tepla 300, PVA Tepla) to remove any carbon residue. The deposition took place in a RF magnetron sputtering system (Nano 38, Kurt J. Lesker), as represented schematically in **Figure 3.1**. The substrates were initially kept at room temperature, with a temperature rise of less than 10 °C detected throughout the deposition. The coating was fabricated from a $MoSe_2$ sputtering target with 99.99% purity and supplied by Stanford Advanced Materials Company. The power applied to the target was kept at 80 W, and the distance between the target and the substrates was maintained at 150 mm. High-purity argon was used as the sputtering gas at a constant flow rate of 20 sccm and a pressure of 0.4 Pa. The coating was fabricated at the Optoelectronics Research Centre (ORC) at the University of Southampton.

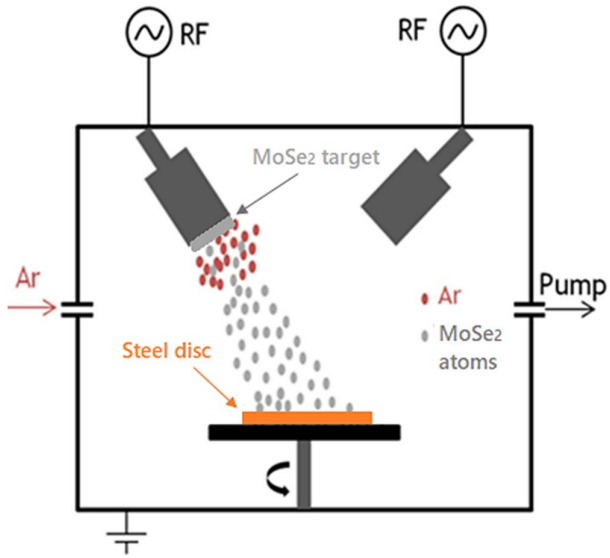

Figure 3.1: Schematic illustration of the deposition chamber used for fabricating $MoSe_2$ coating.

3.1.3 $MoSe_2$/DLC-W coating

$MoSe_2$/DLC-W coating was deposited on the 100Cr6 steel discs. Prior to the deposition, the discs were first ultrasonically cleaned in acetone for 15 minutes. The deposition was carried out in an industrial CemeCon 880/9 MLT coating chamber (400 x 400 x 430 mm) by unbalanced close field magnetron sputtering using DC power supplies. The chamber has four cathodes: cathodes 1 and 2 are positioned with an angular separation of 40°, and the other two

are facing these ones with the same geometry [411]. A schematic illustration of the chamber configuration is shown in **Figure 3.2**. The deposition was performed with four targets, each of which had a purity level of 99.9%: Cr, C, WC, and $MoSe_2$. Pure argon at a constant pressure of 0.58 Pa was used as the sputtering gas. The deposition started with a Cr layer from the Cr target, followed by a DLC-W layer deposited from the C and WC targets. Finally, $MoSe_2$ was deposited as the top layer from the $MoSe_2$ target. A schematic illustration of the deposited coating is shown in **Figure 3.3**. The coating was deposited by AdvaMat, s.r.o. Company in Prague, Czech Republic.

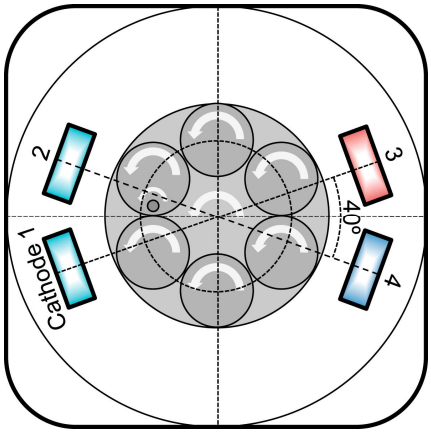

Figure 3.2: Schematic illustration of the deposition chamber used for fabricating $MoSe_2$/DLC-W coating [411].

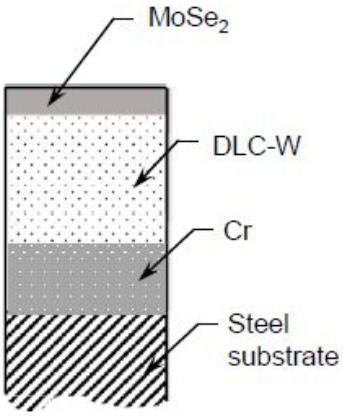

Figure 3.3: Schematic illustration of $MoSe_2$/DLC-W coating.

To determine the thickness of $MoSe_2$/DLC-W coating, a coating cross-section was prepared, as shown in **Figure 3.4**, in accordance with the ASTM B487-85 standard. The coating cross-section was first cut using a diamond cutting blade and then hot mounted in conductive Bakelite. It was then ground using P1200 and P4000 SiC grit papers to remove damaged and deformed surface material resulting from cutting, while limiting the amount of additional surface deformation. Continuous washing with soap solution was undertaken to clean the surface. Subsequently, a 1μm diamond suspension was used to polish the cross-section and achieve a mirror-like surface finish. After polishing, the cross-section was cleaned with acetone and then analysed with an optical microscope (BX51, Olympus) at 100x magnification.

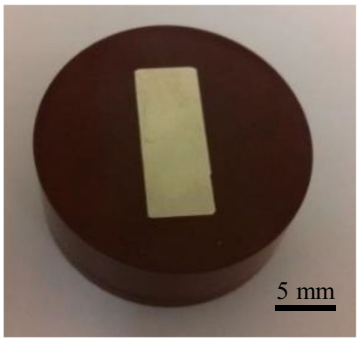

Figure 3.4: Mounted and polished cross-section of $MoSe_2$/DLC-W coating.

3.1.4 AISI 52100 steel balls

In tribological applications, TMD coatings are commonly used to slide against steel counterparts. Accordingly, AISI 52100 steel balls with a diameter of 6 mm and a surface roughness R_a of 10 nm were used in this work as sliding counterparts for the tribological testing of $MoSe_2$ and $MoSe_2$/DLC-W coatings. These balls were supplied by Simply Bearings Ltd. AISI 52100 steel is a through-hardened, high-carbon, chromium-containing low-alloy steel that is widely used for ball bearing applications in the automotive industry, rotating devices, and machines [412]. **Table 3.2** shows the chemical composition of AISI 52100 steel. Another reason for selecting AISI 52100 steel balls was that they are often used for the tribological testing of TMD coatings. This allows for a comparison of the results obtained in the present work with those published in the available literature.

Table 3.2: Chemical composition of AISI 52100 steel in wt% [413].

C	Cr	Mn	P	S	Si	Fe
0.95-1.10	1.30-1.60	0.25	0.03	0.025	0.15-0.30	balance

3.1.5 PAO4 oil lubricant

Polyalphaolefin 4 (PAO4) oil is free of ring structures, double bonds, sulphur, nitrogen components, and waxy hydrocarbons. This results in a synthetic base oil with a high viscosity index, good thermal stability, outstanding resistance to oxidation, and excellent low-temperature performance [90,414]. All these attractive properties make PAO4 oil the primary basestock for synthetic lubricants used in a broad range of industrial and automotive applications such as heavy-duty diesel engines, passenger car engines, wind turbines, transmission fluids, and gear boxes [90]. For this reason, it was chosen in the present work for the tribological testing of $MoSe_2$ and $MoSe_2$/DLC-W coatings in oil-lubricated sliding. The uniformity of the molecular structure of PAO4 oil was another reason for its selection. This uniformity is advantageous for conducting research and facilitates the production of repeatable and reproducible experiments. It is worth mentioning that the PAO4 oil used in the present work was additive-free in order to determine if the coatings themselves can form low-friction tribofilms required for friction reduction without any synergetic or antagonistic influence of oil additives. The oil was supplied by ExxonMobil Corporation, and its properties are presented in **Table 3.3**.

Table 3.3: Basic properties of PAO4 oil [89-91,415,416].

Kinematic viscosity at 25 °C (cSt)	Kinematic viscosity at 40 °C (cSt)	Kinematic viscosity at 60 °C (cSt)	Kinematic viscosity at 80 °C (cSt)	Kinematic viscosity at 100 °C (cSt)	Flash point (°C)	Density at 25 °C (g/cm^3)	Viscosity index
29.67	16.8	9.2	5.7	3.9	220	0.81	126

3.2 Friction and wear testing

The TE77 reciprocating tribometer manufactured by Phoenix Tribology Ltd was used for the evaluation of the tribological properties of $MoSe_2$ and $MoSe_2$/DLC-W coatings. It is a flexible and well-established research machine that is mainly used for the study of materials, coatings, and surface treatments. It is also widely used for the purpose of evaluating the performance of oil lubricants, particularly to assess if they will perform well in a particular part of a machine or if they will be able to endure certain working conditions such as high operating temperature. **Figure 3.5** shows the basic layout of the TE77 reciprocating tribometer and its main components. A motor coupled to an eccentric cam and scotch yoke assembly drives the machine. The scotch yoke converts rotating motion into linear reciprocating motion. The top moving sample is loaded by a loading system and reciprocated mechanically against the fixed lower sample. The lower sample is clamped either in a bath for oil-lubricated testing or on a dry mounting plate. The tribometer can be operated under different conditions of reciprocating frequency, load, and stroke length, with a maximum sliding frequency of 50 Hz, a maximum normal load of 1,000 N, and a maximum stroke length of 25 mm [417]. Altering the location of a spline within the cam housing allows the user to make a manual adjustment to the stroke length. A piezo-electric force transducer measures the frictional force between the stationary sample and its sliding counterpart, while an attached strain-gauge transducer measures the applied load. The output data, including the coefficient of friction and friction force, is recorded in a connected computer with COMPEND 2000 sequence control and data acquisition software. Based on the potential application of materials, different types of test configurations can be employed on the tribometer, including ball-on-flat (point contact), cylinder-on-flat (line contact), and flat-on-flat (area contact).

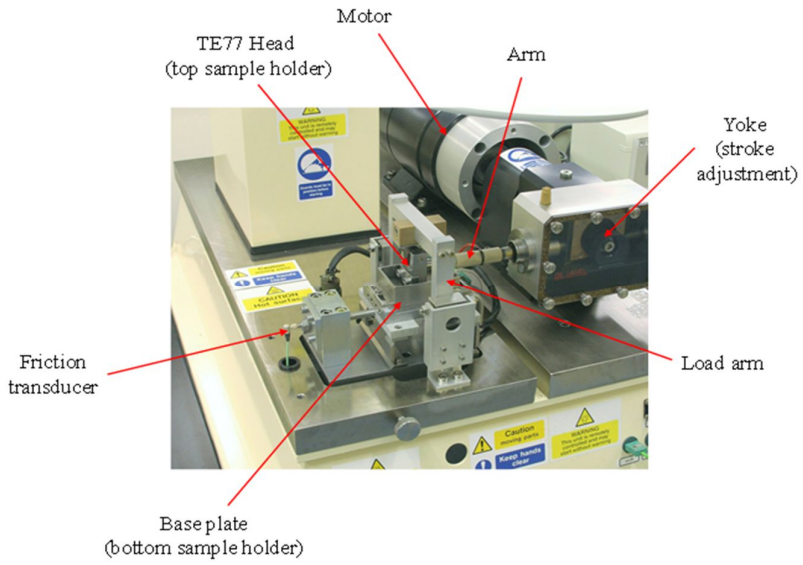

Figure 3.5: Image of the TE77 reciprocating tribometer shows its major components.

3.2.1 Experimental set-up

In this work, a reciprocating ball-on-flat configuration was chosen to simulate the piston ring/cylinder liner contact in a heavy-duty vehicle's internal combustion engine. The configuration is schematically illustrated in **Figure 3.6**. Another reason for choosing this configuration was to avoid misalignment issues between contacting surfaces. This is very important in order to provide consistent results on the tribological behaviour of the coatings. The AISI 52100 steel balls were used as the sliding counterpart materials against the coatings. To achieve a pure sliding condition, the ball was fixed in the oscillating holder to prevent it from rotating and loaded against the stationary coated disc. The disc was held in place on the tribometer's holder by a securing bolt through its central hole. The original contact surface conditions were maintained by using a new ball for each test.

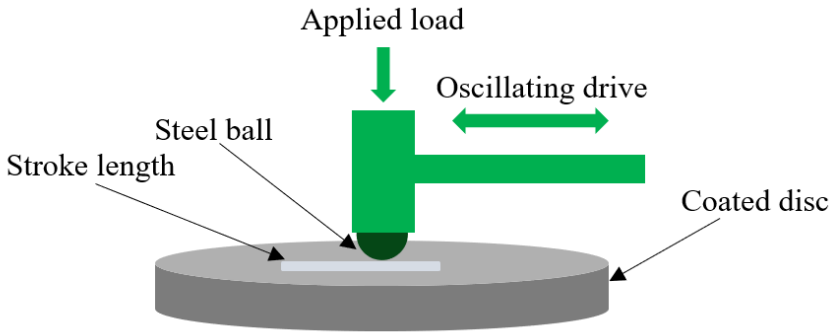

Figure 3.6: Schematic illustration of the reciprocating ball-on-flat test configuration used in the TE77 tribometer.

Before each test, the ball and disc were ultrasonically cleaned in acetone for 5 minutes to remove any contaminants and to maintain identical surface conditions. They were then wiped with lens paper and dried naturally at room temperature. The coatings were tribologically evaluated under both dry and PAO4-lubricated sliding conditions in ambient air, with air humidity ranging from 40% to 50%. Each test was repeated twice under the same test condition to ensure the reliability and reproducibility of the data obtained. For PAO4-lubricated testing, a small amount of PAO4 was spread on the surface of the coated disc prior to each test. It soaked the ball, ensuring that the contact was always completely immersed in oil (only immersed by surface tension, no bath). No additional oil was supplied to the contact during the test. The tests for each sliding condition were carried out on the same coated disc, with a minimum spacing of 10 mm maintained between the tests.

Upon completion of the tests under dry sliding conditions, the tribological pair was ultrasonically cleaned in acetone for 5 minutes and left to dry at room temperature without wiping to avoid removing loosely held tribofilms (if any). For the tests performed in PAO4-lubricated sliding, the tribological pair was cleaned in petroleum ether for 5 minutes to remove residual oil and any contaminants, and then left to dry naturally at room temperature without wiping to avoid removing loosely held tribofilms (if any). The samples were then labelled and stored in sealed plastic bags at room temperature.

3.2.2 Experimental conditions for $MoSe_2$ coating

$MoSe_2$ coating was tribologically tested under dry and PAO4-lubricated sliding conditions at a constant applied load of 5 N, corresponding to a maximum Hertzian contact pressure of 1.12 GPa. The equations (2.2), (2.3), (2.4), and (2.5) were used to calculate this contact pressure (see Appendix. A). This applied load has been used in many published tribological studies of TMD-based coatings, thereby allowing for a direct comparison of the results. The selected test parameters are shown in **Table 3.4**. The oscillating frequency, average sliding speed, and stroke length were set in accordance with the recommendations of an ASTM task group comprised of engine industry representatives [418]. The short test duration of 5 minutes was chosen following trial testing to avoid complete coating failure and substrate exposure. The lambda ratio for PAO4-lubricated sliding was 1.3, indicating that the operational lubrication regime was mixed lubrication. This ratio was determined using equations (2.10) and (2.11) (see Appendix. A).

Table 3.4: Experimental parameters used for the tribological testing of $MoSe_2$ coating.

Oscillating frequency (Hz)	10
Average sliding speed (m/s)	0.2
Stroke length (mm)	10
Test duration (minute)	5
Total sliding distance (m)	60

The coating was also tested at different loads in PAO4-lubricated sliding to investigate the influence of contact load on its tribological properties. Five different loads were used to generate different stress levels: 5 N, 8 N, 10 N, 12 N, and 15 N, corresponding to maximum Hertzian contact pressures of 1.11 GPa, 1.31 GPa, 1.41 GPa, 1.50 GPa, and 1.62 GPa, respectively (see Appendix. A). The same experimental parameters listed in **Table 3.4** were used. The calculated lambda ratios were 1.3 for 5 N and 8 N loads and 1.2 for the rest of loads (see Appendix. A), indicating that the operational lubrication regime was mixed lubrication.

Using the same experimental parameters listed in **Table 3.4** and at an applied load of 5 N, the effect of operating temperature on the tribological performance of the coating under PAO4-lubricated sliding conditions was also examined. An electric heating element placed under the sample holder was used for heating the coated disc. The temperature was controlled using a thermocouple that regulates the temperature according to a user-defined magnitude and was bolted to the disc through its centre hole. The tests were carried out at five different temperatures: 25 °C, 40 °C, 60 °C, 80 °C, and 100 °C. This was done to ensure that a variety of conditions were present that could promote different interactions between the oil and the coating. The calculated lambda ratios for 25 °C, 40 °C, 60 °C, 80 °C, and 100 °C, were 1.3, 0.8, 0.5, 0.3, and 0.2, respectively (see Appendix. B). This suggests that the operational lubrication regime was mixed lubrication at 25 °C and boundary lubrication at the other temperatures.

3.2.3 Experimental conditions for $MoSe_2$/DLC-W coating

$MoSe_2$/DLC-W coating was tested under dry and PAO4-lubricated sliding conditions. Five different contact loads were used: 10 N, 20 N, 30 N, 40 N, and 50 N, corresponding to maximum Hertzian contact pressures of 1.17 GPa, 1.48 GPa, 1.69 GPa, 1.86 GPa, and 2.0 GPa, respectively (see Appendix. C). The selected test parameters are listed in **Table 3.5**. The lambda ratios calculated for sliding with PAO4 lubrication were 1.2 for 40 N and 50 N loads and 1.3 for the rest of the loads (see Appendix. C). This indicates that the operating lubrication regime was mixed lubrication.

Table 3.5: Experimental parameters used for the tribological testing of $MoSe_2$/DLC-W coating.

Oscillating frequency (Hz)	20
Average sliding speed (m/s)	0.4
Stroke length (mm)	10
Test duration (minute)	20
Total sliding distance (m)	480

3.3 Characterisation techniques

3.3.1 X-ray diffraction (XRD)

X-ray diffraction (XRD) is an analytical technique primarily used to analyse the crystalline structure of materials. It basically works by irradiating a sample with a beam of X-rays and then measuring the intensities and scattering angles of the X-rays leaving the sample. XRD is a form of elastic scattering in which the scattered X-rays from a material have the same wavelength as the incoming X-rays but are scattered in different directions. A beam of X-rays can either constructively or destructively interfere with each other when it hits a crystalline structure. The constructive interference is observed when Bragg's law is satisfied [419]:

$$n\lambda = 2d\ sin\theta \tag{3.1}$$

where n is an integer, λ is the wavelength of incident beam of X-rays, d is the distance between atomic planes responsible for reflecting the beam of X-rays, and θ is the Bragg angle between the incident beam of X-rays and the planes of the lattice, as shown in **Figure 3.7**.

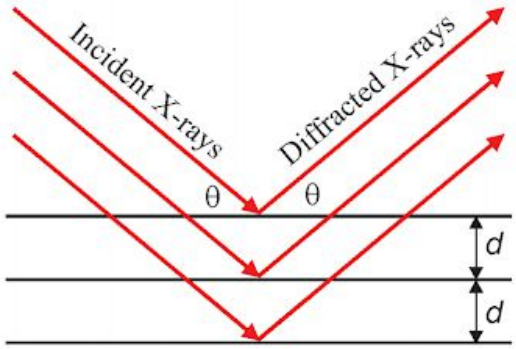

Figure 3.7: Schematic illustration of diffraction of X-rays in accordance with Bragg's law [419].

For XRD analysis, the incident beam of X-rays strikes the surface at different incidence angles, and the intensities of the diffracted X-rays are measured, recorded, and plotted as a function of the angle 2θ. Because each crystalline material has a distinct atomic structure, it diffracts X-rays in a unique characteristic pattern of peaks. Different geometries can be selected in a diffractometer for XRD analysis of materials. The most used geometries are Bragg-Brentano focusing geometry and grazing incidence XRD (GI-XRD) geometry. In Bragg-Brentano

focusing geometry, the source of X-rays and the detector of reflected X-rays must be positioned at the same angle with respect to the sample surface [420,421]. This is necessary to maintain the same angle of incidence and angle of diffraction with respect to the sample surface. Such geometry is practically achieved by moving the source of X-rays and the detector in a circular path, as shown in **Figure 3.8 (a)**. X-rays with large angles of incidence can penetrate a few to several hundred micrometres within the material under investigation, depending on its radiation density. Therefore, for XRD analysis of thin films, the depth of beam penetration may be significantly greater than the film thickness. Consequently, Bragg-Brentano focusing geometry is not suitable for analysing thin films. GI-XRD geometry has been developed to overcome such limitation [421,422]. In this geometry, the incident beam of X-rays strikes the sample at fixed and very small angles of incidence, typically between 1° and 3°, while the detector is rotated to collect the diffracted X-rays [421], as shown in **Figure 3.8 (b)**. With this geometry, the depth of penetration is limited, and the substrate contribution on the diffraction response is avoided.

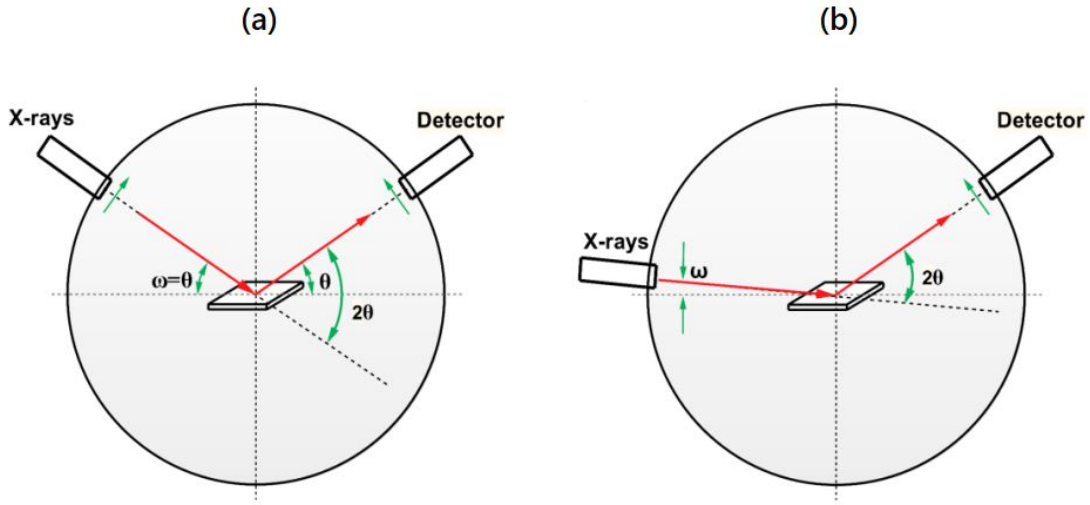

Figure 3.8: Schematic illustration of (a) Bragg-Brentano focusing geometry and (b) GI-XRD geometry [423].

In this work, the crystalline structure of the deposited $MoSe_2$ and $MoSe_2$/DLC-W coatings was evaluated by a GI-XRD diffractometer (SmartLab, Rigaku) operating at an accelerating voltage of 45 kV with Cu Kα radiation (λ = 1.5418 Å). The diffraction patterns were measured over a 2θ angular range between 10° and 80°. The grazing incidence angle of the X-rays was set at 2° for $MoSe_2$ coating and 1° for $MoSe_2$/DLC-W coating. The crystallographic phases contained

in the coatings were identified by comparing the obtained XRD results with the International Centre for Diffraction Data (ICDD) standard cards.

3.3.2 Nanoindentation

Hardness is defined as the resistance of a material to plastic deformation when subjected to a localised compressive force. Nanoindentation is the preferred technique for determining the hardness of thin films, as the penetration depth of traditional hardness measuring techniques would exceed the film thickness. It basically works by pressing a very hard indenter with a special geometry into the surface of a thin film while controlling the applied load and depth of indentation to produce a load-displacement curve, as shown in **Figure 3.9**. The resulting curve serves as the mechanical fingerprint of the thin film, from which its hardness (H) and Young's modulus (E) can be determined using the method proposed by Oliver and Pharr in the following equations [424]:

$$H = \frac{F_{max}}{A_c} \tag{3.2}$$

where F_{max} is the maximum indentation load, and A_c is the projected contact area of the indentation. For the Berkovich indenter, A_c can be determined from the contact depth h_c in the following equation [424]:

$$A_c = 24.5\, {h_c}^2 \tag{3.3}$$

The reduced modulus (E') is calculated using the following equation [424]:

$$E' = \frac{S\sqrt{\pi}}{2\,\beta\sqrt{A_c}} \tag{3.4}$$

where S is the contact stiffness and is equal to the slope of the unloading part of the curve. β is a constant, which depends on the geometry of the indenter. For the Berkovich indenter, β is equal to 1.034 [425]. The Young's modulus (E) of the tested material is calculated from the following equation [424]:

$$E' = \left(\frac{1 - {v_i}^2}{E_i} + \frac{1 - v^2}{E} \right)^{-1} \tag{3.5}$$

where E_i is the Young's modulus of the indenter, v is the Poisson's ratio of the tested material, and v_i is the Poisson's ratio of the indenter.

In nanoindentation, the indents are normally performed in a depth-controlled mode, with the maximum indentation depth not exceeding 10% of the film's thickness [426,427]. This is to ensure that the resulting indentation interaction volume remains within the thin film and to prevent any effect of the substrate on the mechanical properties of the film during measurements.

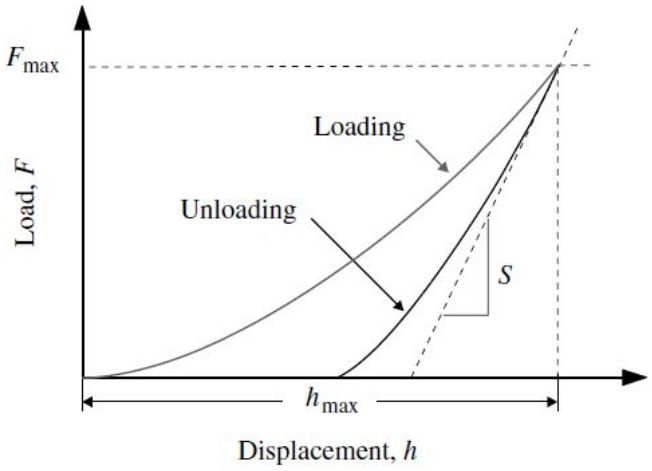

Figure 3.9: Schematic representation of a typical loading-unloading nanoindentation curve [428].

In this work, the mechanical properties of $MoSe_2$ and $MoSe_2$/DLC-W coatings (i.e. hardness H and reduced elastic modulus E') were evaluated by a depth-sensing indentation technique using a nanoindenter equipped with a diamond Berkovich tip having a radius of 5 μm (NanoTest Vantage system, Micro Materials). For $MoSe_2$ coating, all the indentations were done in a depth-controlled mode with a maximum depth of 100 nm, which is below 10% of the thickness of the coating. Each two adjacent indents were spaced 10 μm apart to avoid possible

overlapping of indented areas. There was a total of 25 indents made, and the average values of H and E' were calculated using the method proposed by Oliver and Pharr from the resultant loading-unloading curves [429], which was an in-built module of the software.

For $MoSe_2$/DLC-W coating, the nanoindentation measurements of the top $MoSe_2$ coating layer and the whole coating were performed on the surface of one of the coated steel discs, whereas those of the DLC-W layer were performed on the surface of the prepared coating cross-section. The maximum indentation depth was controlled to be about 10% of each layer thickness, so that the resulting indentation interaction volume remained within the layer, and the results were free of any influence from the substrate or other layers. The maximum indentation depth was chosen to be around 30 nm for the $MoSe_2$ layer, 200 nm for the DLC-W layer, and 350 nm for the whole coating. There was a total of 25 indents performed for each layer, which were spaced 50 μm apart to prevent overlapping of indented areas. The average values of H and E' were then determined from the resulting loading-unloading curves using the method proposed by Oliver and Pharr.

3.3.3 Alicona 3D optical profilometer

The Alicona 3D optical profilometer is a high-resolution 3D measuring instrument commonly used for the measurement of the form and roughness of surfaces. Its main component is a high-precision optical system equipped with different objectives. These objectives have different magnifications, ranging from 2.5x to 100x, and allow for measurements at different resolutions [430]. The profilometer basically works under the principle of "Focus-Variation", which combines an optical system's small depth of focus with vertical scanning. Such an operating principle is depicted in **Figure 3.10**. The light emerging from a white light source is inserted into the optical system and focused on a sample by one of the objectives. Depending on the sample's topography and reflectivity, the light is reflected in many directions when it strikes the sample. A light-sensitive sensor collects all the reflected light. Due to the optical system's small depth of focus, only small areas of the sample are sharply imaged. To conduct a complete surface detection with a full depth of field, the objective is moved vertically in reference to the sample while continuously gathering data from the surface to create a high-resolution 3D image [430,431].

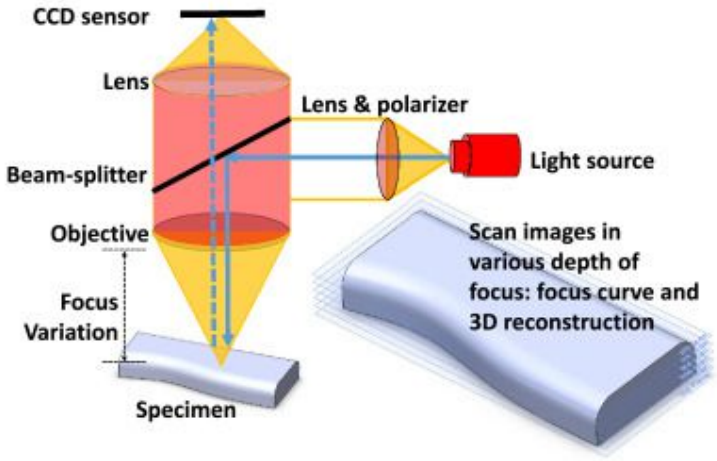

Figure 3.10: Schematic diagram shows the operating principle of "Focus-Variation" employed in the Alicona 3D optical profilometer [432].

In this work, the Alicona profilometer was used to measure the thickness of $MoSe_2$ coating at five points on the wafer of polished borosilicate glass. It was also used to measure 2D cross-sectional profiles from three different zones of the wear tracks of the coatings after tribological testing, as shown in the example in **Figure 3.11**. A 20x objective lens was used, resulting in a vertical resolution of 50 nm. SigmaPlot software was used to calculate the cross-sectional worn area of each profile. The wear volume was then determined by multiplying the averaged cross-sectional worn area by the length of the wear track (i.e. 10 mm). The wear volume of the spherical counterparts V_b was considered to be a spherical cap and calculated using the following equation [433]:

$$V_b = \pi h^2 \left(R - \frac{h}{3}\right) \tag{3.6}$$

where h is the height of the ball wear scar, and R is the radius of the steel ball. h was calculated from the following equation [433]:

$$h = R - \sqrt{(R^2 - m^2)} \tag{3.7}$$

where m is the radius of the ball wear scar and is measured by the profilometer. After calculating the wear volumes of the coating and its counterpart, equation (2.9) was used to calculate their wear rates.

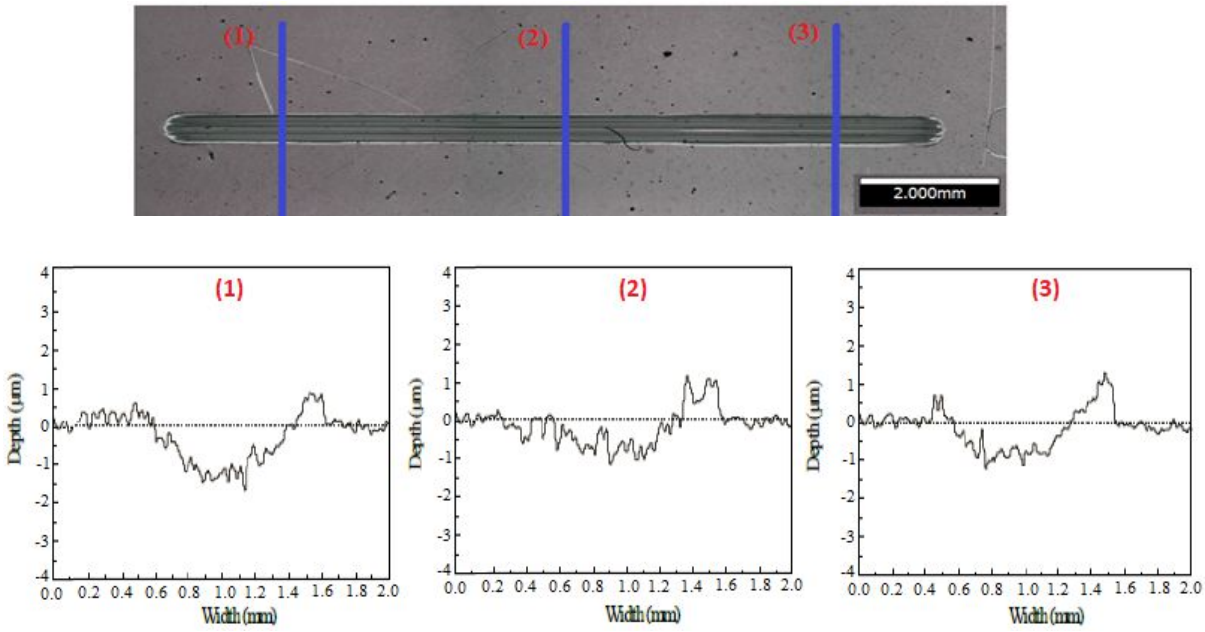

Figure 3.11: Example of three cross-sectional profiles measured by the Alicona 3D profilometer from different zones of a wear track.

3.3.4 Scanning electron microscopy (SEM)

Scanning Electron Microscopy (SEM) is a versatile imaging technique commonly used for the examination and analysis of materials. It basically generates images of a sample by scanning it with a concentrated beam of electrons. The electrons interact with atoms in the sample, creating a variety of signals that carry information about the sample's surface topography and composition. A schematic diagram of a typical SEM is shown in **Figure 3.12**. SEM has four basic components: an electron gun, an electron column consists of a set of electromagnetic lenses, electron detectors, and a sample chamber.

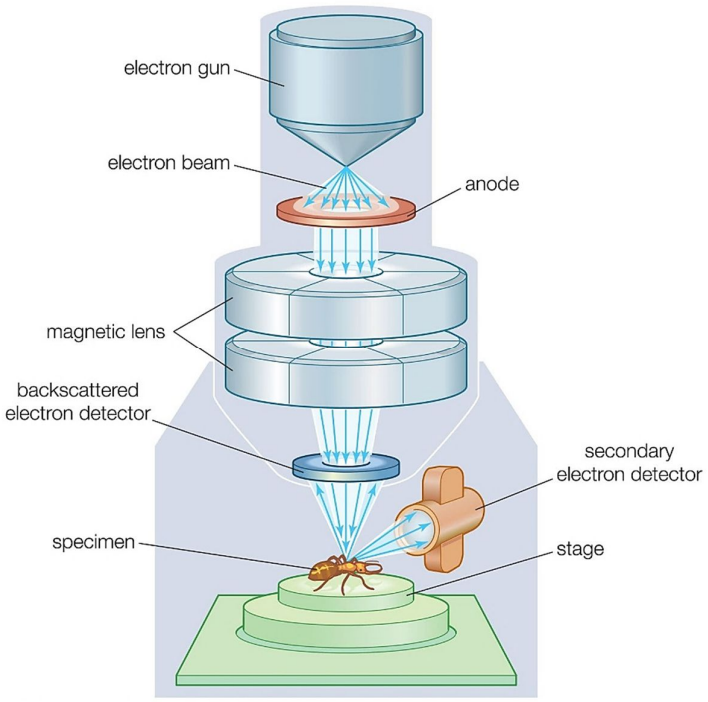

Figure 3.12: Schematic diagram of a typical SEM [434].

In SEM, the column and the chamber must first be evacuated using a combination of vacuum pumps before accurate material and topographical analysis can be performed. This is essential to eliminate the undesirable interference of unwanted particles in air and to avoid electron beam attenuation [435]. At the top of the column, electrons are generated in the electron gun, accelerated down, and passed through a series of electromagnetic lenses to generate a focused beam of electrons, which then strikes the surface of the sample placed on a stage in the sample chamber. As a result of the electron-sample interaction, a number of signals with different interaction volumes are produced, as shown in **Figure 3.13**. Two types of electrons are primarily detected in SEM: secondary electrons (SE) and backscattered electrons (BSE) [435]. Secondary electrons are emitted by the sample's surface or near-surface areas. They are a result of inelastic interactions between the electron beam and the sample. An image exhibiting the topographic characteristics of the surface is obtained after detecting these electrons. Backscattered electrons originate from the electron beam and are reflected back after undergoing elastic interactions with the sample. They emerge from deeper areas of the sample and are highly sensitive to the atomic number. The higher the atomic number, the brighter the material appears in the image. This dependence of the backscattered electrons on the atomic

number is useful for creating images that provide valuable information about the distribution of different elements in the sample [435,436].

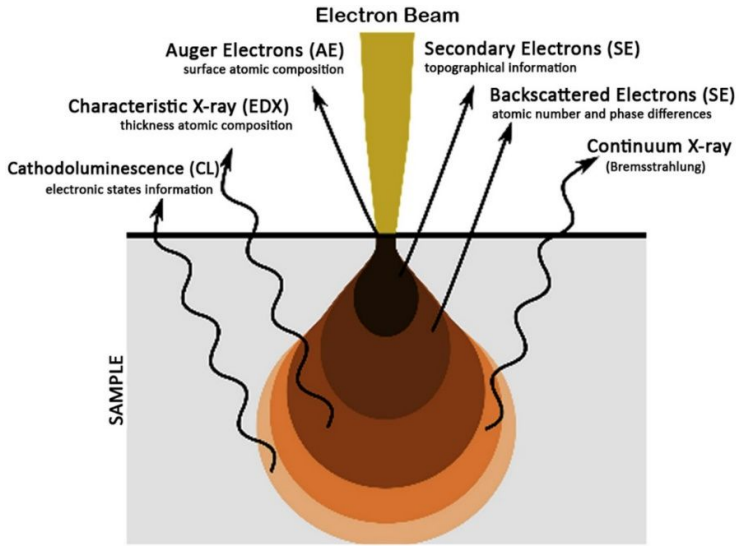

Figure 3.13: Electrons interact with a sample in SEM, producing a variety of signals [437].

In this work, SEM (FEI Quanta 200, FEI) was used to analyse the surface morphology of the worn surfaces of $MoSe_2$ coating and its sliding counterpart after tribological testing. SEM (JSM-6500F, JEOL) was used to observe the prepared cross-section of $MoSe_2$/DLC-W coating. It was also used to examine the surface morphology of its wear tracks and sliding counterpart after tribological testing. All SEM observations were conducted in SE mode at an accelerating voltage of 15 kV, which was found to give the best combination of signal and surface sensitivity.

3.3.5 Energy dispersive X-ray spectroscopy (EDS)

Energy dispersive X-ray spectroscopy (EDS) is a technique that is typically used in conjunction with SEM to detect the chemical elemental composition of materials. It basically works by detecting X-rays emitted by a sample during electron beam bombardment. When the sample is struck by the SEM's electron beam, electrons are released from the sample's atoms, as shown in **Figure 3.14**. The resulting electron holes are then filled with electrons from a higher energy state, and this energy difference can be released in the form of an X-ray. Because the energy

of the emitted X-ray is a characteristic of the element responsible for the emission, the elemental composition of the sample can be determined. An energy-dispersive spectrometer collects the emitted X-rays and measures their intensities and energies. EDS analysis is commonly carried out using two approaches: point analysis and elemental mapping. The former measures the elemental composition at a single point in the sample, whereas the latter is used to show the concentration distribution of different elements in 2D maps of the sample using virtual colours [438-440].

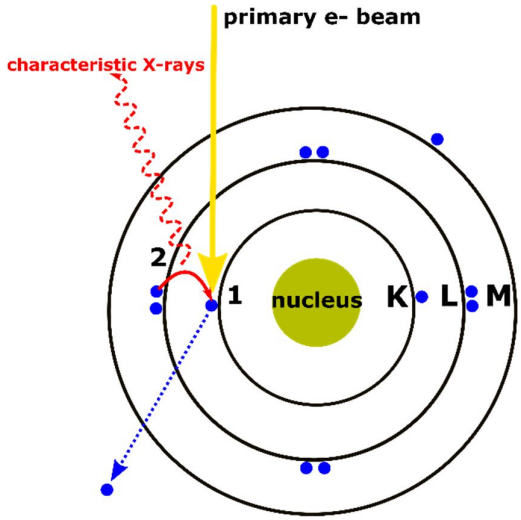

Figure 3.14: Schematic representation of the characteristic X-ray emission during the electron beam-sample interaction [439].

EDS has several drawbacks, limiting its usefulness. Firstly, the technique is insensitive and has a low detection limit. If an element's concentration in the sample is too low, the amount of energy released by X-rays after impacting the sample will not be enough to accurately estimate its percentage. It cannot detect elements with concentrations below 0.1 wt% [441,442]. Secondly, the detection and analysis of light elements with atomic numbers lower than 11 is problematic with EDS [443]. These elements emit X-rays, but their energies are too low to be detected and measured by the EDS spectrometer. The penetration depth is another issue associated with the technique. It is not ideal for high-surface sensitivity analysis since the characteristic X-rays are generally generated at large penetration depths, as shown in **Figure 3.13** [444].

In this work, the chemical composition of $MoSe_2$ coating was measured using EDS (Aztec, Oxford Instruments) integrated into the FEI Quanta 200 SEM. EDS measurements were performed in point analysis mode at five different positions on the surface of one of the coated discs, and the average chemical composition of these measurements was reported. It was also used to determine the chemical composition of the worn surfaces of the coating and its sliding counterpart after tribological testing. The analysis was carried out in both point analysis and elemental mapping modes. The point analysis was used to confirm the existence of certain elements in the worn surfaces and compare them to the background point analysis. The elemental mapping was used to identify the distribution of elements in the worn surfaces. All EDS measurements were done with an accelerating voltage of 15 kV and processed with Aztec software (version 4.2).

EDS (INCA 300, Oxford Instruments) integrated into the JSM-6500F SEM was used to determine the thickness of $MoSe_2$/DLC-W coating from the prepared coating cross-section. It was also used to determine the chemical composition of the worn surfaces of the coating and its sliding counterpart after tribological testing. All EDS measurements were done in the elemental mapping mode, processed using INCA software, and carried out using an accelerating voltage of 15 kV.

3.3.6 Raman spectroscopy

Raman spectroscopy is a technique used for determining the structure and characteristics of molecules based on their vibrational transitions. It is based on the Raman effect, which is defined as an inelastic scattering from a sample when it is illuminated by a monochromatic light. A schematic illustration of a Raman spectrometer is shown in **Figure 3.15**. A monochromatic laser light in the visible range is used to irradiate the sample, and then the scattered light from the surface of the sample is observed. Most of the scattered light will have the same wavelength as the incident light, but some will scatter inelastically and emit at different wavelengths. This shift in the wavelength is induced by the activation of the material's vibrational modes [445]. Only the inelastic scattered light is permitted to pass through a filter and be collected by a spectrometer in order to obtain a Raman spectrum. The spectrum features several peaks and displays the intensity and the wavelength position of each peak. Each peak

corresponds to a specific vibrational mode of a specific molecule, which is used as a fingerprint for identifying the material and distinguish it from others [445,446]. However, one of the main drawbacks of Raman spectroscopy is that it can only detect certain molecules. Molecules that are non-Raman active are undetectable in the analysis. Another drawback is the very weak Raman effect since only a small amount of incident light (typically 0.0000001%) is inelastically scattered [447,448]. This results in low sensitivity of the technique, which makes analysing low concentrations of materials very challenging.

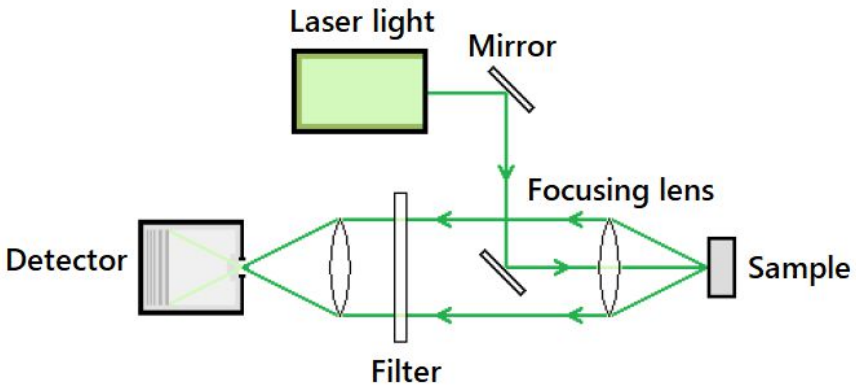

Figure 3.15: Schematic diagram of a Raman spectrometer [449].

In this work, a Raman spectrometer (Renishaw, inVia Reflex) fitted with a green laser of wavelength 532 nm was used to evaluate tribo-induced microstructural changes occurring in the worn surfaces of the coatings and their sliding counterparts after tribological testing. The samples were placed on a glass plate and then interacted with the laser beam at room temperature. A 20x objective lens with a numerical aperture of 0.4 was used, resulting in a laser spot diameter of 1.6 μm. A low laser power of 2 mW was used to prevent structural changes or phase deterioration resulting from the laser's thermal effects [293]. The Raman spectra were collected from different spots of the wear tracks and the ball wear scars. To achieve a better signal-to-noise ratio, all the analysed spots were exposed to the laser for 60 s. The Raman active compounds of interest in this study were $MoSe_2$, MoO_3, and C. The Raman shift region covered was between 100 cm^{-1} and 1800 cm^{-1} based on the positions of $MoSe_2$, MoO_3, and C peaks. During analysis, a Gaussian peak fitting was used to deconvolute the spectra and identify Raman peaks of C.

3.3.7 Focused ion beam (FIB)

Focused ion beam (FIB) is a technique commonly used for preparing samples for transmission electron microscopy (TEM) analysis. All TEM samples must be thinned to tens of nanometres in order to be transparent to the electron beam used for imaging. A focused beam of ions, commonly gallium (Ga) ions, is used in FIB to mill a bulk sample. While SEM monitors the milling procedure, a selected area of the sample can be milled to the desired thickness [450,451]. An ion gun installed in SEM generates the focused beam of ions by applying a very strong electric field. The FIB milling procedure is schematically shown in **Figure 3.16**. The surface of the area of interest is first covered with a protective coating made of either platinum or carbon to protect it from exposure to the ion beam during milling. The area of interest is then milled using a Ga ion beam at a high accelerating voltage of around 30 kV in order to make a section with a thickness of a few micrometres. The prepared section is then removed from the bulk sample and placed on a TEM sample grid. Finally, it is milled again with a Ga ion beam at a low accelerating voltage of around 5 kV to minimise damage and to make a thin slice with a thickness in the range 10-100 nm [450].

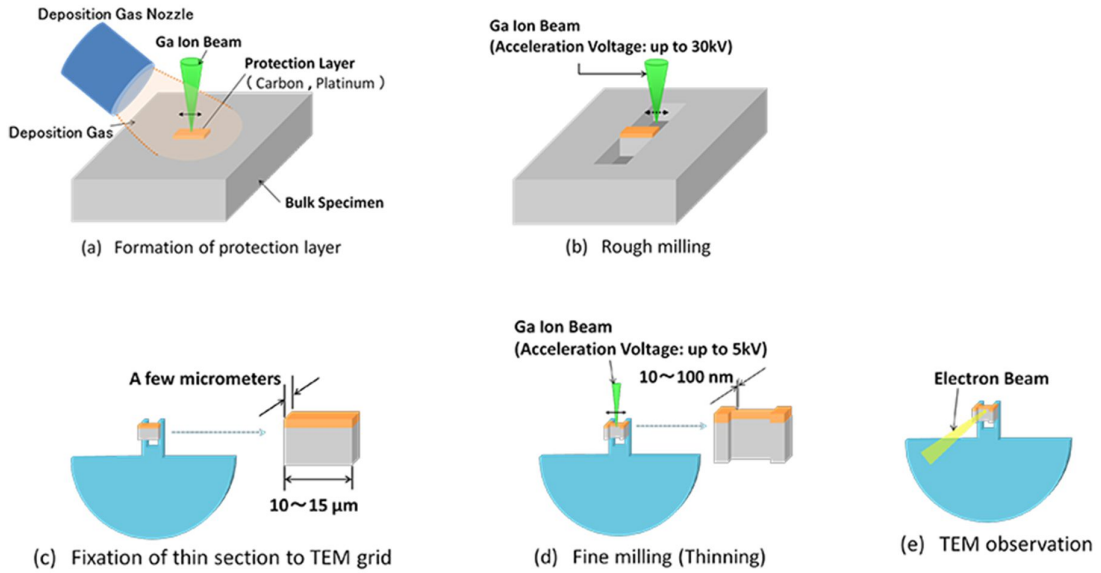

Figure 3.16: (a) Protective layer of platinum or carbon is deposited on the area of interest. (b) Ga ion beam is used to mill the surroundings of the area of interest to prepare a section with a thickness of few micrometres. (c) The section is placed onto a TEM grid. (d) The section is finely milled to make a thin slice with a thickness in the range 10-100 nm. (e) The thinned section is subjected to TEM observation [452].

In this work, a dual-beam FIB-SEM system (FEI Helios G4 CX, Thermo Fisher Scientific) equipped with Ga ions at an accelerating voltage of 30 kV was used to cut four thin lamellae. Three of them were from selected areas in the wear tracks of $MoSe_2$ coating, and one was from the as-deposited coating. These lamellae were subsequently analysed by TEM. Before starting the ion milling, a protective layer of Pt was first deposited to protect the region of interest from exposure to the ion beam during milling. The final thinning was carried out at a low accelerating voltage of 5 kV to minimise the sample damage.

3.3.8 Transmission electron microscopy (TEM)

Transmission electron microscopy (TEM) is a high-resolution imaging technique widely used for the characterisation of nanomaterials in electron microscopy. TEM and SEM both operate based on the same fundamental principles. However, TEM is different from SEM in two key aspects. Firstly, TEM creates an image by collecting electrons that are passing through a very thin sample, whereas SEM creates an image by detecting reflected or knocked-off electrons. Therefore, TEM provides very valuable information on the inner structure of the sample, such as crystal structure and morphology, whereas SEM provides useful information on the surface of the sample and its composition. Secondly, TEM employs a high accelerating voltage between 100 kV and 300 kV to get high-resolution images that can reveal information down to 0.1-0.2 nm [453], whereas SEM usually uses an accelerating voltage of up to 30 kV. A schematic diagram of a typical TEM is shown in **Figure 3.17**. TEM has four basic components: an electron gun, an electron column consists of a set of electromagnetic lenses, a sample stage, and an imaging device.

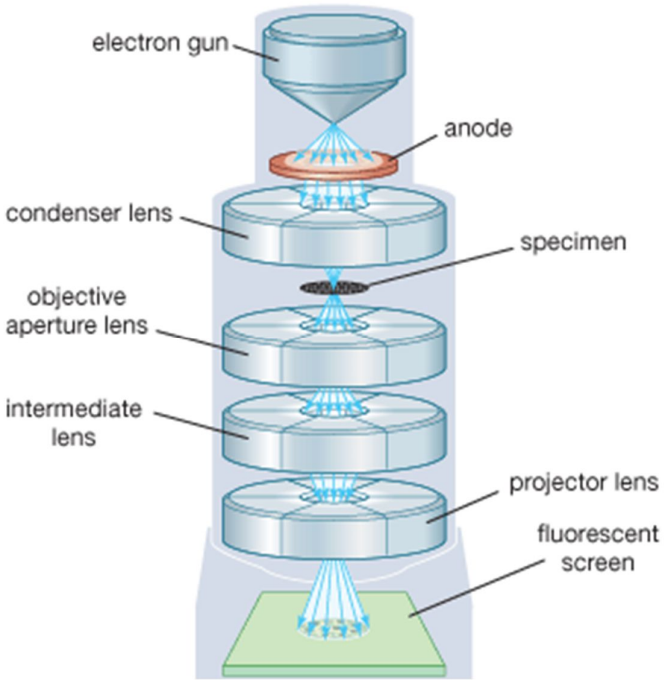

Figure 3.17: Schematic diagram of a typical TEM [454].

In TEM, a source of electrons at the top of the microscope emits electrons with a high energy of up to 300 keV that travel through a high vacuum in the microscope's column [455]. Electromagnetic lenses focus electrons into a very thin beam, which subsequently strikes an ultra-thin sample with a thickness of less than 100 nm [456]. The electrons passing through the sample are either transmitted or diffracted, depending on the sample's thickness and electron transparency. An objective lens focuses this transmitted part onto a fluorescent screen at the bottom of the microscope to generate an image of the sample. This image can be used to conduct high-resolution analyses, which can provide very valuable information about the structure of the sample such as crystal structure, crystal size, morphology, crystal orientation, and crystal defects [455,456].

Bright field imaging (BFI) is the most used imaging mode when generating TEM images. Some parts of a sample can absorb or scatter electrons, resulting in a dark appearance, whereas other parts transmit electrons, resulting in a bright appearance. In the BFI, an aperture selects the transmitted electrons while blocking the scattered ones. Because the transmitted electrons

are used, areas containing crystalline or high-mass materials will appear dark. In dark field imaging (DFI), the scattered electrons are selected, and the transmitted electrons are blocked from entering the aperture. Because of this, areas where there is no electron scattering will appear dark, whereas areas containing materials will appear bright. Another mode of imaging is known as high-resolution transmission electron microscopy (HR-TEM), which uses both the transmitted electron beam and the scattered electron beam to create an interference image. It is the highest resolution imaging technique ever developed and commonly used for analysing the crystal structure and lattice defects in a material on an atomic resolution scale [453,456].

In this work, the direct observation of the nanostructure of $MoSe_2$ coating in the as-deposited coating and in the wear tracks was performed using HR-TEM (Titan Themis Cubed X-FEG, FIE) operating at an accelerating voltage of 300 kV.

Chapter 4: Tribological properties of $MoSe_2$ coating under dry and oil-lubricated sliding conditions

4.1 Introduction

As previously discussed in chapter 2, several tribological studies have reported the great promise of $MoSe_2$ coatings as low-friction coatings for tribological components operating in humid air, with low sensitivity to air humidity, low coefficients of friction, and good wear resistance [43,56-59]. However, the understanding of their tribological behaviour in the published literature has been focused so far on their performance in environments such as humid air, vacuum, and different gas atmospheres under dry sliding conditions, whereas their tribological performance under oil-lubricated sliding conditions has not yet been experimentally studied and remains unexplored. If the suitability of $MoSe_2$ coatings is to be evaluated for tribological applications, an in-depth investigation and understanding of their tribological performance with oil lubrication are needed since most mechanical components are typically used under oil-lubricated conditions.

As discussed in section 2.6.6.3, the tribological behaviour of $MoSe_2$ coatings is highly dependent on the applied load. They often exhibit non-Amontonian friction behaviour, with a drop in their coefficient of friction with increasing load [56,232,309,321]. This load-dependence of the friction behaviour of $MoSe_2$ coatings and other TMD coatings is attributable to an increase in coating dryness caused by friction-induced heating [230,231]. If $MoSe_2$ coatings are used in oil-lubricated contacts, the excellent thermal conductivity of oil lubricants may minimise this friction-induced heating observed with increasing load; hence, their friction response to the increase in the applied load may differ (better or worse). However, there has been no research on the effect of applied load on their tribological behaviour under oil-lubricated conditions.

As discussed in section 2.6.6.2, $MoSe_2$ coatings are very sensitive to the temperatures at which they are used. They often exhibit reduced friction at low temperatures due to a decrease in the relative humidity of the surrounding environment, which is known for its adverse effect on their tribological properties [56,220,225]. On the other hand, their friction increases proportionately with increasing temperature due to a greater degree of oxidation that occurs at higher temperatures [56,220,225]. Oil lubrication has the potential to enhance the tribological properties of $MoSe_2$ coatings at high temperatures. It may protect the coatings from oxidation through a barrier protection mechanism in which an oil layer prevents water vapour and oxygen from penetrating the tribo-system, hence reducing the environment's detrimental influence on their tribological properties. However, the research on the effect of temperature on their tribological properties under oil-lubricated conditions has not yet appeared.

In this chapter, the tribological performance of $MoSe_2$ coating was evaluated under oil-lubricated sliding conditions with PAO4. For comparative purposes, its tribological performance was also evaluated under dry sliding conditions. In addition, its tribological performance was evaluated in PAO4-lubricated sliding at different loads ranging from 5 N to 15 N and at different temperatures ranging from 25 °C to 100 °C in order to assess the effect of these parameters on its tribological performance. The chemical composition of the coating determined by EDS and its mechanical properties measured by nanoindentation are reported first in this chapter. Secondly, its crystalline structure determined by XRD is presented, followed by a discussion of the results obtained from the sliding tests performed using the TE77 reciprocating tribometer. Following this is a discussion of the wear behaviour of the coating and its sliding counterpart assessed by the Alicona profilometer. In order to gain a better understanding of the underlying friction and wear mechanisms involved, the worn surfaces of the coating and its sliding counterpart were analysed using different experimental techniques such as SEM, EDS and Raman spectroscopy, and the results are presented. Finally, the observed friction and wear mechanisms are discussed in detail.

4.2 Results

4.2.1 Chemical composition, thickness, mechanical properties, and cross-sectional morphology

The chemical composition, thickness, and mechanical properties of $MoSe_2$ coating are summarised in **Table 4.1**. A small percentage of oxygen is present in the coating as a result of the residual oxygen in the chamber during deposition and/or contamination of the porous $MoSe_2$ target [175,226,392]. The coating displays a hardness value of 0.83 ± 0.07 GPa, which is reasonable considering its porous and columnar structure, as shown in **Figure 4.1**. TMD coatings in their pure sputtered form exhibit low compactness, high porosity, and columnar cross-sectional morphology [43,185,226]. This causes low hardness, typically in the range 0.3-2 GPa, depending on the deposition parameters used and subsequent surface morphology obtained [43].

Table 4.1: Chemical composition, mechanical properties, and thickness of $MoSe_2$ coating.

Mo (at.%)	Se (at.%)	O (at.%)	H (GPa)	E' (GPa)	Thickness (µm)
32.51 ± 0.2	65.08 ± 0.1	2.41 ± 0.2	0.83 ± 0.07	27.86 ± 1.7	2 ± 0.18

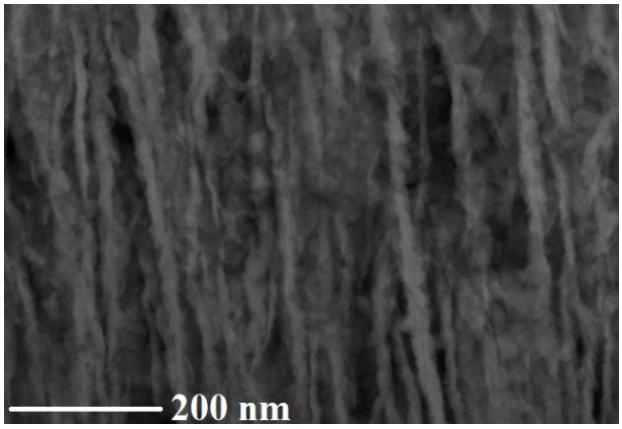

Figure 4.1: TEM cross-sectional image shows a porous and columnar morphology of $MoSe_2$ coating.

4.2.2 Crystalline structure

GI-XRD was performed in order to determine the crystalline structure of $MoSe_2$ coating, and the diffractogram is shown in **Figure 4.2**. The diffraction peaks located at 32.15°, 37.83°, 47.45°, 57.81°, and 67.26° are well corresponding to the crystal planes of (1 0 0), (1 0 3), (1 0 5), (1 1 2), and (2 0 2), respectively, which coincide with the hexagonal $MoSe_2$ crystal structure (ICDD card No. 00-077-1715). The diffractogram does not contain any characteristic XRD peaks other than those belonging to $MoSe_2$, indicating the formation of pure $MoSe_2$ phase only. The diffraction peak assigned to (0 0 2) plane shifts slightly to a lower diffraction angle from 13.69° to 12.65°. This shift suggests a lattice elongation caused by defects such as vacancies, impurities, and dislocations, as reported by Dunn et al. [457]. The broad peak at approximately 37.83° is highly asymmetric with a long tail toward higher angles, which is a typical feature of sputtered TMD coatings [175,185,226,392,458-460]. According to Weise et al. [461], this peak corresponds to a turbostrating stacking of (10L) planes (L = 0,1, 2, 3) and may be described by a 2D arrangement of the basal planes with a dimension of several tens of unit cells.

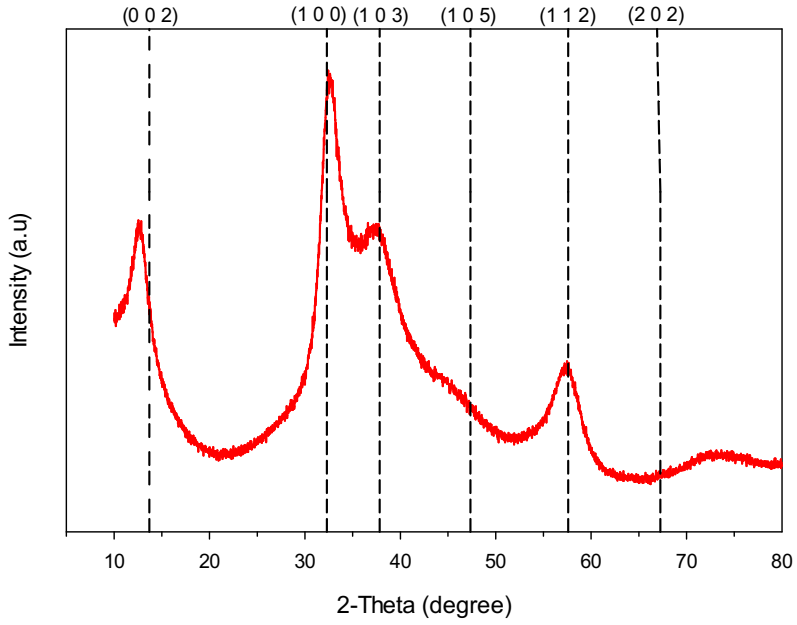

Figure 4.2: GI-XRD diffractogram of $MoSe_2$ coating and standard diffraction lines from (ICDD card No. 00-077-1715).

4.2.3 Friction performance

4.2.3.1 Dry and PAO4-lubricated sliding at 5 N load and 25 °C

Figure 4.3 shows the coefficients of friction of $MoSe_2$ coating as a function of sliding time when tested in dry and PAO4-lubricated sliding at a normal load of 5 N and a temperature of 25 °C. Under both sliding conditions, the friction curves showed similar features where they rapidly increased to the highest values at the start of the tests and next decreased to steady levels. The lubricated test showed typical unadditised oil behaviour, with a high coefficient of friction of 0.1 and large and noticeable fluctuations between 0.08 and 0.14. A different frictional behaviour was observed in dry sliding, where the coating exhibited a low coefficient of friction of 0.054, with very small fluctuations in the friction curve.

The coating experienced an average coefficient of friction of 0.101 in PAO4-lubricated sliding. A low average coefficient of friction of 0.054 was obtained under dry sliding conditions. In other studies, coefficients of friction ranging from 0.05 to 0.06 were reported for pure $MoSe_2$ coatings tested at the same load under dry sliding conditions [56,226,320]. When compared to MoS_2 coating, the coefficient of friction of 0.054 obtained here was significantly less than 0.14 reported for pure MoS_2 coating tested at the same load [56]. This was expected since $MoSe_2$ coating has lower sensitivity to air humidity than MoS_2 coating, as reported by several studies [56,320,462,463]. When comparing the coefficients of friction obtained under both sliding conditions, PAO4-lubricated sliding has a coefficient of friction that is one time higher than that of dry sliding. Such results imply that dry sliding is more advantageous than PAO4-lubricated sliding for the coating to achieve better friction performance.

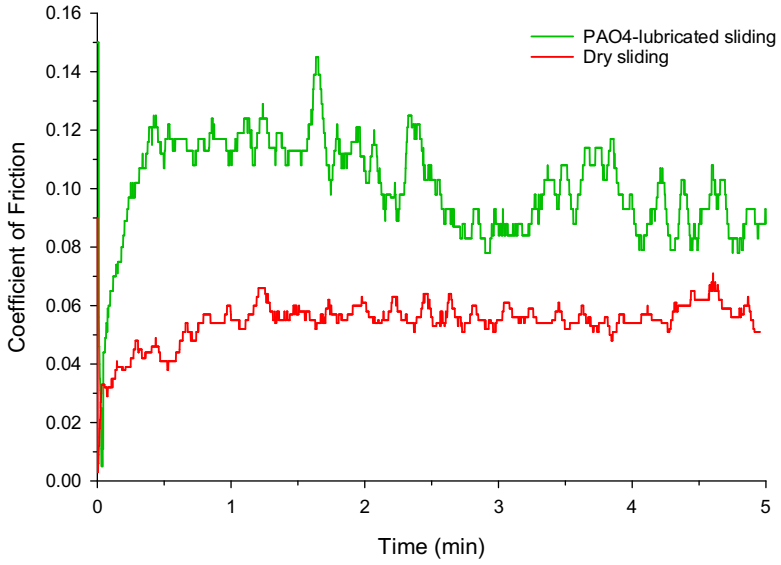

Figure 4.3: Coefficients of friction of $MoSe_2$ coating as a function of sliding time tested in dry and PAO4-lubricated sliding. (Test conditions: counterparts: AISI 52100 steel balls; normal load: 5 N; relative humidity: 40-50%; temperature: 25 °C).

4.2.3.2 PAO4-lubricated sliding at different loads

Figure 4.4 shows the coefficients of friction of $MoSe_2$ coating in PAO4-lubricated sliding when the applied load was increased from 5 N to 8 N, 10 N, 12 N, and 15 N. A general observation is that all the friction curves showed similar features where they rapidly increased to the highest values at the start of the tests, then decreased to the lowest values, and finally steadily increased to low values. No friction spikes were observed at all the applied loads, indicating that there was no metal-to-metal contact, and the friction was governed by the $MoSe_2$ phase. In the test conducted at 8 N load, the coating showed a clear running-in period and a high initial coefficient of friction of 0.09 before reaching a steady-state coefficient of friction of 0.08 after 3 minutes of sliding. With a further increase in the load to 10 N, 12 N, and 15 N, the friction curves showed no running-in period and quickly reached steady-state levels with less noise than that of 8 N load. The best frictional behaviour was observed for the test performed at the highest applied load of 15 N as it resulted in the lowest coefficient of friction and the most stable friction curve compared to other loads. From these friction results, it can be inferred that increasing the applied load provides more favourable friction properties for

$MoSe_2$ coatings under PAO4-lubricated sliding conditions, with lower coefficients of friction and higher degrees of friction stability.

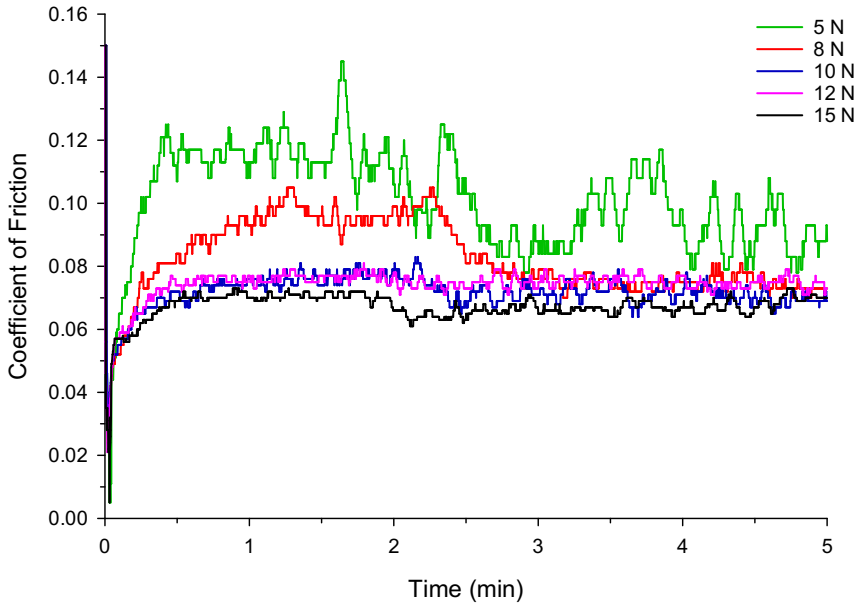

Figure 4.4: Coefficients of friction of $MoSe_2$ coating as a function of sliding time tested under PAO4-lubricated sliding conditions at different loads. (Test conditions: counterparts: AISI 52100 steel balls; relative humidity: 40-50%; temperature: 25 °C).

The average coefficients of friction of the coating from the entire tests are shown in **Figure 4.5**. In general, it can be observed that the coefficient of friction was closely related to the applied load, and as the applied load increased, it decreased. This decrease in the coefficient of friction with increasing load observed here was very similar to the frictional behaviour of pure TMD coatings such as $MoSe_2$ [226] and MoS_2 [224,464], as well as doped ones such as Mo-Se-C [232,321], W-S-C [314,465], and Mo-S-N [51,466] when tested under dry sliding conditions at different loads. The coefficients of friction in the range 0.067-0.101 obtained here at different loads were higher than those reported for $MoSe_2$ coatings evaluated in dry sliding under comparable conditions. They were notably higher than those in the range 0.02-0.05 reported for pure $MoSe_2$ coating tested at loads ranging from 2 N to 15 N in dry sliding [226]. They were also higher than those reported for $MoSe_2$ coatings doped with other elements. For example, $MoSe_2$ coating doped with 15.3 at.% Ti, which showed coefficients of friction in the

range 0.03-0.05 when tested at loads ranging from 2 N to 15 N under dry sliding conditions [467]. In another study, coefficients of friction in the range 0.05-0.09 were reported for $MoSe_2$ coating doped with 61 at.% C when tested at different loads in the range 2-10 N in dry sliding [321].

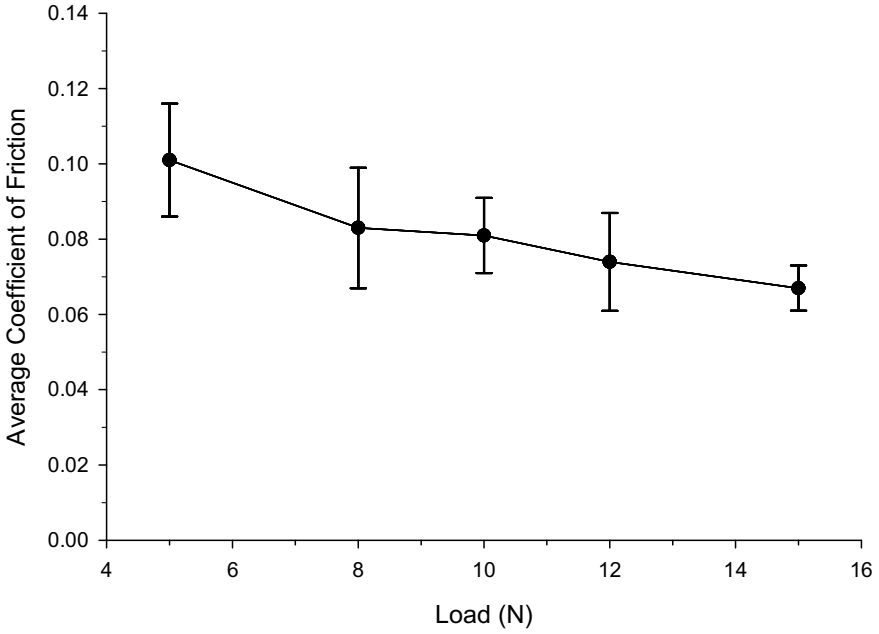

Figure 4.5: Average coefficients of friction of $MoSe_2$ coating tested at different loads under PAO4-lubricated sliding conditions. The error lines correspond to the standard deviation of the mean value.

4.2.3.3 PAO4-lubricated sliding at different temperatures

Figure 4.6 shows the coefficients of friction of $MoSe_2$ coating in PAO4-lubricated sliding when the test temperature was increased from 25 °C to 40 °C, 60 °C, 80 °C, and 100 °C. At 40 °C, the coating initially exhibited a low coefficient of friction of 0.08, but after two minutes of sliding, it rapidly increased to 0.12, with clear fluctuations between 0.09 and 0.13 until the end of the test. The same frictional behaviour was observed at 60 °C. The coefficient of friction was initially low at 0.09, but it quickly increased to 0.11 after three minutes of sliding, with noticeable fluctuations until the end of the test. The friction behaviour improved when the test temperature was increased from 60 °C to 80 °C, as the sliding test done at this temperature resulted in a low coefficient of friction of 0.08 and smaller fluctuations than the tests conducted

at lower temperatures. The test performed at the highest temperature of 100 °C resulted in the best frictional behaviour, with the lowest coefficient of friction of 0.07 and the most stable friction curve when compared to other temperatures. When the coefficients of friction measured at different temperatures are compared, it can be inferred that higher temperatures are more favourable for the coating to achieve better friction performance in PAO4-lubricated sliding.

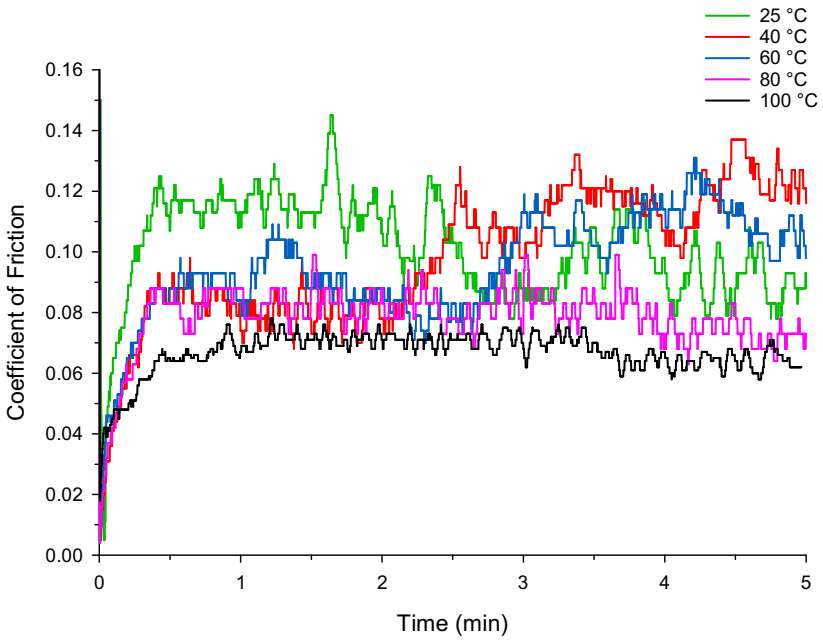

Figure 4.6: Coefficients of friction of $MoSe_2$ coating as a function of sliding time tested under PAO4-lubricated sliding conditions at different temperatures. (Test conditions: counterparts: AISI 52100 steel balls; normal load: 5 N; relative humidity: 40-50%).

Figure 4.7 presents the average coefficients of friction of the coating as a function of test temperature. A decrease in the coefficient of friction with increasing temperature was observed. Such decrease in the coefficient of friction with increasing temperature has also been observed for different TMD coatings tested at different temperatures under dry sliding conditions [225,272,311,459,466]. The coefficients of friction in the range 0.075-0.101 obtained here at different temperatures were higher than those reported in the literature for pure and doped $MoSe_2$ coatings tribologically evaluated in dry sliding under comparable conditions. For example, pure $MoSe_2$ coating showed a stable coefficient of friction of 0.06 when tested at

temperatures ranging from 25 °C to 100 °C [56]. The coefficient of friction of 0.101 measured here at 25 °C was higher than 0.075 obtained in another study for pure $MoSe_2$ coating evaluated at the same temperature [468]. It was also higher than those reported for $MoSe_2$ coatings doped with different Ti contents, ranging from 0.04 to 0.06 [467]. In a different study, $MoSe_2$ coatings doped with different N contents showed low coefficients of friction ranging from 0.055 to 0.065 when tested at 25 °C [468].

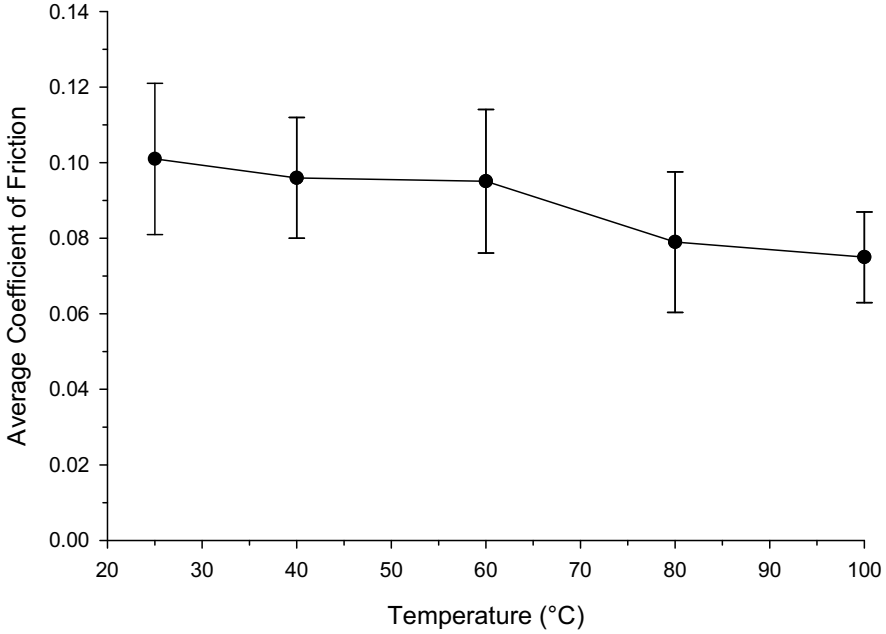

Figure 4.7: Average coefficients of friction of $MoSe_2$ coating tested at different temperatures under PAO4-lubricated sliding conditions. The error lines correspond to the standard deviation of the mean value.

4.2.4 Wear performance

4.2.4.1 Dry and PAO4-lubricated sliding at 5 N load and 25 °C

The wear tracks of the coating were analysed using the Alicona profilometer. **Figure 4.8** displays the cross-sectional profiles measured at three different zones of the wear tracks of the coating tested in dry and PAO4-lubricated sliding. Because the coating had lower hardness and wear resistance than the steel ball, it experienced considerable wear damage under both sliding conditions. This was evidenced by wide and deep wear tracks, as well as a significant number

of wear grooves. Despite the severity of wear, the depth of the wear track did not go beyond the thickness of the $MoSe_2$ layer (i.e. 2 µm) under both sliding conditions. The depth of the wear track of the PAO4-lubricated test was 1.75 µm. The dry sliding test had a wear depth of 1.98 µm, which was very close to the coating/substrate interface. **Figure 4.9** depicts the volumetric wear rates of the coating and its sliding counterpart. In PAO4-lubricated sliding, the coating exhibited a wear rate of 15.2 x 10^{-6} mm^3/N.m, whereas it exhibited a wear rate of 20.8 x 10^{-6} mm^3/N.m in dry sliding. It can be deduced that the addition of PAO4 resulted in a decrease in the wear rate of the coating by 27%, clearly demonstrating the advantage of PAO4 lubrication for improving the wear resistance of the coating. The wear rate measured for the steel ball was much lower than that measured for the coating under both sliding conditions, indicating that the ball was more resistant to wear. The ball tested in dry sliding showed a lower wear rate than the one tested in PAO4-lubricated sliding.

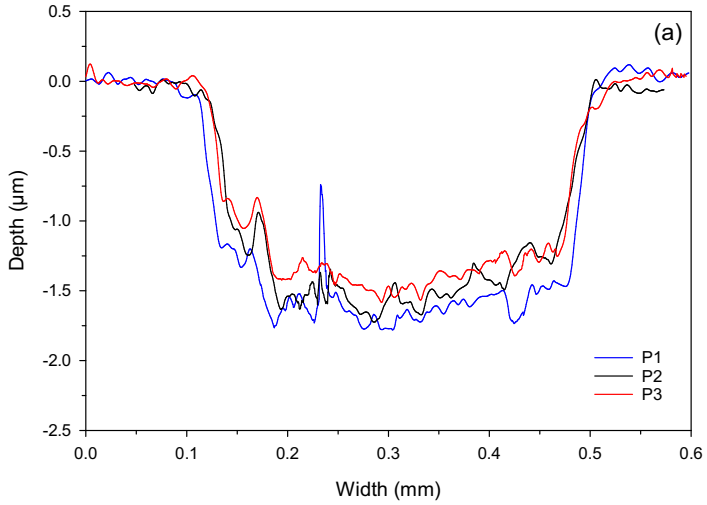

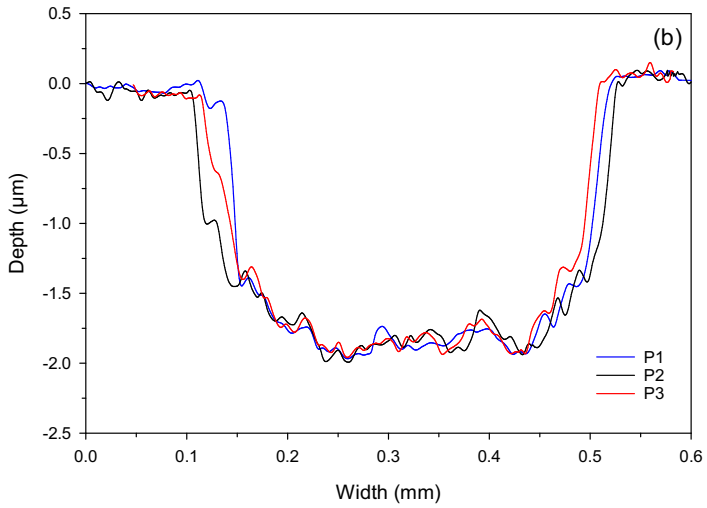

Figure 4.8: Cross-sectional wear track profiles of $MoSe_2$ coating tested at a normal load of 5 N in: (a) PAO4-lubricated sliding and (b) dry sliding. P1 was measured at the centre of wear track, whereas P2 and P3 were measured at its edges.

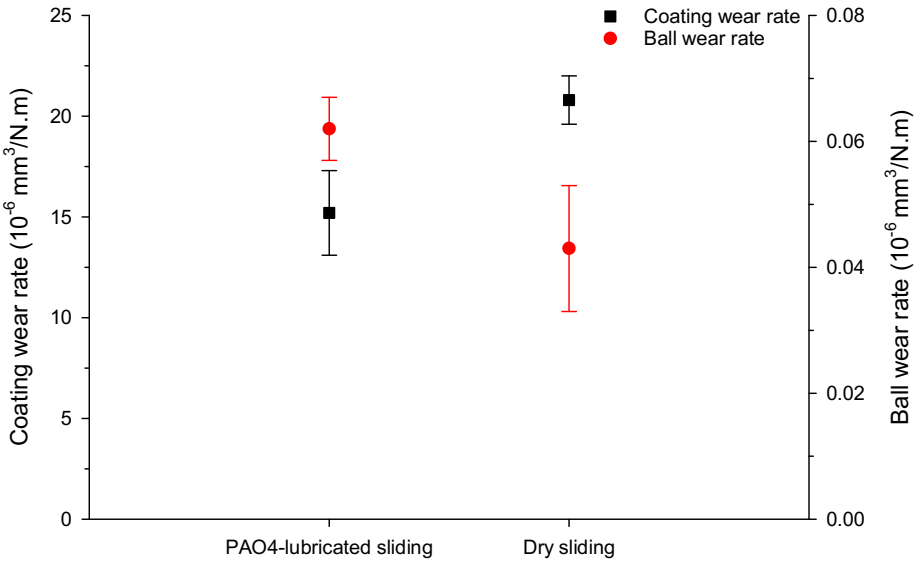

Figure 4.9: Wear rates of $MoSe_2$ coating and its sliding counterpart tested under dry and PAO4-lubricated sliding conditions. The error lines correspond to the standard deviation of the mean value.

4.2.4.2 PAO4-lubricated sliding at different loads

Figure 4.10 presents the cross-sectional profiles of the wear tracks of the coating tested at different loads under PAO4-lubricated sliding conditions. Due to the poor hardness and wear resistance of the coating compared to that of the steel ball, it suffered from appreciable wear at all the applied loads, resulting in wide wear tracks and deep ploughing grooves. Despite the severity of the experienced wear, none of the wear tracks exceeded the thickness of the coating (i.e. 2 µm). The wear track depth was observed to increase with increasing load, peaking at 1.88 µm at the highest load of 15 N. **Figure 4.11** displays the wear rates of the coating and its sliding counterpart tested at different loads. The wear rate of the coating decreased as the applied load increased, following the same decreasing trend as the average coefficient of friction presented in **Figure 4.5**. The minimum wear rate of 9.78 x 10^{-6} mm^3/N.m was obtained at the highest applied load of 15 N. The evolution of the wear rate of the ball followed the same trend as the coating, although the wear rate of the coating was always measured to be significantly higher than that of the ball.

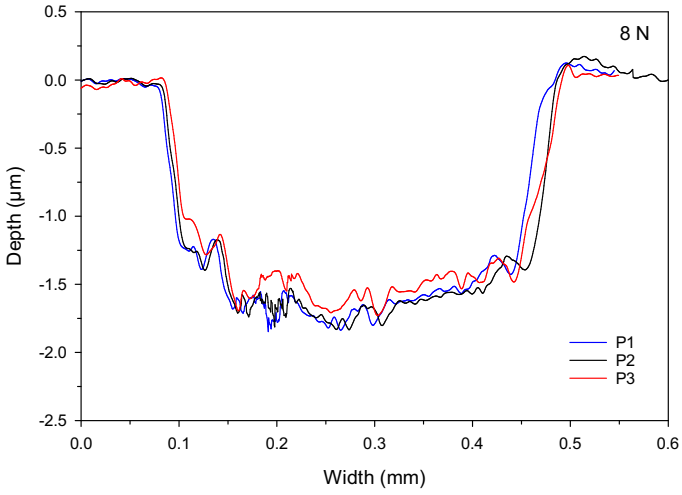

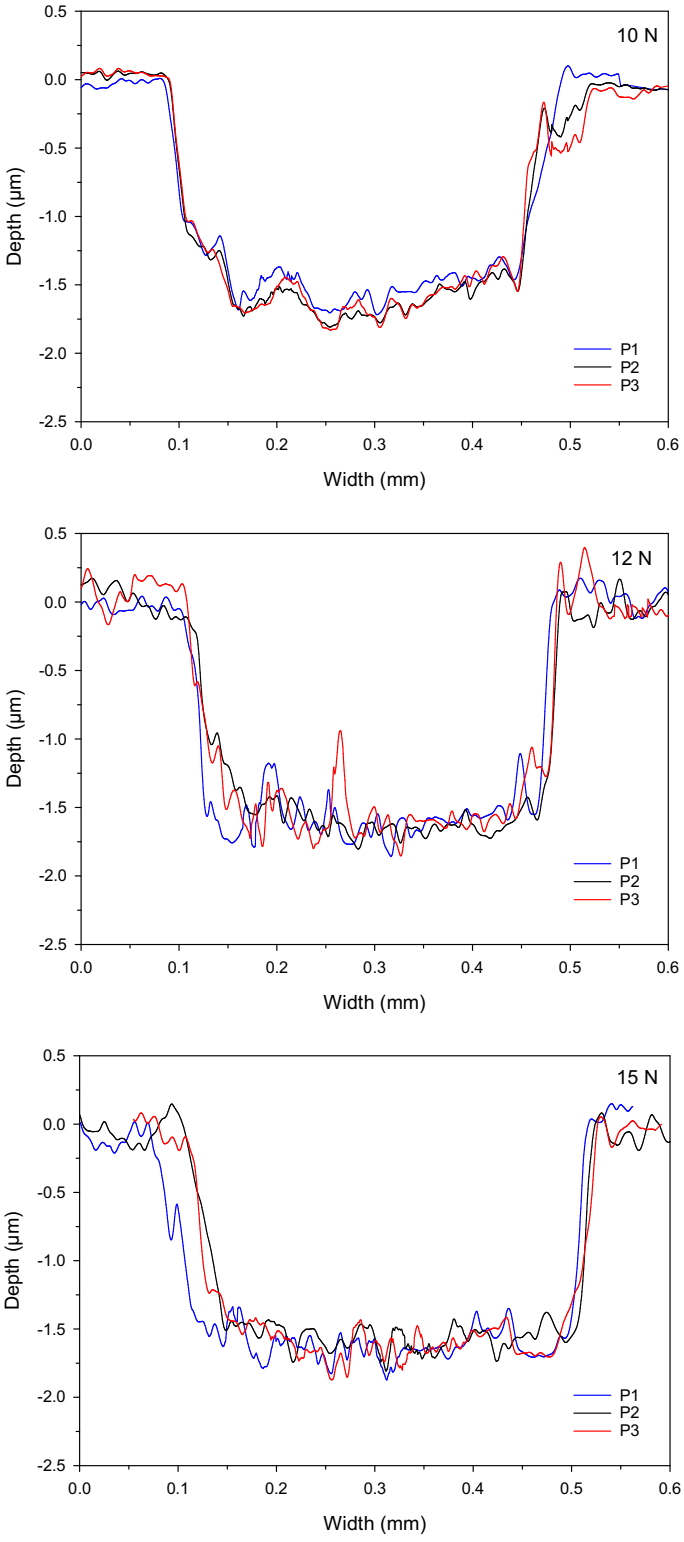

Figure 4.10: Cross-sectional wear track profiles of $MoSe_2$ coating tested in PAO4-lubricated sliding at different loads. P1 was measured at the centre of wear track, whereas P2 and P3 were measured at its edges.

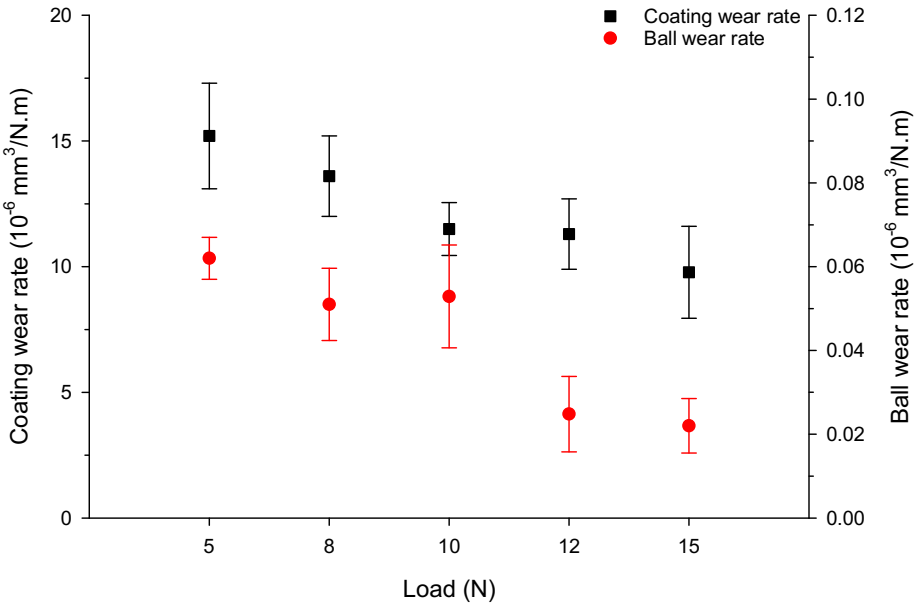

Figure 4.11: Wear rates of $MoSe_2$ coating and its sliding counterpart as a function of applied load. The error lines correspond to the standard deviation of the mean value.

4.2.4.3 PAO4-lubricated sliding at different temperatures

Figure 4.12 presents the cross-sectional profiles of the wear tracks of the coating tested at different temperatures under PAO4-lubricated sliding conditions. The coating was worn out at all the test temperatures, resulting in deep and wide wear tracks. Despite this severity of wear, none of the wear tracks went beyond the coating thickness of 2 µm. The wear depth was observed to decrease with increasing temperature. At 40 °C, the wear depth was 1.75 µm, but it decreased to 1.68 µm when the test temperature was increased to 60 °C. Increasing the temperature further to 80 °C resulted in a wear depth of 1.66 µm. The lowest wear depth of 1.59 µm was obtained at the highest test temperature of 100 °C. **Figure 4.13** displays the wear rates of the coating and its sliding counterpart. With the increase in the test temperature, the wear rate of the coating decreased and followed the same trend as the average coefficient of friction presented in **Figure 4.7**. The minimum wear rate was 11.93 x 10^{-6} mm^3/N.m and obtained at the highest temperature of 100 °C. The wear rate of the ball also decreased with increasing temperature and was much lower than that of the coating at all the temperatures, demonstrating that the ball had better wear resistance.

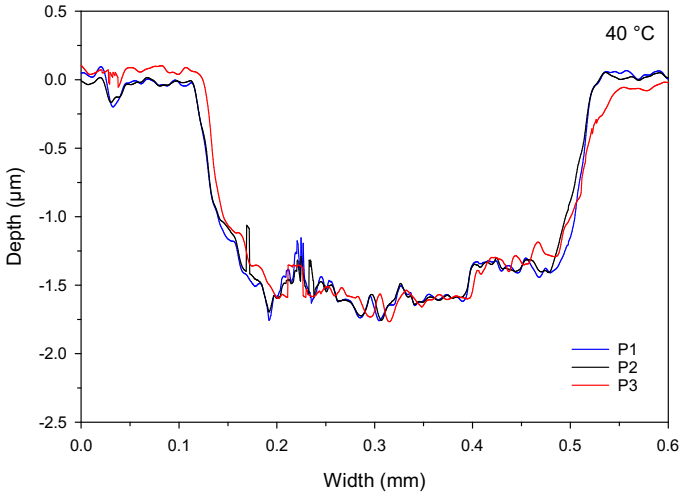
40 °C
Depth (µm)
Width (mm)
P1
P2
P3

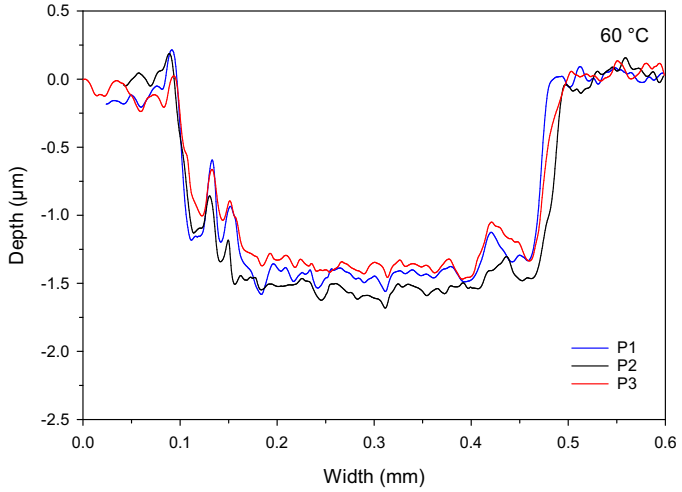
60 °C
Depth (µm)
Width (mm)
P1
P2
P3

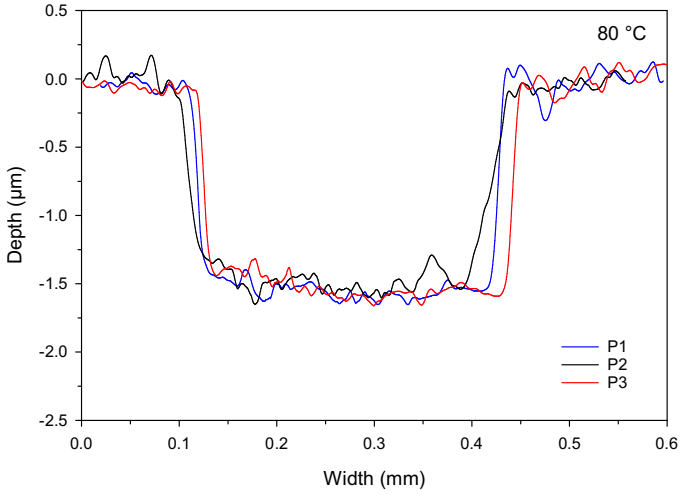
80 °C
Depth (µm)
Width (mm)
P1
P2
P3

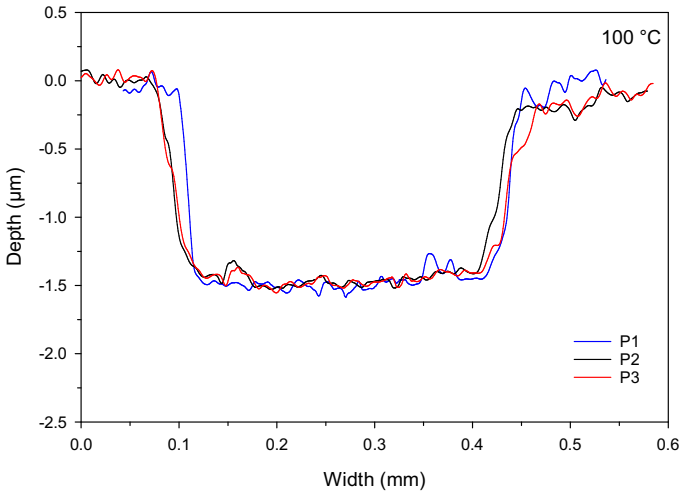

Figure 4.12: Wear track profiles of $MoSe_2$ coating tested under PAO4-lubricated sliding conditions at different temperatures. P1 was measured at the centre of wear track, whereas P2 and P3 were measured at its edges.

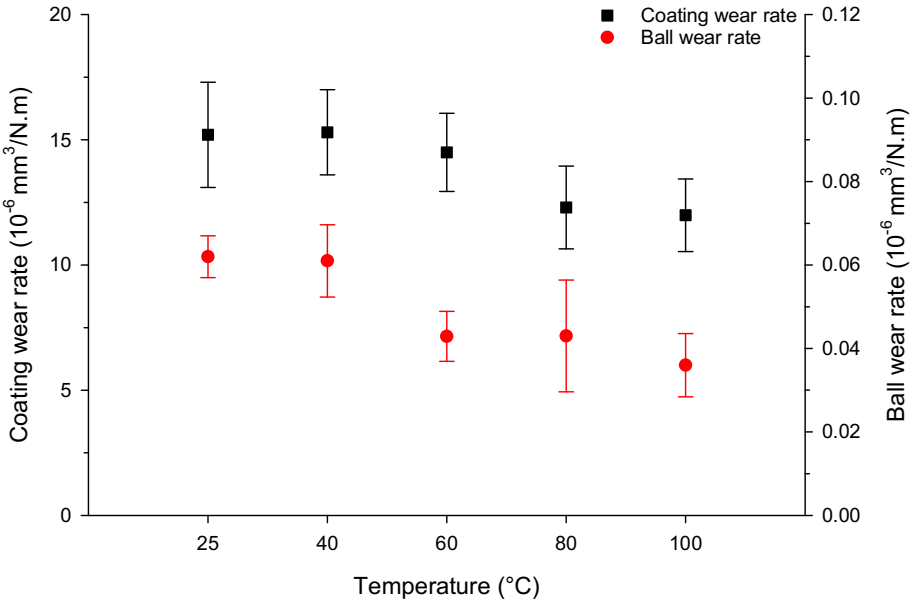

Figure 4.13: Wear rates of $MoSe_2$ coating and its sliding counterpart tested under PAO4-lubricated sliding conditions at different temperatures. The error lines correspond to the standard deviation of the mean value.

4.2.5 Analysis of worn surfaces

4.2.5.1 PAO4-lubricated sliding at 5 N load and 25 °C

To gain more insights into the underlying friction and wear mechanisms, worn surfaces of the coating and its sliding counterpart were further analysed with the help of SEM, EDS, Raman spectroscopy, and TEM. **Figure 4.14** shows SEM image of the wear track of the coating tested in PAO4-lubricated sliding at a normal load of 5 N and 25 °C. The wear track has a width of about 435 μm and a non-uniform appearance. Severe coating delamination and chipping can be observed at its edges, implying deteriorated wear resistance. Pure $MoSe_2$ coating exhibits typical brittle nature and low load-bearing capacity attributed to its columnar and porous morphology [43,469,470]. Brittle chipping and delamination of the coating during sliding are thus expected.

Figure 4.15 displays the EDS elemental mapping of the wear track. The mapping supports and confirms the wear damage seen in the profilometry by revealing a significant difference in the chemical composition of the coating's worn and unworn surfaces. The worn surface shows a dominant presence of iron, originating from the substrate, and a depletion of molybdenum and selenium. This result clearly indicates severe wear of the $MoSe_2$ layer. No evidence of oxygen is detected inside the wear track. As shown in **Figure 4.16**, EDS point analysis performed at the centre of the wear track (point B), which is the area with the most severe damage, shows only a small increase in the intensity of the peak belonging to oxygen compared to that of the as-deposited coating (point A).

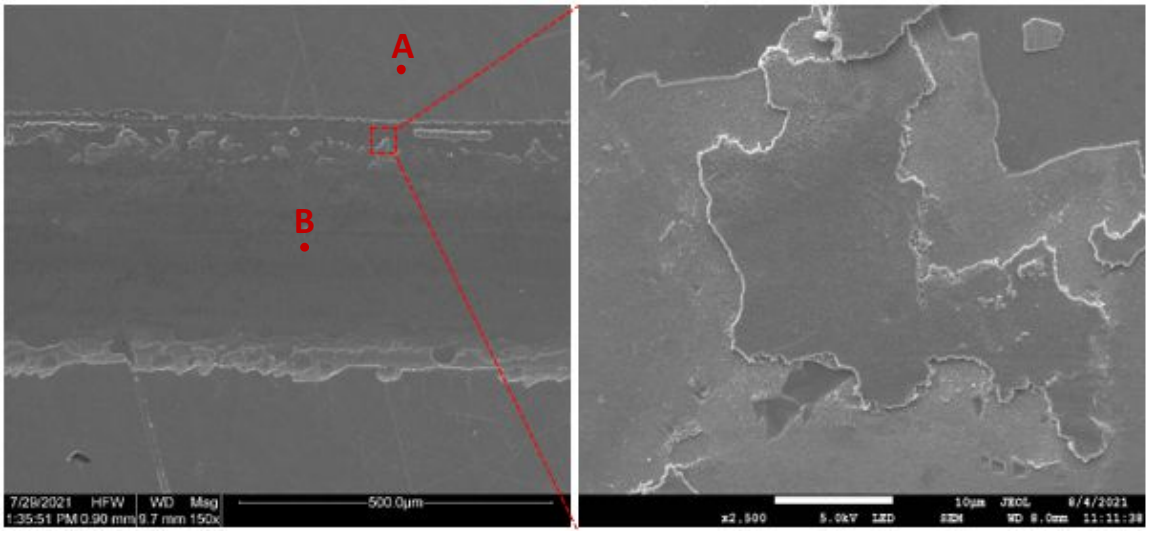

Figure 4.14: (left) SEM image of the wear track of $MoSe_2$ coating tested in PAO4-lubricated sliding at a normal load of 5 N and 25 °C and (right) SEM image shows a close-up view of the top edge of the wear track.

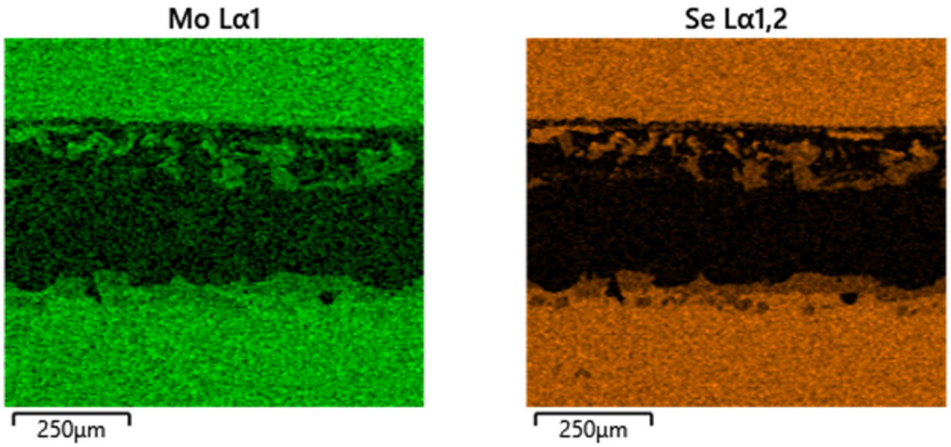

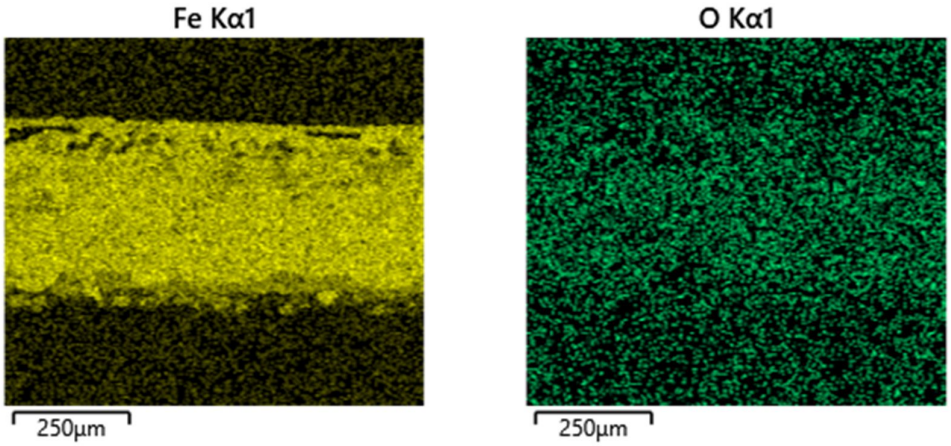

Figure 4.15: EDS mapping of the wear track of $MoSe_2$ coating tested in PAO4-lubricated sliding at a normal load of 5 N and 25 °C.

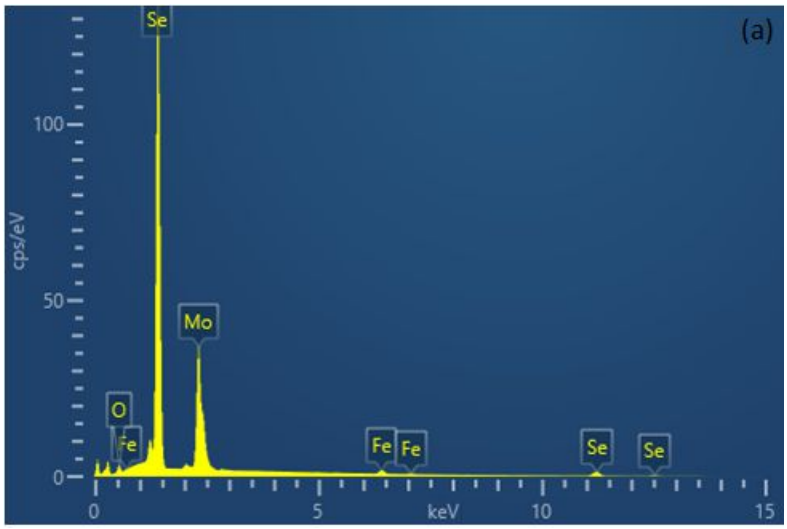

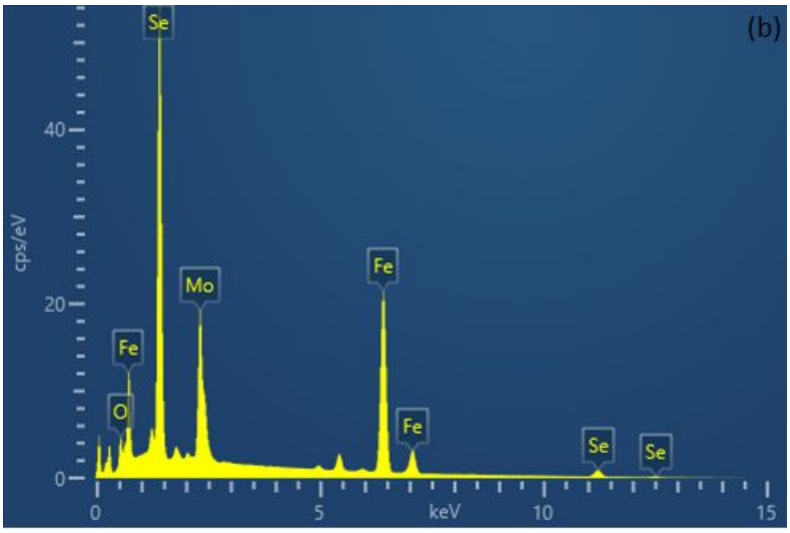

Figure 4.16: EDS point analysis of: (a) the as-deposited $MoSe_2$ coating (point A) and (b) the centre of the wear track of the coating tested in PAO4-lubricated sliding at a normal load of 5 N and 25 °C (point B).

Raman spectroscopy, which has a superficial detection depth and more surface sensitivity than EDS, was used to investigate the possible microstructural changes occurring in the wear tracks of the coating and its sliding counterpart. **Figure 4.17** shows the Raman spectrum of the as-deposited coating as a reference and the spectra acquired from different positions of the wear track of the coating tested in PAO4-lubricated sliding at a normal load of 5 N and 25 °C. The Raman spectrum of the as-deposited coating shows five peaks corresponding to $MoSe_2$ at wavenumbers 155 cm^{-1}, 235 cm^{-1}, 290 cm^{-1}, 443 cm^{-1}, and 596 cm^{-1} [392,471]. The Raman spectra acquired from different positions of the wear track show that the wear track is still largely covered with $MoSe_2$ material despite the severity of the experienced wear. These spectra appear to be similar to the spectrum of the as-deposited coating. This similarity suggests that $MoSe_2$ coating did not undergo any tribo-induced structural changes in its crystallinity inside the wear track. Similar findings have also been reported in which Raman spectroscopy did not detect any changes in the structure of TMD coatings inside wear tracks [49,52,472]. No evidence of the formation of MoO_3 was found in all the analysed positions of the wear track.

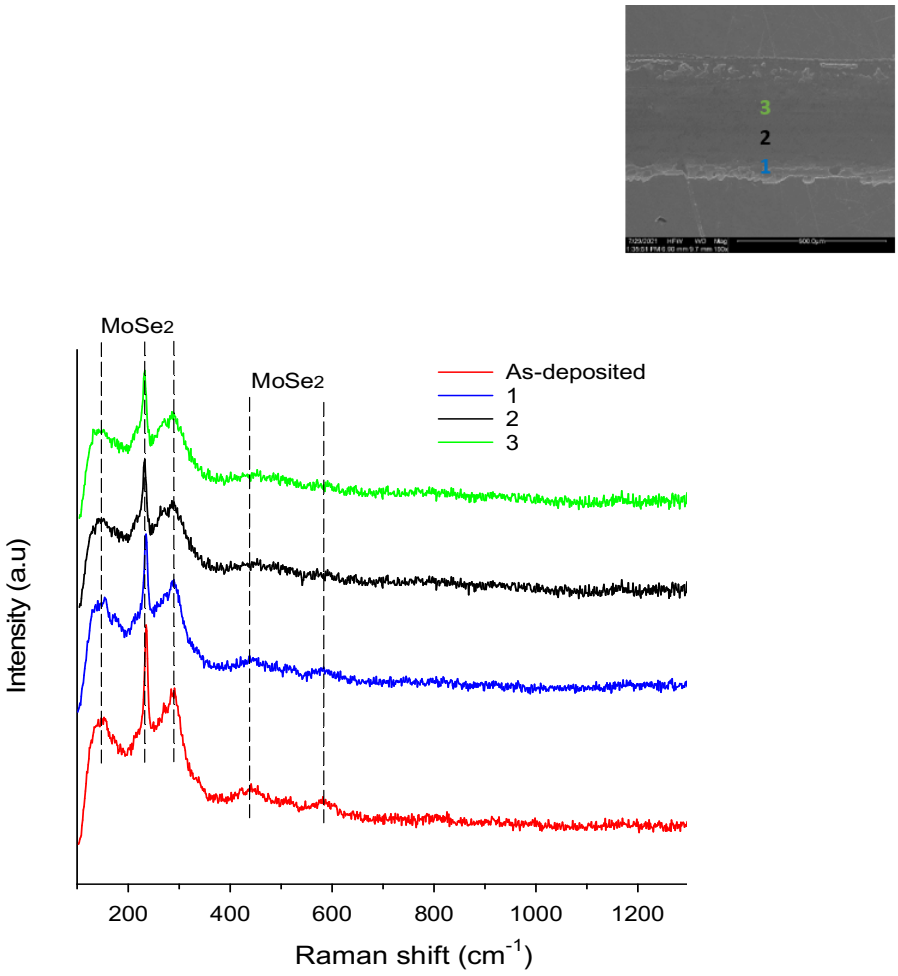

Figure 4.17: Raman spectra acquired from different positions of the wear track of $MoSe_2$ coating tested in PAO4-lubricated sliding at a normal load of 5 N and 25 °C.

The results of Raman spectroscopy carried out in different positions of the wear track suggest that the coating did not undergo any tribo-induced structural changes in its crystallinity during sliding in PAO4. This indicates that a well-ordered crystalline $MoSe_2$ tribolayer with basal planes aligned parallel to the sliding surface might not form in the wear track. To confirm such hypothesis, a thin lamella was extracted from the wear track and subjected to TEM analysis, as shown in **Figure 4.18**. The TEM image shows no signs of the crystallisation of $MoSe_2$ in the topmost surface of the wear track, confirming the results of Raman spectroscopy. Below the wear track surface, the basal planes of $MoSe_2$ are either perpendicular to the wear track surface or randomly oriented. These planes are incapable of serving as easy slip planes, which are required for reducing friction in TMD coatings. Such results suggest that PAO4 inhibited the

shear-induced formation of a well-ordered $MoSe_2$ tribolayer, consequently leading to a high coefficient of friction.

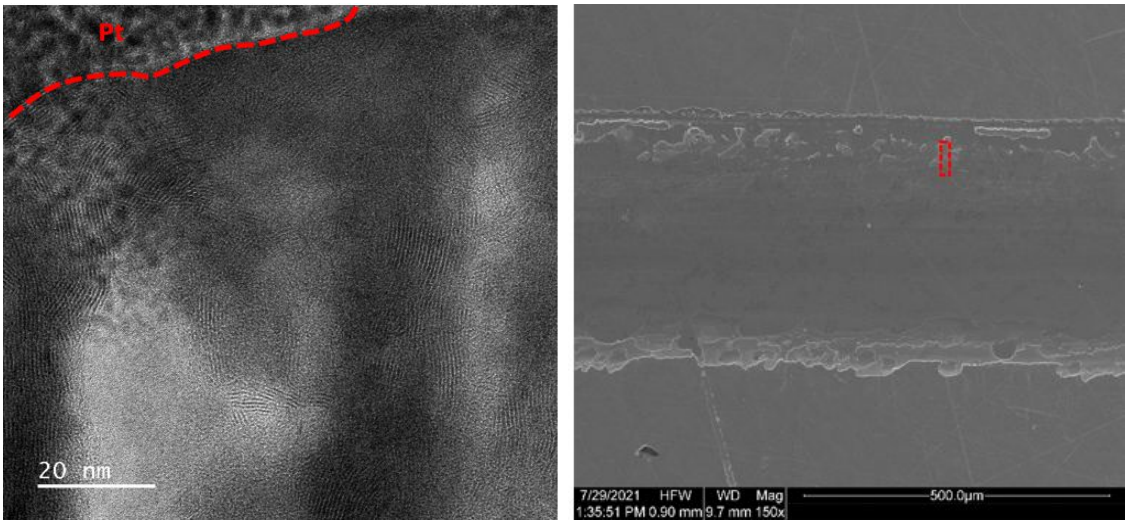

Figure 4.18: (left) TEM image of the topmost surface of the wear track of $MoSe_2$ coating tested in PAO4-lubricated sliding at a normal load of 5 N and 25 °C and (right) SEM image shows the location of the FIB cut from the wear track. The TEM image shows no evidence of the formation of a crystalline $MoSe_2$ tribolayer. The basal planes of $MoSe_2$ are either perpendicular to the wear track surface or randomly orientated.

Figure 4.19 shows the surface morphology of the ball wear scar tested against the coating in PAO4-lubricated sliding at a normal load of 5 N and 25 °C. The scar is circular in shape, exhibits a smooth appearance, and has a large diameter of about 385 µm. Some wear particles can be seen around the edges of the wear scar. The EDS mapping of this ball wear scar is shown in **Figure 4.20**. The mapping shows the presence of some molybdenum and selenium in the wear scar, indicating the transfer and adherence of some coating material to the ball during sliding. It should be noted that this transfer layer was not evenly distributed throughout the wear scar, but rather adhered to two edges. A reason for this could be the presence of PAO4, which acted as a barrier between the sliding surfaces and prevented the coating material from being transferred to its sliding counterpart.

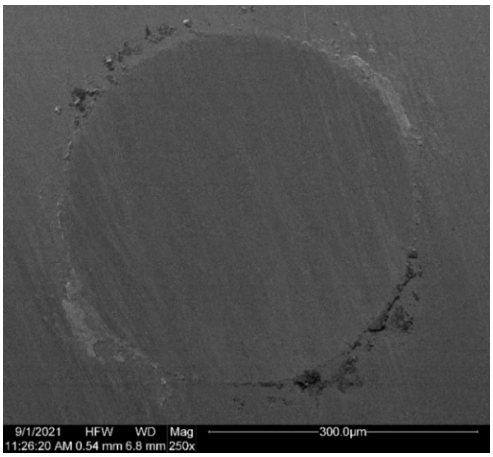

Figure 4.19: SEM image of the ball wear scar tested against $MoSe_2$ coating in PAO4-lubricated sliding at a normal load of 5 N and 25 °C.

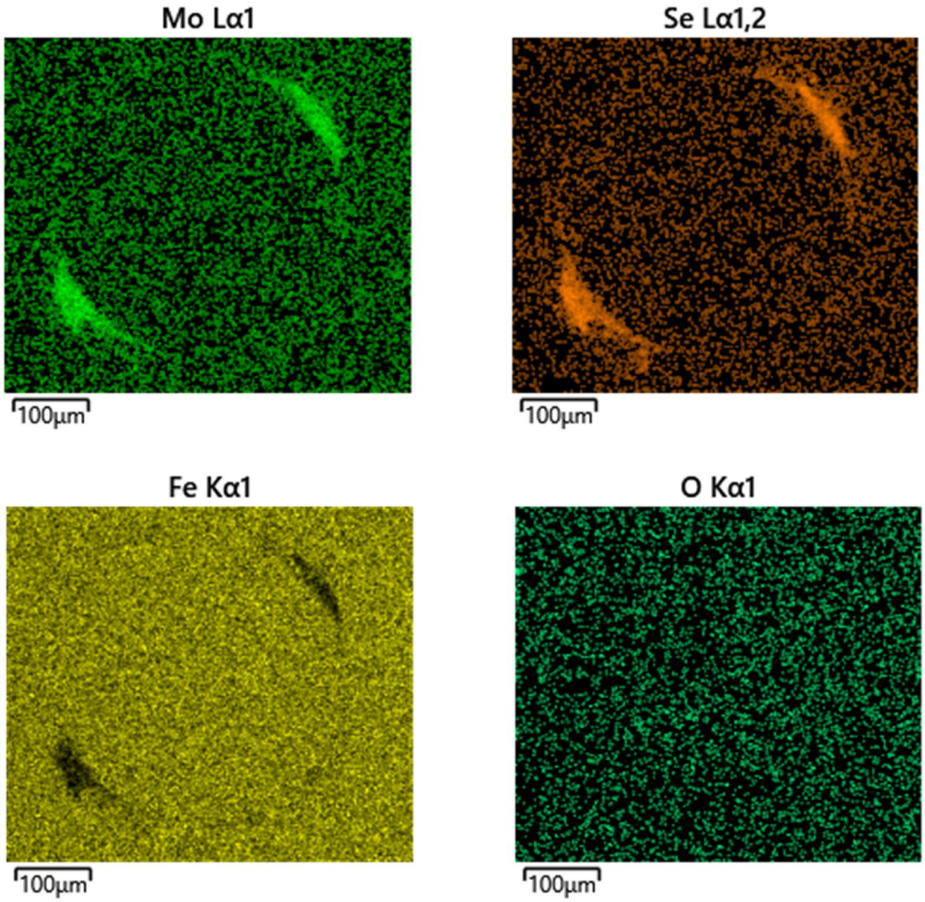

Figure 4.20: EDS mapping of the ball wear scar tested against $MoSe_2$ coating in PAO4-lubricated sliding at a normal load of 5 N and 25 °C.

Figure 4.21 shows the Raman spectra acquired from different positions of the ball wear scar tested in PAO4-lubricated sliding at a normal load of 5 N and 25 °C. A general observation is that these spectra differ significantly from those acquired from the wear track shown in **Figure 4.17**. The Raman spectrum acquired from the centre of the ball wear scar (i.e. position 3) reveals very broad and not easily identifiable $MoSe_2$ peaks. This suggests that there is a small amount of the coating material at the centre of the ball wear scar. Clear peaks of $MoSe_2$ with smaller intensities than those of the as-deposited coating are only observed at positions 2 and 3 of the ball wear scar. The Raman spectra acquired from the centre and edge of the ball wear scar (i.e. positions 3 and 1) show the presence of two broad peaks at wavenumbers 815 cm^{-1} and 940 cm^{-1} attributable to MoO_3 [221,473]. When compared to the intensities of $MoSe_2$ peaks in the as-deposited coating, the lower intensities of $MoSe_2$ peaks at all the analysed positions of the ball wear scar clearly indicate that only a very small amount of the coating transferred and adhered to the ball during sliding, further supporting and confirming the results of EDS.

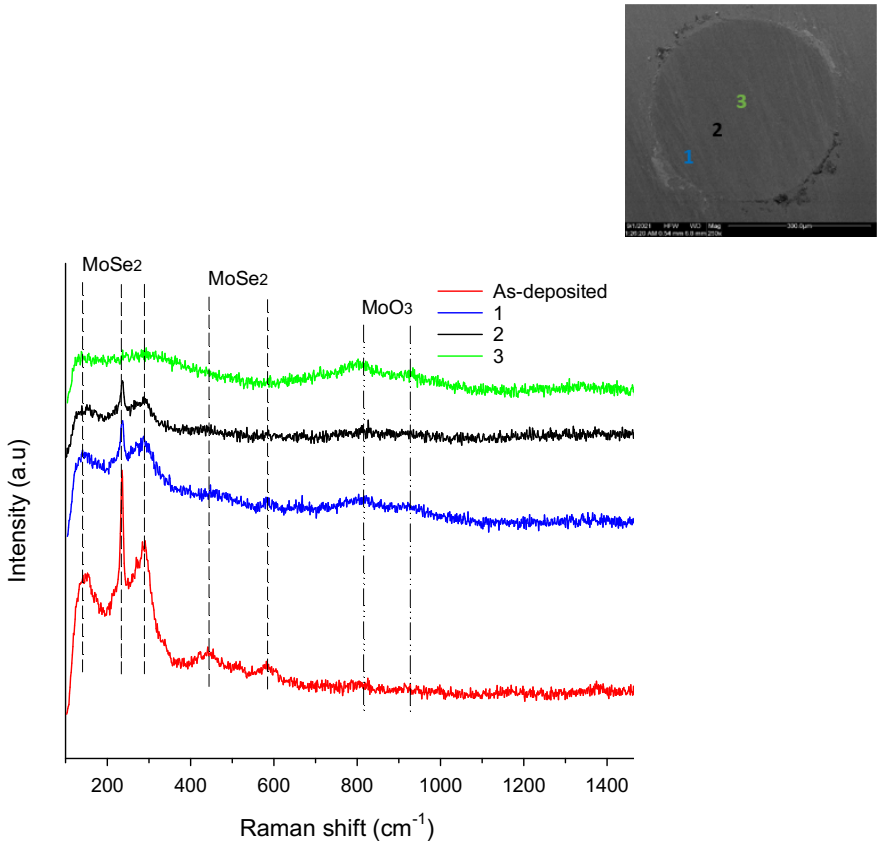

Figure 4.21: Raman spectra acquired from different positions of the ball wear scar tested against $MoSe_2$ coating in PAO4-lubricated sliding at a normal load of 5 N and 25 °C.

4.2.5.2 Dry sliding at 5 N load and 25 °C

Figure 4.22 shows SEM image of the wear track of the coating tested in dry sliding at a normal load of 5 N and 25 °C. The wear track has a width of 455 µm, which is wider than the wear track of the PAO4-lubricated sliding test. A closer look revealed that the coating exhibited delamination around the edges of the wear track, similar to what was observed at edges of the wear track of the PAO4-lubricated sliding test. **Figure 4.23** shows the EDS mapping of this wear track. It demonstrates a high concentration of iron, originating from the substrate within the wear track, as well as a depletion of molybdenum and selenium compared to the untested coating surface. This indicates that the $MoSe_2$ layer was severely worn out during dry sliding. The presence of oxygen is also observed within the wear track. As shown in **Figure 4.24**, EDS point analysis performed at the centre of the wear track (point B), which is the area with the most severe damage, shows a significant increase in the intensity of the peak belonging to oxygen compared to that of the as-deposited coating (point A). This is likely be the reaction of the substrate with oxygen in the surrounding atmosphere, forming iron oxides.

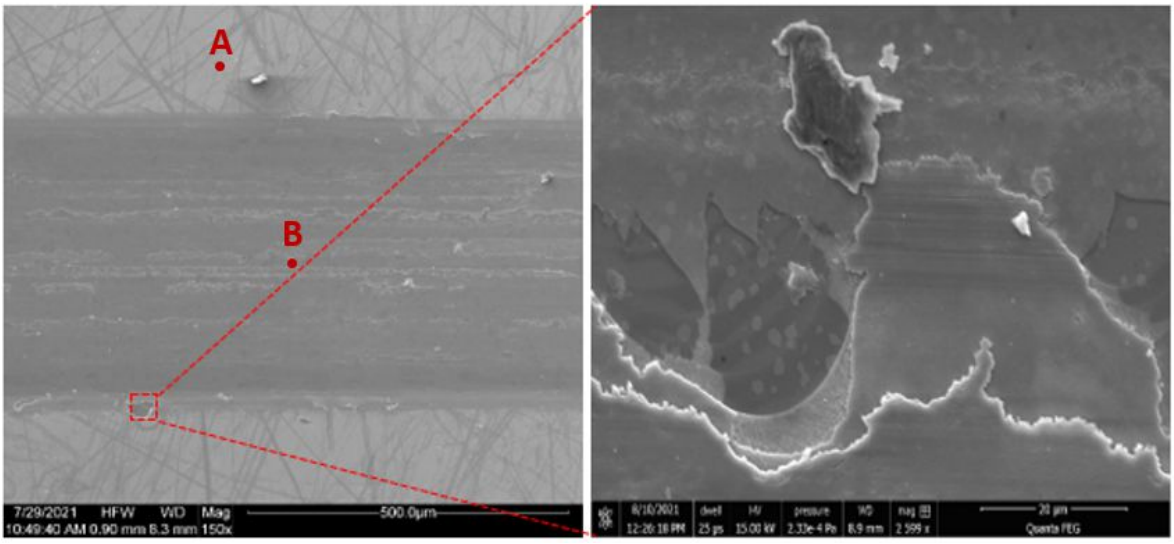

Figure 4.22: (left) SEM image of the wear track of $MoSe_2$ coating tested in dry sliding at a normal load of 5 N and 25 °C and (right) SEM image shows a close-up view of the bottom edge of the wear track.

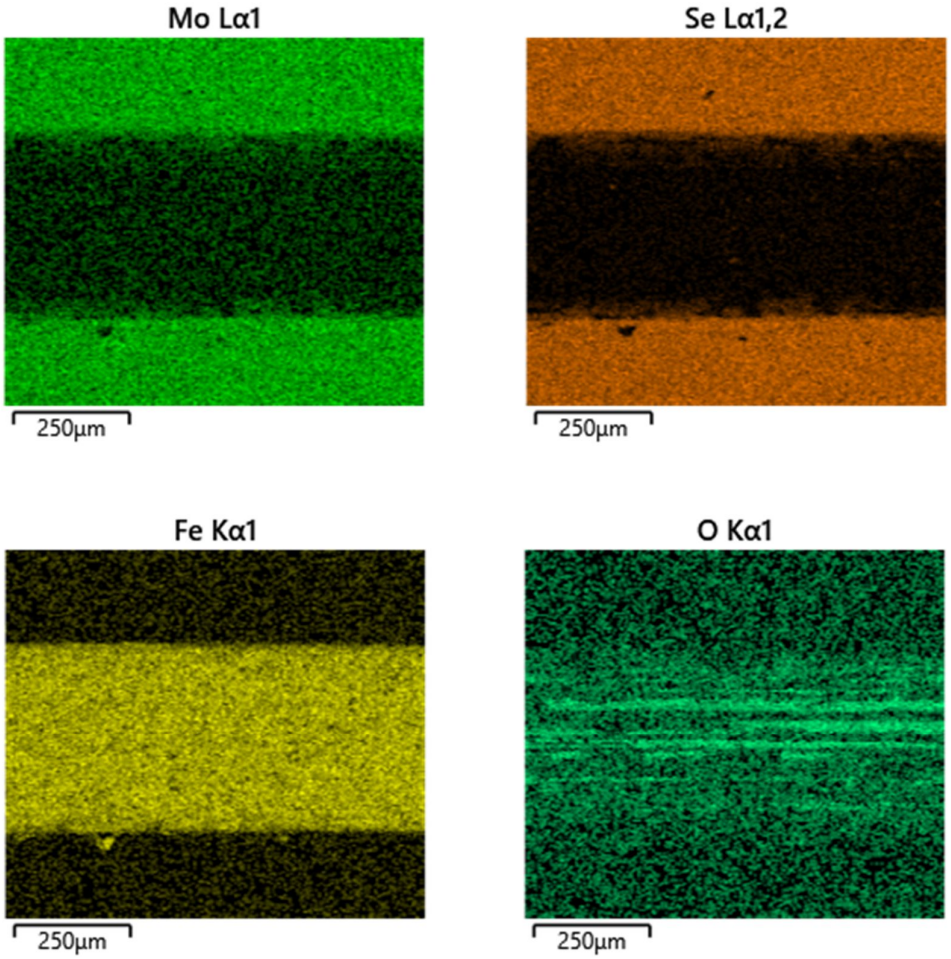

Figure 4.23: EDS mapping of the wear track of $MoSe_2$ coating tested in dry sliding at a normal load of 5 N and 25 °C.

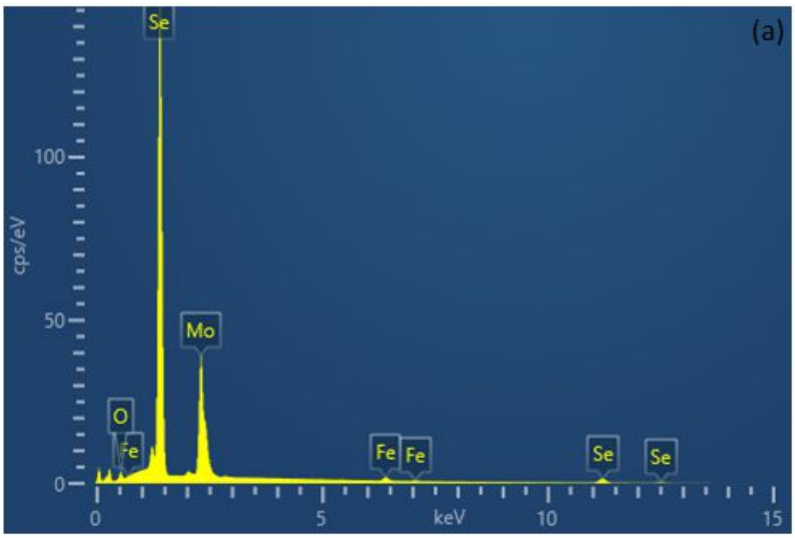

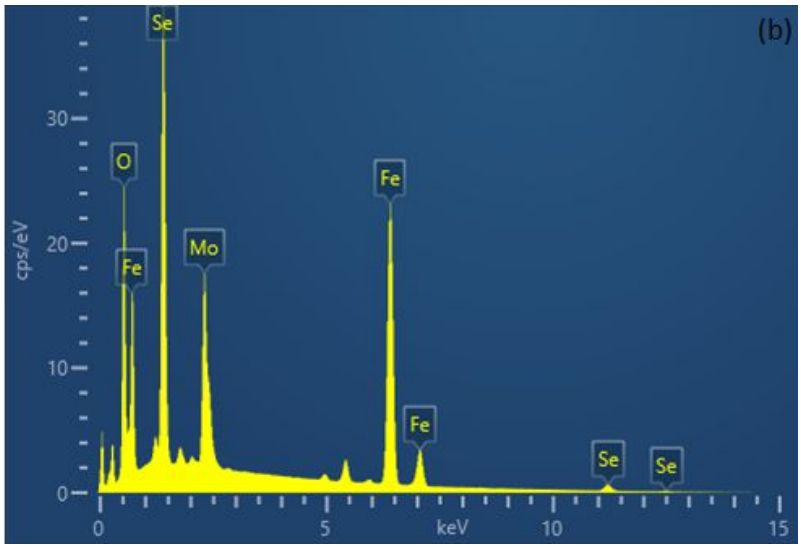

Figure 4.24: EDS point analysis of: (a) the as-deposited $MoSe_2$ coating (point A) and (b) the centre of the wear track of the coating tested in dry sliding at a normal load of 5 N and 25 °C (point B).

Figure 4.25 shows the Raman spectrum of the as-deposited coating as a reference and the spectra acquired from different positions of the wear track of the coating tested in dry sliding at a normal load of 5 N and 25 °C. The Raman spectrum of the as-deposited coating shows five peaks belonging to $MoSe_2$ at wavenumbers 155 cm^{-1}, 235 cm^{-1}, 290 cm^{-1}, 443 cm^{-1}, and 596 cm^{-1} [392,471]. The Raman spectra collected from the centre and edge of the wear track (i.e. positions 3 and 1) show that $MoSe_2$ peak at 235 cm^{-1} has a higher intensity and is sharper than the one observed in the as-deposited coating. This suggests that a crystalline $MoSe_2$ tribolayer was formed in the wear track during sliding, which is consistent with what was found in the wear tracks of $MoSe_2$ coatings tested under dry sliding conditions in several studies [225,392,467,474,475]. The existence of two broad peaks at wavenumbers 815 cm^{-1} and 940 cm^{-1} belonging to MoO_3 at positions 2 and 3 indicates that the coating underwent an oxidation reaction during sliding. This result is different from the wear track of the PAO4-lubricated sliding test shown in **Figure 4.17**, which did not show the presence of any peak belonging to MoO_3. This is a clear indication of the beneficial role of PAO4 in sealing the contact and protecting the coating from oxidation.

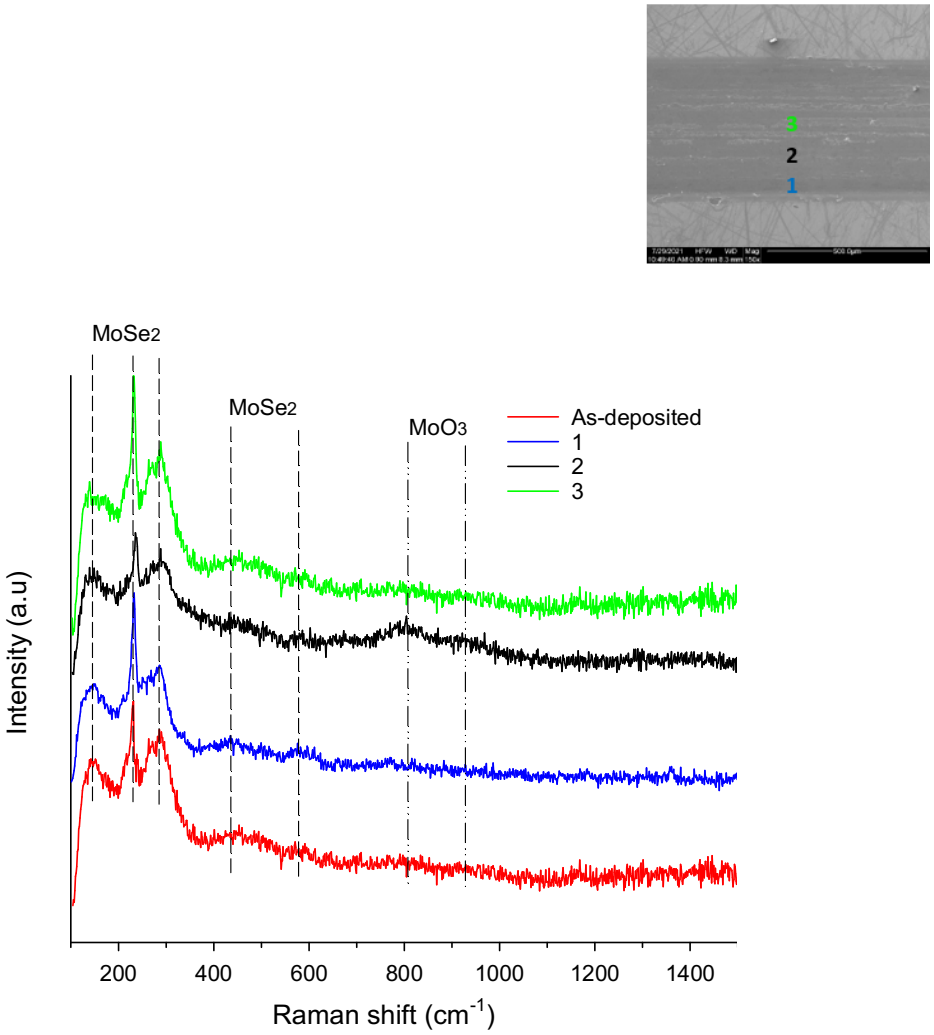

Figure 4.25: Raman spectra acquired from different positions of the wear track of $MoSe_2$ coating tested in dry sliding at a normal load of 5 N and 25 °C.

The results of Raman spectroscopy carried out in different positions of the wear track suggest that a well-ordered $MoSe_2$ tribolayer likely formed in the wear track of the coating during dry sliding. To confirm such hypothesis, a thin lamella was extracted from the wear track and subjected to TEM analysis, as shown in **Figure 4.26**. The TEM image reveals the formation of a crystalline $MoSe_2$ tribolayer in the topmost surface of the wear track. This contrasts with the original coating microstructure, which is mostly amorphous with a small number of $MoSe_2$ nanocrystals. This TEM observation strongly supports the previously mentioned observation from Raman spectroscopy. The formed tribolayer has a thickness of approximately 10 nm and consists of parallelly aligned $MoSe_2$ basal planes to the sliding direction. These perfectly

aligned planes resulted in a low interfacial shear strength at the sliding interface, thus giving rise to a low coefficient of friction in dry sliding.

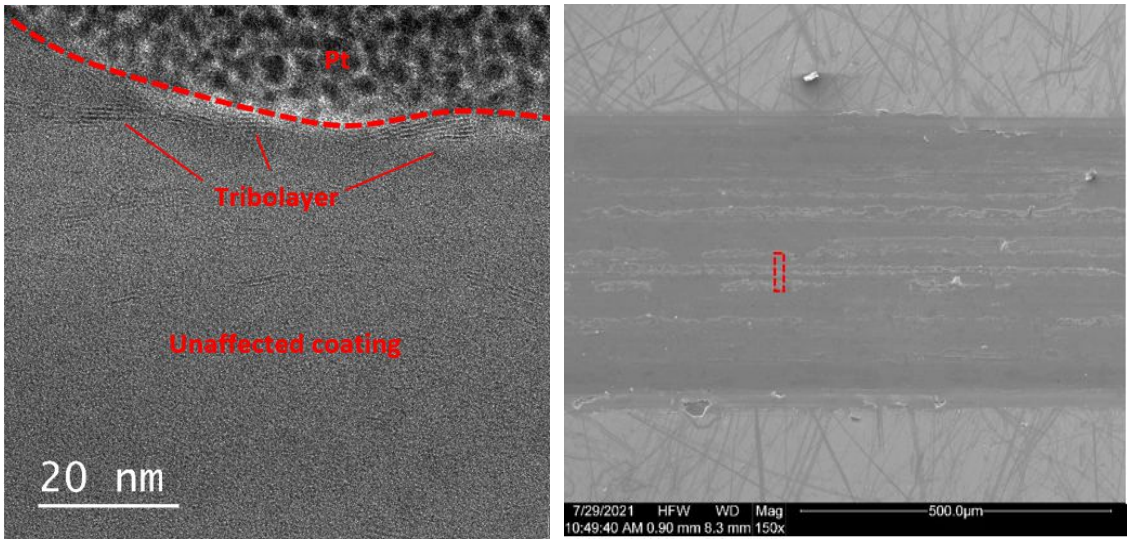

Figure 4.26: (left) TEM image of the topmost surface of the wear track of $MoSe_2$ coating tested in dry sliding at a normal load of 5 N and 25 °C and (right) SEM image shows the location of the FIB cut from the wear track. The TEM image shows the formation of a crystalline $MoSe_2$ tribolayer with its basal planes perfectly aligned parallel to the sliding direction. The unaffected coating shows $MoSe_2$ nanocrystals embedded in an amorphous microstructure.

Figure 4.27 shows the surface morphology of the ball wear scar tested against the coating in dry sliding at a normal load of 5 N and 25 °C. The scar is elliptical in shape, and there is a clear sign of abrasive wear, as indicated by the presence of multiple scratches parallel to the sliding direction. Moreover, the ball wear scar is covered with a transfer layer formed during sliding against the coating. EDS analysis was carried out to determine the chemical composition of this layer. The elemental maps are displayed in **Figure 4.28**, which show that this transfer layer is rich in molybdenum and selenium, implying wear of $MoSe_2$ coating, followed by its transfer and adherence to the ball during sliding. Unlike the ball wear scar of the PAO4-lubricated sliding test shown in **Figure 4.19**, the transfer layer here is quite evenly distributed and covers major parts of the wear scar. The presence of oxygen is also observed. This could be due to oxidation of the coating or the steel ball.

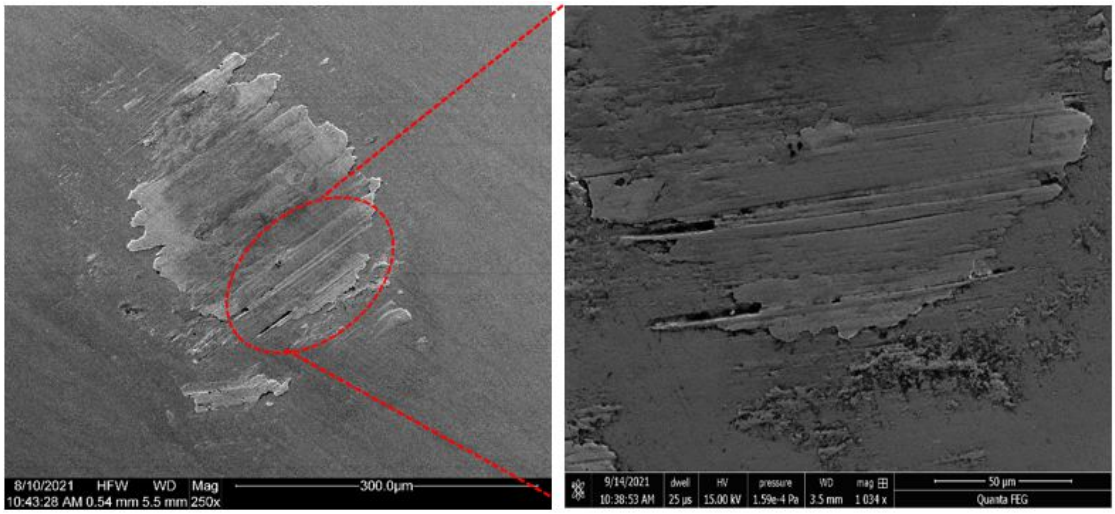

Figure 4.27: (left) SEM image of the ball wear scar tested against $MoSe_2$ coating in dry sliding at a normal load of 5 N and 25 °C and (right) SEM image shows a close-up view of the bottom edge of the wear scar.

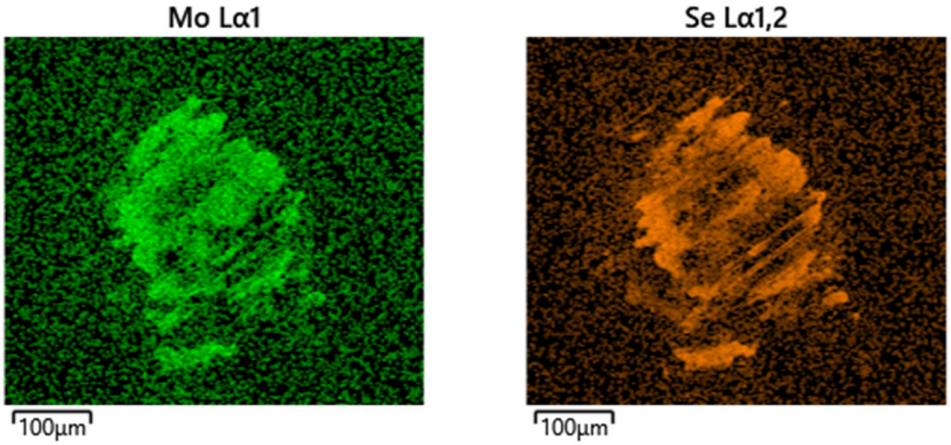

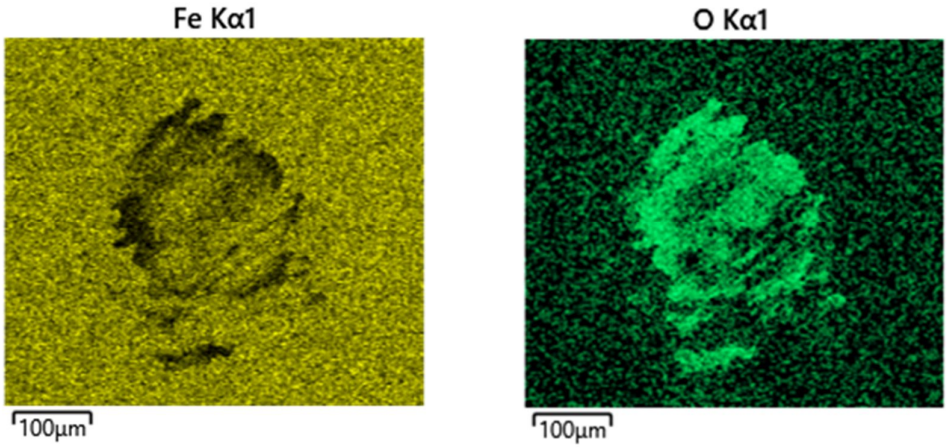

Figure 4.28: EDS mapping of the ball wear scar tested against $MoSe_2$ coating in dry sliding at a normal load of 5 N and 25 °C.

Figure 4.29 shows the Raman spectra acquired from different positions of the ball wear scar tested against the coating in dry sliding at a normal load of 5 N and 25 °C. All the analysed positions of the ball wear scar reveal the presence of a significant amount of adhered $MoSe_2$ material. This differs from the ball wear scar of the PAO4-lubricated sliding test shown in **Figure 4.21**, where the presence of oil considerably impeded the transfer of the coating material. Peaks belonging to MoO_3 are observed at all the analysed positions. When comparing the intensities of MoO_3 peaks observed in the ball wear scars, the dry sliding test has more intense peaks than the PAO4-lubricated sliding test. This demonstrates the beneficial role of PAO4 in protecting the coating from oxidation during sliding.

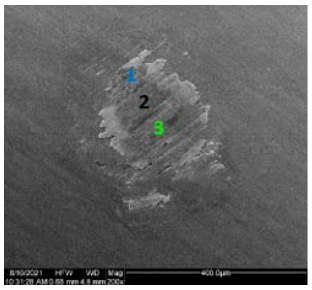

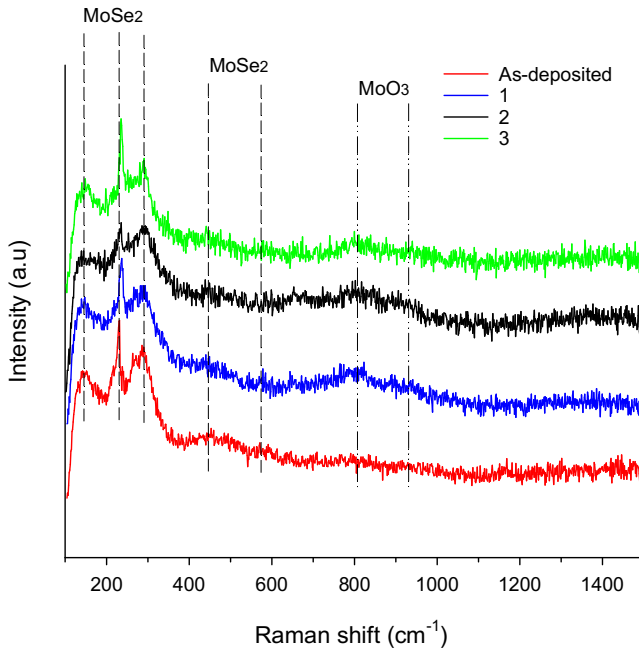

Figure 4.29: Raman spectra acquired from different positions of the ball wear scar tested against $MoSe_2$ coating in dry sliding at a normal load of 5 N and 25 °C.

4.2.5.3 PAO4-lubricated sliding at 15 N load and 25 °C

Figure 4.30 shows SEM image of the wear track of the coating tested at a normal load of 15 N under PAO4-lubricated sliding conditions. The wear track has a non-uniform appearance and a width of about 480 µm, which is wider than the wear track of the 5 N load test. A closer examination with higher magnification revealed that the coating exhibited delamination around the edges of the wear track. **Figure 4.31** shows the EDS mapping of this wear track. It reveals the dominance of iron within the wear track, originating from the substrate, and a depletion of molybdenum and selenium compared to the untested coating surface. This is an indicator of serious wear of the $MoSe_2$ layer during sliding. No evidence of oxygen is detected inside the

wear track. As shown in **Figure 4.32**, EDS point analysis performed at the centre of the wear track (point B) displays only a small increase in the intensity of the peak belonging to oxygen compared to that of the as-deposited coating (point A).

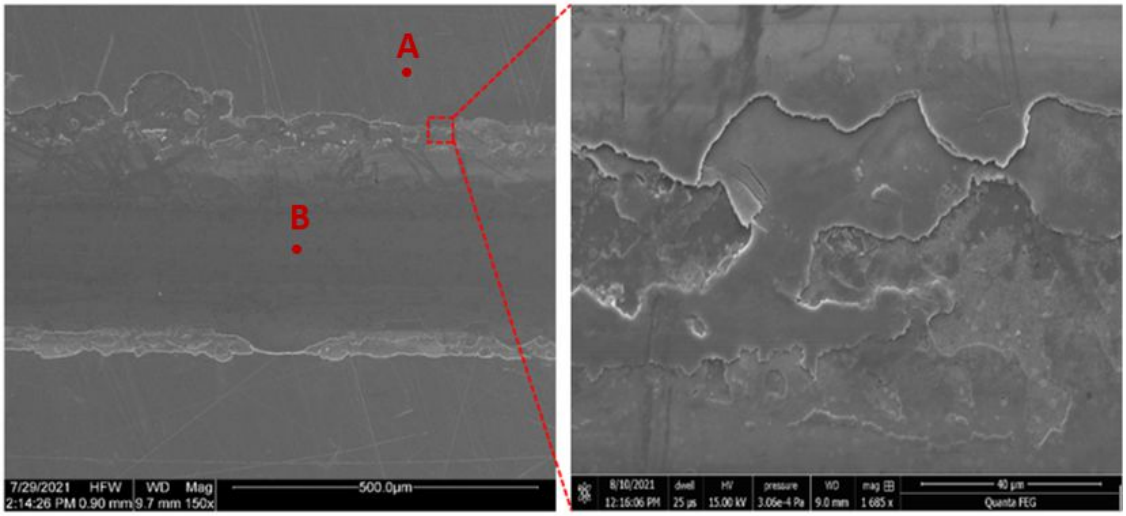

Figure 4.30: (left) SEM image of the wear track of $MoSe_2$ coating tested at a normal load of 15 N in PAO4-lubricated sliding and (right) SEM image shows a close-up view of the top edge of the wear track.

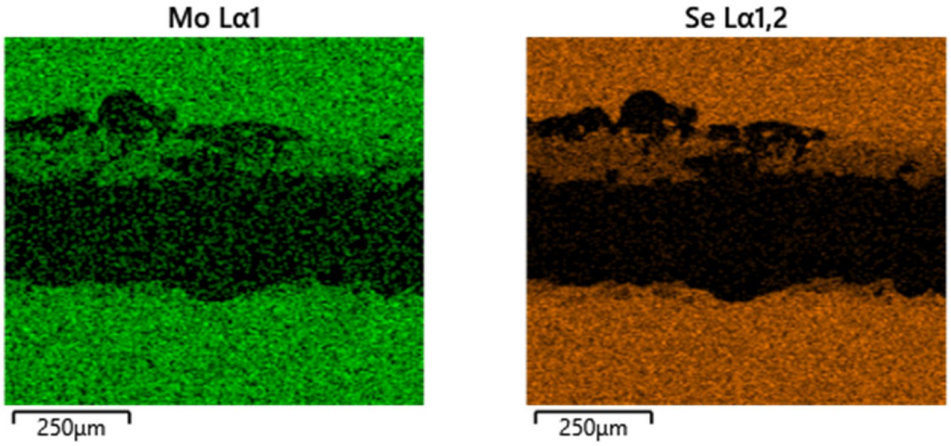

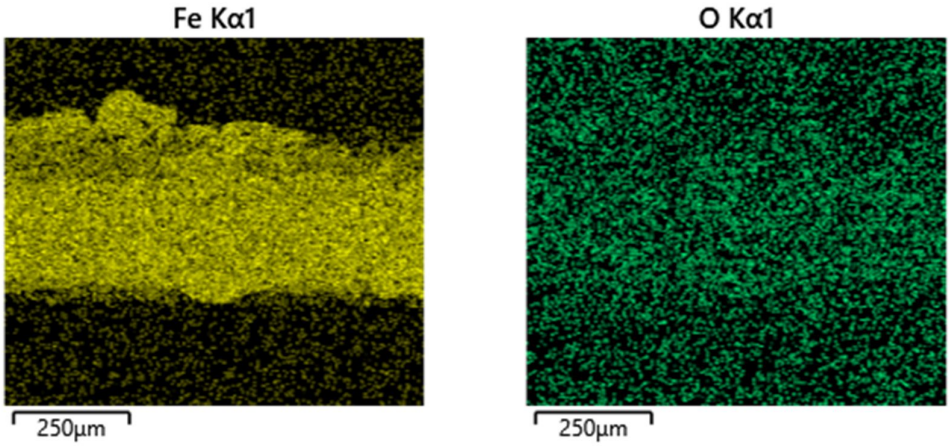

Figure 4.31: EDS mapping of the wear track of $MoSe_2$ coating tested at a normal load of 15 N in PAO4-lubricated sliding.

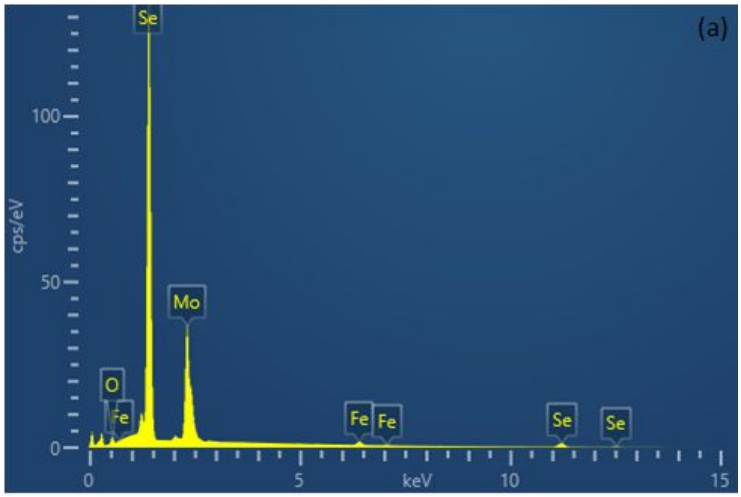

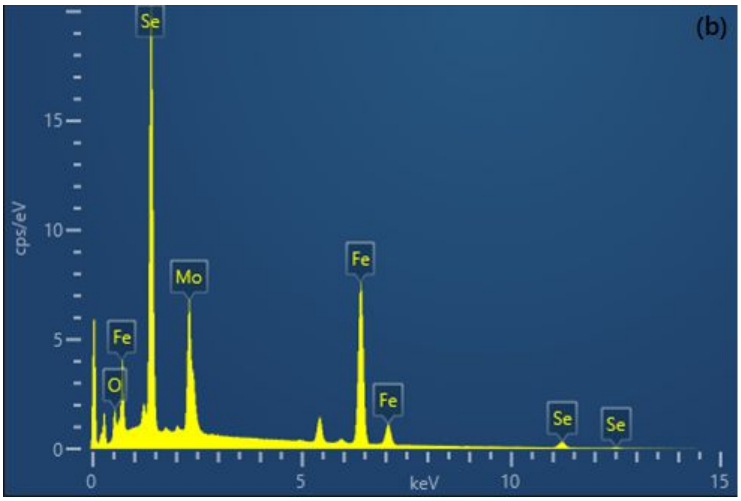

Figure 4.32: EDS point analysis of: (a) the as-deposited $MoSe_2$ coating (point A) and (b) the centre of the wear track of the coating tested at a normal load of 15 N in PAO4-lubricated sliding (point B).

Figure 4.33 shows the Raman spectrum of the as-deposited $MoSe_2$ coating as a reference and the spectra acquired from different positions of the wear track of the coating tested at a normal load of 15 N in PAO4-lubricated sliding. The Raman spectrum of the as-deposited coating shows five peaks belonging to $MoSe_2$ at wavenumbers 155 cm^{-1}, 235 cm^{-1}, 290 cm^{-1}, 443 cm^{-1}, and 596 cm^{-1} [392,471]. The Raman spectra acquired from different positions of the wear track appeared to be similar to that of the as-deposited coating. The only exception is the Raman spectrum acquired from the centre of the wear track (i.e. position 3) in which $MoSe_2$ peaks were broader and less pronounced than those of the as-deposited coating. This suggests that less $MoSe_2$ material remained at the centre of the wear track. This was expected since the contact pressure was the highest at the centre of the wear track, resulting in more removal of the $MoSe_2$ layer. There is no evidence of the formation of MoO_3 in any of the spectra acquired from different positions of the wear track.

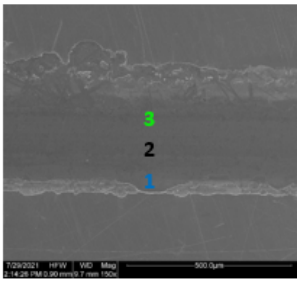

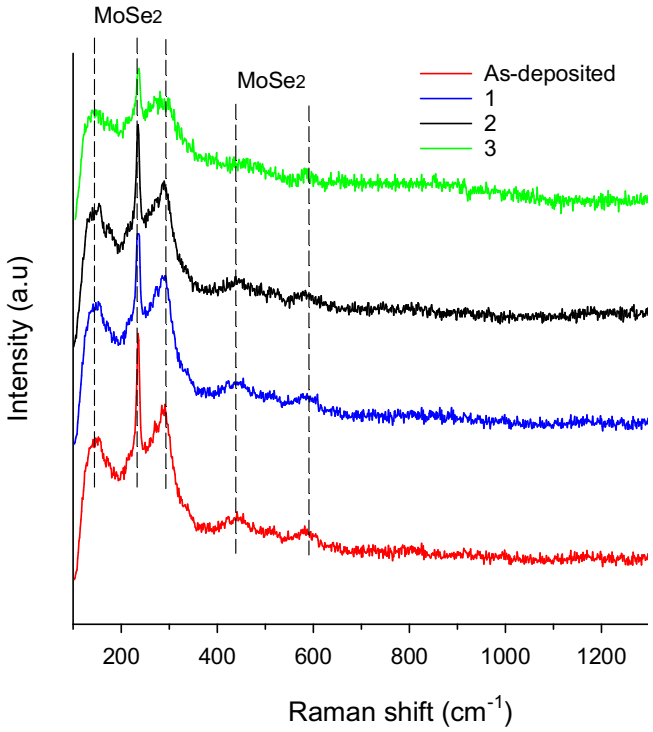

Figure 4.33: Raman spectra acquired from different positions of the wear track of $MoSe_2$ coating tested at a normal load of 15 N in PAO4-lubricated sliding.

The structure of the coating inside the wear track was analysed using TEM, as shown in **Figure 4.34**. The TEM image shows that the coating did not undergo any tribo-induced structural changes in its crystallinity, similar to what was observed in the wear track of the 5 N load test shown in **Figure 4.18**. In the topmost surface of the wear track, the basal planes of $MoSe_2$ coating are either perpendicular to the sliding direction or randomly oriented. These planes are incapable of functioning as easy slip planes, which are required for reducing friction in TMD coatings. This result suggests that PAO4 inhibited the shear-induced formation of a well-

ordered $MoSe_2$ tribolayer. It also suggests that there was another factor that contributed to the observed drop in the coefficient of friction with increasing load.

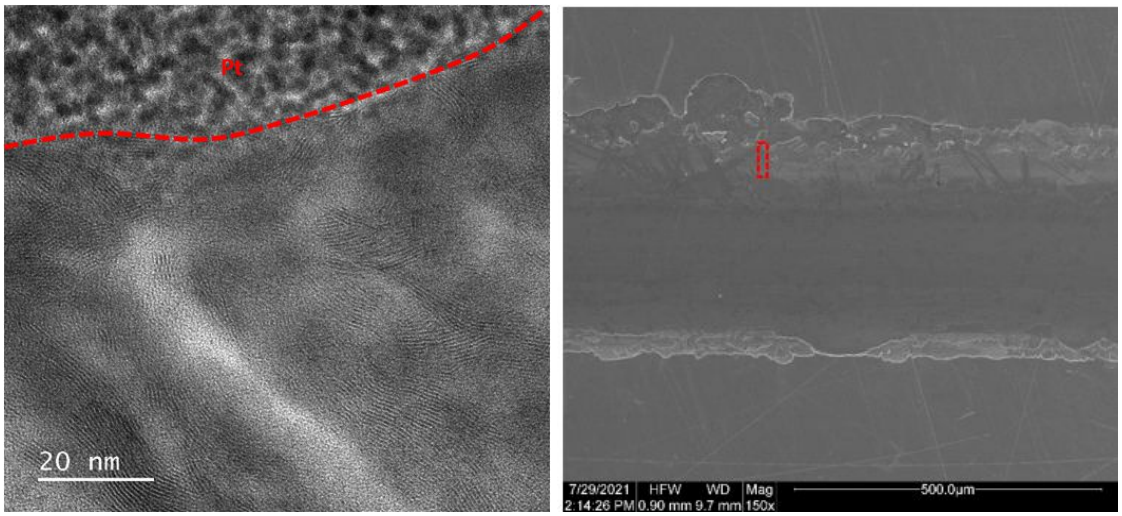

Figure 4.34: (left) TEM image of the topmost surface of the wear track of $MoSe_2$ coating tested in PAO4-lubricated sliding at a normal load of 15 N and (right) SEM image shows the location of the FIB cut from the wear track. The TEM image shows no evidence of the formation of a well-ordered $MoSe_2$ tribolayer. The basal planes of $MoSe_2$ in the topmost surface of the wear track are either perpendicular to the sliding direction or randomly orientated.

Figure 4.35 shows the surface morphology of the ball wear scar tasted against the coating at a normal load of 15 N in PAO4-lubricated sliding. The wear scar has a smaller diameter than the wear scar of the 5 N load test and is covered with a tribolayer formed during sliding. This tribolayer is uniformly distributed and covers a large area of the wear scar, unlike the ball wear scar of the 5 N load test shown in **Figure 4.19**. The chemical composition of this layer was determined by EDS, as shown in **Figure 4.36**, which reveals that this layer is rich in molybdenum and selenium, implying wear of $MoSe_2$ coating, followed by its transfer and adherence to the ball during sliding.

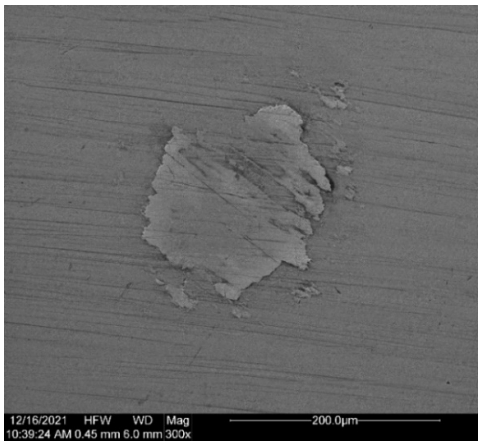

Figure 4.35: SEM image of the ball wear scar tested against $MoSe_2$ coating at a normal load of 15 N in PAO4-lubricated sliding.

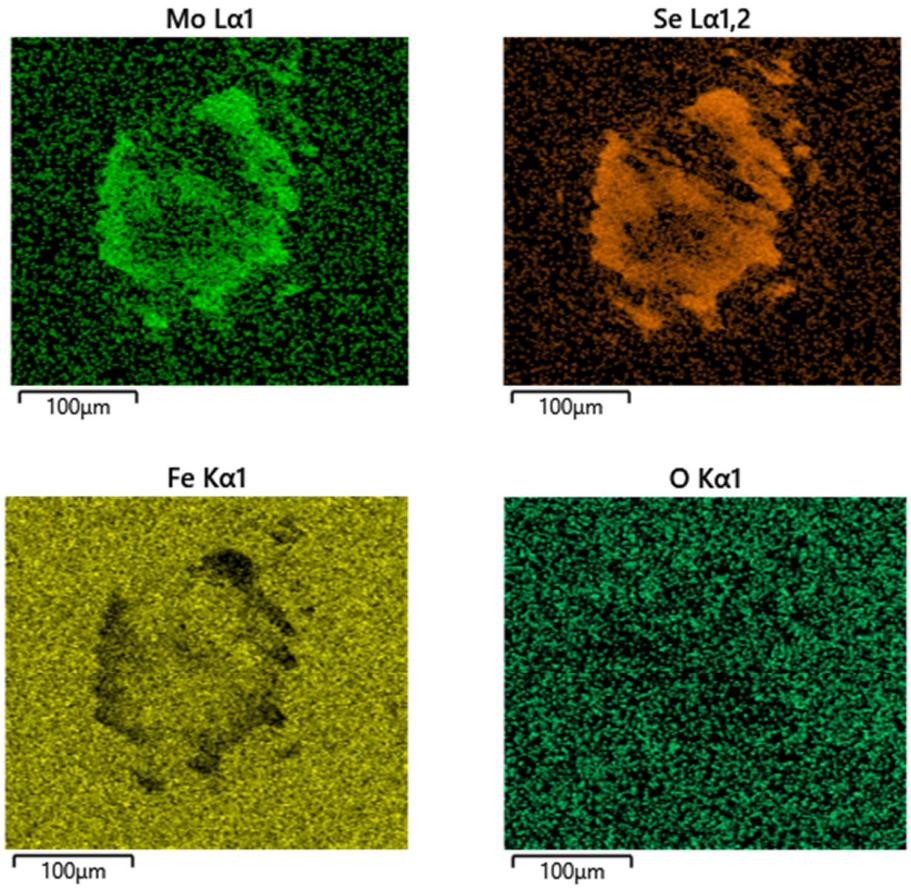

Figure 4.36: EDS mapping of the ball wear scar tested against $MoSe_2$ coating at a normal load of 15 N in PAO4-lubricated sliding.

Figure 4.37 shows the Raman spectra acquired from different positions of the ball wear scar tested against the coating at a normal load of 15 N in PAO4-lubricated sliding. All the analysed positions of the ball wear scar reveal the presence of a significant amount of adhered $MoSe_2$ material. This contrasts with the ball wear scar of the 5 N load test, where the transfer of the coating material was considerably inhibited. $MoSe_2$ peaks at positions 1 and 2 are less pronounced and much broader than those of the as-deposited coating, indicating the presence of a less organised $MoSe_2$ structure at these positions. The Raman spectra acquired from these two positions also show two broad peaks belonging to MoO_3 at wavenumbers 815 cm^{-1} and 940 cm^{-1} [221,473], implying oxidation of $MoSe_2$.

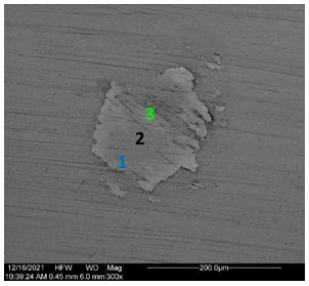

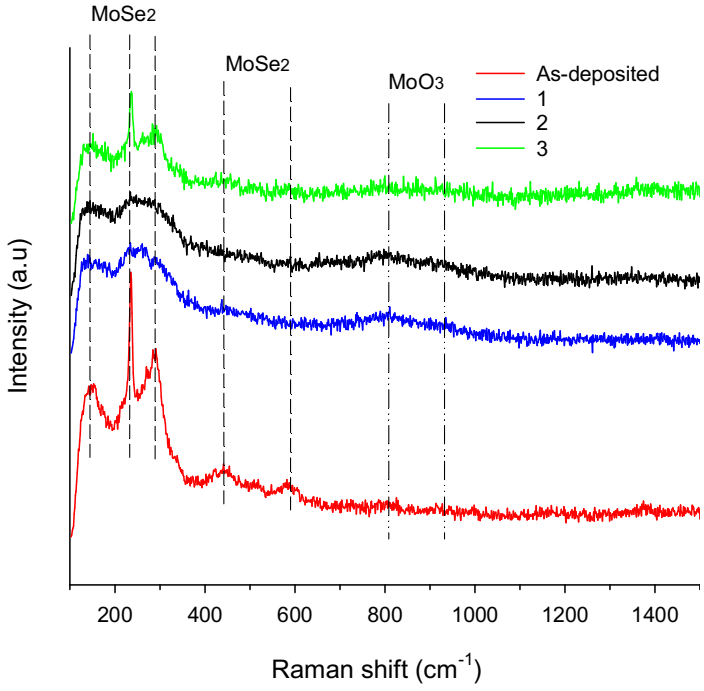

Figure 4.37: Raman spectra acquired from different positions of the ball wear scar tested against $MoSe_2$ coating at a normal load of 15 N in PAO4-lubricated sliding.

4.2.5.4 PAO4-lubricated sliding at 5 N load and 100 °C

Figure 4.38 shows SEM image of the wear track of the coating tested at 100 °C under PAO4-lubricated sliding conditions. An irregular shape of the track can be observed where the width varies along the length of the track. In addition, severe coating delamination and chipping can be observed at the edges of the wear track, implying deteriorated wear resistance. **Figure 4.39** shows the EDS mapping of this wear track. It reveals the dominance of iron within the wear track, originating from the substrate, and a depletion of molybdenum and selenium as compared to the untested coating surface. No evidence of oxygen is detected inside the wear track. As shown in **Figure 4.40**, EDS point analysis performed at the centre of the wear track (point B) shows only a small increase in the intensity of the peak belonging to oxygen compared to that of the as-deposited coating (point A). This demonstrates the positive effect of PAO4 in sealing the contact and preventing oxidation of the coating during sliding.

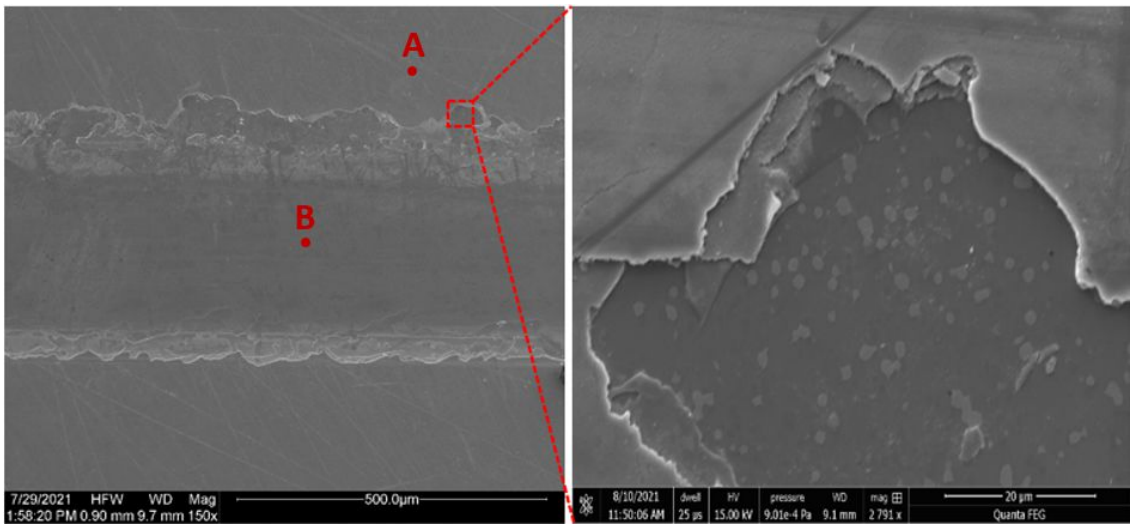

Figure 4.38: (left) SEM image of the wear track of $MoSe_2$ coating tested at a temperature of 100 °C in PAO4-lubricated sliding and (right) SEM image shows a close-up view of the top edge of the wear track.

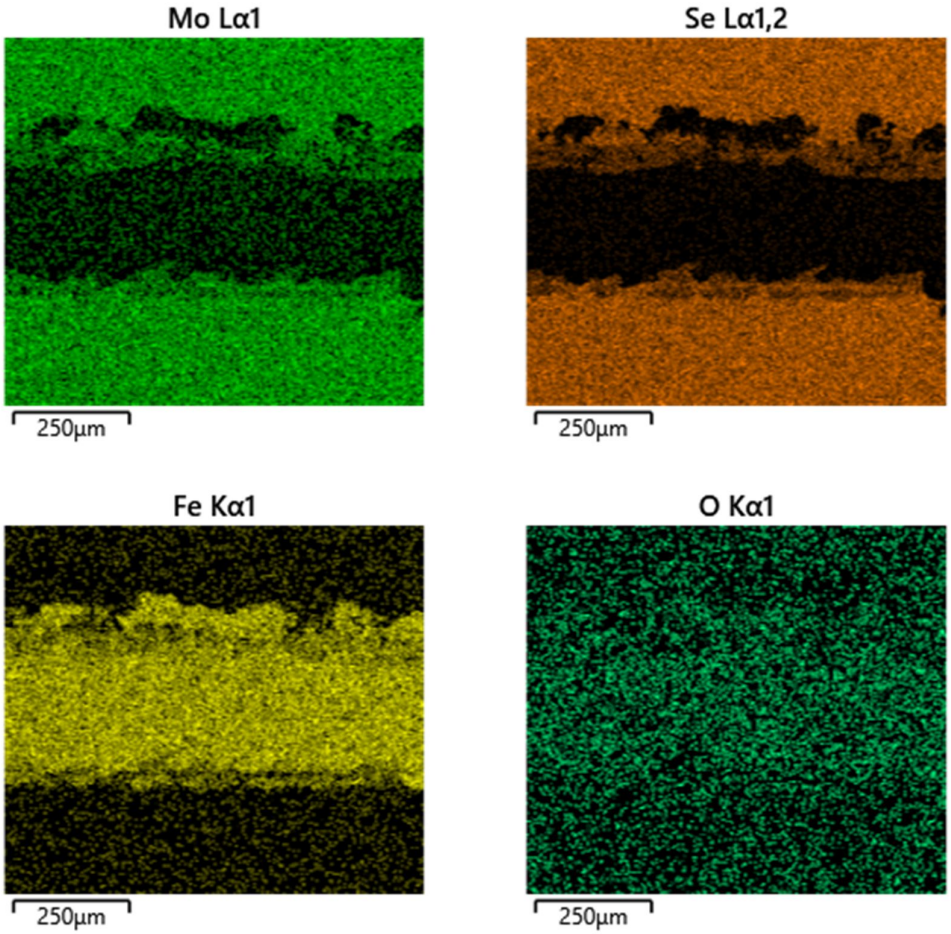

Figure 4.39: EDS mapping of the wear track of $MoSe_2$ coating tested at a temperature of 100 °C in PAO4-lubricated sliding.

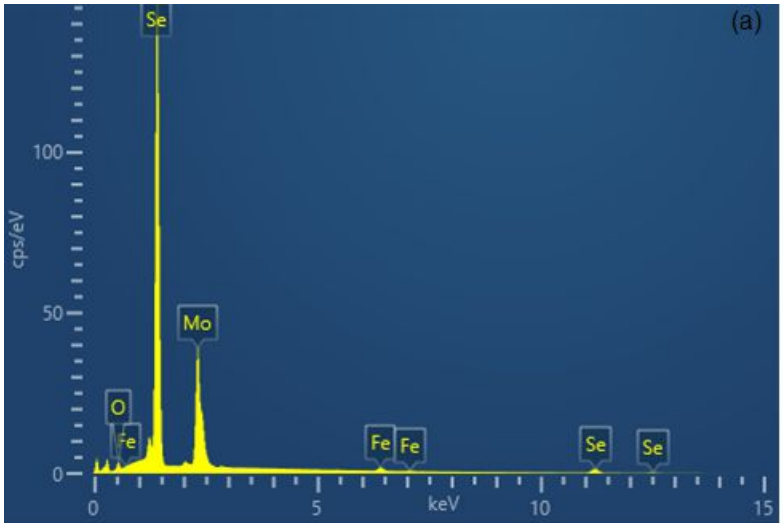

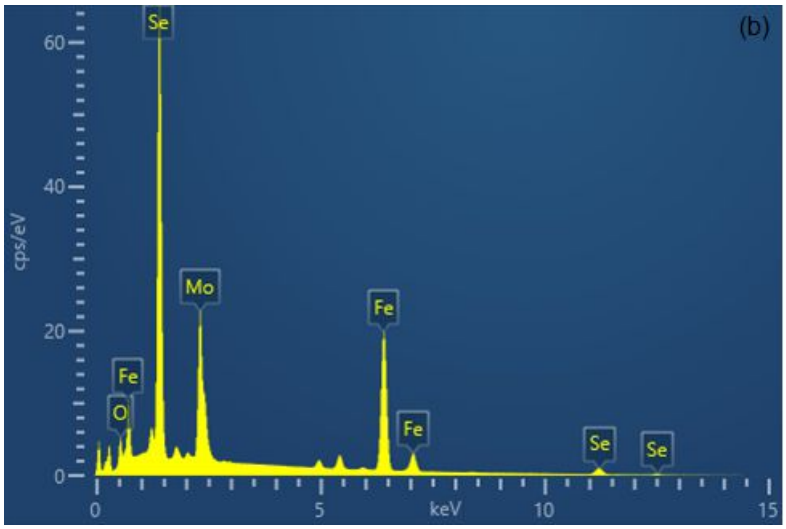

Figure 4.40: EDS point analysis of: (a) the as-deposited $MoSe_2$ coating (point A) and (b) the centre of the wear track of the coating (point B) tested at a temperature of 100 °C in PAO4-lubricated sliding.

The Raman spectra acquired from different positions of the wear track of the coating tested at 100 °C in PAO4-lubricated sliding are shown in **Figure 4.41**. The Raman spectrum of the as-deposited coating (reference) shows five peaks corresponding to $MoSe_2$ at wavenumbers 155 cm^{-1}, 235 cm^{-1}, 290 cm^{-1}, 443 cm^{-1}, and 596 cm^{-1} [392,471]. The Raman spectra acquired from the wear track show that $MoSe_2$ material is still present in all the analysed positions in significant amounts. These spectra appear to be similar to those of the as-deposited coating. This similarity suggests that $MoSe_2$ coating did not undergo any tribo-induced structural changes in its crystallinity during sliding. No evidence of the formation of MoO_3 is detected in all the analysed positions of the wear track.

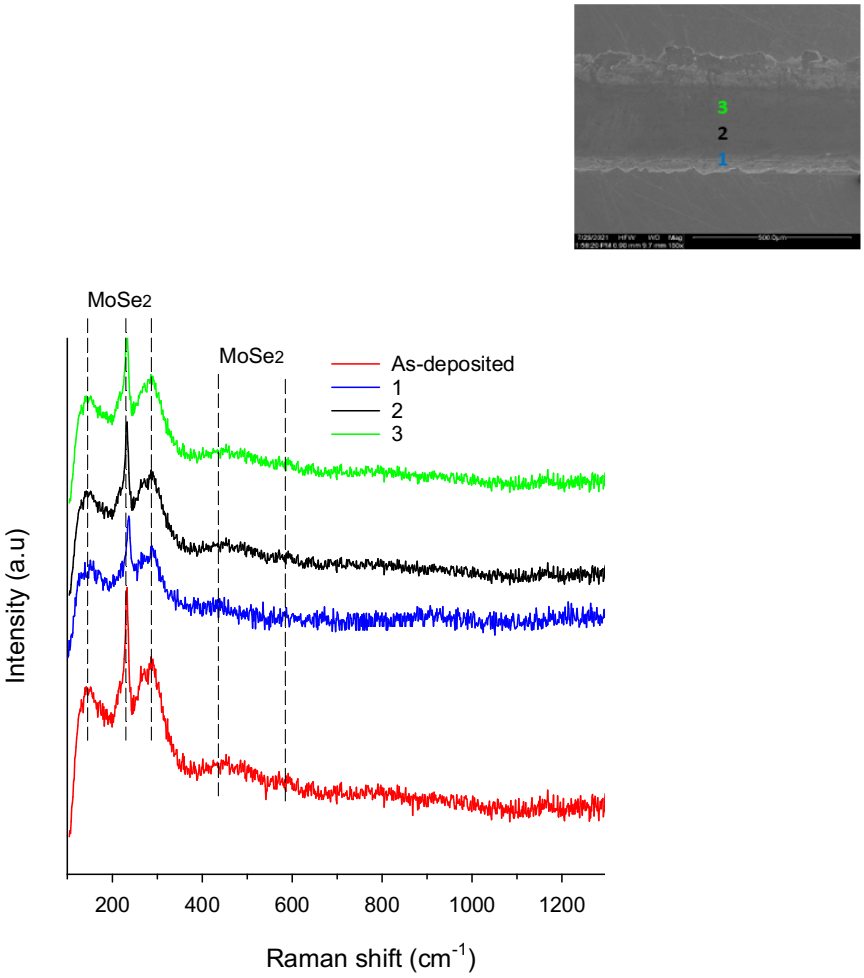

Figure 4.41: Raman spectra acquired from different positions of the wear track of $MoSe_2$ coating tested at a temperature of 100 °C in PAO4-lubricated sliding.

Figure 4.42 shows the surface morphology of the ball wear scar tasted against the coating at 100 °C in PAO4-lubricated sliding. The ball wear scar is elliptical in shape and smaller in size than the ball wear scar of the 25 °C temperature test shown in **Figure 4.19**. It can be seen that there is a build-up of wear debris at two edges of the ball wear scar. **Figure 4.43** shows the EDS mapping of this ball wear scar. It shows enrichment of molybdenum and selenium at two edges of the ball wear scar, implying wear of $MoSe_2$ coating, followed by its transfer and adherence to the ball during sliding. Unlike the ball wear scar of the 25 °C temperature test, the transfer layer here covers major parts of the ball wear scar. The mapping also shows the presence of oxygen, suggesting oxidation of $MoSe_2$ coating or its sliding counterpart.

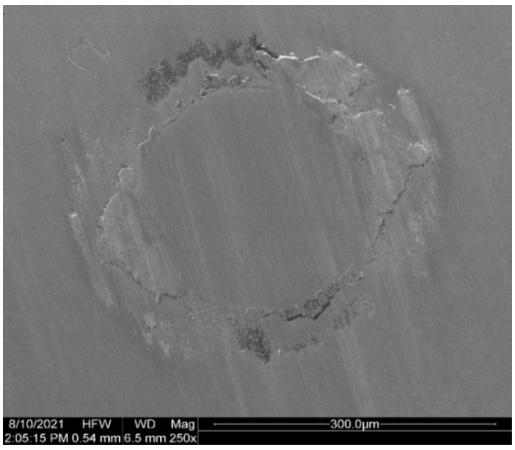

Figure 4.42: SEM image of the ball wear scar tested against $MoSe_2$ coating at a temperature of 100 °C in PAO4-lubricated sliding.

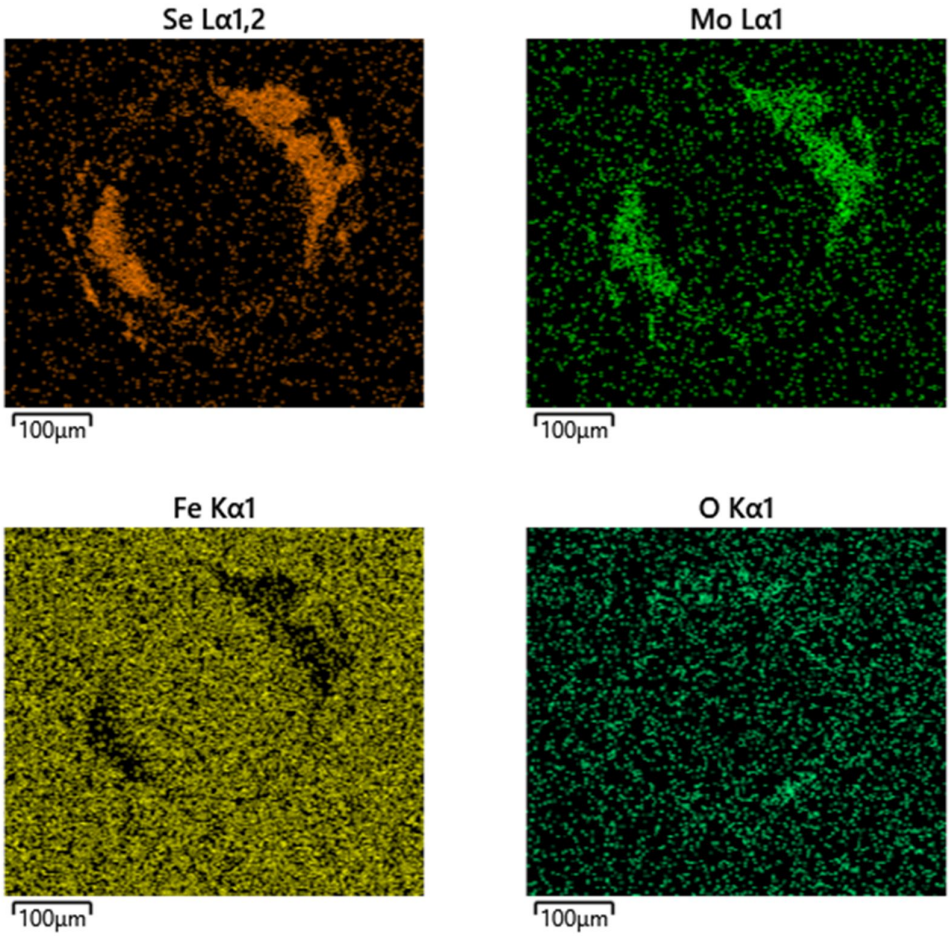

Figure 4.43: EDS mapping of the ball wear scar tested against $MoSe_2$ coating at a temperature of 100 °C in PAO4-lubricated sliding.

Figure 4.44 shows the Raman spectra acquired from different positions of the ball wear scar tested against the coating at 100 °C in PAO4-lubricated sliding. The Raman spectrum acquired from the centre of the ball wear scar (i.e. position 3) shows five peaks belonging to $MoSe_2$ at wavenumbers 155 cm^{-1}, 235 cm^{-1}, 290 cm^{-1}, 443 cm^{-1}, and 596 cm^{-1} [392,471]. The low intensity of these peaks is a clear indication that only a small amount of the coating material transferred and adhered to the centre of the ball during sliding, further supporting and confirming the results obtained from EDS. The Raman spectrum acquired from the centre of the ball wear scar also shows two peaks belonging to MoO_3 at wavenumbers 815 cm^{-1} and 940 cm^{-1} [221,473], suggesting oxidation of $MoSe_2$. Intense and clear peaks of $MoSe_2$ are only observed at positions 1 and 2 of the ball wear scar. The Raman spectrum acquired from the edge of the wear scar (i.e. position 1) shows the presence of two broad peaks at wavenumbers 815 cm^{-1} and 940 cm^{-1} belonging to MoO_3. When comparing the ball wear scars of 25 °C and 100 °C temperature tests, the intensities of $MoSe_2$ peaks in each scar are different, with the one of the 100 °C temperature test having more intense peaks than those seen in the wear scar of the 25 °C temperature test. This suggests that when the test was conducted at 100 °C, there was a higher transfer of the coating material to the ball.

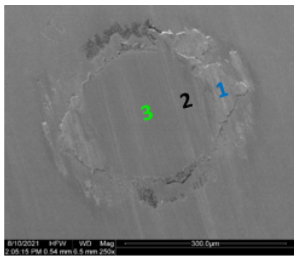

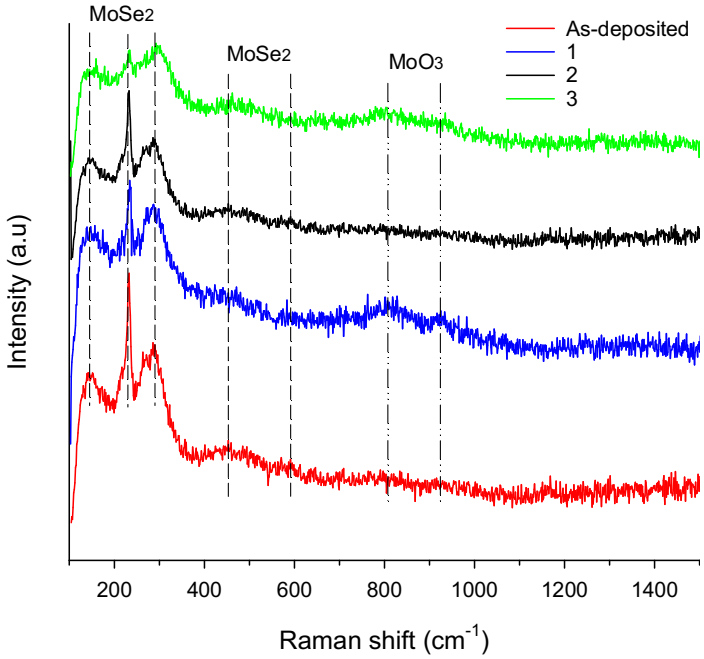

Figure 4.44: Raman spectra acquired from different positions of the ball wear scar tested against $MoSe_2$ coating at a temperature of 100 °C in PAO4-lubricated sliding.

4.3 Discussions

4.3.1 Effect of oil lubrication

As previously discussed in section 2.6.3, the low-friction mechanism of TMD coatings is governed by two key factors: (a) the transfer of worn material from the coating surface to its counterpart, resulting in predominantly self-mated coating/coating contact with easy interfacial sliding and (b) the formation of a crystalline tribolayer in the coating wear track with TMD basal planes aligned parallel to the sliding direction, facilitating interlamellar slip with minimal frictional resistance to motion [42,43,226,309,320,392,467,475,476].

In PAO4-lubricated sliding, the formation of the above mentioned tribologically beneficial transfer layer was significantly hindered. This was evidenced by EDS analysis and Raman spectroscopy, which showed that only a very small amount of $MoSe_2$ material transferred to the steel ball during sliding and adhered to two edges. This left most of the steel ball surface not sufficiently covered by a uniformly distributed $MoSe_2$-rich transfer layer, which is required for imparting low interfacial shear between the contacting surfaces. Such behaviour consequently resulted in a higher coefficient of friction, as well as a higher wear rate of the steel ball when compared to dry sliding. It could also account for the high instability observed in the friction curve of the PAO4-lubricated sliding test. On the other hand, a crystalline $MoSe_2$ tribolayer did not form in the topmost surface of the wear track. This was evidenced by TEM examination of the wear track, which did not show the formation of a $MoSe_2$ tribolayer with a beneficial alignment of basal planes parallel to the sliding direction. Therefore, it is possible to infer that PAO4 played a key role in the friction performance of $MoSe_2$ coating by significantly hindering the coating material being transferred to its sliding counterpart and preventing the formation of a low-friction $MoSe_2$ tribolayer. These two factors contributed to the observed higher coefficient of friction when compared to dry sliding.

In dry sliding, EDS analysis and Raman spectroscopy showed that the ball wear scar was fully covered by a relatively well-adherent $MoSe_2$ layer transferred from the coating to its counterpart during sliding. The formation of this lubricious transfer layer prevented direct contact between the sliding surfaces and resulted in low friction. It also provided the ball with significant protection against wear, resulting in a low wear rate. On the other hand, TEM examination of the wear track of the dry sliding test revealed the formation of a crystalline $MoSe_2$ tribolayer in the topmost surface of the wear track with $MoSe_2$ basal planes perfectly aligned parallel to the sliding direction. This tribolayer was formed by a sliding-induced crystallisation of the originally amorphous $MoSe_2$ material. The amorphous to crystalline phase transformation in the topmost surface of the wear track was also reported for different TMD coatings tested under dry sliding conditions [162,467,306,477,478]. Therefore, it can be inferred that the presence of easily sheared $MoSe_2$ basal planes in the topmost surface of the wear track and the formation of a uniform and compact transfer layer covering the steel counterpart were together responsible for the observed lower coefficient of friction when compared to PAO4-lubricated sliding.

As discussed earlier in section 2.6.6.1, TMD coatings can react with oxygen in the surrounding atmosphere during tribo-testing, forming metal oxides such as MoO_3 and WO_3. The formation of these oxides at the sliding interface is very detrimental for the wear resistance of the coatings and their sliding counterparts. This is because they act as abrasive particles and result in severe surface deterioration and ploughing of sliding surfaces [112,165,166,193,254,479]. EDS analysis of the wear track of the coating tested in dry sliding revealed a significant presence of oxygen. This indicates that a tribo-oxidation reaction took place during sliding. This was further supported by Raman spectroscopy, which revealed several peaks belonging to MoO_3. The newly formed MoO_3 particles, being harder than $MoSe_2$, led to severe abrasion and ploughing of the coating, consequently increasing its wear rate. In PAO4-lubricated sliding, EDS analysis did not detect any oxygen in the wear track. Similarly, Raman analysis of the wear track did not detect any peaks that could be identified as those of MoO_3. These findings demonstrate a positive effect of PAO4 on the wear resistance of the coating by acting as a sealant and contributing to reduce the formation of hard metal oxides that can abrade and damage sliding surfaces. This protection from oxidation provided by PAO4 led to a reduction in the wear rate of the coating by 27% when compared to dry sliding. If low wear is the main goal, then it can be deduced from the present results that PAO4 can play a vital role in significantly improving the wear resistance of the coating by acting as a sealant and protecting sliding surfaces from oxidation. With regards to the wear mechanisms observed, SEM and EDS analysis of the worn surfaces of both sliding conditions revealed the occurrence of abrasive wear, as evidenced by the presence of multiple scratches and wear grooves in the wear tracks, and adhesive wear, as evidenced by the detachment and adherence of the coating material to its sliding counterpart. Delamination wear was another detected wear mechanism at the edges of the wear tracks.

Based on the results mentioned above, the possible friction and wear mechanisms of the currently studied $MoSe_2$ coating under dry and PAO4-lubricated sliding conditions are deduced, as illustrated in **Figure 4.45**. In PAO4-lubricated sliding, the oil acted as a barrier and significantly hindered the transfer of the coating material to the sliding counterpart. This made it impossible for the formation of a beneficial transfer layer on the counterpart surface. Consequently, direct contact between the sliding surfaces could not be prevented. The oil also prevented the formation of a crystalline $MoSe_2$ tribolayer in the topmost surface of the wear

track. These two factors contributed to the observed higher coefficient of friction when compared to dry sliding. Nevertheless, PAO4 made a significant contribution to the enhancement of the coating's wear resistance by performing the function of a sealant and preventing the formation of MoO_3 particles, which would have otherwise abraded the surfaces and led to increased wear. Compared to PAO4-lubricated sliding, the coating's excellent friction performance in dry sliding was attributable to two main factors. The first one was the tribo-induced formation of a uniform and compact coating transfer layer on the sliding counterpart, which effectively blocked direct contact between the sliding surfaces. The second factor was the presence of a crystalline $MoSe_2$ tribolayer in the topmost surface of the wear track, with $MoSe_2$ basal planes perfectly aligned parallel to the sliding direction, resulting in a low interfacial shear strength at the sliding interface. The combined effect of these two factors led to the observed lower coefficient of friction when compared to PAO4-lubricated sliding. However, oxidation of $MoSe_2$ material was inevitable during the tribo-testing in dry sliding, leading to the formation of MoO_3 particles. These newly formed particles with abrasive properties increased the abrasion of $MoSe_2$ coating, accounting for the observed higher coating wear rate when compared to PAO4-lubricated sliding.

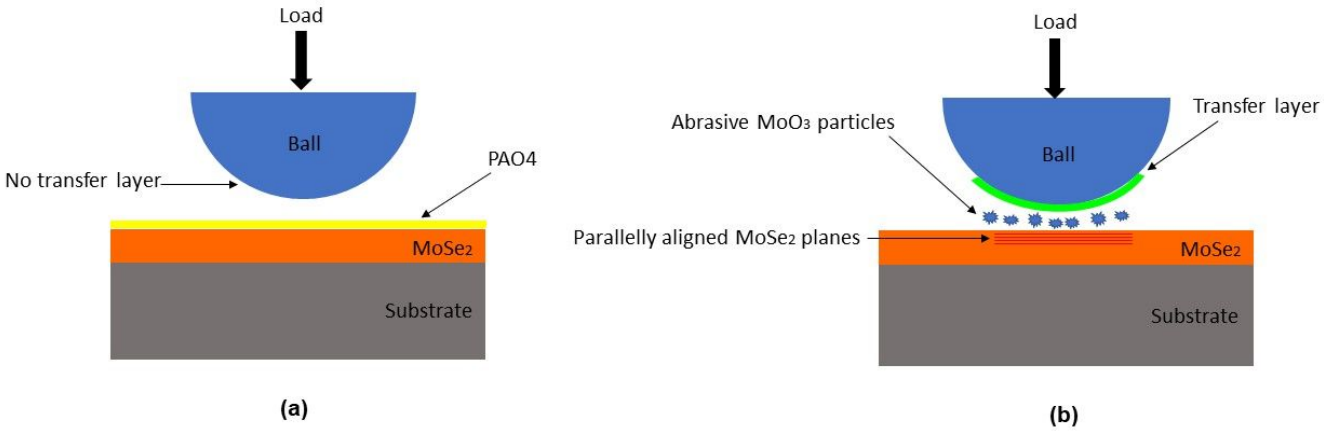

Figure 4.45: Schematic representation of the possible friction and wear mechanisms responsible for the tribological performance of $MoSe_2$ coating in: (a) PAO4-lubricated sliding and (b) dry sliding.

4.3.2 Effect of applied load in oil-lubricated sliding

When the coating was tribologically tested in PAO4-lubricated sliding at different loads ranging from 5 N to 15 N, its coefficient of friction and wear rate were observed to show a decreasing trend with increasing load. The highest coefficient of friction and wear rate were observed at 5 N load, whereas the lowest coefficient of friction and wear rate were observed at 15 N load.

As discussed earlier in section 2.6.6.3, TMD coatings typically exhibit a reduction in the coefficient of friction with increasing load. Various hypotheses have been proposed to explain this phenomenon. According to Midgley [230] and Gansheimer [231], the decrease in the coefficient of friction displayed by TMD coatings with increasing load is due to frictional heating at the sliding interface, which induces drying of air humidity. In this study, the tribological tests at different loads were performed in PAO4, which is known to have excellent thermal conductivity and can effectively contribute to the dissipation of friction-induced heat generated at the sliding interface. Therefore, the decrease in the coefficient of friction observed here in response to the increase in the applied load cannot be attributed to frictional heating.

Several researchers suggest that increasing the applied load can enhance the formation of a TMD tribolayer and result in a higher degree of order and parallel alignment of TMD basal planes, thereby lowering the interfacial shear strength and the coefficient of friction [204,226,232]. However, this was not the case in the current study. The Raman spectra collected from different positions of the wear tracks of 5 N and 15 N load tests were identical to the Raman spectrum collected from the as-deposited coating, indicating that the crystallinity of the coating inside the wear tracks did not change structurally after sliding at both loads. To confirm such hypothesis, thin lamellae were taken from the wear tracks of both loads and subjected to TEM imaging. The TEM results confirmed the results of Raman spectroscopy by revealing that the topmost surfaces of both wear tracks did not contain any well-ordered $MoSe_2$ tribolayers with $MoSe_2$ basal planes perfectly aligned parallel to the sliding direction. Based on these results, the decrease in the coefficient of friction with increasing load observed here cannot be attributed to the formation of a well-ordered $MoSe_2$ tribolayer or an increase in the alignment of $MoSe_2$ basal planes parallel to sliding direction.

Since there were no tribo-induced structural changes in the worn surfaces of the coating during sliding at the two different loads, the difference in the friction behaviour should be strongly related to changes in the sliding counterparts. Meng et al. [224] studied the effect of contact load on the tribological properties of MoS_2 coatings under dry sliding conditions. The coefficient of friction was found to decrease with increasing load. They ascribed this decrease in the coefficient of friction with increasing load to an increase in the formation of a compact MoS_2 transfer layer on its sliding counterpart with increasing load. The same behaviour was observed here. EDS analysis of the ball wear scar of the 5 N load test showed that a transfer layer of the coating was not sufficiently formed on the ball wear scar since only a very small amount of the coating transferred to the ball and concentrated mainly at two edges of the ball wear scar. Consequently, most of the ball surface was not covered by a uniformly distributed $MoSe_2$-rich transfer layer required to impart low interfacial shear between the sliding surfaces. Such behaviour consequently resulted in the highest coefficient of friction, as well as the highest wear rate at 5 N load. On the other hand, EDS analysis showed that almost the whole ball wear scar of the 15 N load test was covered by a uniformly distributed $MoSe_2$-rich transfer layer. The formation of this lubricious transfer layer prevented direct contact between the sliding surfaces and was enough for achieving a stable and low coefficient of friction and decreasing the wear rate of the coating. Therefore, it can be deduced from the present results that the observed decrease in the coefficient of friction and wear rate of the coating with increasing load can be explained by an increase in the formation of a $MoSe_2$ transfer layer on its sliding counterpart with increasing load.

4.3.3 Effect of operating temperature in oil-lubricated sliding

When the coating was tribologically tested in PAO4-lubricated sliding at different temperatures of 25 °C, 40 °C, 60 °C, 80 °C, and 100 °C, its coefficient of friction and wear rate were found to decrease with increasing temperature. It exhibited the highest coefficient of friction and wear rate at the lowest temperature of 25 °C. On the other hand, it exhibited the lowest coefficient of friction and wear rate at the highest temperature of 100 °C. It is obvious from these results that the operating temperature has a significant effect on the frictional properties and wear behaviour of $MoSe_2$ coatings under oil-lubricated conditions.

Kubart et al. [56] studied the effect of operating temperature on the friction behaviour of $MoSe_2$ and MoS_2 coatings under dry sliding conditions. The coefficient of friction of both coatings decreased with increasing temperature up to 100 °C. They attributed this decrease in friction with increasing temperature to the decrease in relative humidity of the atmosphere surrounding the tested coating samples, which eliminated the adverse effect of air humidity in increasing friction. In this study, the wear tracks of the 25 °C and 100 °C temperatures tests were compared and found to have similar features. Both tracks were subjected to EDS analysis, which revealed no indication of oxygen. This was further verified by Raman spectroscopy, which revealed no peaks belonging to MoO_3 in any of the two wear tracks studied. Therefore, the decrease in the coefficient of friction with increasing temperature observed here cannot be attributed to the decrease in relative humidity of the atmosphere surrounding the heated coating sample. This suggests that there is another factor contributing to the observed decrease in friction with increasing temperature. When the ball wear scars from both temperature tests were analysed, a noticeable difference was observed. EDS and Raman analysis of the ball wear scar of the 25 °C temperature test showed that a $MoSe_2$ transfer layer was not sufficiently formed on the wear scar since only a very small amount of $MoSe_2$ material transferred to the ball and was concentrated primarily at two edges of the wear scar. Consequently, most of the ball surface was not covered by a uniformly distributed $MoSe_2$ transfer layer required to impart minimal interfacial shear between the sliding surfaces. As a result, the coefficient of friction and wear rate were the highest at 25 °C. It might also explain the significant level of instability observed in the friction curve at this temperature. On the other hand, EDS analysis and Raman spectroscopy revealed that a considerable amount of $MoSe_2$ material covered a large area of the ball wear scar of the 100 °C temperature test. The formation of this lubricious transfer layer avoided direct contact between the sliding surfaces and resulted in the lowest coefficient of friction and wear rate. Based on these results, the increase in the formation of a $MoSe_2$ transfer layer on the sliding counterpart with increasing temperature was responsible for the observed decrease in the coefficient of friction and wear rate of the coating with increasing temperature.

4.4 Summary

In this chapter, the tribological properties of $MoSe_2$ coating were evaluated under dry and PAO4-lubricated sliding conditions using the TE77 reciprocating tribometer. To study the effect of applied load and operating temperature on its tribological properties in PAO-

lubricated sliding, the coating was also tribologically tested at different loads and temperatures. The most important findings, which can be drawn from the experimental results are as follows:

1. In PAO4-lubricated sliding, the coating exhibited a high coefficient of friction, which was one time higher than the one obtained in dry sliding. The characterisation of the coating wear track showed that a low-friction $MoSe_2$ tribolayer, which is known to be crucial for the low-friction mechanism of this type of coatings, was not formed. Furthermore, the formation of a beneficial transfer layer on the sliding counterpart was prohibited. Both factors contributed to the observed higher coefficient of friction when compared to dry sliding.

2. In contrast to the friction result, the coating showed better wear resistance in PAO4-lubricated sliding, with a wear rate that was 27% lower than that obtained in dry sliding. This improvement in the coating's wear resistance was due to the presence of PAO4 at the sliding interface, which acted as a sealant and protected the coating against oxidation.

3. In dry sliding, the excellent friction performance was a result of two main factors. Firstly, the formation of a uniform and compact coating transfer layer on the sliding counterpart, thereby effectively blocking direct contact between the sliding surfaces. Secondly, the presence of a crystalline $MoSe_2$ tribolayer in the topmost surface of the wear track with a superficial alignment of the basal planes parallel to the sliding direction, leading to a low interfacial shear strength at the sliding interface. These two factors together resulted in the lower coefficient of friction when compared to PAO4-lubricated sliding.

4. In dry sliding, the coating inevitably oxidised, resulting in the formation of MoO_3 particles. These newly formed particles with abrasive properties deteriorated the wear resistance of the coating and led to the higher coating wear rate when compared to PAO4-lubricated sliding.

5. The coefficient of friction and wear rate of the coating showed a decreasing trend with increasing load or temperature. This decrease in the coefficient of friction and wear rate

was caused by an increase in the formation of a beneficial $MoSe_2$ transfer layer on the sliding counterpart with increasing load or temperature.

Chapter 5: Tribological properties of $MoSe_2$/DLC-W coating under dry and oil-lubricated sliding conditions

5.1 Introduction

In chapter 4, $MoSe_2$ coating showed excessive wear damage under different testing conditions of load and temperature because of its low hardness and poor wear resistance. DLC coatings are used in several industrial applications due to their excellent mechanical properties, low friction, and great wear resistance. As previously discussed in section 2.6.9, fabricating layered structures is one method for improving the mechanical properties and tribological performance of pure TMD coatings. The Combination of DLC and $MoSe_2$ coatings has the great potential to endow $MoSe_2$ coating with excellent mechanical and tribological properties.

In this chapter, $MoSe_2$/DLC-W coating was tribologically evaluated under PAO4-lubricated sliding conditions. For comparative purposes, its tribological performance was also evaluated under dry sliding conditions. This chapter begins by presenting the results obtained from SEM and EDS in order to determine the thickness of the coating. This is followed by a discussion of its mechanical properties measured by nanoindentation and crystalline structure determined by XRD. Following this is a discussion of its frictional properties and wear behaviour evaluated by the TE77 reciprocating tribometer. After tribological testing, the worn surfaces of the coating and its sliding counterpart were analysed using SEM, EDS, and Raman spectroscopy, and the results are presented. Finally, the observed friction and wear mechanisms are discussed in detail.

5.2 Results

5.2.1 Thickness and mechanical properties

SEM and EDS were used to examine the cross-sectional morphology and elemental composition of $MoSe_2$/DLC-W coating, and the results are shown in **Figure 5.1**. The coating has a total thickness of 4 μm and is deposited on a Cr adhesion layer of 1.2 μm in thickness. The top $MoSe_2$ layer is very thin with a thickness of only 0.3 μm, whereas the DLC-W layer is thick with a thickness of 2.5 μm. The interface between these two coating layers is almost indistinguishable. The coating structure is generally compact, and the interfaces between the different layers are tightly bonded without noticeable delamination or peeling.

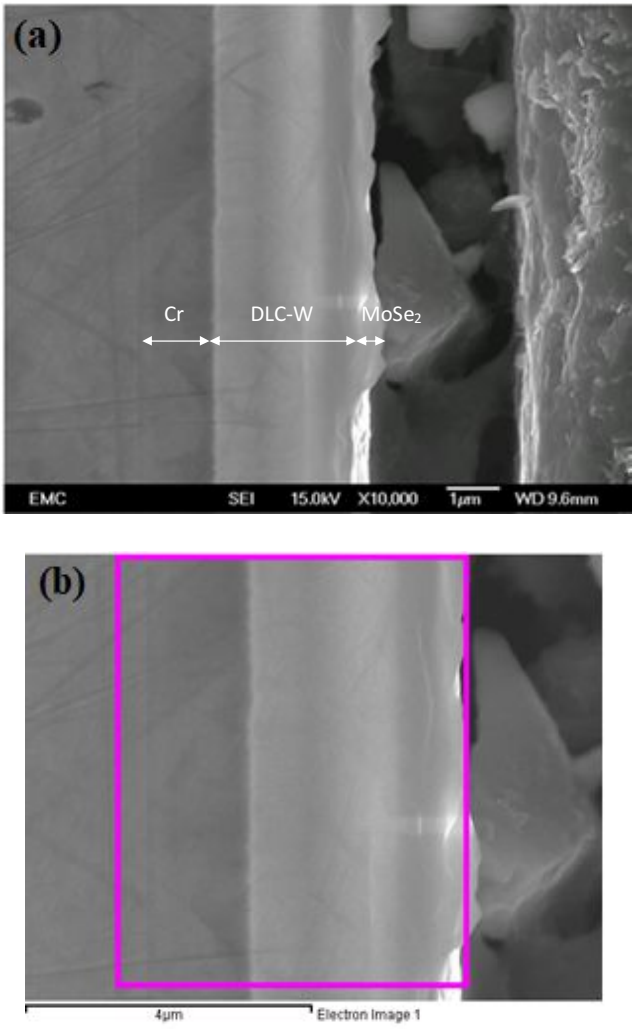

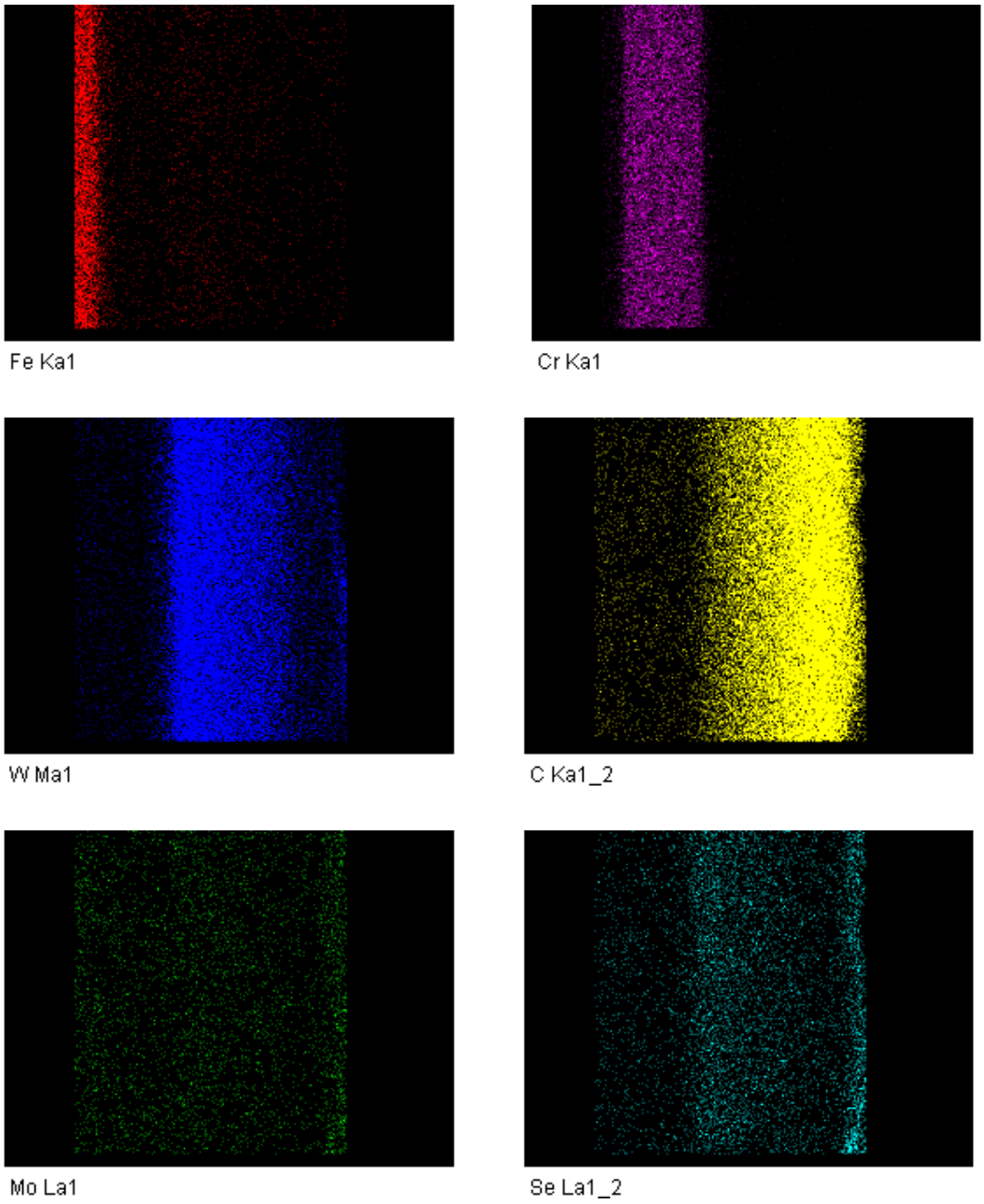

Figure 5.1: (a) SEM image of the prepared cross-section of $MoSe_2$/DLC-W coating and (b) the corresponding EDS analysis of this cross-section.

The mechanical properties of the coating evaluated by nanoindentation are listed in **Table 5.1**. The top $MoSe_2$ layer has hardness of 1.8 ± 0.49 GPa, which is much lower than 14.59 ± 1.38 measured for the DLC-W layer. The addition of the DLC-W layer to the coating structure improves its mechanical properties by increasing the hardness to 3.37 ± 0.25 GPa, which is

higher than that of the top $MoSe_2$ layer. This improvement in the hardness can be ascribed to the presence of the hard DLC-W layer, as well as a hardening effect resulting from several interfaces parallel to the substrate surface [480]. These interfaces enhance the mechanical properties by acting as energy dissipating and crack propagation reducing sites [480,481], making the coating more resistant to plastic deformation. The hardness measured here for $MoSe_2$/DLC-W coating is comparable to those reported in prior studies for Mo-Se-C coating doped with 61 at.% C (3.2 GPa) [392] and Mo-Se-C coating doped with 60 at.% C (3.4 GPa) [232].

Table 5.1: Mechanical properties of $MoSe_2$/DLC-W coating and its individual layers.

	$MoSe_2$ layer	**DLC-W layer**	**Whole coating**
***H* (GPa)**	1.8 ± 0.49	14.59 ± 1.38	3.37 ± 0.25
***E′* (GPa)**	57.2 ± 8.73	124.56 ± 6.81	124.25 ± 6.33

5.2.2 Crystalline structure

GI-XRD was performed in order to determine the crystalline structure of the coating, and the diffractogram is shown in **Figure 5.2**. The diffraction peaks located at 31.49°, 37.95°, 47.46°, 56.97°, and 65.60° are well corresponding to the crystal planes of (1 0 0), (1 0 3), (1 0 5), (0 0 8), and (2 0 0), respectively, which coincide with the hexagonal $MoSe_2$ crystal structure (ICDD card No. 00-017-0887). The diffraction peak assigned to (0 0 2) plane shifts slightly to a lower diffraction angle from 13.74° to 12.21°.This shift suggests a lattice expansion caused by defects such as vacancies, impurities, and dislocations as reported by Dunn et al. [457]. The broad peak at approximately 37.95° is highly asymmetric with a long tail toward higher angles, which is a typical feature of sputtered TMD coatings [175,185,226,392,458-461]. According to Weise et al. [461], this peak corresponds to a turbostrating stacking of (10L) $MoSe_2$ planes, with L having values of 0, 1, 2, 3, etc. This turbostrating stacking of the (10L) planes is caused by the weak bonding between the Se-Mo-Se layers in the $MoSe_2$ structure and can be described by a 2D arrangement of the basal planes with a dimension of several tens of unit cells [461].

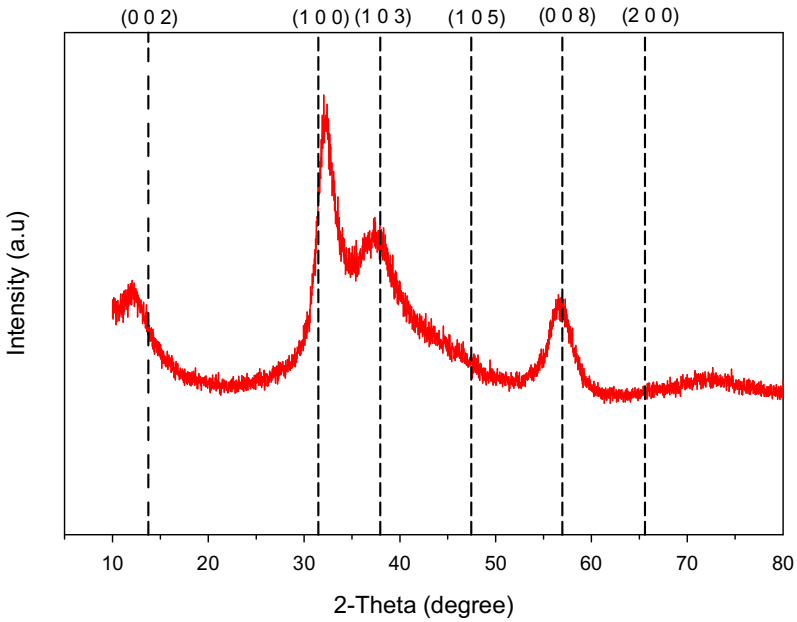

Figure 5.2: GI-XRD diffractogram of $MoSe_2$/DLC-W coating and standard diffraction lines from (ICDD card No. 00-017-0887).

5.2.3 Friction performance

Figure 5.3 shows the coefficients of friction of $MoSe_2$/DLC-W coating as a function of sliding time when tested under dry and PAO4-lubricated sliding conditions with a variation of loads from 10 N to 50 N. **Figure 5.3 (a)** shows the friction curves obtained at 10 N load, where a clear running-in period is observed, especially for the lubricated sliding test. Under both sliding conditions, the coefficient of friction showed unstable behaviour and was accompanied by noticeable and large fluctuations throughout the test duration. **Figure 5.3 (b)** shows the friction curves obtained at 20 N load. This load resulted in a shorter running-in period and less fluctuations in the friction curves when compared to those of the 10 N load. **Figure 5.3 (c)** shows the friction curves obtained at 30 N load. The lubricated sliding test exhibited a short running-in period, and no fluctuations in the friction curve can be observed. There was no clear running-in period seen in the friction curve of the dry sliding test. However, fluctuations can be observed after about 12 minutes of sliding. **Figure 5.3 (d)** shows the friction curves obtained at 40 N load. A very short running-in period was observed for the lubricated sliding test, and the coefficient of friction quickly reached a stabilised low level and remained steady until the end of the test. A different frictional behaviour was observed in dry sliding where the coating

initially exhibited a low and stable coefficient of friction of 0.02. However, after three minutes of sliding, it drastically fluctuated and steeply increased, reaching a value close to 0.35 at the end of the test. **Figure 5.3 (e)** shows the friction curves obtained at 50 N load, where no running-in period was observed for either of the sliding conditions. During the lubricated sliding test, a steady-state friction behaviour was observed throughout the sliding duration. At the beginning of the dry sliding test, the coefficient of friction was quite low; however, after 7.5 minutes of sliding, high fluctuations were observed in the friction curve, and the coefficient of friction rapidly rose to a value higher than 0.6, indicating potential failure of the coating.

Different running-in durations were observed for different loads. The running-in period was longer for lower loads up to 30 N, and the coefficient of friction decreased monotonically until it reached a low steady-state level. When subjected to higher loads of 40 N and 50 N, the running-in period was extremely short, and the coefficient of friction was less noisy and reached a stabilised steady-state level faster than that of the lower load. The observed decrease in the coefficient of friction and the increase in the friction stability with increasing load have also been reported for Mo-Se-C coatings [232,320], Mo-Se-N coatings [226], Mo-S-N coatings [466], and W-S-C coatings [314] when tested at different loads under dry sliding conditions.

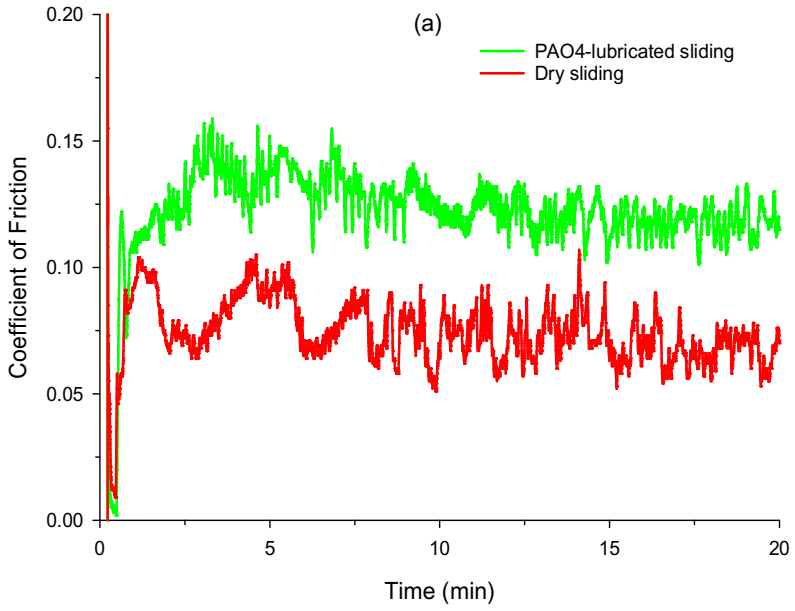

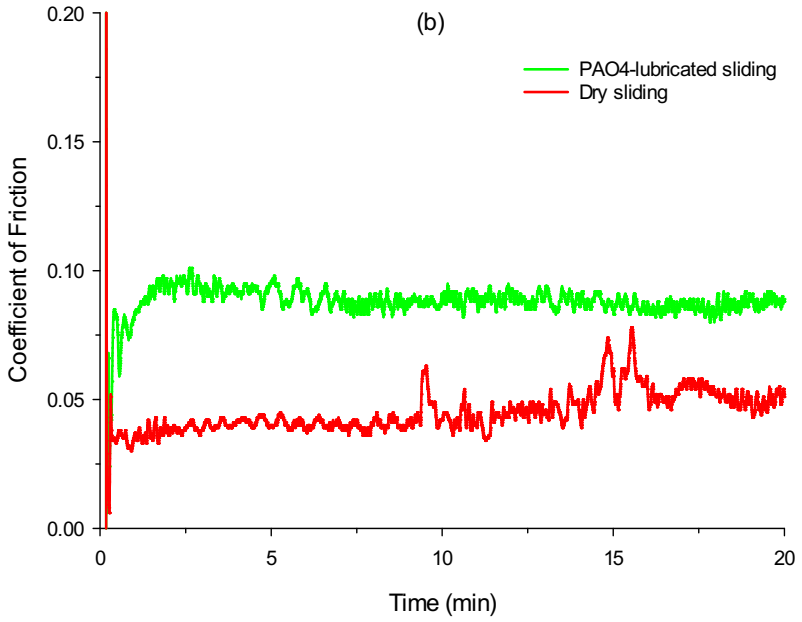
(b)
PAO4-lubricated sliding
Dry sliding
Coefficient of Friction
0.20
0.15
0.10
0.05
0.00
0
5
10
15
20
Time (min)

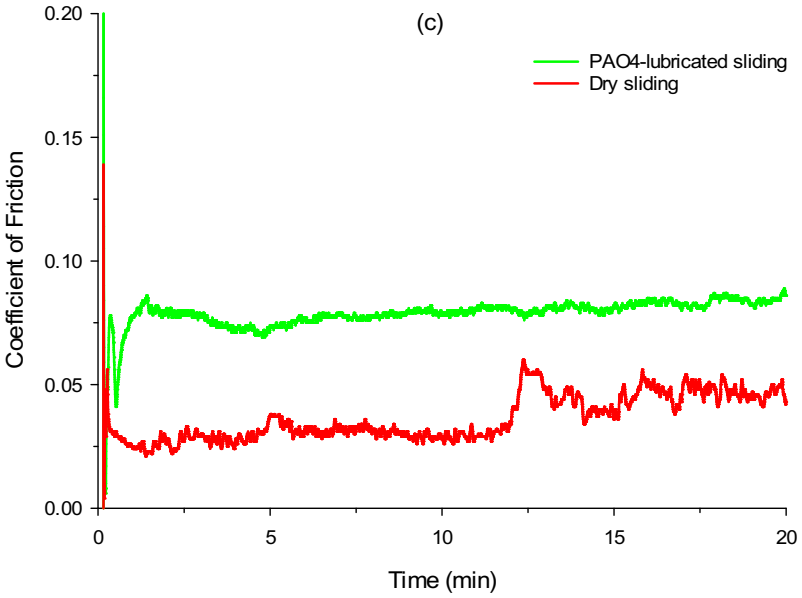
(c)
PAO4-lubricated sliding
Dry sliding
Coefficient of Friction
0.20
0.15
0.10
0.05
0.00
0
5
10
15
20
Time (min)

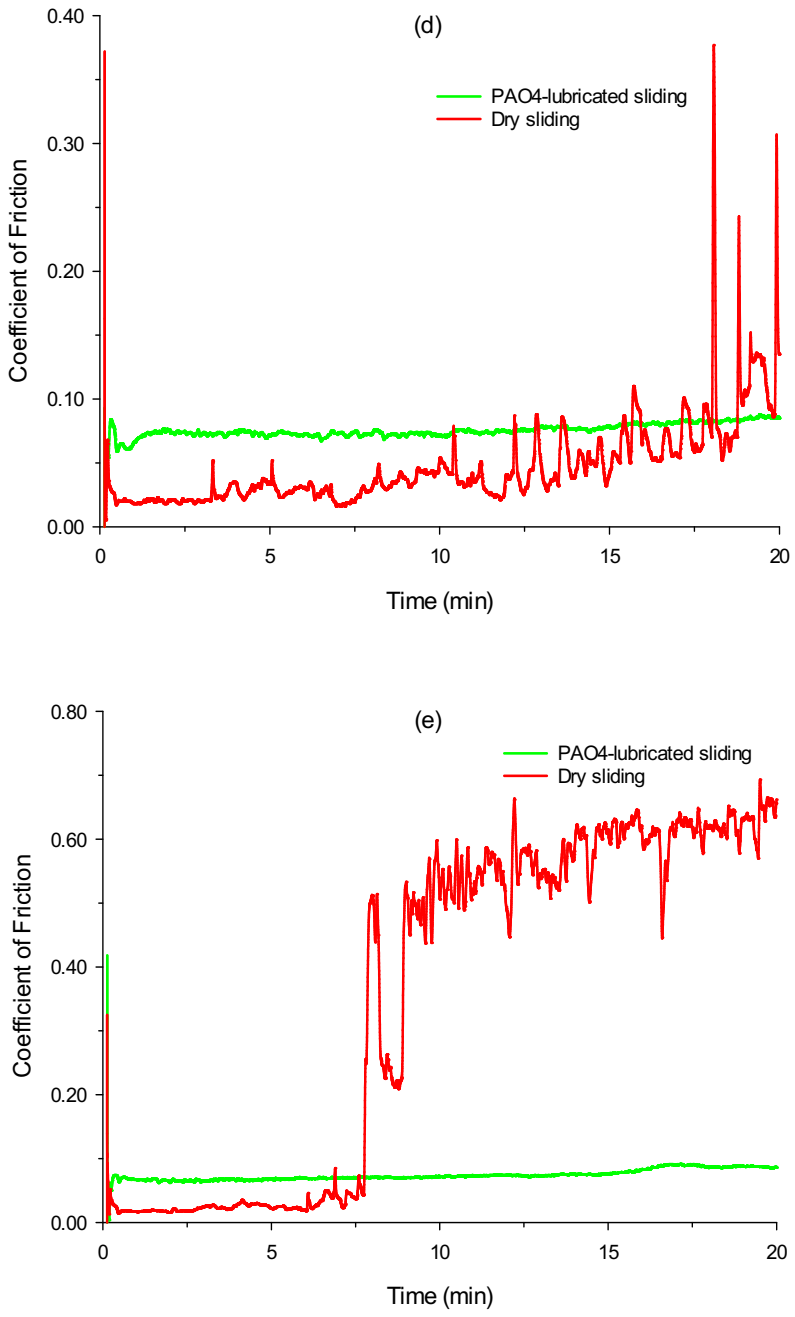

Figure 5.3: Coefficients of friction of $MoSe_2$/DLC-W coating as a function of sliding time when tested in dry and PAO4-lubricated sliding at different loads: (a) 10 N, (b) 20 N, (c) 30 N, (d) 40 N, and (e) 50 N. (Test conditions: counterparts: AISI 52100 steel balls; relative humidity: 40-50%; temperature: 25 °C).

Figure 5.4 presents the average coefficients of friction of the coating from the entire tests. Under both sliding conditions, the coefficient of friction showed a decreasing trend with increasing applied load. This reduction of the coefficient of friction with increasing load of the currently studied coating is very similar to the frictional behaviour of pure TMD coatings [224,226-228,482,483], doped TMD coatings [214,314,465,484-486], and layered coating structures based on TMD coatings [487-489] when tribologically tested at different loads under dry sliding conditions.

In PAO4-lubricated sliding, the coefficient of friction decreased from 0.12 to 0.075 when the load was increased from 10 N to 20 N. When the load was increased to 30 N, the coefficient of friction decreased to 0.064. Increasing the load further to 40 and 50 N resulted in almost the same coefficient of friction of 0.065. When compared to pure $MoSe_2$ coating, the coefficient of friction measured here at 10 N load was higher than 0.081 measured for $MoSe_2$ coating at the same load in chapter 4.

In dry sliding, the coefficient of friction was 0.085 at 10 N load. When the load was increased to 20 N and 30 N, the coefficient of friction dropped to values of 0.055 and 0.045, respectively. Increasing the load further to 40 N resulted in a further decrease in the coefficient of friction to 0.042. The lowest coefficient of friction of 0.025 was achieved at the highest applied load of 50 N without considering the high fluctuations in the friction curve observed after 7.5 minutes of sliding, as shown in **Figure 5.3 (e)**. The average coefficients of friction in the range 0.025-0.085 obtained here at different loads were considerably smaller than those reported for other TMD coating systems tested at comparable dry sliding conditions such as Mo-Se-C coatings with coefficients of friction in the range 0.05-0.2 [43], W-Se-C coatings with coefficients of friction in the range 0.1-0.16 [490], W-S-C coatings with coefficients of friction in the range 0.075-0.2 [312], and Mo-S-C coatings with coefficients of friction in the range 0.05-0.15 [291]. Comparing both sliding conditions, the coefficient of friction obtained here in PAO4-lubricated sliding was 1.4-2.6 times higher than that obtained in dry sliding. Such results imply that dry sliding is more favourable than PAO4-lubricated sliding for the coating to achieve better friction performance.

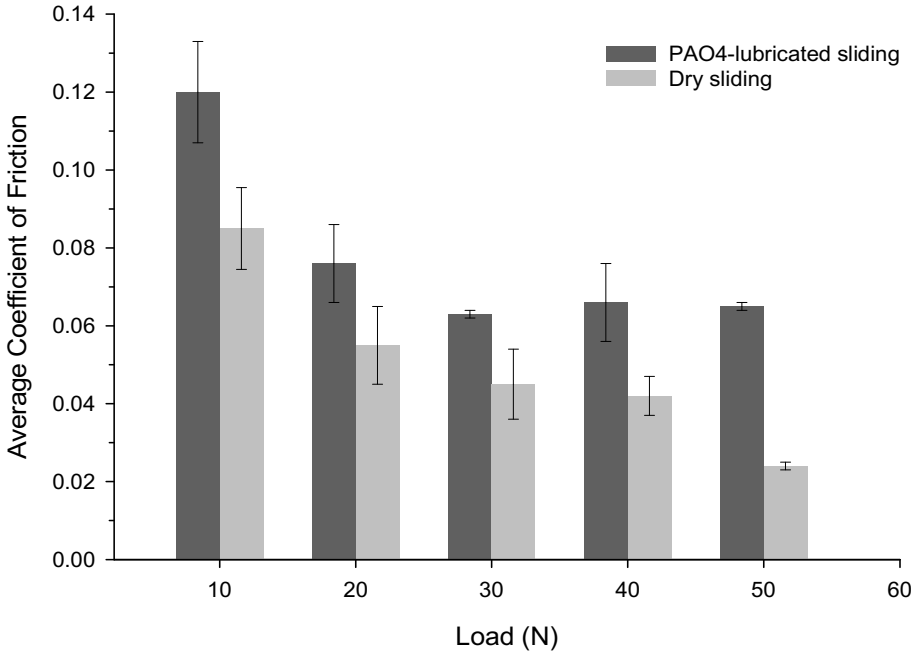

Figure 5.4: Average coefficients of friction of $MoSe_2$/DLC-W coating as a function of applied load tested in dry and PAO4-lubricated sliding. Note that the fluctuations seen in the friction curve after 7.5 minutes of dry sliding at a normal load of 50 N were not included in the measurement of the average coefficient of friction. The error lines correspond to the standard deviation of the mean value.

5.2.4 Wear performance

5.2.4.1 PAO4-lubricated sliding

Figure 5.5 presents the cross-sectional profiles of the wear tracks of the coating tested under PAO4-lubricated sliding conditions at different loads. In each test, the top $MoSe_2$ layer with a thickness of 0.3 m was observed to be worn out, exposing the intermediate DLC-W layer to sliding. The wear depth was observed to increase with increasing load up to 40 N. The lowest wear depth of 0.40 μm was obtained at the lowest load of 10 N. It increased to 0.75 μm when the load was increased to 20 N. Increasing the load further to 30 N resulted in a wear depth of 1.61 μm, which was nearly double that obtained at 20 N. The highest wear depth of 1.75 μm was observed at 40 N load. The situation was different when the applied load was further increased to 50 N. The wear depth measured at this load was 0.05 μm. This indicates the possibility of a transfer layer accumulating on the wear track, which would lower the wear

track depth. Although there was a general tendency for the wear track depth to increase with increasing applied load, the depths of all the wear tracks were still within the thickness of the DLC-W layer. This means that the incorporation of the DLC-W layer was beneficial in providing the coating system with substantial protection against wear and preventing direct contact between the sliding surfaces.

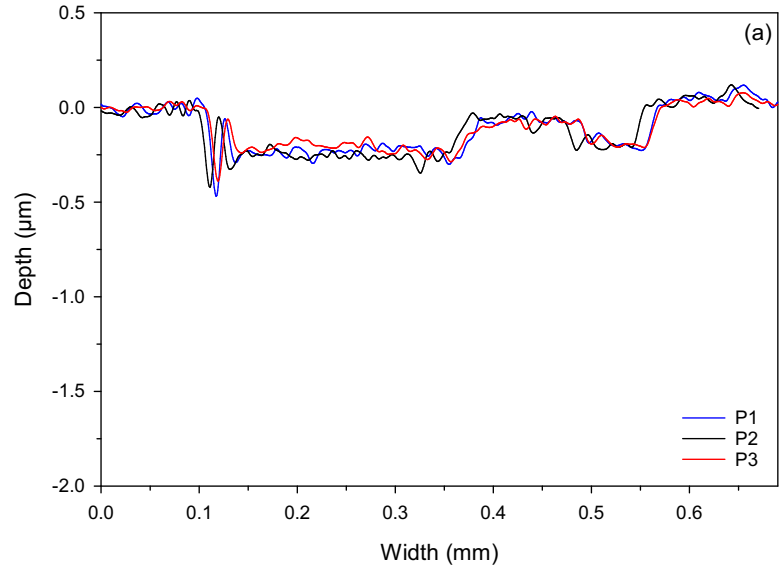

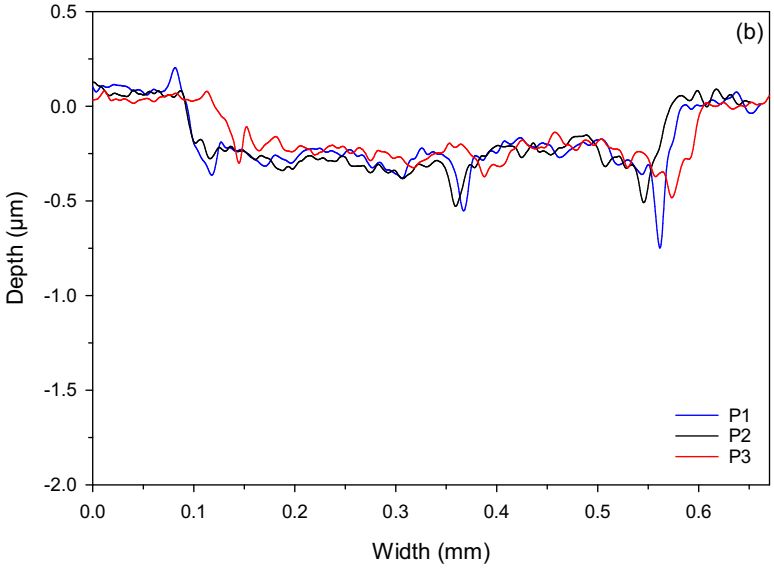

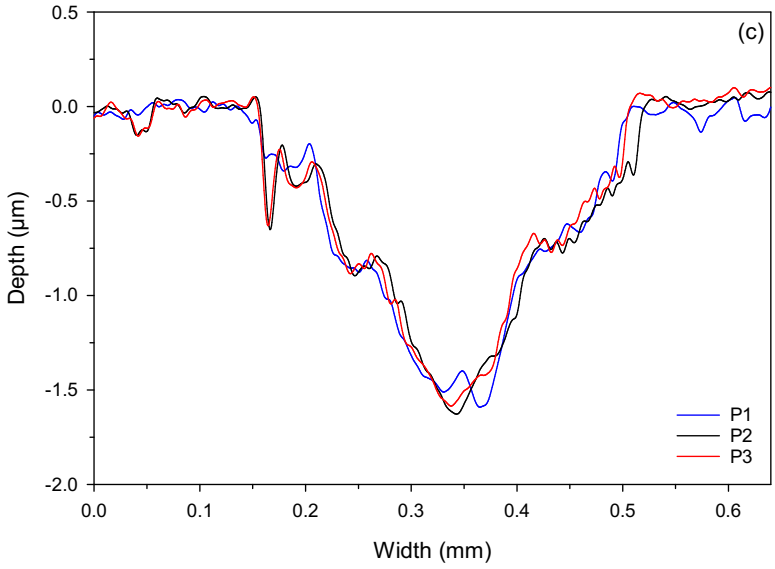
(c)
Depth (μm)
Width (mm)
P1
P2
P3
0.5
0.0
-0.5
-1.0
-1.5
-2.0
0.0
0.1
0.2
0.3
0.4
0.5
0.6

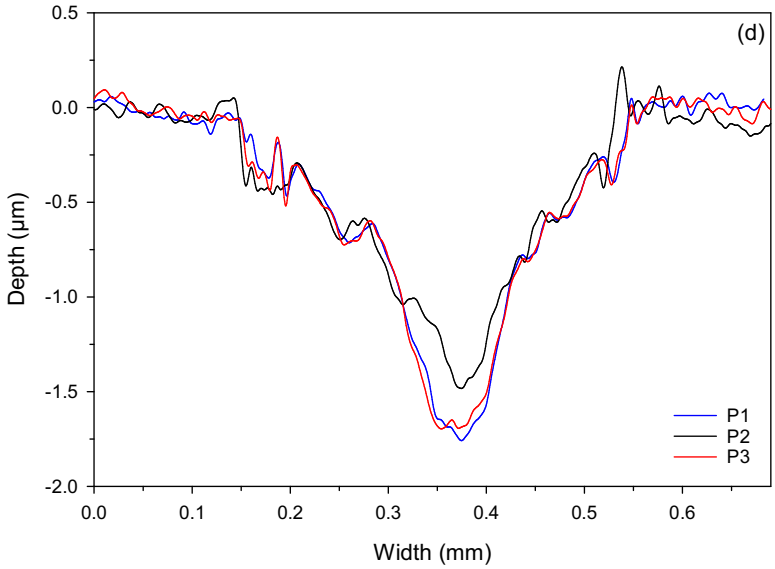
(d)
Depth (μm)
Width (mm)
P1
P2
P3
0.5
0.0
-0.5
-1.0
-1.5
-2.0
0.0
0.1
0.2
0.3
0.4
0.5
0.6

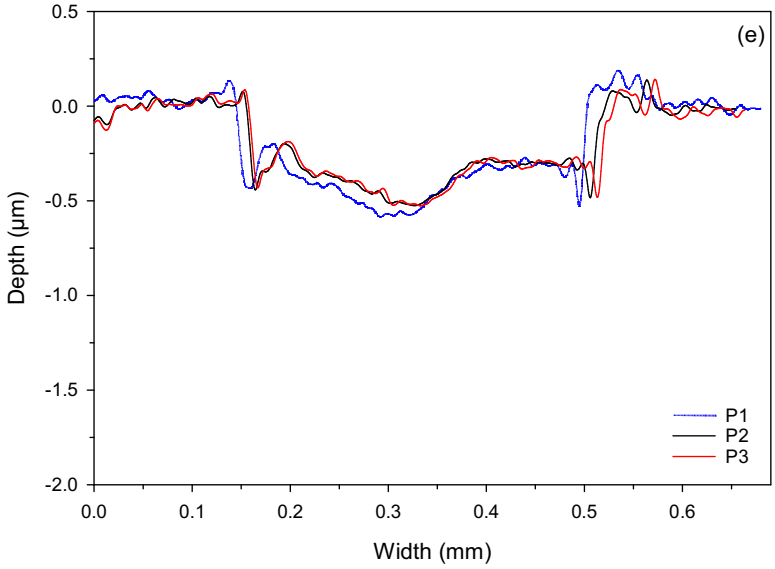

Figure 5.5: Cross-sectional wear track profiles of $MoSe_2$/DLC-W coating tested in PAO4-lubricated sliding at different loads: (a) 10 N, (b) 20 N, (c) 30 N, (d) 40 N, and (e) 50 N. P1 was measured at the centre of wear track, whereas P2 and P3 were measured at its edges.

Figure 5.6 shows the wear rates of the coating and its sliding counterpart tested under PAO4-lubricated sliding conditions at different loads. With the increase in the applied load, the wear rate of the coating generally decreased and followed the same trend as the average coefficient of friction presented in **Figure 5.4**. The minimum wear rate was 0.126 x 10^{-6} mm^3/N.m and obtained at the highest applied load of 50 N. At all the applied loads, the wear rate measured for the steel ball was much lower than that of the coating, indicating that the ball was more resistant to wear.

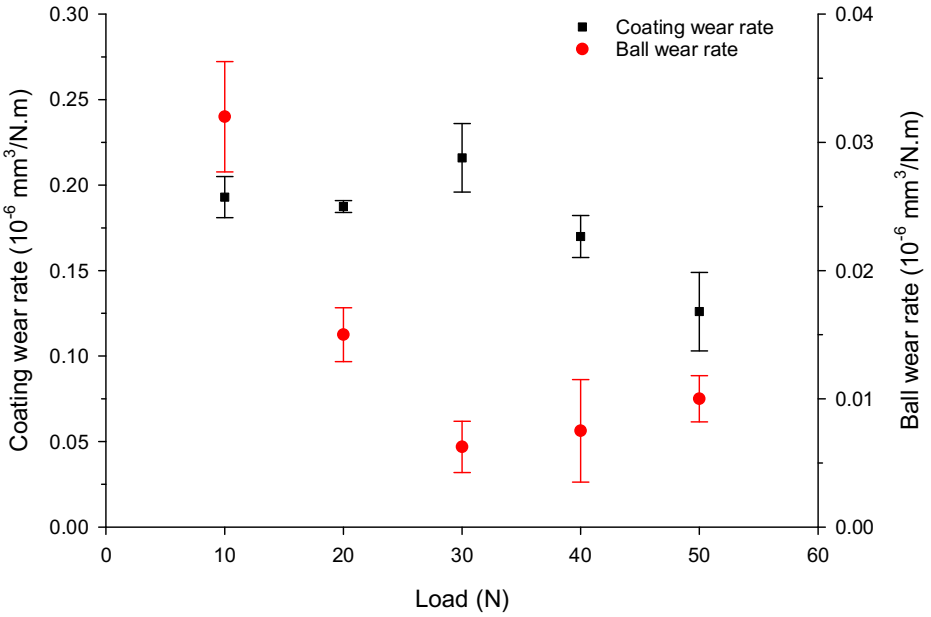

Figure 5.6: Wear rates of $MoSe_2$/DLC-W coating and its sliding counterpart tested at different loads in PAO4-lubricated sliding. The error lines correspond to the standard deviation of the mean value.

5.2.4.2 Dry sliding

Figure 5.7 presents the cross-sectional wear track profiles of the coating tested at different loads under dry sliding conditions. Increasing the applied load resulted in different wear track widths and depths. The wear track depth was observed to increase with increasing load from a minimum of 1.1 µm at 10 N load to a maximum of 4 µm at 50 N load. The wear track width was approximately 0.4 mm for the loads up to 30 N, and then increased to 0.8 mm and 1.6 mm for 40 N and 50 N loads, respectively. As a result, 10 N and 50 N loads resulted in the smallest and highest wear volumes, respectively. For each of the sliding tests, the top $MoSe_2$ layer with a thickness of 0.3 µm was worn out, exposing the intermediate DLC-W layer to sliding. This occurred at loads up to 40 N. However, at the highest applied load of 50 N, the intermediate DLC-W layer and the Cr adhesion layer were both abraded, exposing the steel substrate to sliding. The interactions between the substrate/Cr layer and the steel ball caused the high fluctuations observed in the friction curve shown in **Figure 5.3 (e)**.

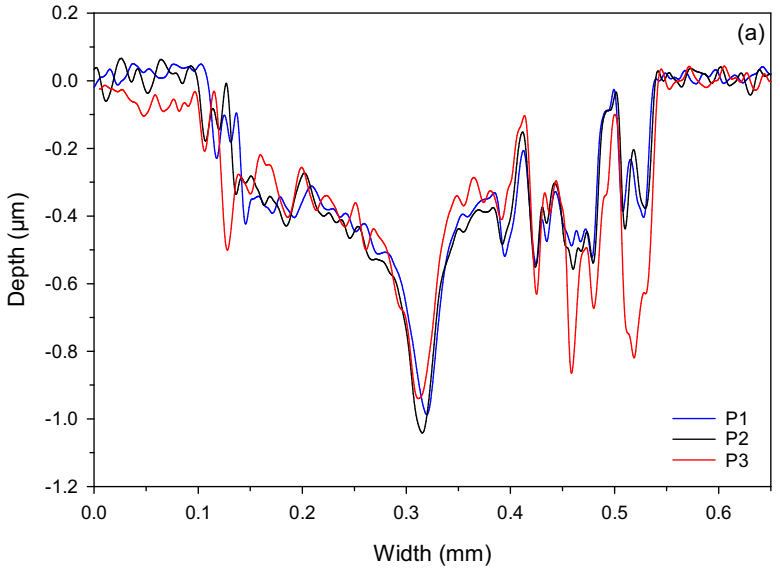
(a)
Depth (μm)
Width (mm)
P1
P2
P3
0.2
0.0
-0.2
-0.4
-0.6
-0.8
-1.0
-1.2
0.0
0.1
0.2
0.3
0.4
0.5
0.6

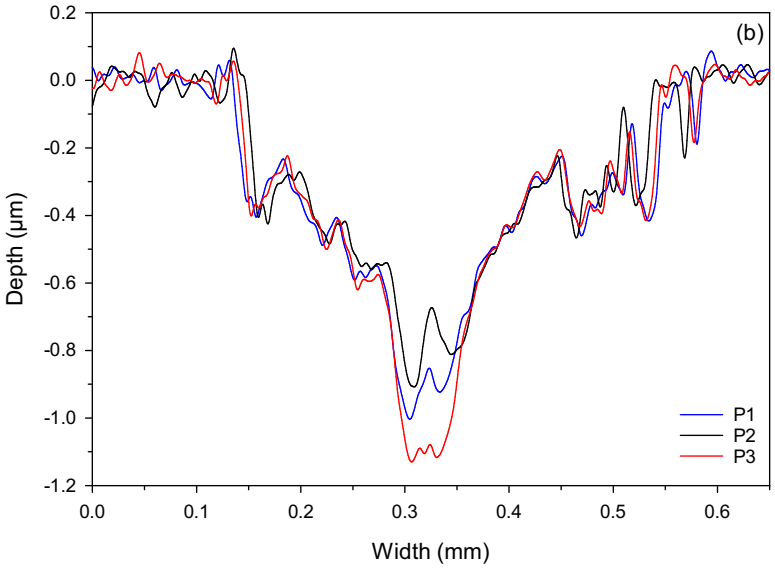
(b)
Depth (μm)
Width (mm)
P1
P2
P3
0.2
0.0
-0.2
-0.4
-0.6
-0.8
-1.0
-1.2
0.0
0.1
0.2
0.3
0.4
0.5
0.6

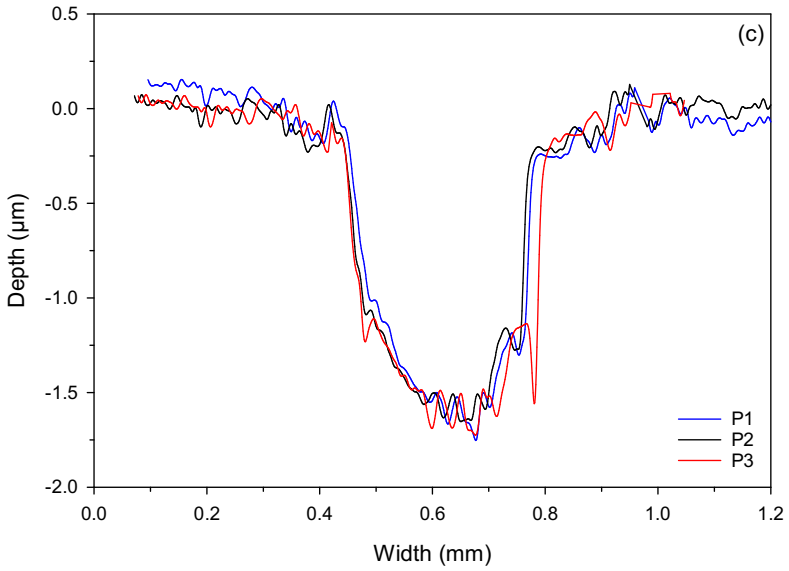
(c)
Depth (μm)
Width (mm)
P1
P2
P3
0.5
0.0
-0.5
-1.0
-1.5
-2.0
0.0
0.2
0.4
0.6
0.8
1.0
1.2

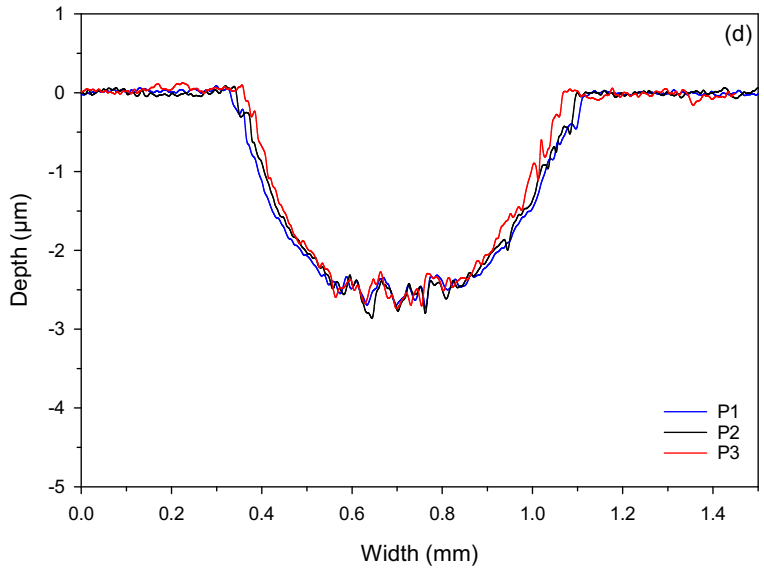
(d)
Depth (μm)
Width (mm)
P1
P2
P3
1
0
-1
-2
-3
-4
-5
0.0
0.2
0.4
0.6
0.8
1.0
1.2
1.4

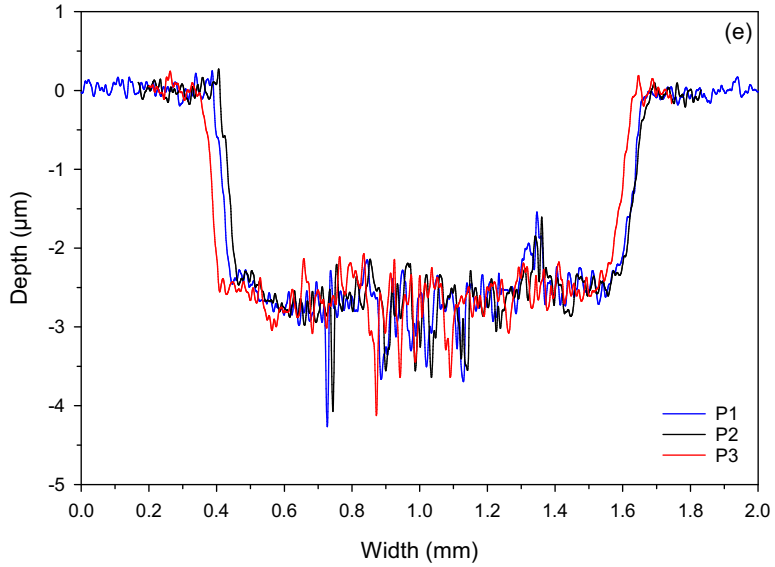

Figure 5.7: Cross-sectional wear track profiles of $MoSe_2$/DLC-W coating tested in dry sliding at different loads: (a) 10 N, (b) 20 N, (c) 30 N, (d) 40 N, and (e) 50 N. Note that there are different scales for the width and depth axes. P1 was measured at the centre of wear track, whereas P2 and P3 were measured at its edges.

Figure 5.8 presents the wear rates of the coating and its sliding counterpart tested under dry sliding conditions at different loads. In contrast to PAO4-lubricated sliding, the wear rate of both sliding surfaces was observed to increase with increasing load up to 40 N. When the load was further increased to 50 N, a complete failure of the coating was observed. This failure caused severe damage to the ball surface and led to the highest wear rate of the ball. In general, the wear rate of the coating was found to be 3-4 times higher than the wear rate of the ball, indicating higher hardness and better wear resistance of the ball.

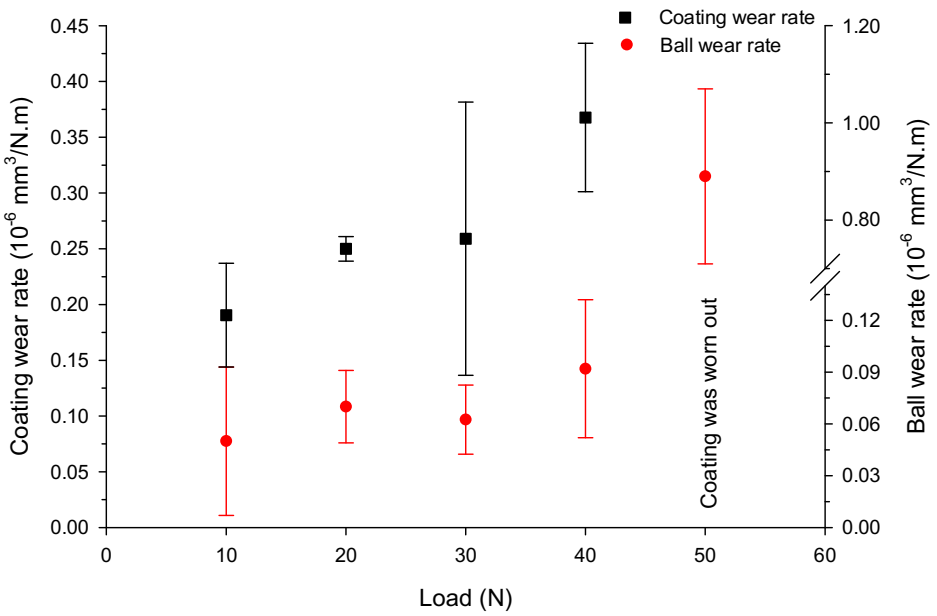

Figure 5.8: Wear rates of $MoSe_2$/DLC-W coating and its sliding counterpart tested at different loads in dry sliding. The error lines correspond to the standard deviation of the mean value.

Figure 5.9 compares the wear rates of the coating obtained under both sliding conditions. For dry sliding, the wear rate of the coating was observed to increase with increasing applied load from 10 N to 40 N. Increasing the load further to 50 N ultimately damaged the coating and exposed the substrate to sliding. For PAO4-lubricated sliding, the wear rate of the coating was observed to increase with increasing load up to 30 N and then decrease until reaching the lowest wear rate at 50 N load. At all the applied loads, the wear rate of the coating obtained in PAO-lubricated sliding was lower than the one obtained in dry sliding. This indicates the positive effect of PAO4 in improving the wear resistance of the coating.

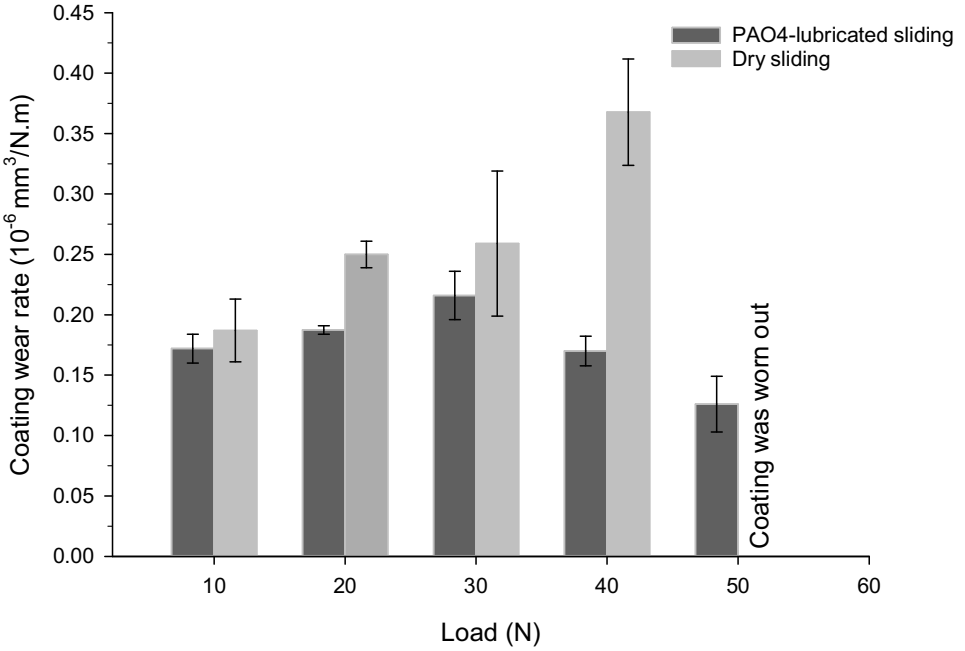

Figure 5.9: Wear rates of $MoSe_2$/DLC-W coating tested at different loads in dry and PAO4-lubricated sliding. The error lines correspond to the standard deviation of the mean value.

5.2.5 Analysis of worn surfaces

5.2.5.1 PAO4-lubricated sliding

Figure 5.10 shows SEM images of the wear tracks of the coating evaluated at different loads under PAO4-lubricated sliding conditions. It is clearly visible that the top $MoSe_2$ layer was subjected to severe wear during sliding at all applied loads, demonstrating that $MoSe_2$ coating in its pure form has a low load-bearing capacity and poor wear resistance. All the wear tracks exhibited scratches and deep ploughing grooves along the direction of sliding, showing that abrasive wear was a major wear mechanism. The severity of this abrasive wear was observed to increase with increasing load due to an increase in the contact pressure, which resulted in more coating material being worn out.

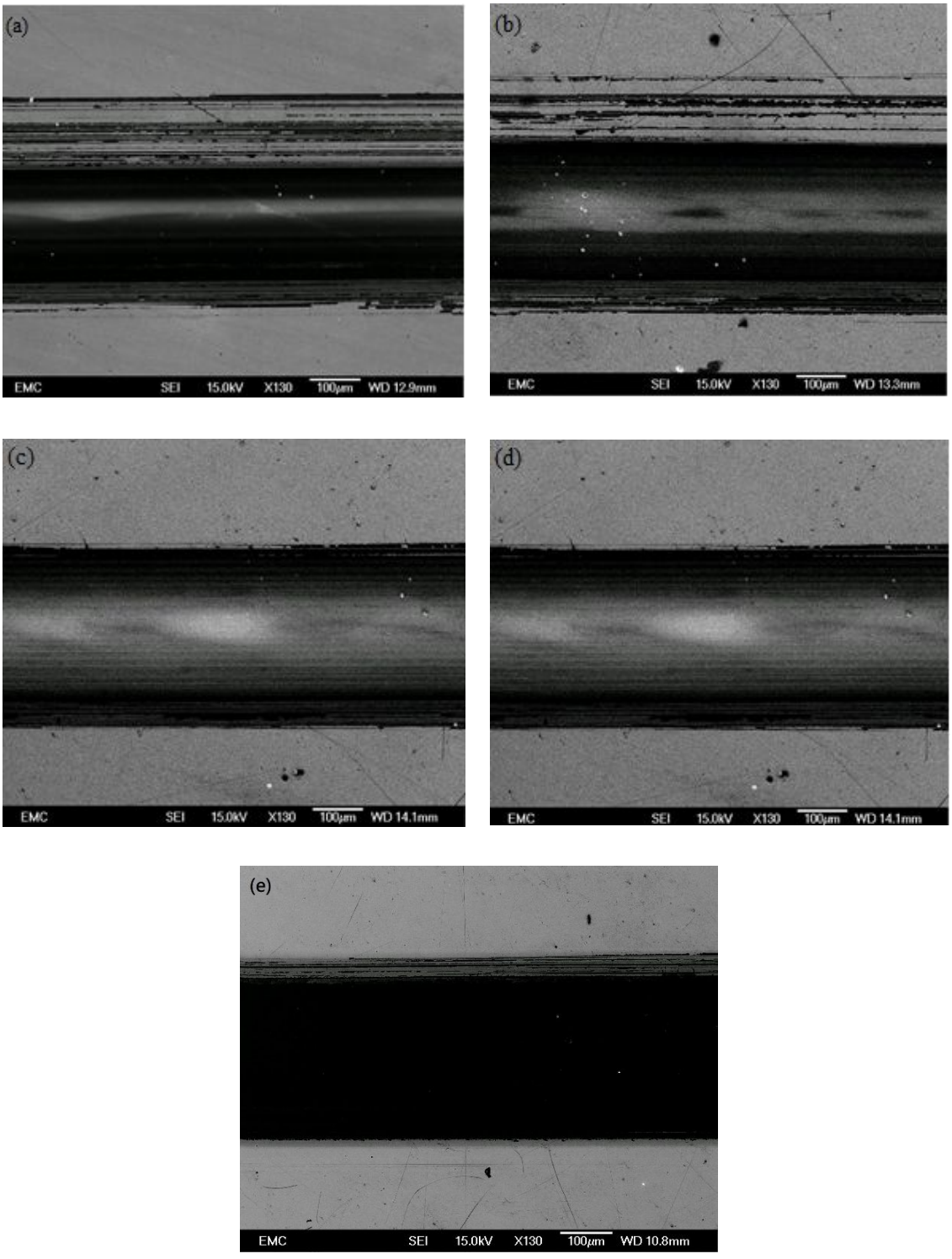

Figure 5.10: SEM images of the wear tracks of $MoSe_2$/DLC-W coating tested in PAO4-lubricated sliding at different loads: (a) 10 N, (b) 20 N, (c) 30 N, (d) 40 N, and (e) 50 N.

Figure 5.11 shows the EDS mapping of the wear track of the coating tested at 10 N load in PAO4-lubricated sliding. This mapping supports and confirms the wear damage seen in the profilometry by revealing a significant difference in the chemical composition between the worn and unworn surfaces of the coating. The mapped area (shown by a yellow rectangle) clearly shows the dominant presence of carbon and tungsten within the wear track, originating from the DLC-W layer, and a depletion of molybdenum and selenium. This indicates severe wear of the top $MoSe_2$ layer and exposure of the DLC-W layer to sliding. No presence of oxygen was observed either inside or outside the wear track. Iron was also not observed, indicating that the incorporation of the DLC-W layer was of a substantial benefit to the coating system by reducing the severity of wear and preventing direct contact between the sliding surfaces.

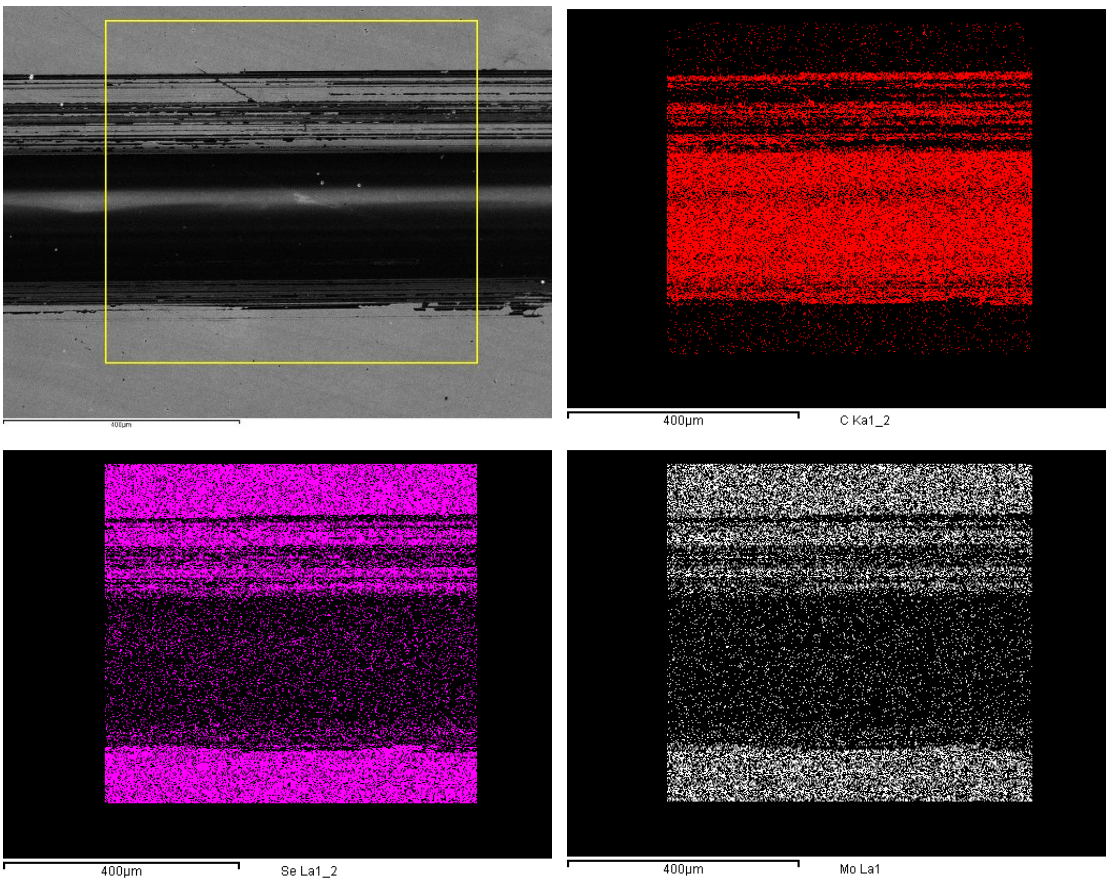

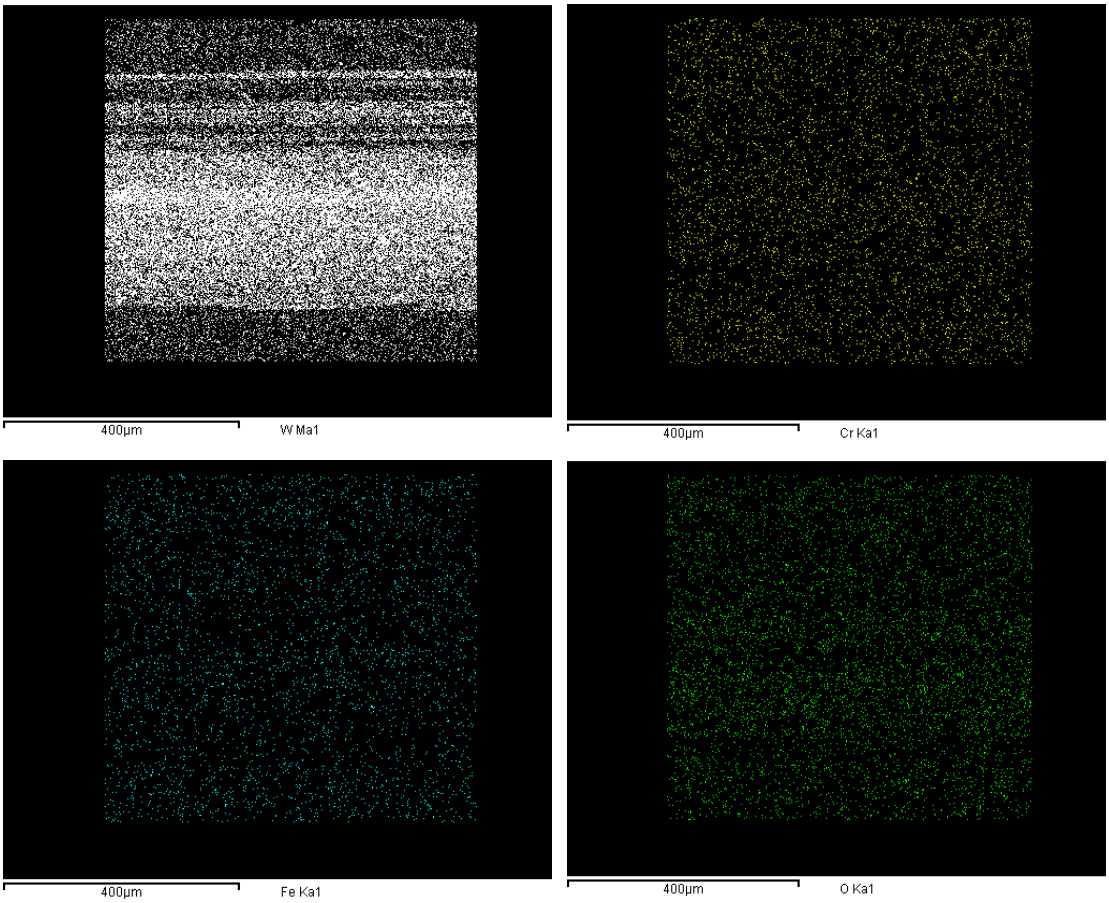

Figure 5.11: EDS mapping of the wear track of $MoSe_2$/DLC-W coating tested at a normal load of 10 N in PAO4-lubricated sliding.

Figure 5.12 shows the Raman spectrum of the as-deposited coating as a reference and the Raman spectra acquired from different positions of the wear track of the coating tested in PAO4-lubricated sliding at 10 N load. The Raman spectrum of the as-deposited coating shows five peaks corresponding to $MoSe_2$ at wavenumbers 155 cm^{-1}, 235 cm^{-1}, 290 cm^{-1}, 443 cm^{-1}, and 596 cm^{-1} [392,471]. It also shows the presence of three broad peaks at wavenumbers 815 cm^{-1}, 860 cm^{-1}, and 940 cm^{-1} belonging to MoO_3 [221,392,473]. The Raman spectra acquired from different positions of the wear track show that the wear track is still covered with $MoSe_2$ material despite the severity of wear. The Raman spectrum acquired from the edge of the wear track (position 1) shows five peaks corresponding to $MoSe_2$ at wavenumbers 155 cm^{-1}, 235 cm^{-1}, 290 cm^{-1}, 443 cm^{-1}, and 596 cm^{-1}. It also shows the presence of three peaks belonging to MoO_3 at wavenumbers 815 cm^{-1}, 860 cm^{-1}, and 940 cm^{-1}, and a broad peak between 1000 cm^{-}

^{1} and 1800 cm^{-1}. This broad peak is a combination of the *G* peak, arising from the bond stretching of sp^2 carbon atoms in aromatic rings and chains, and the *D* peak arising from the breathing modes of sp^2 carbon atoms in aromatic rings only [49,293,379,380]. After deconvolution of this peak using Gaussian peak fitting, the positions of the *D* and *G* peaks are at wavenumbers 1347 cm^{-1} and 1533 cm^{-1}, respectively. Raman analysis shows that the material at position 2 consists mostly of $MoSe_2$ with small amounts of carbon and MoO_3. The Raman spectrum acquired from the centre of the wear track (position 3) shows a peak at wavenumber 860 cm^{-1} belonging to MoO_3, and a broad peak between 1000 cm^{-1} and 1800 cm^{-1}. After deconvolution of this broad peak using Gaussian peak fitting, the positions of the *D* and *G* peaks are at wavenumbers 1332 cm^{-1} and 1533 cm^{-1}, respectively. No peaks corresponding to $MoSe_2$ are observed at the centre of the wear track. It is probable that the high contact pressure at the centre of the wear track resulted in complete removal of the $MoSe_2$ layer and exposure of the DLC-W layer, leading to the absence of $MoSe_2$ peaks and domination of carbon peaks.

According to Ferrari and Robertson [380], a change in the intensity ratio (I_D/I_G) of the *D* and *G* peaks and the *G* peak position can indirectly reflect the relative change of sp^2 and sp^3 bonds. They pointed out that the shift of the *G* peak position to a higher wavenumber and the increase in the (I_D/I_G) ratio are associated with a decreased sp^3 content and an increased sp^2 content. **Table 5.2** lists the (I_D/I_G) ratios and the *G* peak positions of the Raman spectra acquired from the edge and centre of the wear track. It can be seen that the *G* peak position did not change and remained at a constant wavenumber of 1533 cm^{-1} for the two analysed positions. This is an indication that carbon did not undergo any significant change in its bond structure and, consequently, graphitisation of the DLC-W layer did not occur during sliding in PAO4. The I_D/I_G ratio decreased from 0.43 at position 1 to 0.37 at position 3, indicating a higher sp^3 content and an increase of amorphisation at position 3.

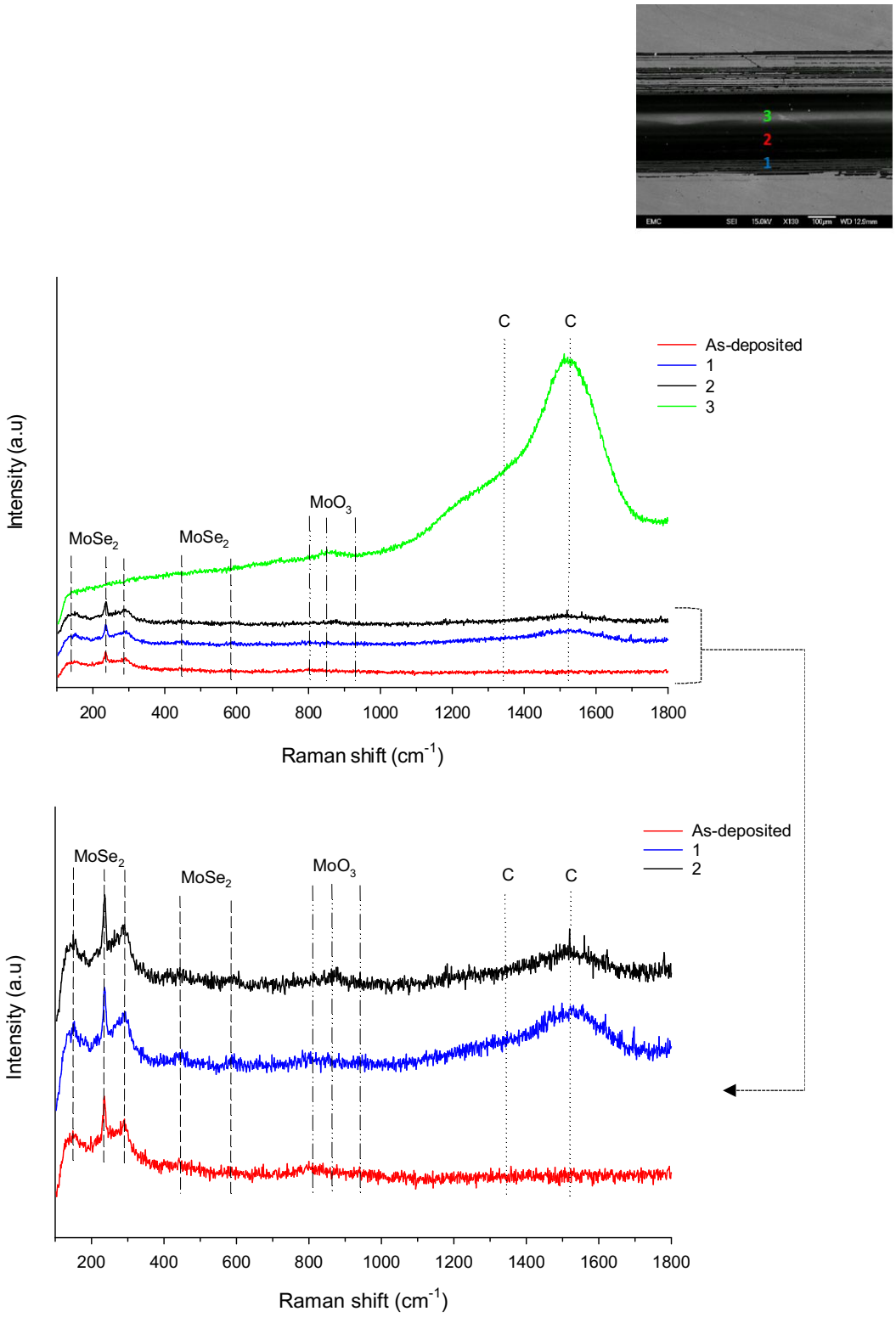

Figure 5.12: Raman spectra acquired from different positions of the wear track of $MoSe_2$/DLC-W coating tested at a normal load of 10 N in PAO4-lubricated sliding.

Table 5.2: I_D/I_G ratios and *G* peak positions of the Raman spectra acquired from the wear track of $MoSe_2$/DLC-W coating tested at a normal load of 10 N in PAO4-lubricated sliding.

Position	I_D/I_G	*G* peak position (cm^{-1})
1	0.43	1533
3	0.37	1533

Figure 5.13 shows SEM images of the ball wear scars tested against the coating in PAO4-lubricated sliding at different loads. The wear scars were circular in shape and exhibited a rough appearance. Several scratches aligned parallel to the sliding direction were observed on all the wear scars, indicating abrasion of the steel balls during sliding at all the applied loads.

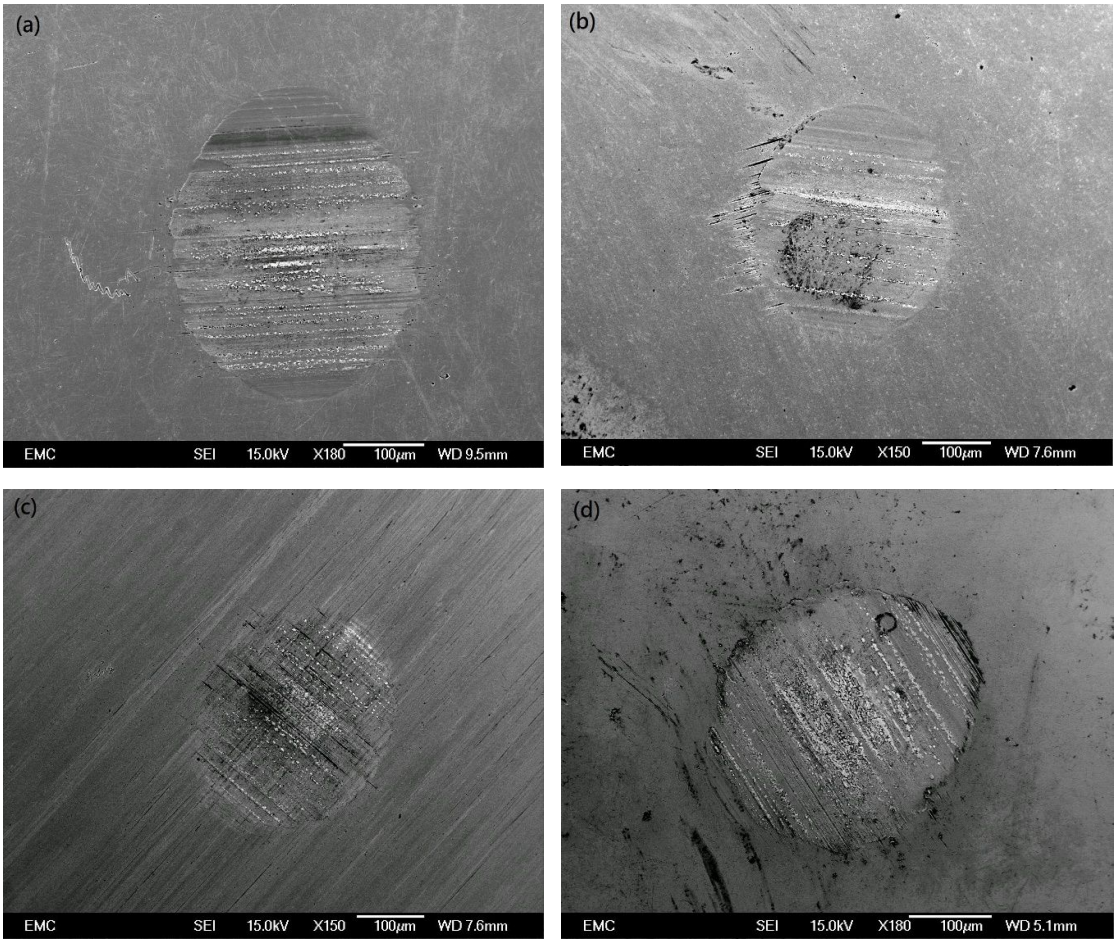

Figure 5.13: SEM images of the ball wear scars tested against $MoSe_2$/DLC-W coating in PAO4-lubricated sliding at different loads: (a) 10 N, (b) 20 N, (c) 30 N, (d) 40 N, and (e) 50 N. Note that the images are at different magnifications.

Figure 5.14 shows the EDS mapping of the ball wear scar tested against the coating at 10 N load in PAO4-lubricated sliding. The mapped area (shown by a yellow rectangle) shows the adherence of some coating material to the ball during sliding, suggesting that adhesive wear was another wear mechanism. The composition of this transfer layer consists of molybdenum, selenium, and tungsten. The top $MoSe_2$ layer was worn out during sliding, followed by the transfer of some of this layer to the ball surface. As the top layer was worn out, the intermediate DLC-W layer was exposed to sliding. This resulted in the transfer of some tungsten from the DLC-W layer to the ball surface. It should be noted that this transfer layer was not uniformly distributed on the ball wear scar, but rather adhered to several scratches along the sliding direction. A reason for this could be the presence of PAO4 at the sliding interface, which acted as a barrier between the coating and its counterpart and prevented the coating material from transferring.

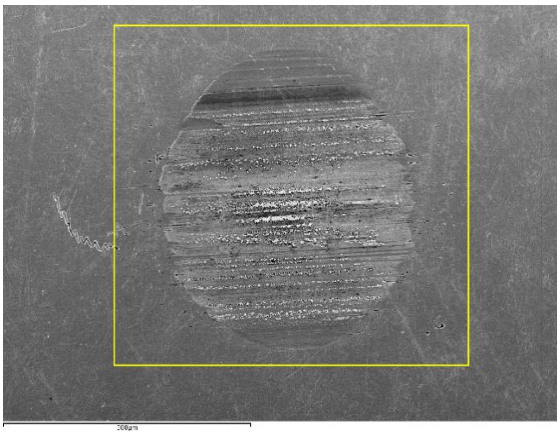

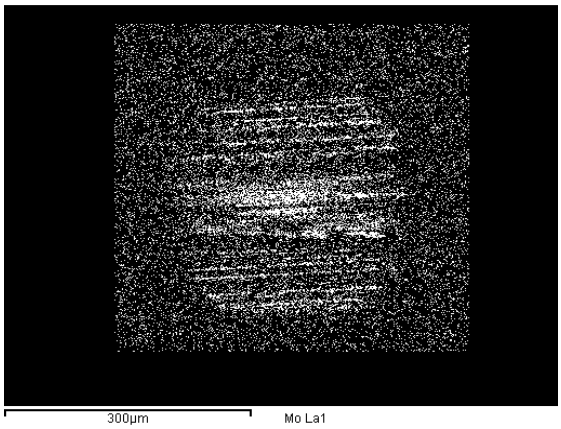
300µm
Mo La1

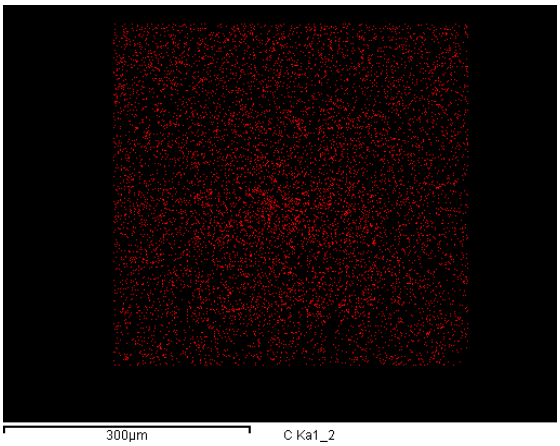
300µm
C Ka1_2

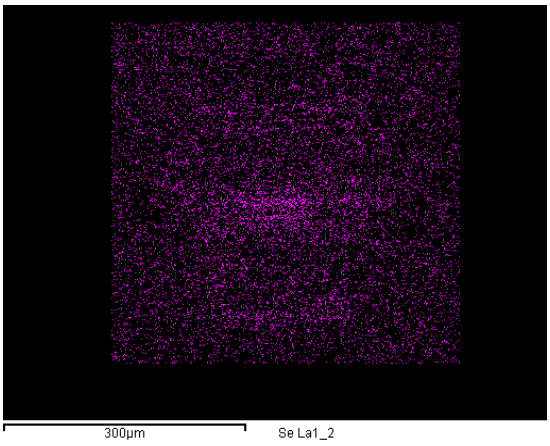
300µm
Se La1_2

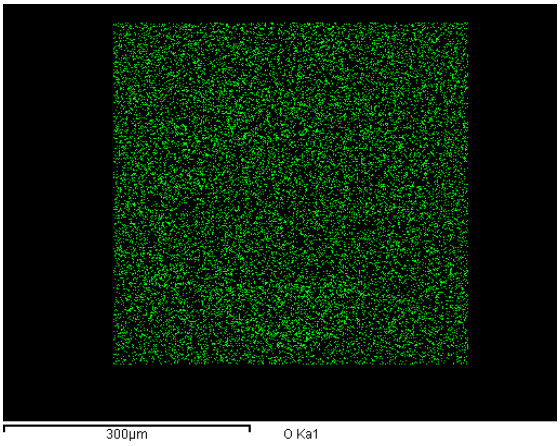
300µm
O Ka1

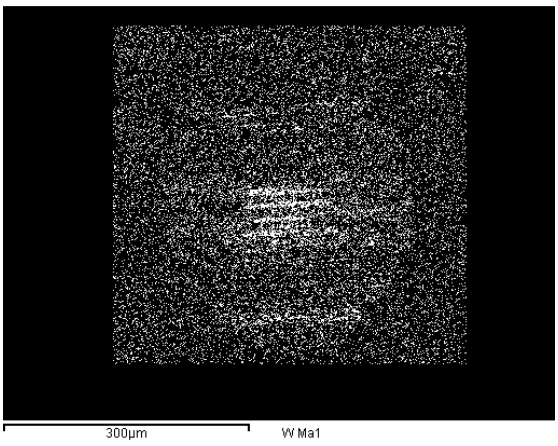
300µm
W Ma1

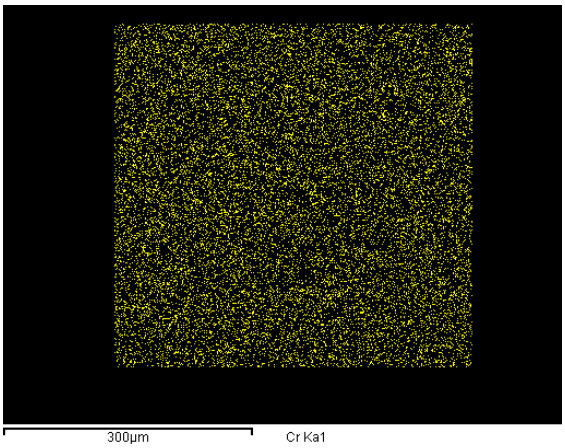

Figure 5.14: EDS mapping of the ball wear scar tested against $MoSe_2$/DLC-W coating at a normal load of 10 N in PAO4-lubricated sliding.

Figure 5.15 shows the Raman spectra acquired from different positions of the ball wear scar tested against the coating at 10 N load in PAO4-lubricated sliding. It can be observed that the Raman spectra acquired from the ball wear scar differ significantly from those acquired from the wear track shown in **Figure 5.12**. Raman analysis reveals very broad and not easily identifiable peaks belonging to $MoSe_2$, MoO_3, and C at the centre of the ball wear scar and position 2. The low intensity of these peaks is a clear indication that only a very small amount of the coating material transferred and adhered to the ball during sliding, further supporting and confirming the results obtained from EDS. Clear peaks of $MoSe_2$ and MoO_3 are observed only at the edge of the wear scar (position 1).

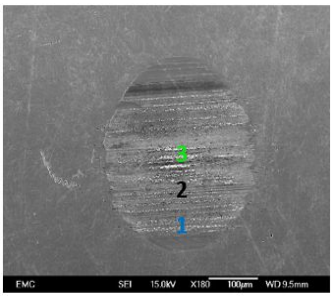

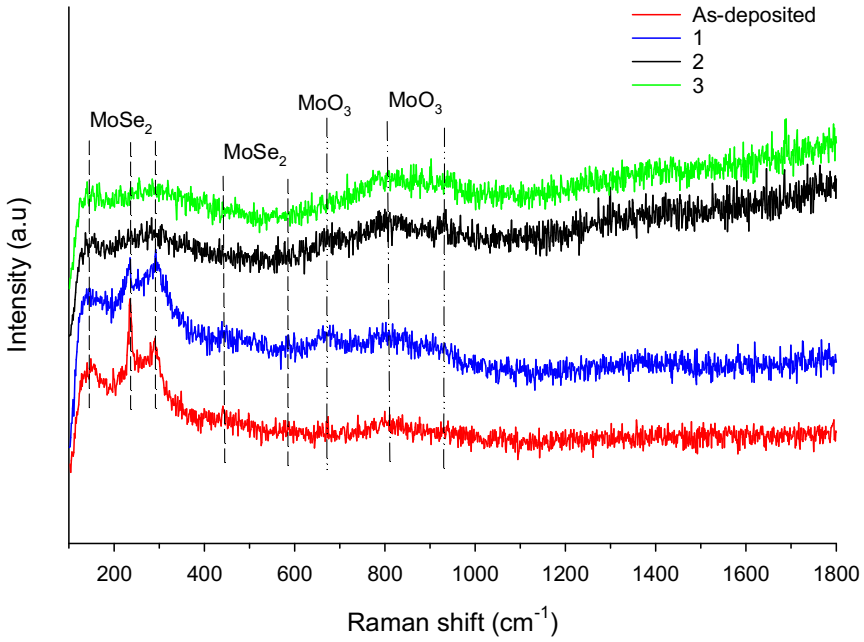

Figure 5.15: Raman spectra acquired from different positions of the ball wear scar tested against $MoSe_2$/DLC-W coating at a normal load of 10 N in PAO4-lubricated sliding.

5.2.5.2 Dry sliding

Figure 5.16 shows SEM images of the wear tracks of the coating tested in dry sliding at different loads. It can be seen that significant abrasive wear occurred at all the applied loads, as evidenced by the presence of multiple scratches and wear grooves parallel to the sliding direction. The degree of this abrasive wear was observed to increase with increasing applied load because of increasing contact pressure.

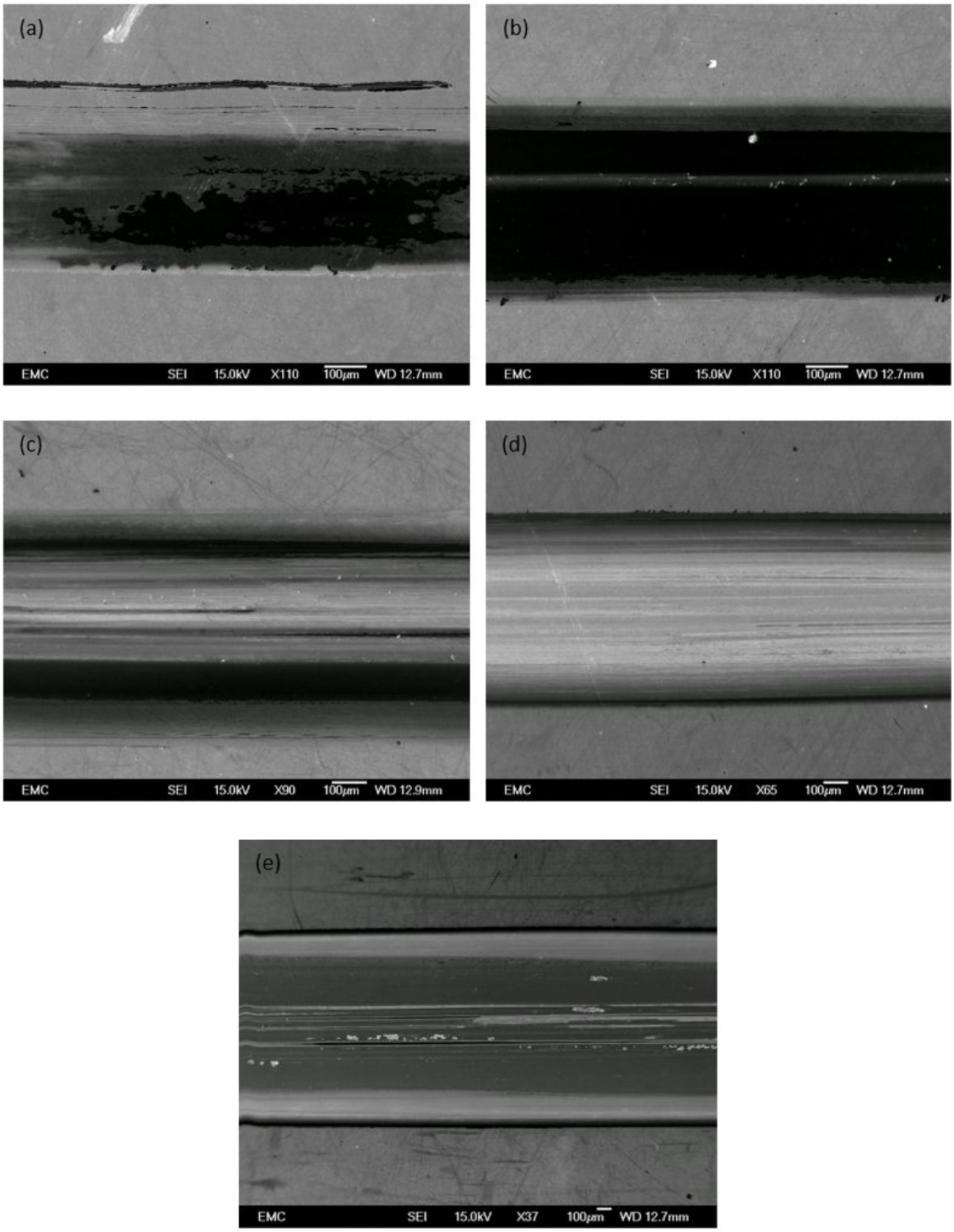

Figure 5.16: SEM images of the wear tracks of $MoSe_2$/DLC-W coating tested in dry sliding at different loads: (a) 10 N, (b) 20 N, (c) 30 N, (d) 40 N, and (e) 50 N. Note that the images are at different magnifications.

Figure 5.17 shows the EDS mapping of the wear track of the coating tested in dry sliding at 10 N load. The mapped area (shown by a yellow rectangle) shows a high concentration of carbon and tungsten within the wear track, originating from the DLC-W layer, and a depletion of molybdenum and selenium as compared to the untested surface of the coating. This indicates that the top $MoSe_2$ layer was severely worn out during sliding, whereas the DLC-W layer reduced the severity of wear and prevented the direct metal-to-metal contact. In contrast to the wear track of the PAO4-lubricated sliding test, the presence of oxygen was also observed inside the wear track. A possible reason for this could be the reaction of the coating material with oxygen in the surrounding atmosphere during sliding, leading to the formation of metal oxides as reaction products.

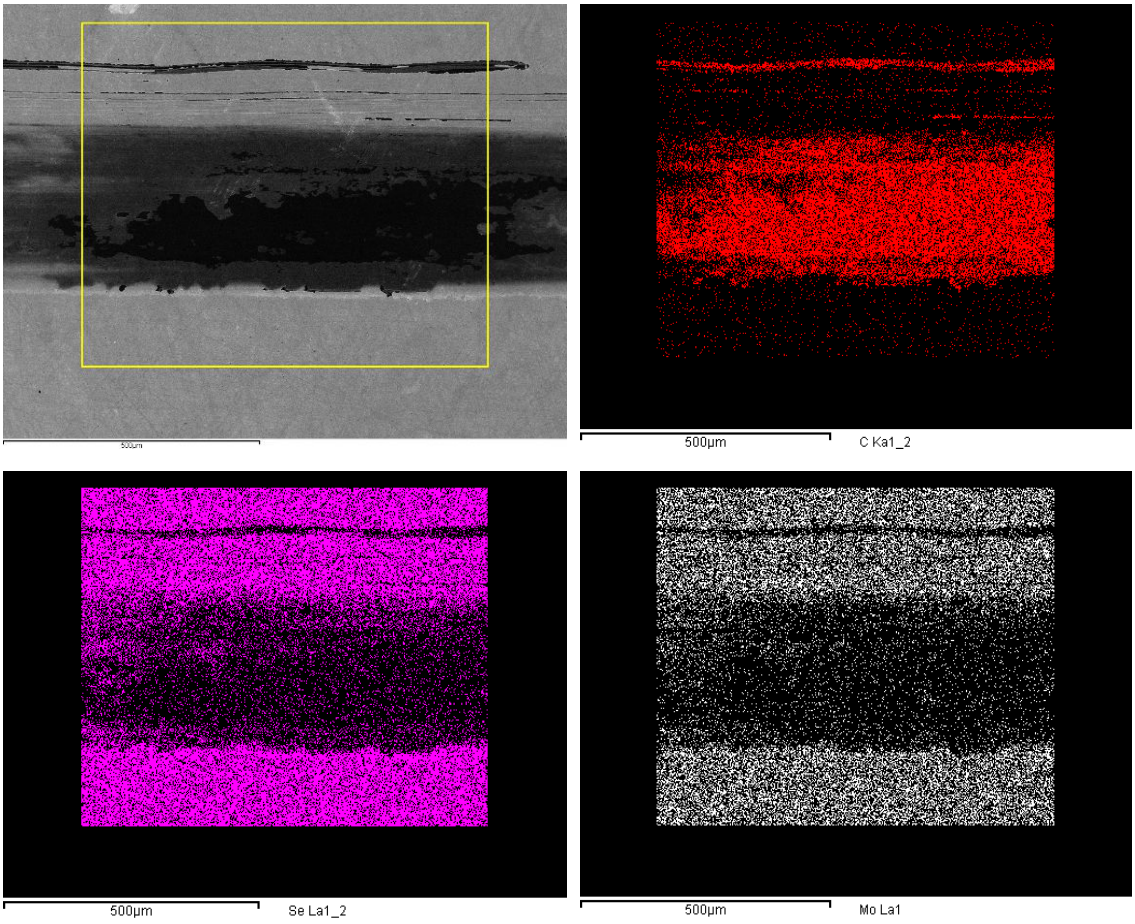

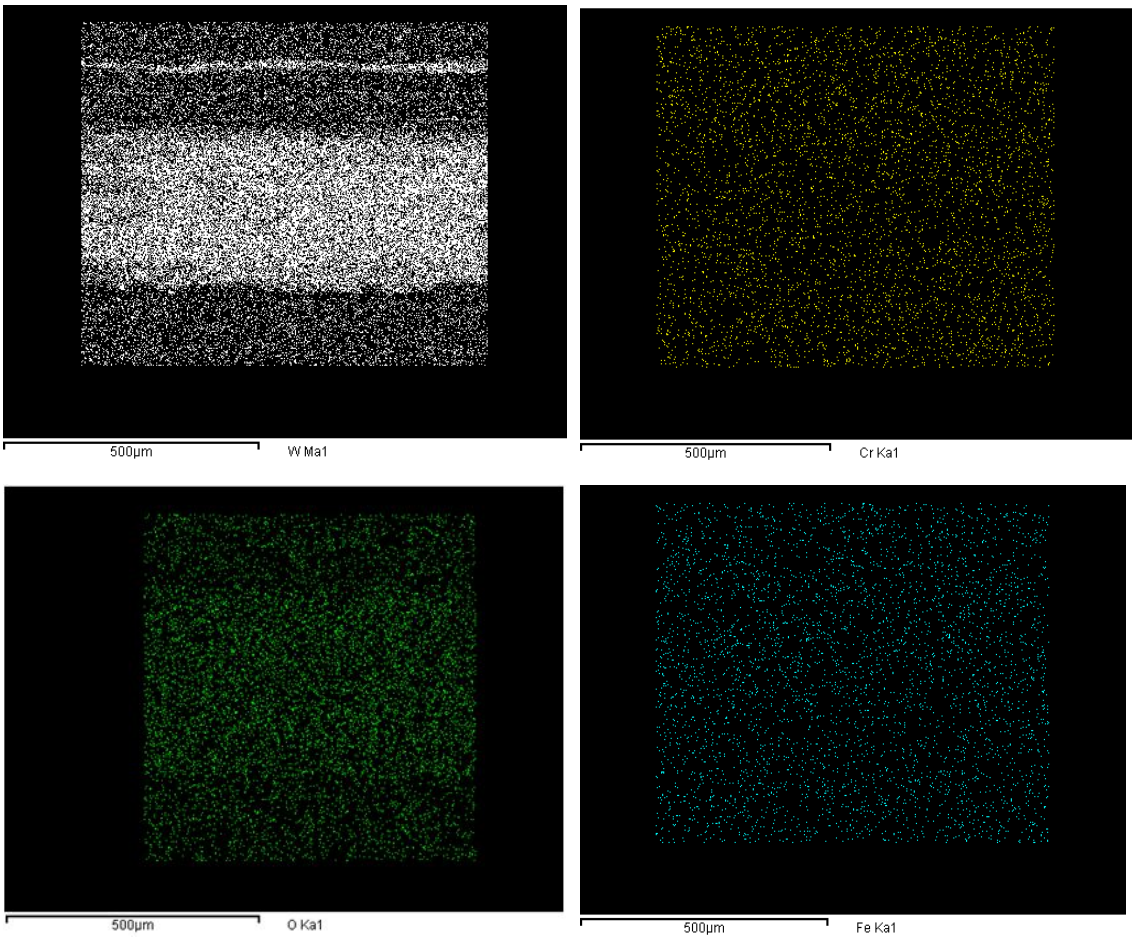

Figure 5.17: EDS mapping of the wear track of $MoSe_2$/DLC-W coating tested at a normal load of 10 N in dry sliding.

Figure 5.18 shows the Raman spectrum of the as-deposited coating as a reference and the Raman spectra acquired from different positions of the wear track of the coating tested at 10 N load in dry sliding. The Raman spectrum of the as-deposited coating shows five peaks corresponding to $MoSe_2$ at wavenumbers 155 cm^{-1}, 235 cm^{-1}, 290 cm^{-1}, 443 cm^{-1}, and 596 cm^{-1} [392,471]. The Raman spectrum acquired from the centre of the wear track (position 3) shows clear peaks between wavenumbers 1000 cm^{-1} and 1800 cm^{-1} corresponding to the *D* and *G* peaks of carbon. There is also a peak at wavenumber 860 cm^{-1} belonging to MoO_3 [392]. No evident peaks of $MoSe_2$ were detected at the centre of the wear track, similar to what was observed at the centre of the wear track of the PAO4-lubricated sliding test. It is likely that the high contact pressure at the centre of the wear track completely removed the $MoSe_2$ layer and exposed the DLC-W layer to sliding. This caused $MoSe_2$ peaks to disappear in the Raman

spectrum. The Raman spectra acquired from positions 1 and 2 show peaks belonging to $MoSe_2$, MoO_3, and C. $MoSe_2$ peaks at position 1 are more intense and sharper than those observed at position 2, indicating a highly ordered structure of $MoSe_2$ material.

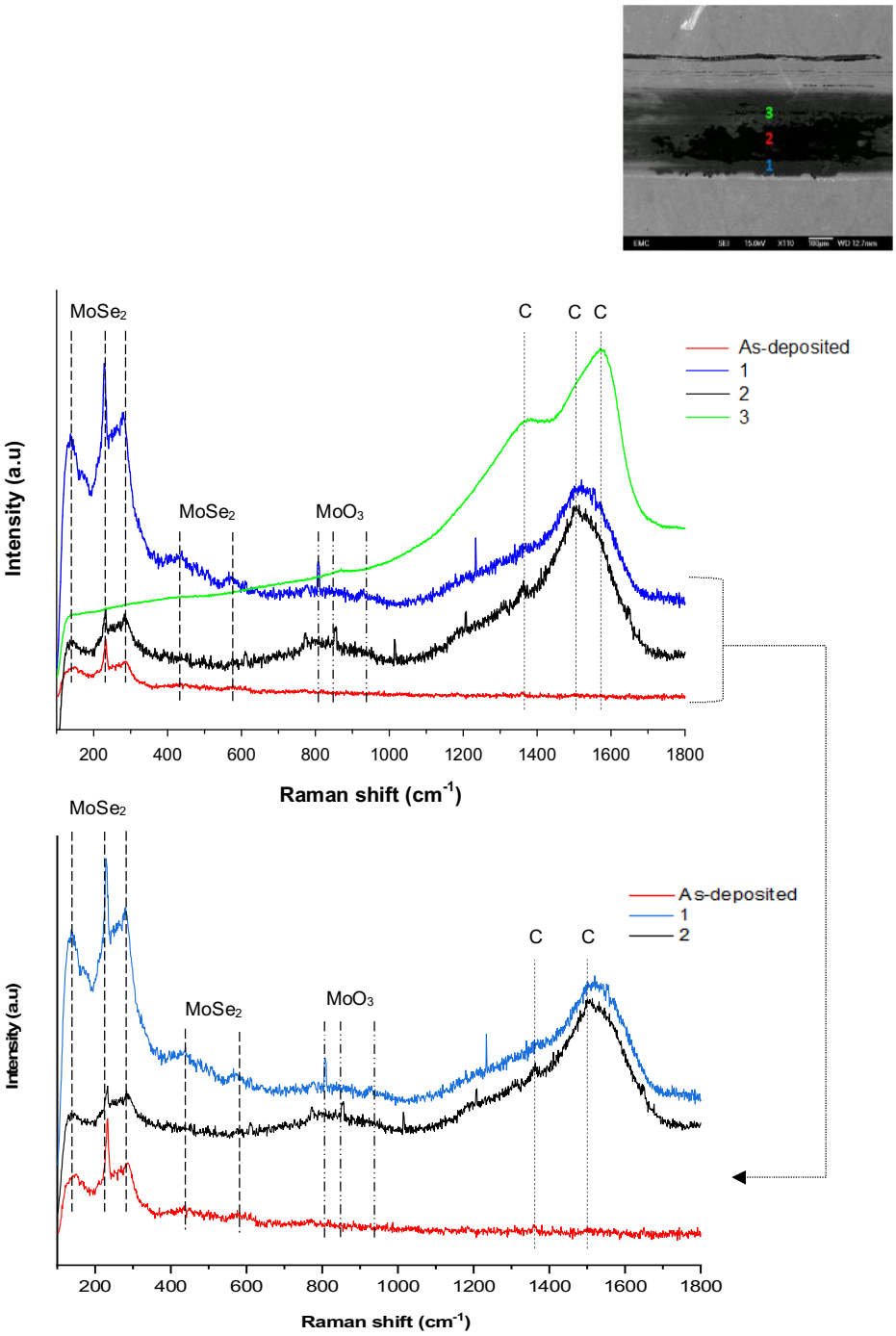

Figure 5.18: Raman spectra acquired from different positions of the wear track of $MoSe_2$/DLC-W coating tested at a normal load of 10 N in dry sliding.

After deconvolution and fitting of the Raman spectra using Gaussian peak fitting, the I_D/I_G ratios and the *G* peak positions are listed in **Table 5.3**. At positions 1 and 2, the *G* peak position remained almost the same, but it shifted noticeably towards a higher wavenumber at position 3. Simultaneously, the I_D/I_G ratio remained almost the same at positions 1 and 2, but it increased to 0.97 at position 3. Due to the amorphous nature of the DLC-W layer, an increase in the I_D/I_G ratio and an upward shift of the *G* peak position suggest ordering and graphitisation of carbon at position 3.

Table 5.3: I_D/I_G ratios and *G* peak positions of the Raman spectra acquired from the wear track of $MoSe_2$/DLC-W coating tested at a normal load of 10 N in dry sliding.

Position	$\boldsymbol{I_D/I_G}$	***G* peak position (cm^{-1})**
1	0.55	1535
2	0.54	1532
3	0.97	1570

Figure 5.19 shows SEM images of the ball wear scars tested against the coating in dry sliding at different applied loads. The wear scars were circular in shape and exhibited a rough appearance. The diameter of the wear scar was observed to increase with increasing applied load due to an increased contact pressure. Several scratches aligned parallel to the sliding direction were observed on some of the wear scars, indicating abrasion of the steel balls during sliding. A clearly noticeable formation of a transfer layer can be seen on the wear scar of 10 N load.

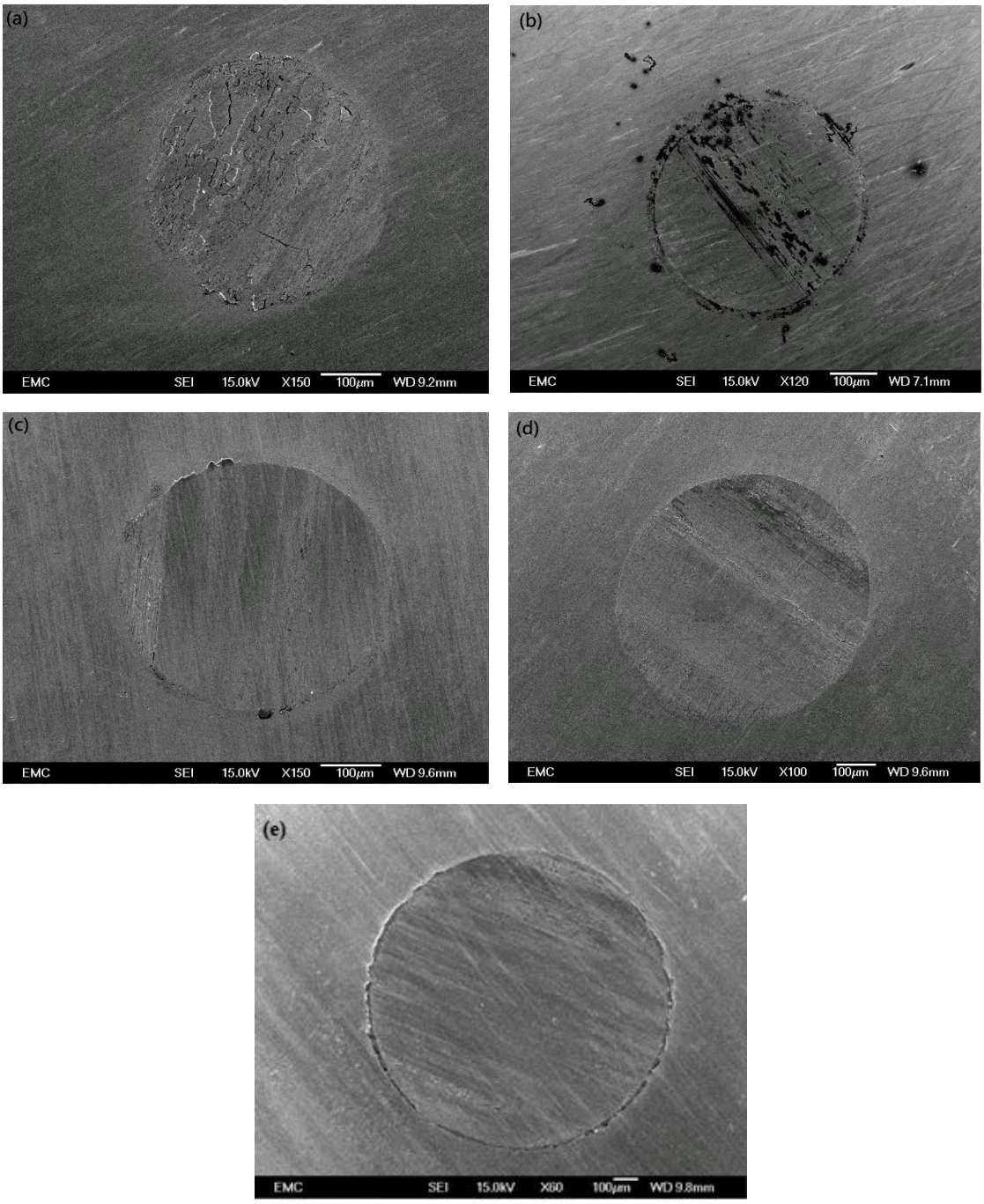

Figure 5.19: SEM images of the ball wear scars tested against $MoSe_2$/DLC-W coating in dry sliding at different loads: (a) 10 N, (b) 20 N, (c) 30 N, (d) 40 N, and (e) 50 N. Note that the images are at different magnifications.

Figure 5.20 shows the EDS mapping of the ball wear scar tested against the coating in dry sliding at 10 N load. The mapped area (shown by a yellow rectangle) shows the presence of

molybdenum and selenium in major areas of the wear scar. This suggests that some of the coating material transferred and adhered to the ball surface during sliding. The presence of oxygen was also observed. This could be due to the oxidisation of the coating material or the steel ball. It should be mentioned that, unlike the ball wear scar of the PAO4-lubricated sliding test shown in **Figure 5.13**, the transfer layer here was quite evenly distributed and covered major parts of the ball wear scar.

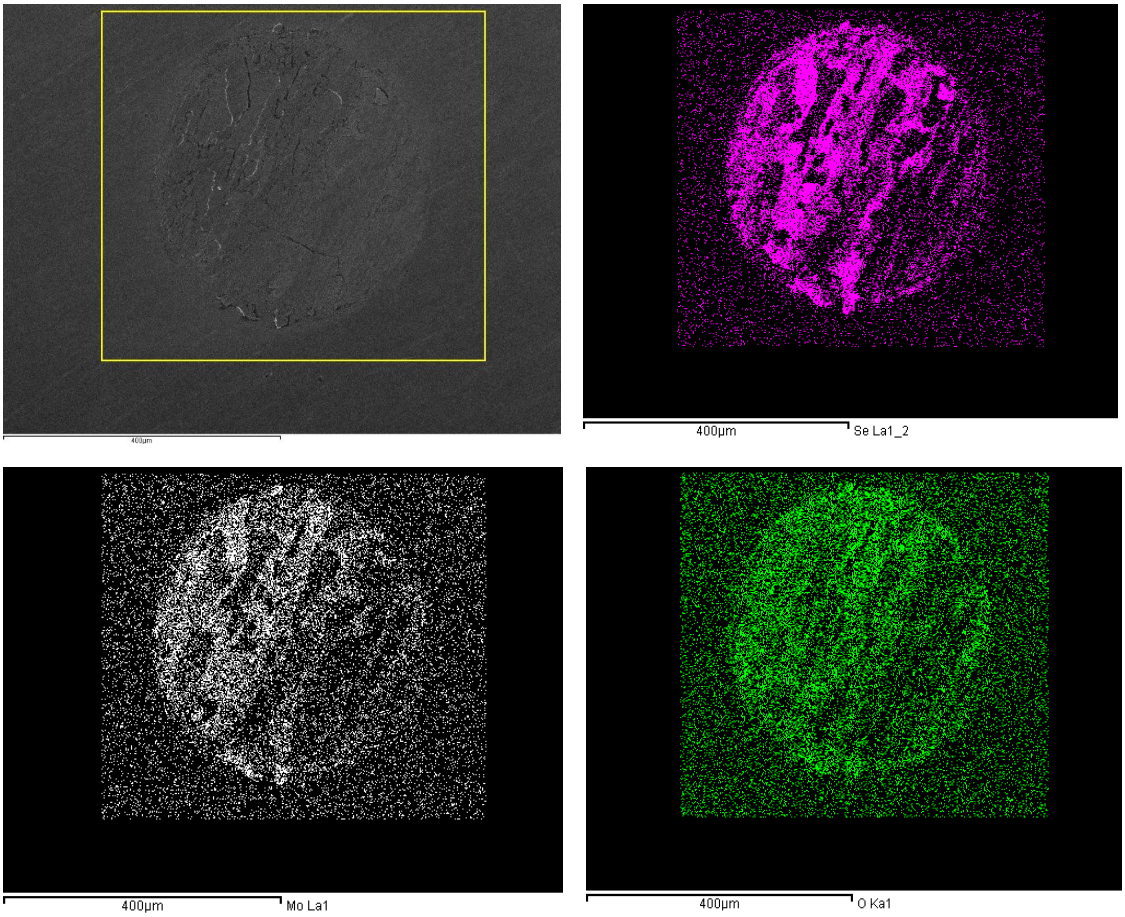

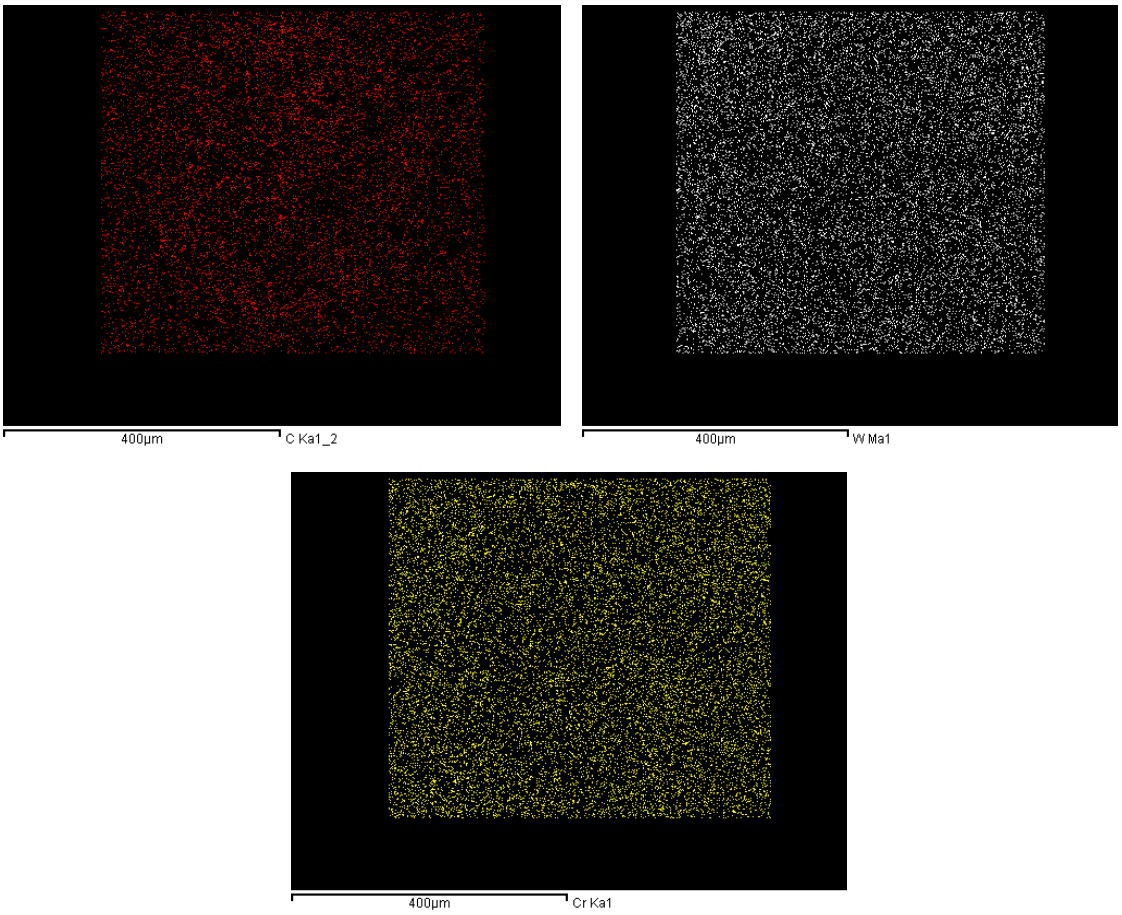

Figure 5.20: EDS mapping of the ball wear scar tested against $MoSe_2$/DLC-W coating at a normal load of 10 N in dry sliding.

Figure 5.21 shows the Raman spectra acquired from different positions of the ball wear scar tested against the coating at 10 N load in dry sliding. In general, all the examined positions show the presence of $MoSe_2$ and C materials with variable relative intensities. This was different from the PAO4-lubricated sliding test, where the presence of oil greatly inhibited the transfer of the coating material. The intensity and sharpness of $MoSe_2$ peaks are observed to increase towards the edges of the ball wear scar. The Raman spectrum acquired from the centre of the ball wear scar (position 3) shows clear peaks corresponding to $MoSe_2$, MoO_3, and C. The Raman spectra acquired from the edge of the ball wear scar (position 1) and the wear debris show clear peaks of $MoSe_2$ and MoO_3 and less pronounced peaks of C. When comparing the intensities of the peaks belonging to MoO_3 in the ball wear scars, the dry sliding test has more

intense peaks than the PAO4-lubricated sliding test. This is a clear indication of the PAO4's positive effect in sealing the contact and protecting the coating from oxidation.

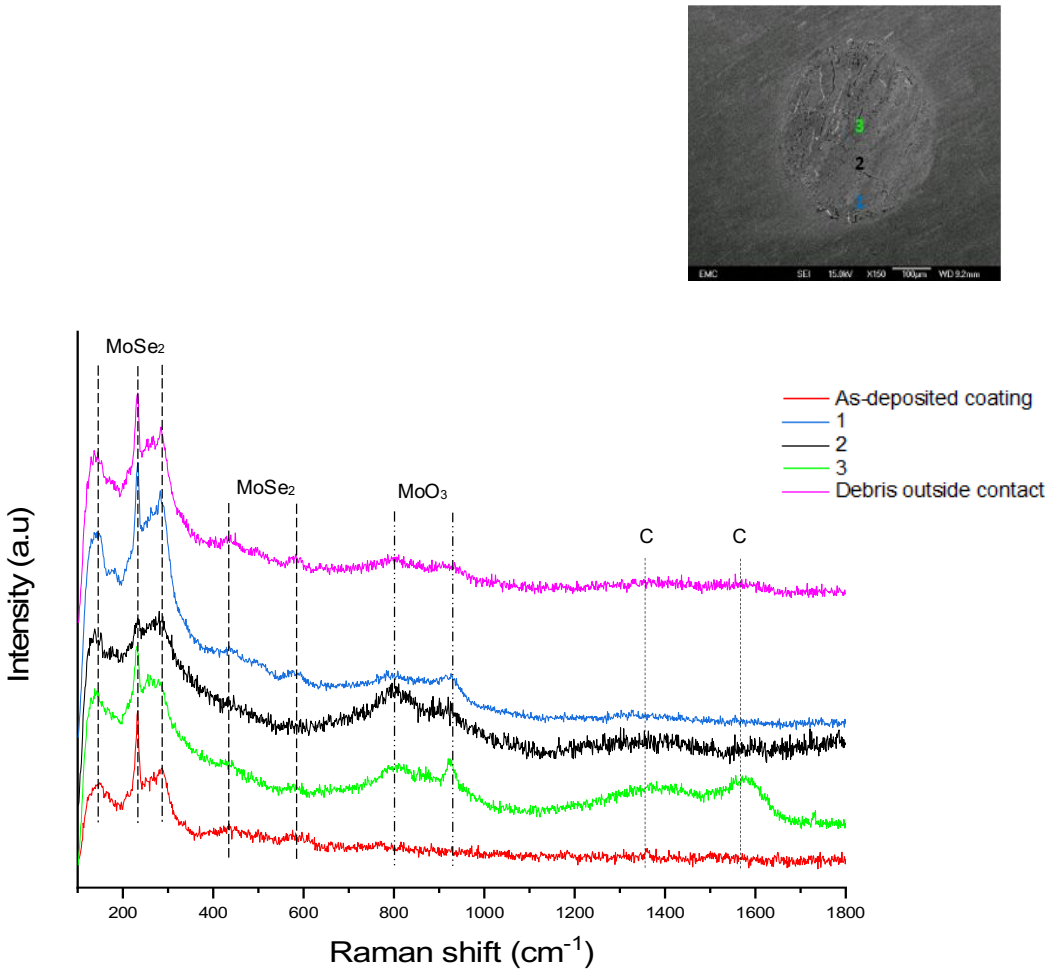

Figure 5.21: Raman spectra acquired from different positions of the ball wear scar tested against $MoSe_2$/DLC-W coating at a normal load of 10 N in dry sliding.

5.3 Discussions

5.3.1 Friction performance

As previously discussed in section 2.7.2, the friction-induced graphitisation of carbon and the formation of a transfer layer on the coating's sliding counterpart govern the low-friction mechanism of DLC coatings [373-376]. On the other hand, the low-friction mechanism of

TMD coatings is governed by the formation of a crystalline tribolayer in the topmost surface of the coating and the formation of a sliding-induced transfer layer on the coating's counterpart [42,43,226,309,320,392,467,475,476].

In PAO4-lubricated sliding, the formation of the abovementioned tribologically beneficial transfer layers of TMD and DLC coatings was significantly hindered. This was evidenced by EDS analysis and Raman spectroscopy, which showed that only a very small amount of $MoSe_2$ and carbon transferred to the steel ball during sliding. This left most of the steel ball surface not sufficiently covered by a uniformly distributed transfer layer, which is required for imparting low interfacial shear between the sliding surfaces. On the other hand, Raman spectroscopy did not detect any graphitised carbon in the wear track, providing evidence that PAO4 hindered the graphitisation of carbon during sliding. A similar behaviour was also observed for W-DLC coatings [491] and DLC coatings [492] tested in base oils, where the graphitisation of carbon was inhibited by oil lubrication, leading to high coefficients of friction. Therefore, it is possible to infer that PAO4 played a key role in the friction performance of $MoSe_2$/DLC-W coating by significantly hindering the coating material from being transferred to its sliding counterpart and preventing the graphitisation of carbon during sliding. These two factors together contributed to the observed higher coefficient of friction in PAO4-lubricated sliding when compared to dry sliding.

In dry sliding, profilometry, SEM, and EDS analysis showed that the top $MoSe_2$ layer was severely worn out, leaving the intermediate DLC-W layer exposed to sliding. Raman spectroscopy showed that this newly exposed layer was subjected to friction-induced graphitisation, which led to the formation of a soft graphitised carbon structure. This structure facilitated easy sliding between the coating and its counterpart. In contrast to the ball wear scar of the PAO4-lubricated sliding test, EDS analysis and Raman spectroscopy showed that the ball wear scar of the dry sliding test was fully covered by a relatively well-adherent layer transferred from the coating to its counterpart during sliding. The formation of this lubricious transfer layer prevented direct contact between the sliding surfaces. The existence of an easily sheared graphitised carbon structure in the wear track and the formation of a uniformly distributed transfer coating layer covering the steel counterpart were all together responsible

for the observed decrease in the coefficient of friction in dry sliding when compared to PAO4-lubricated sliding.

5.3.2 Wear performance

Although graphitisation is desirable for DLC coatings to achieve low friction, it has a detrimental effect on their mechanical properties and wear resistance. The formation of soft graphitised carbon makes the coatings more susceptible to wear and transfer to their sliding counterparts, consequently weakening the overall structural integrity of the coatings and resulting in deteriorated wear performance [493,494].

In PAO4-lubricated sliding, since the steel ball was harder than the top $MoSe_2$ layer, it abraded the layer and exposed the intermediate DLC-W layer to sliding at all the applied loads. As discussed in the previous section, PAO4 hindered the transformation of the DLC-W layer into a soft graphitised carbon structure and prevented the transfer of the coating material to the counterpart surface. This greatly added to the protection of the coating and mitigated the severity of wear. Moreover, PAO4 acted as a sealant and contributed to reducing the formation of hard metal oxides that could abrade and damage the sliding surfaces. These two effects of the PAO4 lubrication were responsible for the improved wear resistance and lower wear rates observed for the coating in PAO4-lubricated sliding when compared to dry sliding. If low wear is the main goal, then it can be deduced from the results that PAO4 can play a vital role in significantly improving the wear resistance of the coating by preventing the graphitisation of carbon and reducing the degree of metal oxidation.

In dry sliding, the coating showed completely different wear behaviour from that observed in PAO4-lubricated sliding. Its wear rate increased with increasing load until it was completely worn out at the highest applied load of 50 N. The characterisation of the worn surfaces by EDS revealed a significant presence of oxygen in the wear track of the coating tested at 10 N load, indicating that a tribo-oxidation reaction took place during sliding. This was further supported by Raman spectroscopy, which revealed the existence of several peaks belonging to MoO_3 in the analysed positions of the wear track. These newly formed MoO_3 particles, being harder

than $MoSe_2$, led to severe abrasion of the top $MoSe_2$ layer and exposure of the intermediate DLC-W layer to sliding. The DLC-W layer underwent a graphitisation reaction and transformed into a soft graphitised carbon structure, as evidenced by Raman spectroscopy. It is well established that the durability of DLC coatings decreases with increasing load because the degree of graphitisation becomes more pronounced as the load increases [377,494-496]. In this study, with increasing load up to 40 N in dry sliding, an increased wear rate was observed due to increased graphitisation and its negative consequences on the structural integrity of the DLC-W layer. When the tribological test was performed at the highest applied load of 50 N, both the intermediate DLC-W layer and the Cr adhesion layer were unable to maintain their integrities and were consequently abraded. This left the steel substrate exposed to sliding, giving rise to large fluctuations in the friction curve and a high coefficient of friction. Based on these results, the higher wear rates of the coating observed in dry sliding when compared to PAO4-lubricated sliding were caused by the formation of MoO_3 particles abrading the sliding surfaces and the transformation of the DLC-W layer into a soft graphitised carbon.

With regards to the wear mechanisms observed, SEM and EDS analysis of the wear tracks and the ball wear scars of both sliding conditions revealed the occurrence of dominant abrasive wear, as evidenced by the presence of multiple scratches and wear grooves in the wear tracks. Adhesive wear was another detected wear mechanism, as evidenced by the detachment and adherence of the coating material to its sliding counterpart.

5.5.3 Schematic of possible friction and wear mechanisms

Based on the results mentioned above, the possible friction and wear mechanisms of the currently studied $MoSe_2$/DLC-W coating in dry and PAO4-lubricated sliding are deduced, as illustrated in **Figure 5.22**. Under PAO4 lubrication, the oil acted as a barrier between the sliding surfaces and significantly hindered the transfer of the coating material to its sliding counterpart. This made it impossible for the formation of a beneficial transfer layer on the counterpart surface. Consequently, direct contact between the sliding surfaces could not be prevented, resulting in a high coefficient of friction. Another reason for the high friction of the coating in PAO4-lubricated sliding was the suppression of the transformation of the DLC-W layer into a soft graphitised carbon structure, which is required for reducing the shear strength at the sliding

interface. Contrary to the friction results, the coating exhibited better wear resistance and lower wear rates in PAO4-lubricated sliding than in dry sliding because of two major factors. Firstly, the existence of PAO4 at the sliding interface hindered the graphitisation of the DLC-W layer, which is known to make the coating more susceptible to wear and transfer to the sliding counterpart. Secondly, PAO4 acted as a sealant and protected the sliding surfaces from the formation of metal oxides such as MoO_3, which are known to increase the abrasive wear and deteriorate the wear performance of the coating and its sliding counterpart.

In dry sliding, the excellent friction performance of the coating when compared to PAO4-lubricated sliding was attributed to two main reasons. Firstly, the formation of a soft graphitised carbon structure, which caused an easy slip between the sliding surfaces. The second reason was the tribo-induced formation of a uniform and compact coating transfer layer on the sliding counterpart, which effectively blocked direct contact between the sliding surfaces. However, oxidation of the $MoSe_2$ layer was inevitable during sliding, leading to the formation of MoO_3 particles. These newly formed particles with abrasive properties increased the abrasion of the sliding surfaces. Moreover, the graphitisation of the DLC-W layer increased the consumption of the coating and reduced its structural integrity. Both factors accounted for the higher wear rates of the coatings in dry sliding when compared to PAO4-lubricated sliding.

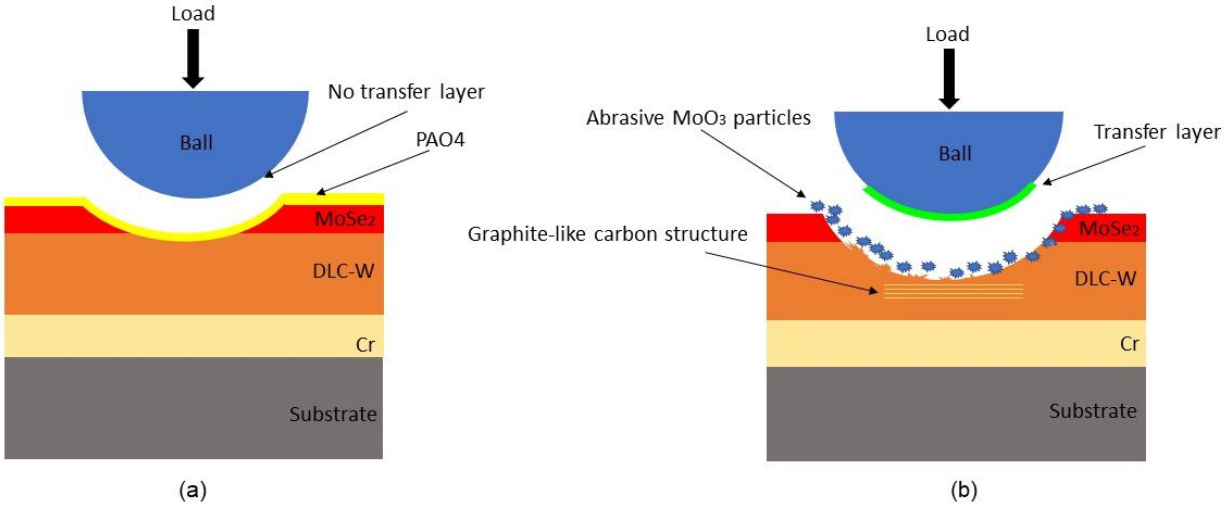

Figure 5.22: Schematic diagram of the possible friction and wear mechanisms responsible for the tribological performance of $MoSe_2$/DLC-W coating tested in: (a) PAO4-lubricated sliding and (b) dry sliding.

5.4 Summary

In this chapter, the tribological properties of $MoSe_2$/DLC-W coating were examined in dry and PAO4-lubricated sliding at different applied loads using the TE77 reciprocating tribometer. The most important findings, which can be drawn from the experimental results are as follows:

1. Under both sliding conditions, the coefficient of friction exhibited a decreasing trend with increasing applied load. The coefficient of friction obtained in PAO4-lubricated sliding was 1.4-2.6 times higher than that of dry sliding.

2. In PAO4-lubricated sliding, the characterisation of the coating and its sliding counterpart revealed that the oil significantly hindered the transfer of the coating material to the sliding counterpart. This made it impossible for the formation of a beneficial transfer layer on the counterpart surface. Consequently, direct contact between the sliding surfaces could not be prevented. The oil also prevented the friction-induced graphitisation of the DLC-W layer during sliding. These two factors contributed to the observed higher friction when compared to dry sliding.

3. In dry sliding, the characterisation of the coating and its sliding counterpart revealed that the ball wear scar was fully covered by a well-adherent layer transferred from the coating to the ball during sliding. The formation of this lubricious transfer layer prevented direct contact between the sliding surfaces. Moreover, friction-induced graphitisation of the DLC-W layer was observed, resulting in the formation of a soft graphitised carbon structure. This structure facilitated easy slip between the sliding surfaces. These two factors led to the observed lower coefficients of friction when compared to PAO4-lubricated sliding.

4. When the coating was tested in PAO4-lubricated sliding, its wear rate decreased with increasing applied load. In contrast, its wear rate increased with the increase in the applied load in dry sliding until it was completely worn out at the highest applied load. The wear rate measured in PAO4-lubricated sliding was 1.1-2.3 times lower than that of dry sliding.

5. In PAO4-lubricated sliding, the oil prevented the DLC-W layer from changing into a soft graphitised carbon and from transferring to the counterpart surface. This significantly contributed to reduce the consumption of the coating and mitigate the severity of wear during sliding. The oil also provided the coating with significant protection against the formation of abrasive MoO_3 particles. These two effects of the PAO4 lubrication were responsible for the improved wear resistance and lower wear rates observed for the coating in PAO4-lubricated sliding.

6. In dry sliding, the reaction of $MoSe_2$ with oxygen in the surrounding atmosphere was inevitable during sliding, resulting in the formation of MoO_3 particles, which abraded the sliding surfaces and reduced their wear resistance. Moreover, the graphitisation of the DLC-W layer increased the consumption of the coating and reduced its structural integrity. Both factors accounted for the reduced wear resistance and higher wear rates of the coating in dry sliding.

Chapter 6: Conclusions and future work

6.1 Overview

Reducing friction in the piston rings/cylinder liner tribo-pair is a key enabler for minimising fuel consumption, boosting efficiency, and minimising hazardous gas emissions in a heavy-duty vehicle's internal combustion engine. Low-friction coatings can contribute to better lubrication with oils and play a significant role in achieving these goals. Among them, $MoSe_2$ coating has a high potential to fulfil these goals owing to its high thermal stability, low sensitivity to air humidity, low coefficient of friction, and good wear resistance. To evaluate the potential of $MoSe_2$ coating for the piston rings/cylinder liner tribo-pair, a thorough investigation and understanding of its tribological performance with oil lubrication is needed since this tribo-pair is routinely used under oil-lubricated conditions. However, the literature survey undertaken reveals that there is a lack of knowledge and understanding of how this promising coating interacts with oil lubrication. The present work was undertaken to widen the knowledge of $MoSe_2$ coating by deeply investigating its tribological properties under oil-lubricated sliding conditions.

In the present work, $MoSe_2$ and $MoSe_2$/DLC-W coatings were deposited on steel discs using magnetron sputtering and characterised by several experimental techniques. Their tribological properties were evaluated using the TE77 reciprocating tribometer in dry and PAO4-lubricated sliding. $MoSe_2$ coating was also tribologically evaluated in PAO4-lubricated sliding at different contact loads and different temperatures to understand the influence of these operating parameters on its tribological properties. After carrying out the tribological tests, different experimental techniques including profilometry, SEM, EDS, Raman spectroscopy, FIB, and TEM were used for analysing the worn surfaces of the coatings and their counterparts.

6.2 Conclusions

The important conclusions, which can be drawn from the experimental results in this work, are as follows:

1. When $MoSe_2$ coating was evaluated in PAO4-lubricated sliding, it demonstrated a high coefficient of friction, which was one time higher than that obtained in dry sliding. The characterisation of the wear track of the coating revealed that a low-friction $MoSe_2$ tribolayer, which is known to be essential for the low-friction mechanism of this type of coatings, did not form. Similarly, on the sliding counterpart, the formation of a beneficial transfer layer was suppressed by the oil. The combined effect of these two factors accounted for the observed high coefficient of friction in PAO4-lubricated sliding. In contrast to the friction result, the coating demonstrated better wear resistance in PAO4-lubricated sliding, with a wear rate that was 27% lower than the one obtained in dry sliding. This improvement in the coating's wear resistance was caused by the presence of PAO4 at the sliding interface, which acted as a sealant and prevented the formation of abrasive metal oxides.

2. $MoSe_2$ coating showed better friction performance in dry sliding than in PAO4-lubricated sliding. Two factors contributed to this excellent friction performance. Firstly, the formation of a uniform and compact transfer layer of the coating on its sliding counterpart effectively blocked direct contact between the sliding surfaces and resulted in predominantly self-mated $MoSe_2$/$MoSe_2$ interfacial sliding. Secondly, the formation of a crystalline $MoSe_2$ tribolayer in the topmost surface of the wear track with $MoSe_2$ basal planes aligned parallel to the sliding direction. Contrary to the friction results, the coating inevitably reacted with oxygen in the surrounding atmosphere during dry sliding, forming metal oxides at the sliding interface. The formation of these oxides deteriorated its wear resistance and caused a higher wear rate when compared to PAO4-lubricated sliding.

3. When the tribological properties of $MoSe_2$ coating were evaluated under different conditions of load and temperature in PAO4-lubricated sliding, its coefficient of friction and wear rate were found to be load- and temperature-dependent. Both showed a

decreasing trend with increasing load or temperature, which was attributed to an increase in the formation of a beneficial $MoSe_2$ transfer layer on the sliding counterpart with increasing load or temperature. This makes the coating suitable for use in oil-lubricated mechanical components operating under conditions of high loads and temperatures.

4. When the tribological properties of $MoSe_2$/DLC-W coating were evaluated at different loads in PAO4-lubricated sliding, the coefficient of friction decreased with increasing applied load. However, it was 1.4-2.6 times higher than that obtained in dry sliding. The characterisation of the coating and its sliding counterpart revealed that the oil significantly hindered the transfer of the coating material to the sliding counterpart. This made it impossible for the formation of a beneficial transfer layer on the counterpart surface. Consequently, direct contact between the sliding surfaces could not be prevented. The oil also prevented the friction-induced graphitisation of the DLC-W layer during sliding. These two factors contributed to the higher friction observed in PAO4-lubricated sliding when compared to dry sliding.

5. In dry sliding, the characterisation of $MoSe_2$/DLC-W coating and its sliding counterpart revealed that the ball wear scar was covered by a uniformly distributed layer transferred from the coating to the ball during sliding. The formation of this lubricious transfer layer prevented direct contact between the sliding surfaces. A soft graphitised carbon structure was also formed in the wear track because of friction-induced graphitisation of the DLC-W layer. This structure facilitated easy slip between the sliding surfaces. The combined effect of these two factors accounted for the lower coefficients of friction observed in dry sliding when compared to PAO4-lubricated sliding.

6. When $MoSe_2$/DLC-W coating was evaluated in PAO4-lubricated sliding, its wear rate was 1.1-2.3 times lower than that of dry sliding. The oil prevented the DLC-W layer from changing into a soft graphitised carbon and from transferring to the counterpart surface. This significantly contributed to reducing the consumption of the coating and mitigating the severity of wear. The oil also provided the coating with significant protection against the formation of abrasive metal oxides. These two effects of the

PAO4 lubrication were responsible for the improved wear resistance and lower wear rates in PAO4-lubricated sliding.

7. When $MoSe_2$/DLC-W coating was evaluated in dry sliding, the top $MoSe_2$ layer inevitably reacted with oxygen in the surrounding atmosphere, resulting in the formation of MoO_3 particles. These newly formed particles with abrasive properties increased the abrasion of the coating and reduced its wear resistance. Moreover, the graphitisation of the DLC-W layer increased the consumption of the coating and reduced its structural integrity. Both factors accounted for the reduced wear resistance and higher wear rates in dry sliding.

6.3 Suggestions for future work

The present work provided some insights into the tribological properties of $MoSe_2$ coating in oil-lubricated sliding. The results presented here are merely an indication of the huge amount of work yet to be done in this direction. There are several topics that emerge as candidates for further in-depth study:

6.3.1 Tribological examination of doped-$MoSe_2$ coatings under oil-lubricated sliding conditions

One of the main drawbacks of pure TMD coatings prepared by magnetron sputtering is their low mechanical properties and limited wear resistance. In the present work, $MoSe_2$ coating was used in its pure form to find out if the coating itself could generate the beneficial tribolayer that is needed to reduce friction and wear, as well as to rule out any synergetic or antagonistic effects of doping elements. During tribological testing, however, the coating failed to provide an adequate level of wear protection and was susceptible to significant wear damage. The formation of excessive wear particles at the sliding interface is very detrimental to the friction and wear properties of sliding surfaces since these particles can abrade the surfaces and destroy any formed beneficial tribological layers.

For $MoSe_2$ coating to be successfully used in tribological applications, it must be hard and offer sufficient wear resistance. The mechanical and tribological properties of TMD coatings are strongly influenced by their chemical composition. As previously discussed, doping $MoSe_2$ coating with other elements such as carbon and titanium is one effective approach that can be used to improve its mechanical properties and wear resistance. By controlling the amount and type of doping elements, the mechanical and tribological properties of the coating can be tailored to give better performance. A future direction of research can be the evaluation of the tribological properties of doped-$MoSe_2$ coatings under oil-lubricated sliding conditions.

6.3.2 Study of the influence of oil lubrication on the tribological properties of $MoSe_2$ coatings using numerical simulation

In the present work, the influence of oil lubrication on the tribological properties of $MoSe_2$ coating was investigated experimentally using the TE77 tribometer. Studies by means of numerical simulation can enrich the understanding of the effect of oil lubrication on its tribological performance and allows for the verification of the tribological results obtained in this work. A future direction of research can be the use of numerical simulation to study the influence of oil lubrication on the tribological properties of $MoSe_2$ coating and compare the results obtained from numerical simulation with the experimental results presented in this work.

6.3.3 Investigation of the effect of oil additives on the tribological performance of $MoSe_2$ coatings

A wide range of oil additives are often added to lubricating oils to avoid metal-to-metal contact and minimise friction and wear. It is well established that these additives reduce friction and wear by forming self-lubricating layers on contacting surfaces. However, since these additives are typically optimised for ferrous-base surfaces, the mechanisms by which they reduce friction and wear may be different when they are used in combination with $MoSe_2$ coatings. Furthermore, when a mechanical component operates in the presence of oil containing different additives, the competition for free surface sites is strong from surface-active additives. Under such conditions, the self-lubricating layers may be impossible to develop and bond to contacting surfaces when using triboactive coatings such as $MoSe_2$ coatings. Therefore, it is essential to understand how $MoSe_2$ coatings interact with oil additives since this would allow

additive solutions to be customised for $MoSe_2$ coatings. A future direction of research can be the study of the influence of oil additives on the friction and wear performance of $MoSe_2$ coatings.

6.3.4 Evaluation of the tribological performance of $MoSe_2$ coatings under oil-lubricated conditions at low contact pressures

The high contact pressures (≥1 GPa) used in this work resulted in $MoSe_2$ coating having more desirable tribological properties with low coefficients of friction and wear rates. However, in real-world tribological applications, much lower contact pressures are used. It is unclear how $MoSe_2$ coating will tribologically respond at such low contact pressures. When the contact pressure is decreased, the question arises whether the coating will be capable of forming a transfer layer on its sliding counterpart needed for minimising friction and wear. A future direction of research can be the evaluation of the tribological performance of $MoSe_2$ coatings at low contact pressures under oil-lubricated conditions.

6.3.5 Assessment of the tribological properties of WSe_2 coating under oil-lubricated conditions

This work was focused only on $MoSe_2$ coating. Several tribological studies have demonstrated that WSe_2 coating is superior to traditional MoS_2 and WS_2 coatings for tribological applications in vacuum and humid air due to its higher chemical stability and lower sensitivity to air humidity [186-190]. However, there is still a lack of knowledge about the tribological performance of this promising coating under oil-lubricated conditions. A future direction of research can be the study of the tribological behaviour of WSe_2 coating under oil-lubricated conditions.

References

[1] R. J. Javid, A. Nejat, and K. Hayhoe, "Selection of CO_2 mitigation strategies for road transportation in the United States using a multi-criteria approach," *Renew. Sustain. Energy Rev.*, vol. 38, pp. 960–972, 2014.

[2] J. Cooper, A. Hawkes, and P. Balcombe, "Life cycle environmental impacts of natural gas drivetrains used in UK road freighting and impacts to UK emission targets," *Sci. Total Environ.*, vol. 674, pp. 482–493, 2019.

[3] G. Fontaras *et al.*, "An experimental evaluation of the methodology proposed for the monitoring and certification of CO_2 emissions from heavy-duty vehicles in Europe," *Energy*, vol. 102, pp. 354–364, 2016.

[4] K. Holmberg, P. Andersson, N. O. Nylund, K. Mäkelä, and A. Erdemir, "Global energy consumption due to friction in trucks and buses," *Tribol. Int.*, vol. 78, pp. 94–114, 2014.

[5] S. J. G. Cooper and G. P. Hammond, "'Decarbonising' UK industry : towards a cleaner economy," *Proc. Inst. Civ. Eng.*, vol. 171, no. 4, pp. 147–157, 2018.

[6] Department for Transport, "Decarbonising Transport: Setting the Challenge,". [Online]. Available: https://assets.publishing.service.gov.uk/government/uploads/system/uploads/attachment_data/file/932122/decarbonising-transport-setting-the-challenge.pdf.

[7] S. Pye, F. G. N. Li, J. Price, and B. Fais, "Achieving net-zero emissions through the reframing of UK national targets in the post-Paris Agreement era," *Nat. Energy*, vol. 2, no. 3, pp. 1–8, 2017.

[8] J. Moavenzadeh, M. Torres-Montoya, and T. Gange, "Repowering Transport: Project White Paper," in *World Economic Forum*, 2011.

[9] G. Kalghatgi, "Development of Fuel/Engine Systems—The Way Forward to Sustainable Transport," *Engineering*, vol. 5, no. 3, pp. 510–518, 2019.

[10] G. Kalghatgi, "Is it really the end of internal combustion engines and petroleum in transport?," *Appl. Energy*, vol. 225, pp. 965–974, 2018.

[11] H. A. Bonges and A. C. Lusk, "Addressing electric vehicle (EV) sales and range anxiety through parking layout, policy and regulation," *Transp. Res. Part A Policy Pract.*, vol. 83, pp. 63–73, 2016.

[12] A. Poullikkas, "Sustainable options for electric vehicle technologies," *Renew. Sustain. Energy Rev.*, vol. 41, pp. 1277–1287, 2015.

[13] S. Iwan, K. Kijewska, and D. Kijewski, "Possibilities of Applying Electrically Powered Vehicles in Urban Freight Transport," *Procedia - Soc. Behav. Sci.*, vol. 151, pp. 87–101, 2014.

[14] C. J. James, "Analysis of parasitic losses in heavy duty diesel engines," (Doctoral dissertation, Massachusetts Institute of Technology), 2012.

[15] M. Söderfjäll, H. M. Herbst, R. Larsson, and A. Almqvist, "Influence on friction from

piston ring design, cylinder liner roughness and lubricant properties," *Tribol. Int.*, vol. 116, pp. 272–284, 2017.

[16] K. D. Lawrence and B. Ramamoorthy, "Multi-surface topography targeted plateau honing for the processing of cylinder liner surfaces of automotive engines," *Appl. Surf. Sci.*, vol. 365, pp. 19–30, 2016.

[17] K. Holmberg and A. Erdemir, "The impact of tribology on energy use and CO_2 emission globally and in combustion engine and electric cars," *Tribol. Int.*, vol. 135, pp. 389–396, 2019.

[18] K. Holmberg *et al.*, "Residual stresses in TiN, DLC and MoS_2 coated surfaces with regard to their tribological fracture behaviour," *Wear*, vol. 267, no. 12, pp. 2142–2156, 2009.

[19] C. Donnet and A. Erdemir, *Tribology of Diamond-Like Carbon Films: fundamentals and applications*. New York: Springer, 2008.

[20] M. Kano, "Diamond-like carbon coating applied to automotive engine components," *Tribol. Online*, vol. 9, no. 3, pp. 135–142, 2014.

[21] M. Kano, "DLC coating technology applied to sliding parts of automotive engine," *New Diam. Front. Carbon Technol.*, vol. 16, no. 4, pp. 201–210, 2006.

[22] R. Ferreira, J. Martins, Ó. Carvalho, L. Sobral, S. Carvalho, and F. Silva, "Tribological solutions for engine piston ring surfaces: an overview on the materials and manufacturing," *Mater. Manuf. Process.*, vol. 35, no. 5, pp. 498–520, 2020.

[23] R. Gåhlin, M. Larsson, and P. Hedenqvist, "ME-C:H coatings in motor vehicles," *Wear*, vol. 249, no. 3–4, pp. 302–309, 2001.

[24] S. V. Hainsworth and N. J. Uhure, "Diamond like carbon coatings for tribology: Production techniques, characterisation methods and applications," *Int. Mater. Rev.*, vol. 52, no. 3, pp. 153–174, 2007.

[25] H. Abdullah Tasdemir *et al.*, "Ultra-low friction of tetrahedral amorphous diamond-like carbon (ta-C DLC) under boundary lubrication in poly alpha-olefin (PAO) with additives," *Tribol. Int.*, vol. 65, pp. 286–294, 2013.

[26] B. Vengudusamy, R. A. Mufti, G. D. Lamb, J. H. Green, and H. A. Spikes, "Friction properties of DLC/DLC contacts in base oil," *Tribol. Int.*, vol. 44, no. 7–8, pp. 922–932, 2011.

[27] B. Vengudusamy, J. H. Green, G. D. Lamb, and H. A. Spikes, "Durability of ZDDP tribofilms formed in DLC/DLC contacts," *Tribol. Lett.*, vol. 51, no. 3, pp. 469–478, 2013.

[28] S. Equey, S. Roos, U. Mueller, R. Hauert, N. D. Spencer, and R. Crockett, "Reactions of zinc-free anti-wear additives in DLC/DLC and steel/steel contacts," *Tribol. Int.*, vol. 41, no. 11, pp. 1090–1096, 2008.

[29] S. Equey, S. Roos, U. Mueller, R. Hauert, N. D. Spencer, and R. Crockett, "Tribofilm formation from ZnDTP on diamond-like carbon," *Wear*, vol. 264, no. 3–4, pp. 316–321, 2008.

[30] M. Kano *et al.*, "Ultralow friction of DLC in presence of glycerol mono-oleate

(GMO)," *Tribol. Lett.*, vol. 18, no. 2, pp. 245–251, 2005.

[31] M. Kalin, J. Vižintin, J. Barriga, K. Vercammen, K. van Acker, and A. Arnšek, "The effect of doping elements and oil additives on the tribological performance of boundary-lubricated DLC/DLC contacts," *Tribol. Lett.*, vol. 17, no. 4, pp. 679–688, 2004.

[32] B. Kržan, F. Novotny-Farkas, and J. Vižintin, "Tribological behavior of tungsten-doped DLC coating under oil lubrication," *Tribol. Int.*, vol. 42, no. 2, pp. 229–235, 2009.

[33] K. Topolovec-Miklozic, F. Lockwood, and H. Spikes, "Behaviour of boundary lubricating additives on DLC coatings," *Wear*, vol. 265, no. 11–12, pp. 1893–1901, 2008.

[34] B. Podgornik, S. Jacobson, and S. Hogmark, "DLC coating of boundary lubricated components–Advantages of coating one of the contact surfaces rather than both or none," *Tribol. Int.*, vol. 36, no. 11, pp. 843–849, 2003.

[35] T. Haque, A. Morina, A. Neville, R. Kapadia, and S. Arrowsmith, "Non-ferrous coating/lubricant interactions in tribological contacts: Assessment of tribofilms," *Tribol. Int.*, vol. 40, no. 10-12, pp. 1603–1612, 2007.

[36] M. Kalin and J. Vižintin, "Differences in the tribological mechanisms when using non-doped, metal-doped (Ti, WC), and non-metal-doped (Si) diamond-like carbon against steel under boundary lubrication, with and without oil additives," *Thin Solid Films*, vol. 515, no. 4, pp. 2734–2747, 2006.

[37] S. Zhang, X. L. Bui, and Y. Fu, "Magnetron sputtered hard a-C coatings of very high toughness," *Surf. Coatings Technol.*, vol. 167, no. 2–3, pp. 137–142, 2003.

[38] N. B. Dahotre and S. Nayak, "Nanocoatings for engine application," *Surf. Coatings Technol.*, vol. 194, no. 1, pp. 58–67, 2005.

[39] C. Wei and J. Y. Yen, "Effect of film thickness and interlayer on the adhesion strength of diamond like carbon films on different substrates," *Diam. Relat. Mater.*, vol. 16, no. 4-7, pp. 1325–1330, 2007.

[40] Q. Wei, A. K. Sharma, J. Sankar, and J. Narayan, "Mechanical properties of diamond-like carbon composite thin films prepared by pulsed laser deposition," *Compos. Part B Eng.*, vol. 30, no. 7, pp. 675–684, 1999.

[41] Y. Oka, M. Kirinuki, Y. Nishimura, K. Azuma, E. Fujiwara, and M. Yatsuzuka, "Measurement of residual stress in DLC films prepared by plasma-based ion implantation and deposition," *Surf. Coatings Technol.*, vol. 186, no. 1–2, pp. 141–145, 2004.

[42] T. Polcar and A. Cavaleiro, "Self-adaptive low friction coatings based on transition metal dichalcogenides," *Thin Solid Films*, vol. 519, no. 12, pp. 4037–4044, 2011.

[43] T. Polcar and A. Cavaleiro, "Review on self-lubricant transition metal dichalcogenide nanocomposite coatings alloyed with carbon," *Surf. Coatings Technol.*, vol. 206, no. 4, pp. 686–695, 2011.

[44] C. Donnet and A. Erdemir, "Solid lubricant coatings: Recent developments and future

trends," *Tribol. Lett.*, vol. 17, no. 3, pp. 389–397, 2004.

[45] N. M. Renevier, V. C. Fox, D. G. Teer, and J. Hampshire, "Coating characteristics and tribological properties of sputter-deposited MoS_2/metal composite coatings deposited by closed field unbalanced magnetron sputter ion plating," *Surf. Coatings Technol.*, vol. 127, no. 1, pp. 24–37, 2000.

[46] E. Arslan, F. Bülbül, and I. Efeoglu, "The Structural and Tribological Properties of MoS_2-Ti composite solid lubricants," *Tribology Transactions*, vol. 47, no. 2, pp. 218–226, 2004.

[47] J. D. Holbery *et al.*, "Alloying MoS_2 with Al and Au: Structure and tribological performance," *Surf. Coatings Technol.*, vol. 169–170, pp. 716–720, 2003.

[48] K. J. Wahl, D. N. Dunn, and I. L. Singer, "Wear behavior of Pb-Mo-S solid lubricating coatings," *Wear*, vol. 230, no. 2, pp. 175–183, 1999.

[49] J. V. Pimentel, T. Polcar, and A. Cavaleiro, "Structural, mechanical and tribological properties of Mo-S-C solid lubricant coating," *Surf. Coatings Technol.*, vol. 205, no. 10, pp. 3274–3279, 2011.

[50] B. H. Rho and K. W. Kim, "Tribological behaviour and wear mechanism of MoS_2-Cr coatings sliding against various counterbody," *Tribol. Int.*, vol. 36, no. 1, pp. 11–23, 2003.

[51] T. Hudec *et al.*, "Structure, mechanical and tribological properties of Mo-S-N solid lubricant coatings," *Appl. Surf. Sci.*, vol. 486, pp. 1–14, 2019.

[52] X. Zhang, L. Qiao, L. Chai, J. Xu, L. Shi, and P. Wang, "Structural, mechanical and tribological properties of Mo-S-N solid lubricant films," *Surf. Coatings Technol.*, vol. 296, pp. 185–191, 2016.

[53] D. G. Teer, "New solid lubricant coatings," *Wear*, vol. 250–251, pp. 1068–1074, 2001.

[54] V. Fox, A. Jones, N. M. Renevier, and D. G. Teer, "Hard lubricating coatings for cutting and forming tools and mechanical components," *Surf. Coatings Technol.*, vol. 125, no. 1–3, pp. 347–353, 2000.

[55] N. M. Renevier, J. Hamphire, V. C. Fox, J. Witts, T. Allen, and D. G. Teer, "Advantages of using self-lubricating, hard, wear-resistant MoS_2-based coatings," *Surf. Coatings Technol.*, vol. 142–144, pp. 67–77, 2001.

[56] T. Kubart, T. Polcar, L. Kopecký, R. Novák, and D. Nováková, "Temperature dependence of tribological properties of MoS_2 and $MoSe_2$ coatings," *Surf. Coatings Technol.*, vol. 193, no. 1-3, pp. 230–233, 2005.

[57] H. E. S. R.L. Johnson, "Fundamental Considerations for Future Solid Lubricants," *NASA TM X-52659*, 1969.

[58] W. A. Brainard, "The thermal stability and friction of the disulfides, diselenides, and ditellurides of molybdenum and tungsten in vaccum (10^{-9} to 10^{-6} Torr)," *NASA Tech. Note D-5141*, pp. 1–26, 1968.

[59] A. Rapuc, H. Wang, and T. Polcar, "Nanotribology of transition metal dichalcogenide flakes deposited by chemical vapour deposition: The influence of chemical composition and sliding speed on nanoscale friction of monolayers," *Appl. Surf. Sci.*,

vol. 556, p. 149762, 2021.

[60] S. Glavatskih and E. Höglund, “Tribotronics-Towards active tribology,” *Tribol. Int.*, vol. 41, no. 9–10, pp. 934–939, 2008.

[61] B. Bhushan, *Introduction to Tribology*. Chichester: John Wiley & Sons, 2013.

[62] J. P. Davim, *Mechanical and industrial engineering: historical aspects and future directions*. Heidelberg: Springer, 2022.

[63] L. M. Hutchings, *Triblology: Friction and wear of engineering materials*. London: CRC Press, 1992.

[64] G. W. Stachowiak and A. W. Batchelor, *Engineering Tribology*. London: Elsevier, 2014.

[65] R. S. Dwyer-Joyce, “Tribological Design Data Part 3 : Contact Mechanics Introduction - Contact Stresses and Failure,” *Tribol. Gr. Inst. Mech. Eng.*, vol. 1, pp. 1–17, 1997.

[66] J. A. Norris, K. J. Stabile, and R. H. Jinnah, “An introduction to tribology.,” *J. Surg. Orthop. Adv.*, pp. 2–5, 2008.

[67] A. R. Lansdown, *Lubrication and Lubricant Selection*, 3rd ed. London: Professional Engineering Publishing limited, 2004.

[68] F. Al-Bender and J. Swevers, “Characterization of Friction Force Dynamics,” *IEEE Control Syst. Mag.*, vol. 28, no. 6, pp. 64–81, 2008.

[69] F. Bowden and D. Tabor, *The Friction and Lubrication of Solids*. Oxford: Clarendon Press, 1950.

[70] R. Colaço and A. P. Serro, “Nanoscale wear of hard materials: An overview,” *Curr. Opin. Colloid Interface Sci.*, vol. 47, pp. 118–125, 2020.

[71] C. Leriche, S. Franklin, and B. Weber, “Measuring multi-asperity wear with nanoscale precision,” *Wear*, vol. 498–499, no. 1, p. 204284, 2022.

[72] J. J. Kauzlarich and J. A. Williams, “Archard wear and component geometry,” *Proc. Inst. Mech. Eng. Part J J. Eng. Tribol.*, vol. 215, no. 4, pp. 387–398, 2001.

[73] S. Ahmed and V. S. Dakre, Eds., *Tribology and Characterization of Surface Coatings*. John Wiley & Sons, 2022.

[74] D. K. Dwivedi, “Adhesive wear behaviour of cast aluminium-silicon alloys: Overview,” *Mater. Des.*, vol. 31, no. 5, pp. 2517–2531, 2010.

[75] M. Salot, “Study on wear resistance of Al-Si alloy using a 3-body dry abrasive wear testing machine,” *NCIME, Indus Univ. Ahmedabad*, vol. 4, pp. 1–6, 2016.

[76] R. C. Cozza, “A study on friction coefficient and wear coefficient of coated systems submitted to micro-scale abrasion tests,” *Surf. Coat. Technol.*, vol. 215, pp. 224–233, 2013.

[77] R. I. Trezona, D. N. Allsopp, and I. M. Hutchings, “Transitions between two-body and three-body abrasive wear: influence of test conditions in the microscale abrasive wear test,” *Wear*, vol. 225–229, no. 5, pp. 205–214, 1999.

[78] B. Hydrogels and T. Yamaguchi, “Propagation of fatigue cracks in friction of brittle

hydrogels," *Gels*, vol. 4, no. 53, pp. 1–13, 2018.

[79] S. Wan *et al.*, "Investigating the corrosion-fatigue wear on CrN coated piston rings from laboratory wear tests and field trial studies," *Wear*, vol. 432–433, p. 202940, 2019.

[80] E. C. Fitch, *Proactive Maintenance for Mechanical Systems*. Oxford: Elsevier, 2013.

[81] A. Vellore *et al.*, "Ni-Doped MoS_2 Dry Film Lubricant Life," *Adv. Mater. Interfaces*, vol. 7, no. 22, pp. 1–11, 2020.

[82] S. Wen and P. Huang, *Principles of Tribology*. John Wiley & Sons, 2011.

[83] W. J. Bartz, "Tribology, lubricants and lubrication engineering - a review," *Wear*, vol. 49, no. 1, pp. 1–18, 1978.

[84] A. M. Nassar, N. S. Ahmed, H. S. Abdel-Hameed, and A. F. El-Kafrawy, "Synthesis and utilization of non-metallic detergent/dispersant and antioxidant additives for lubricating engine oil," *Tribol. Int.*, vol. 93, pp. 297–305, 2016.

[85] C. J. Reeves, A. Siddaiah, and P. L. Menezes, "A Review on the Science and Technology of Natural and Synthetic Biolubricants," *J. Bio- Tribo-Corrosion*, vol. 3, no. 1, pp. 1–27, 2017.

[86] Leslie R. Rudnick, *Synthetics, mineral oils, and bio-based lubricants: chemistry and technology*, 2nd ed. Boca Raton: CRC Press, 2013.

[87] Abdelaziz, A. I. M. Elamin, I. H. M. Gasmelseed, and G. A. Abdalla, "Conditioning of Castor Oil to be Use as Lubricant," *Int. J. Chem. Nat. Sci.*, vol. 4, no. 5, pp. 409–411, 2016.

[88] P. J. Blau, *Friction science and technology: from concepts to applications*. New York: CRC Press, 2008.

[89] G. B. Bantchev and G. Biresaw, "Film-forming properties of blends of high-oleic sunflower oil with polyalkyl glycol," *JAOCS, J. Am. Oil Chem. Soc.*, vol. 89, no. 12, pp. 2227–2235, 2012.

[90] ExxonMobil, "Polyalphaolefin (PAO) Fluid." [Online]. Available: https://www.exxonmobilchemical.com/en/chemicals/webapi/dps/v1/datasheets/150000000349/0/en.

[91] G. Tatsumi, M. Ratoi, Y. Shitara, K. Sakamoto, and B. G. Mellor, "Effect of lubrication on friction and wear properties of PEEK with steel counterparts," *Tribol. Online*, vol. 14, no. 5, pp. 345–352, 2019.

[92] B. J. Hamrock, S. R. Schmid, and B. O. Jacobson, *Fundamentals of Fluid Film Lubrication*. Boca Raton: CRC Press, 2004.

[93] G. Dwivedi, P. Verma, and M. P. Sharma, "Impact of oil and biodiesel on engine operation in cold climatic condition," *J. Mater. Environ. Sci.*, vol. 7, no. 12, pp. 4540–4555, 2016.

[94] D. Ljubas, H. Krpan, and I. Matanović, "Influence of engine oils dilution by fuels on their viscosity, flash point and fire point," *Nafta*, vol. 61, no. 2, pp. 73–79, 2010.

[95] P. Wang, Y. Wang, Y. Sun, Z. Cao, W. Zhu, and H. Wang, "Thermal and

Spectroscopic Studies of the Thermal-Oxidation Stabilities of Lubricants," *J. Appl. Spectrosc.*, vol. 88, no. 4, pp. 847–854, 2021.

[96] U. Abdulfatai, A. Uzairu, S. Uba, and G. A. Shallangwa, "Molecular design of antioxidant lubricating oil additives via QSPR and analysis dynamic simulation method," *Heliyon*, vol. 5, no. 11, pp. 1–4, 2019.

[97] S. Korcek, R. K. Jensen, M. D. Johnson, and J. Sorab, "Fuel efficient engine oils, additive interactions, boundary friction, and wear," *Tribol. Ser.*, vol. 36, no. 1, pp. 13–24, 1999.

[98] J. D. Summers-Smith, *An introductory guide to industrial tribology*. London: Mechanical Engineering Publications, 1994.

[99] E. O. Aluyor and M. Ori-jesu, "Biodegradation of mineral oils–A review," *African J. Biotechnol.*, vol. 8, no. 6, pp. 915–920, 2009.

[100] N. S. Ahmed, A. M. Nassar, R. M. Nasser, M. E. Abdel Raouf, and A. F. El-Kafrawy, "Novel terpolymers as pour point depressants and viscosity modifiers for lube oil," *Pet. Sci. Technol.*, vol. 32, no. 6, pp. 680–687, 2014.

[101] B. J. Hamrock and D. Dowson, "Isothermal elastohydrodynamic lubrication of point contacts: Part III—fully flooded results," *J. Lubr. Technol.*, vol. 99, no. 2, pp. 264–275, 1977.

[102] M. D. Marko, "The impact of lubricant film thickness and ball bearings failures," *Lubricants*, vol. 7, no. 6, p. 48, 2019.

[103] P. Nowak, K. Kucharska, and M. Kamiński, "Ecological and health effects of lubricant oils emitted into the environment," *Int. J. Environ. Res. Public Health*, vol. 16, no. 16, pp. 1–13, 2019.

[104] W. R. Murphy, D. A. Blain, and A. S. Galiano-Roth, "Synthetics basics benefits of synthetic lubricants in industrial," *J. Synth. Lubr.*, vol. 18, no. 4, pp. 301–325, 2002.

[105] N. W. M. Zulkifli, S. S. N. Azman, M. A. Kalam, H. H. Masjuki, R. Yunus, and M. Gulzar, "Lubricity of bio-based lubricant derived from different chemically modified fatty acid methyl ester," *Tribol. Int.*, vol. 93, pp. 555–562, 2016.

[106] S. M. Prasanth, P. S. Kumar, S. Harish, M. Rishikesh, S. Nanda, and D. V. N. Vo, "Application of biomass derived products in mid-size automotive industries: A review," *Chemosphere*, vol. 280, pp. 1–15, 2021.

[107] R. Hatti-Kaul, U. Törnvall, L. Gustafsson, and P. Börjesson, "Industrial biotechnology for the production of bio-based chemicals–a cradle-to-grave perspective," *Trends Biotechnol.*, vol. 25, no. 3, pp. 119–124, 2007.

[108] A. Z. Syahir *et al.*, "A review on bio-based lubricants and their applications," *J. Clean. Prod.*, vol. 168, pp. 997–1016, 2017.

[109] S. Z. Erhan, B. K. Sharma, and J. M. Perez, "Oxidation and low temperature stability of vegetable oil-based lubricants," *Ind. Crops Prod.*, vol. 24, no. 3, pp. 292–299, 2006.

[110] I. Madanhire and C. Mbohwa, *Mitigating environmental impact of petroleum lubricants*. Berlin: Springer, 2016.

[111] R. I. Taylor, "Tribology and energy efficiency: from molecules to lubricated contacts to complete machines," *Faraday Discuss.*, vol. 156, pp. 361–382, 2012.

[112] C. Grossiord, K. Varlot, J. Martin, T. Le Mogne, and C. Esnouf, "MoS_2 single sheet lubrication by molybdenum," *Tribol. Int.*, vol. 31, no. 12, pp. 737–743, 1999.

[113] J. Dawczyk, N. Morgan, J. Russo, and H. Spikes, "Film thickness and friction of ZDDP tribofilms," *Tribol. Lett.*, vol. 67, no. 2, pp. 1–15, 2019.

[114] J. Takadoum, *Materials and Surface Engineering in Tribology*. John Wiley & Sons, 2008.

[115] S. Zhu, J. Cheng, Z. Qiao, and J. Yang, "High temperature solid-lubricating materials: A review," *Tribol. Int.*, vol. 133, no. 4, pp. 206–223, 2019.

[116] H. Wang, B. Xu, and J. Liu, *Micro and nano sulfide solid lubrication*. Beijing: Springer Science & Business Media, 2013.

[117] K. Miyoshi, *Solid lubrication fundamentals and applications*. Boca Raton: CRC Press, 2019.

[118] B. Chen, Q. Bi, J. Yang, Y. Xia, and J. Hao, "Tribological properties of solid lubricants (graphite, h-BN) for Cu-based P/M friction composites," *Tribol. Int.*, vol. 41, no. 12, pp. 1145–1152, 2008.

[119] A. Erdemir, "Review of engineered tribological interfaces for improved boundary lubrication," *Tribol. Int.*, vol. 38, no. 3, pp. 249–256, 2005.

[120] P. L. Menezes, S. P. Ingole, M. Nosonovsky, S. V. Kailas, and M. R. Lovell, *Tribology for scientists and engineers*. New York: Springer, 2013.

[121] H. Unal, A. Mimaroglu, U. Kadioglu, and H. Ekiz, "Sliding friction and wear behaviour of polytetrafluoroethylene and its composites under dry conditions," *Mater. Des.*, vol. 25, no. 3, pp. 239–245, 2004.

[122] B. Bhushan, *Modern tribology handbook, two volume set*. Boca Raton: CRC press, 2000.

[123] E. F. Rico, I. Minondo, and D. G. Cuervo, "The effectiveness of PTFE nanoparticle powder as an EP additive to mineral base oils," *Wear*, vol. 262, no. 11–12, pp. 1399–1406, 2007.

[124] N. Kumar, V. Saini, and J. Bijwe, "Performance properties of lithium greases with PTFE particles as additive: controlling parameter-size or shape?," *Tribol. Int.*, vol. 148, no. 6, pp. 1–11, 2020.

[125] S. M. Aouadi, H. Gao, A. Martini, T. W. Scharf, and C. Muratore, "Lubricious oxide coatings for extreme temperature applications: A review," *Surf. Coatings Technol.*, vol. 257, pp. 266–277, 2014.

[126] M. Chhowalla, H. S. Shin, G. Eda, L. J. Li, K. P. Loh, and H. Zhang, "The chemistry of two-dimensional layered transition metal dichalcogenide nanosheets," *Nat. Chem.*, vol. 5, no. 4, pp. 263–275, 2013.

[127] J. Silva-Guillén, P. San-Jose, and R. Roldán, "Electronic band structure of transition metal dichalcogenides from ab initio and Slater–Koster tight-binding model," *Appl.*

Sci., vol. 6, no. 10, p. 284, 2016.

[128] Y. C. Lin *et al.*, "Atomically thin resonant tunnel diodes built from synthetic van der Waals heterostructures," *Nat. Commun.*, vol. 6, pp. 4–9, 2015.

[129] H. J. Chuang *et al.*, "High Mobility WSe_2 p- and n-Type Field-Effect Transistors Contacted by Highly Doped Graphene for Low-Resistance Contacts," *Nano Lett.*, vol. 14, no. 6, pp. 3594–3601, 2014.

[130] Z. Yin *et al.*, "Single-layer MoS_2 phototransistors," *ACS Nano*, vol. 6, no. 1, pp. 74–80, 2012.

[131] B. W. H. Baugher, H. O. H. Churchill, Y. Yang, and P. Jarillo-Herrero, "Optoelectronic devices based on electrically tunable p-n diodes in a monolayer dichalcogenide," *Nat. Nanotechnol.*, vol. 9, no. 4, pp. 262–267, 2014.

[132] B. Cho *et al.*, "Chemical Sensing of 2D Graphene/MoS_2 Heterostructure device," *ACS Appl. Mater. Interfaces*, vol. 7, no. 30, pp. 16775–16780, 2015.

[133] B. Liu, L. Chen, G. Liu, A. N. Abbas, M. Fathi, and C. Zhou, "High-performance chemical sensing using Schottky-contacted chemical vapor deposition grown monolayer MoS_2 transistors," *ACS Nano*, vol. 8, no. 5, pp. 5304–5314, 2014.

[134] C. Feng, J. Ma, H. Li, R. Zeng, Z. Guo, and H. Liu, "Synthesis of molybdenum disulfide (MoS_2) for lithium ion battery applications," *Mater. Res. Bull.*, vol. 44, no. 9, pp. 1811–1815, 2009.

[135] S. Ratha and C. S. Rout, "Supercapacitor electrodes based on layered tungsten disulfide-reduced graphene oxide hybrids synthesized by a facile hydrothermal method," *ACS Appl. Mater. Interfaces*, vol. 5, no. 21, pp. 11427–11433, 2013.

[136] J. M. Ge *et al.*, "$MoSe_2$/N-Doped Carbon as Anodes for Potassium-Ion Batteries," *Adv. Energy Mater.*, vol. 8, no. 29, pp. 1–7, 2018.

[137] A. A. Alazemi, A. D. Dysart, X. L. Phuah, V. G. Pol, and F. Sadeghi, "MoS_2 nanolayer coated carbon spheres as an oil additive for enhanced tribological performance," *Carbon N. Y.*, vol. 110, pp. 367–377, 2016.

[138] V. An, Y. Irtegov, and C. de Izarra, "Study of Tribological Properties of Nanolamellar WS_2 and MoS_2 as Additives to Lubricants," *J. Nanomater.*, vol. 2014, pp. 1–8, 2014.

[139] P. U. Aldana, F. Dassenoy, B. Vacher, T. Le Mogne, and B. Thiebaut, "WS_2 nanoparticles anti-wear and friction reducing properties on rough surfaces in the presence of ZDDP additive," *Tribol. Int.*, vol. 102, pp. 213–221, 2016.

[140] H. Waghray, T. S. Lee, and B. J. Tatarchuk, "A study of the tribological and electrical properties of sputtered and burnished transition metal dichalcogenide films," *Surf. Coatings Technol.*, vol. 76–77, no. 2, pp. 415–420, 1995.

[141] Y. Qin, D. Xiong, and J. Li, "Characterization and friction behavior of LST/PEO duplex-treated Ti6Al4V alloy with burnished MoS_2 film," *Appl. Surf. Sci.*, vol. 347, pp. 475–484, 2015.

[142] M. F. Cardinal, P. A. Castro, J. Baxi, H. Liang, and F. J. Williams, "Characterization and frictional behavior of nanostructured Ni-W-MoS_2 composite coatings," *Surf. Coatings Technol.*, vol. 204, no. 1–2, pp. 85–90, 2009.

[143] Y. Yao, S. Yao, L. Zhang, and H. Wang, “Electrodeposition and mechanical and corrosion resistance properties of Ni-W/SiC nanocomposite coatings,” *Mater. Lett.*, vol. 61, no. 1, pp. 67–70, 2007.

[144] Q. Cheng, Z. Yao, F. Zhang, S. Zhang, and M. Oleksander, “Microstructure and tribological property of Ni–MoS_2 composite coatings prepared by ultrasonic and mechanical stirring electrodeposition,” *Mater. Res. Express*, vol. 6, no. 12, pp. 126–137, 2020.

[145] B. Podgornik, D. Hren, and J. Vižintin, “Low-friction behaviour of boundary-lubricated diamond-like carbon coatings containing tungsten,” *Thin Solid Films*, vol. 476, no. 1, pp. 92–100, 2005.

[146] F. Gustavsson, P. Forsberg, and S. Jacobson, “Friction and wear behaviour of low-friction coatings in conventional and alternative fuels,” *Tribol. Int.*, vol. 48, pp. 22–28, 2012.

[147] F. Gustavsson, P. Forsberg, V. Renman, and S. Jacobson, “Formation of tribologically beneficial layer on counter surface with smart chemical design of DLC coating in fuel contact,” *Tribol. - Mater. Surfaces Interfaces*, vol. 6, no. 3, pp. 102–108, 2012.

[148] B. Podgornik, D. Hren, J. Vižintin, S. Jacobson, N. Stavlid, and S. Hogmark, “Combination of DLC coatings and EP additives for improved tribological behaviour of boundary lubricated surfaces,” *Wear*, vol. 261, no. 1, pp. 32–40, 2006.

[149] W. Choi, N. Choudhary, G. H. Han, J. Park, D. Akinwande, and Y. H. Lee, “Recent development of two-dimensional transition metal dichalcogenides and their applications,” *Mater. Today*, vol. 20, no. 3, pp. 116–130, 2017.

[150] C. Muratore, J. E. Bultman, S. M. Aouadi, and A. A. Voevodin, “In situ Raman spectroscopy for examination of high temperature tribological processes,” *Wear*, vol. 270, no. 3–4, pp. 140–145, 2011.

[151] F. Gustavsson and S. Jacobson, “Diverse mechanisms of friction induced self-organisation into a low-friction material–An overview of WS_2 tribofilm formation,” *Tribol. Int.*, vol. 101, pp. 340–347, 2016.

[152] H. Cao, F. Wen, J. T. M. De Hosson, and Y. T. Pei, “Instant WS_2 platelets reorientation of self-adaptive WS_2/a-C tribocoating,” *Mater. Lett.*, vol. 229, pp. 64–67, 2018.

[153] G. Levita, A. Cavaleiro, E. Molinari, T. Polcar, and M. C. Righi, “Sliding properties of MoS_2 layers: Load and interlayer orientation effects,” *J. Phys. Chem. C*, vol. 118, no. 25, pp. 13809–13816, 2014.

[154] T. W. Scharf and I. L. Singer, “Monitoring transfer films and friction instabilities with in situ Raman tribometry,” *Tribol. Lett.*, vol. 14, no. 1, pp. 3–8, 2003.

[155] I. L. Singer, S. D. Dvorak, K. J. Wahl, and T. W. Scharf, “Role of third bodies in friction and wear of protective coatings,” *J. Vac. Sci. Technol. A Vacuum, Surfaces, Film.*, vol. 21, no. 5, pp. S232–S240, 2003.

[156] K. J. Wahl and I. L. Singer, “Role of the third body in life enhancement of MoS_2,” *Tribol. Ser.*, vol. 31, pp. 407–413, 1996.

[157] I. L. Singer, “Mechanics and chemistry of solids in sliding contact,” *Langmuir*, vol. 12, no. 19, pp. 4486–4491, 1996.

[158] S. Fayeulle, P. D. Ehni, and I. L. Singer, “Paper V (ii) Role of transfer films in wear of MoS_2 coatings,” *Tribol. Ser.*, vol. 17, no. C, pp. 129–138, 1990.

[159] L. Isaeva *et al.*, “Amorphous W-S-N thin films: The atomic structure behind ultra-low friction,” *Acta Mater.*, vol. 82, pp. 84–93, 2015.

[160] J. R. Lince, “Effective application of solid lubricants in spacecraft mechanisms,” *Lubricants*, vol. 8, no. 7, pp. 1–57, 2020.

[161] N. Takahashi and S. Kashiwaya, “High resolution transmission electron microscopy observation of the MoS_2-Au interface formed due to stick-slip of MoS_2 sliding on Au in relation to the friction trace,” *Wear*, vol. 206, no. 1–2, pp. 8–14, 1997.

[162] J. Sundberg *et al.*, “Influence of Ti addition on the structure and properties of low-friction W-S-C coatings,” *Surf. Coatings Technol.*, vol. 232, pp. 340–348, 2013.

[163] J. R. Lince, “Doped MoS_2 coatings and their tribology,” in *Encyclopedia of Tribology*, Boston: Springer, 2013.

[164] H. M. K. D. G. Paul A. Singh, “An improved solid lubricant for bearings operating in space and terrestrial environements,” *44th Aerosp. Mech. Symp.*, vol. 44, pp. 141–150, 2018.

[165] A. Savan, E. Pflüger, P. Voumard, A. Schröer, and M. Simmonds, “Modern solid lubrication: Recent developments and applications of MoS_2,” *Lubr. Sci.*, vol. 12, no. 2, pp. 185–203, 2000.

[166] A. R. Lansdown, *Molybdenum disulphide lubrication*. Amsterdam: Elsevier, 1999.

[167] E. W. Roberts and W. B. Price, “In-vacuo, tribological properties of ‘high-rate’ sputtered MoS_2 applied to metal and ceramic substrates,” *MRS Proc.*, vol. 140, no. 251, pp. 140–251, 1988.

[168] B. . Scott, “An overview of lubrication and associated materials for vacuum service,” *AIP Conf. Proc.*, vol. 192, no. 1, pp. 39–51, 1989.

[169] T. Spalvins, “Lubrication with sputtered MoS_2 films: Principles, operation, and limitations,” *J. Mater. Eng. Perform.*, vol. 1, no. 3, pp. 347–351, 1992.

[170] C. Donnet, J. M. Martin, T. Le Mogne, and M. Belin, “Super-low friction of MoS_2 coatings in various environments,” *Tribol. Int.*, vol. 29, no. 2, pp. 123–128, 1996.

[171] J. M. Martin, C. Donnet, T. Le Mogne, and T. Epicier, “Superlubricity of molybdenum disulphide,” *Phys. Rev. B*, vol. 48, no. 14, pp. 10583–10586, 1993.

[172] H. E. Sliney, “Solid lubricant materials for high temperatures–a review,” *Tribol. Int.*, vol. 15, no. 5, pp. 303–315, 1982.

[173] B. Vierneusel, T. Schneider, S. Tremmel, S. Wartzack, and T. Gradt, “Humidity resistant MoS_2 coatings deposited by unbalanced magnetron sputtering,” *Surf. Coatings Technol.*, vol. 235, pp. 97–107, 2013.

[174] I. L. Singer, S. Fayeulle, and P. D. Ehni, “Wear behavior of triode-sputtered MoS_2 coatings in dry sliding contact with steel and ceramics,” *Wear*, vol. 195, no. 1–2, pp.

7–20, 1996.

[175] T. Bin Yaqub, T. Vuchkov, P. Sanguino, T. Polcar, and A. Cavaleiro, “Comparative Study of DC and RF Sputtered $MoSe_2$ Coatings Containing Carbon—An Approach to Optimize Stoichiometry, Microstructure, Crystallinity and Hardness,” *Coatings*, vol. 10, no. 2, p. 133, 2020.

[176] J. C. Bernède, “About the preferential sputtering of chalcogen from transition metal dichalcogenide compounds and the determination of compound stoichiometry from XPS peak positions,” *Appl. Surf. Sci.*, vol. 171, no. 1–2, pp. 15–20, 2001.

[177] B. M. U. Scherzer, “Sputtering by particle bombardment II,” *Topics in Applied Physics*, vol. 52, pp. 271–355, 1983.

[178] I. M. Allam, “Solid lubricants for applications at elevated temperatures: A review,” *J. Mater. Sci.*, vol. 26, pp. 3977–3984, 1991.

[179] A. P. Nayak *et al.*, “Pressure-Modulated Conductivity, Carrier Density, and Mobility of Multilayered Tungsten Disulfide,” *ACS Nano*, no. 9, pp. 9117–9123, 2015.

[180] L. Rapoport, N. Fleischer, and R. Tenne, “Fullerene-like WS_2 nanoparticles: Superior lubricants for harsh conditions,” *Adv. Mater.*, vol. 15, no. 7–8, pp. 651–655, 2003.

[181] X. Li *et al.*, “Tribological properties of WS_2 coatings deposited on textured surfaces by electrohydrodynamic atomization,” *Surf. Coatings Technol.*, vol. 352, no. 2, pp. 128–143, 2018.

[182] K. C. Wong, X. Lu, J. Cotter, D. T. Eadie, P. C. Wong, and K. A. R. Mitchell, “Surface and friction characterization of MoS_2 and WS_2 third body thin films under simulated wheel/rail rolling-sliding contact,” *Wear*, vol. 264, no. 7–8, pp. 526–534, 2008.

[183] F. J. Clauss, *Solid lubricants and self-lubricating solids*. London: Elsevier, 2012.

[184] S. V. Prasad, I. S. Zabinski, and N. T. McDevitt, “Friction behavior of pulsed laser deposited tungsten disulfide films,” *Tribol. Trans.*, vol. 38, no. 1, pp. 57–62, 1995.

[185] S. Xu *et al.*, “In-situ friction and wear responses of WS_2 films to space environment: Vacuum and atomic oxygen,” *Appl. Surf. Sci.*, vol. 447, pp. 368–373, 2018.

[186] D. V. Shtansky *et al.*, “Structure and tribological properties of WSex, WSex/TiN, WSex/TiCN and WSex/TiSiN coatings,” *Surf. Coatings Technol.*, vol. 183, no. 2–3, pp. 328–336, 2004.

[187] S. Domínguez-Meister, T. C. Rojas, M. Brizuela, and J. C. Sánchez-López, “Solid lubricant behavior of MoS_2 and WSe_2-based nanocomposite coatings,” *Sci. Technol. Adv. Mater.*, vol. 18, no. 1, pp. 122–133, 2017.

[188] S. Dominguez-Meister, A. Justo, and J. C. Sanchez-Lopez, “Synthesis and tribological properties of WSex films prepared by magnetron sputtering,” *Mater. Chem. Phys.*, vol. 142, no. 1, pp. 186–194, 2013.

[189] S. Domi nguez-Meister, M. Conte, A. Igartua, T. C. Rojas, and J. C. Sánchez-Lopez, “Self-lubricity of WSex nanocomposite coatings,” *ACS Appl. Mater. Interfaces*, vol. 7, no. 15, pp. 7979–7986, 2015.

[190] D. V. Shtansky, A. N. Sheveyko, D. I. Sorokin, L. C. Lev, B. N. Mavrin, and P. V. Kiryukhantsev-Korneev, "Structure and properties of multi-component and multilayer TiCrBN/WSex coatings deposited by sputtering of TiCrB and WSe_2 targets," *Surf. Coatings Technol.*, vol. 202, no. 24, pp. 5953–5961, 2008.

[191] M. C. Simmonds, A. Savan, E. Pflüger, and H. Van Swygenhoven, "Mechanical and tribological performance of MoS_2 co-sputtered composites," *Surf. Coatings Technol.*, vol. 126, no. 1, pp. 15–24, 2000.

[192] M. Steinmann, A. Müller, and H. Meerkamm, "A new type of tribological coating for machine elements based on carbon, molybdenum disulphide and titanium diboride," *Tribol. Int.*, vol. 37, no. 11, pp. 879–885, 2004.

[193] D. Y. Wang, C. L. Chang, and W. Y. Ho, "Microstructure analysis of MoS_2 deposited on diamond-like carbon films for wear improvement," *Surf. Coatings Technol.*, vol. 111, no. 2–3, pp. 123–127, 1999.

[194] C. S. Sandu, T. Polcar, and A. Cavaleiro, "TEM investigation of MoSeC films," *Microsc. Microanal.*, vol. 14, no. 4, pp. 7–10, 2008.

[195] M. R. Hilton, R. Bauer, and P. D. Fleischauer, "Tribological performance and deformation of sputter-deposited MoS_2 solid lubricant films during sliding wear and indentation contact," *Thin Solid Films*, no. 2, pp. 219–236, 1990.

[196] X. Gao *et al.*, "Structural, Mechanical, and Tribological Properties of WS_2-Al Nanocomposite Film for Space Application," *Tribol. Lett.*, vol. 66, no. 4, pp. 1–12, 2018.

[197] G. Jayaram, N. Doraiswamy, L. D. Marks, and M. R. Hilton, "Ultrahigh vacuum high resolution transmission electron microscopy of sputter-deposited MoS_2 thin films," *Surf. Coatings Technol.*, vol. 68–69, no. 1, pp. 439–445, 1994.

[198] T. Spalvins, "Morphological and frictional behavior of sputtered MoS_2 films," *Thin Solid Films*, vol. 96, no. 1, pp. 17–24, 1982.

[199] S. Xu *et al.*, "Morphology evolution of Ag alloyed WS_2 films and the significantly enhanced mechanical and tribological properties," *Surf. Coatings Technol.*, vol. 238, pp. 197–206, 2014.

[200] B. Peng, H. Zhang, H. Shao, Y. Xu, X. Zhang, and H. Zhu, "Thermal conductivity of monolayer MoS_2, $MoSe_2$, and WS_2: Interplay of mass effect, interatomic bonding and anharmonicity," *RSC Adv.*, vol. 6, no. 7, pp. 5767–5773, 2016.

[201] S. Sahoo, A. P. S. Gaur, M. Ahmadi, M. J. F. Guinel, and R. S. Katiyar, "Temperature-dependent Raman studies and thermal conductivity of few-layer MoS_2," *J. Phys. Chem. C*, vol. 117, no. 17, pp. 9042–9047, 2013.

[202] J. J. Bae *et al.*, "Thickness-dependent in-plane thermal conductivity of suspended MoS_2 grown by chemical vapor deposition," *Nanoscale*, vol. 9, no. 7, pp. 2541–2547, 2017.

[203] C. Muratore *et al.*, "Thermal anisotropy in nano-crystalline MoS_2 thin films," *Phys. Chem. Chem. Phys.*, vol. 16, no. 3, pp. 1008–1014, 2014.

[204] F. Gustavsson, F. Svahn, U. Bexell, and S. Jacobson, "Nanoparticle based and

sputtered WS_2 low-friction coatings–Differences and similarities with respect to friction mechanisms and tribofilm formation," *Surf. Coatings Technol.*, vol. 232, pp. 616–626, 2013.

[205] T. W. Scharf and S. V. Prasad, "Solid lubricants: a review," *J. Mater. Sci.*, vol. 48, no. 2, pp. 511–531, 2013.

[206] T. W. Scharf, A. Rajendran, R. Banerjee, and F. Sequeda, "Growth, structure and friction behavior of titanium doped tungsten disulphide (Ti-WS_2) nanocomposite thin films," *Thin Solid Films*, vol. 517, no. 19, pp. 5666–5675, 2009.

[207] Z. Chen, X. He, C. Xiao, and S. H. Kim, "Effect of humidity on friction and Wear-A critical review," *Lubricants*, vol. 6, no. 3, pp. 1–26, 2018.

[208] X. Zhao, G. Zhang, L. Wang, and Q. Xue, "The Tribological Mechanism of MoS_2 Film under Different Humidity," *Tribol. Lett.*, vol. 65, no. 2, pp. 1–8, 2017.

[209] J. P. Nabot, A. Aubert, R. Gillet, and P. Renaux, "Cathodic sputtering for preparation of lubrication films," *Surf. Coatings Technol.*, vol. 43–44, no. 2, pp. 629–639, 1990.

[210] X. Zhang, B. Prakash, W. Lauwerens, X. Zhu, J. He, and J. P. Celis, "Low-friction MoSx coatings resistant to wear in ambient air of low and high relative humidity," *Tribol. Lett.*, vol. 14, no. 2, pp. 131–135, 2003.

[211] L. Joly-Pottuz and M. Iwaki, "Superlubricity of Tungsten Disulfide Coatings in Ultra High Vacuum," in *Superlubricity*, Elsevier, pp. 227–236, 2007.

[212] S. Watanabe, J. Noshiro, and S. Miyake, "Tribological characteristics of WS_2/MoS_2 solid lubricating multilayer films," *Surf. Coatings Technol.*, vol. 183, no. 2–3, pp. 347–351, 2003.

[213] A. Nossa and A. Cavaleiro, "The influence of the addition of C and N on the wear behaviour of W-S-C/N coatings," *Surf. Coatings Technol.*, vol. 142–144, pp. 984–991, 2001.

[214] A. Nossa and A. Cavaleiro, "Mechanical behaviour of W-S-N and W-S-C sputtered coatings deposited with a Ti interlayer," *Surf. Coatings Technol.*, vol. 163–164, pp. 552–560, 2003.

[215] A. Nossa, A. Cavaleiro, N. J. M. Carvalho, B. J. Kooi, and J. T. M. De Hosson, "On the microstructure of tungsten disulfide films alloyed with carbon and nitrogen," *Thin Solid Films*, vol. 484, no. 1–2, pp. 389–395, 2005.

[216] H. S. Khare and D. L. Burris, "The effects of environmental water and oxygen on the temperature-dependent friction of sputtered molybdenum disulfide," *Tribol. Lett.*, vol. 52, no. 3, pp. 485–493, 2013.

[217] E. P. Kingsbury, "Solid film lubrication at high temperature," *A S L E Trans.*, vol. 1, no. 1, pp. 121–123, 1958.

[218] H. S. Khare and D. L. Burris, "Surface and subsurface contributions of oxidation and moisture to room temperature friction of molybdenum disulfide," *Tribol. Lett.*, vol. 53, no. 1, pp. 329–336, 2014.

[219] H. Torres, M. Rodríguez Ripoll, and B. Prakash, "Tribological behaviour of self-lubricating materials at high temperatures," *Int. Mater. Rev.*, vol. 63, no. 5, pp. 309–

340, 2018.

[220] J. Caessa, T. Vuchkov, T. Bin Yaqub, and A. Cavaleiro, “On the microstructural, mechanical and tribological properties of Mo-Se-C coatings and their potential for friction reduction against rubber,” *Materials (Basel).*, vol. 14, no. 6, 2021.

[221] B. C. Windom, W. G. Sawyer, and D. W. Hahn, “A Raman spectroscopic study of MoS_2 and MoO_3: Applications to tribological systems,” *Tribol. Lett.*, vol. 42, no. 3, pp. 301–310, 2011.

[222] M. Yamamoto, T. L. Einstein, M. S. Fuhrer, and W. G. Cullen, “Anisotropic etching of atomically thin MoS_2,” *J. Phys. Chem. C*, vol. 117, no. 48, pp. 25643–25649, 2013.

[223] W. L. Spychalski, M. Pisarek, and R. Szoszkiewicz, “Microscale Insight into Oxidation of Single MoS_2 Crystals in Air,” *J. Phys. Chem. C*, vol. 121, no. 46, pp. 26027–26033, 2017.

[224] F. Meng, C. Yang, and H. Han, “Study on tribological performances of MoS_2 coating at high temperature,” *Proc. Inst. Mech. Eng. Part J J. Eng. Tribol.*, vol. 232, no. 8, pp. 964–973, 2018.

[225] T. Polcar, M. Evaristo, M. Stuebeur, and A. Cavaleiro, “Mechanical and tribological properties of sputtered Mo–Se–C coatings,” *Wear*, vol. 266, no. 3–4, pp. 393–397, 2009.

[226] T. Hudec *et al.*, “Structure, mechanical and tribological properties of $MoSe_2$ and Mo-Se-N solid lubricant coatings,” *Surf. Coatings Technol.*, vol. 405, p. 126536, 2021.

[227] J. K. Lancaster, “A review of the influence of environmental humidity and water on friction, lubrication and wear,” *Tribol. Int.*, vol. 23, no. 6, pp. 371–389, 1990.

[228] J. L. Grosseau-Poussard, P. Moine, and M. Brendle, “Shear strength measurements of parallel MoSx thin films,” *Thin Solid Films*, vol. 307, no. 1–2, pp. 163–168, 1997.

[229] E. Serpini *et al.*, “Nanoscale frictional properties of ordered and disordered MoS_2,” *Tribol. Int.*, vol. 136, pp. 67–74, 2019.

[230] J. W. Midgley, “The Frictional Properties of Molybdenum Disulphide,” *Jour Inst. Pet.*, vol. 42, pp. 312–315, 1956.

[231] J. Gänsheimer, “Influence of Certain Vapors and Liquids on the Frictional Properties of Molybdenum Disulfide,” *A S L E Trans.*, vol. 10, no. 4, pp. 390–399, 1967.

[232] T. Polcar, M. Evaristo, R. Colaço, C. Silviu Sandu, and A. Cavaleiro, “Nanoscale triboactivity: The response of Mo-Se-C coatings to sliding,” *Acta Mater.*, vol. 56, no. 18, pp. 5101–5111, 2008.

[233] L. E. Seitzman, R. N. Bolster, and I. L. Singer, “Effects of temperature and ion-to-atom ratio on the orientation of IBAD MoS_2 coatings,” *Thin Solid Films*, vol. 260, no. 2, pp. 143–147, 1995.

[234] R. N. Bolster, I. L. Singer, J. C. Wegand, S. Fayeulle, and C. R. Gossett, “Preparation by ion-beam-assisted deposition, analysis and tribological behavior of MoS_2 films,” *Surf. Coatings Technol.*, vol. 46, no. 2, pp. 207–2116, 1991.

[235] J. L. Grosseau-Poussard, P. Moine, and J. P. Villain, “Microstructural and tribological

characterization of MoSx coatings produced by high-energy ion-beam-assisted deposition, Thin Solid Films," *Thin Solid Films*, vol. 224, no. 1, pp. 52–57, 1993.

[236] Y. Lian, H. Chen, J. Deng, B. Yao, D. Deng, and S. Lei, "Preparation and property characterization of WS_2 coatings deposited on micro-nano textured surfaces of cemented carbide at different WS_2 target currents," *Int. J. Refract. Met. Hard Mater.*, vol. 72, pp. 286–291, 2018.

[237] D. Kokalj *et al.*, "Controlling the structural, mechanical and frictional properties of MoSx coatings by high-power impulse magnetron sputtering," *Coatings*, vol. 10, no. 8, p. 755, 2020.

[238] J. F. Curry *et al.*, "Highly Oriented MoS_2 Coatings: Tribology and Environmental Stability," *Tribol. Lett.*, vol. 64, no. 1, pp. 1–9, 2016.

[239] R. Zhang *et al.*, "Modification of structure and wear resistance of closed-field unbalanced-magnetron sputtered MoS_2 film by vacuum-heat-treatment," *Surf. Coatings Technol.*, vol. 401, p.126215, 2020.

[240] C. Muratore and A. A. Voevodin, "Control of molybdenum disulfide basal plane orientation during coating growth in pulsed magnetron sputtering discharges," *Thin Solid Films*, vol. 517, no. 19, pp. 5605–5610, 2009.

[241] V. Buck, "Preparation and properties of different types of sputtered MoS_2 films," *Wear*, vol. 114, no. 3, pp. 263–274, 1987.

[242] J. Moser and F. Lévy, "Growth mechanisms and near-interface structure in relation to orientation of MOS_2 sputtered thin films," *J. Mater. Res.*, vol. 7, no. 3, pp. 734–740, 1992.

[243] F. Lévy and J. Moser, "High-resolution cross-sectional studies and properties of molybdenite coatings," *Surf. Coatings Technol.*, vol. 68–69, pp. 433–438, 1994.

[244] J. Moser, F. Lévy, and F. Bussy, "Composition and growth mode of MoSx sputtered films," *J. Vac. Sci. Technol. A Vacuum, Surfaces, Film.*, vol. 12, no. 2, pp. 494–500, 1994.

[245] M. Regula, C. Ballif, J. H. Moser, and F. Lévy, "Structural, chemical, and electrical characterisation of reactively sputtered WSx thin films," *Thin Solid Films*, vol. 280, no. 1–2, pp. 67–75, 1996.

[246] X. Zhang, R. G. Vitchev, W. Lauwerens, L. Stals, J. He, and J. P. Celis, "Effect of crystallographic orientation on fretting wear behaviour of MoSx coatings in dry and humid air," *Thin Solid Films*, vol. 396, no. 1–2, pp. 69–77, 2001.

[247] R. Bichsel and F. Levy, "Morphological and compositional properties of $MoSe_2$ films prepared by r.f. magnetron sputtering, Thin Solid Films," *Thin Solid Films*, vol. 116, no. 4, pp. 367–372, 1984.

[248] M. Hu *et al.*, "Low Deposition Temperature-Induced Changes of the Microstructure and Tribological Property of WS_2 Film," *Coatings*, vol. 9, no. 4, p. 227, 2019.

[249] B. C. Stupp, "Synergistic effects of metals co-sputtered with MoS_2," *Thin Solid Films*, vol. 84, no. 3, pp. 257–266, 1981.

[250] D. G. Teer, J. Hampshire, V. Fox, and V. Bellido-Gonzalez, "The tribological

properties of MoS_2/metal composite coatings deposited by closed field magnetron sputtering," *Surf. Coatings Technol.*, vol. 94–95, pp. 572–577, 1997.

[251] E. Arslan, F. Bülbül, A. Alsaran, A. Celik, and I. Efeoglu, "The effect of deposition parameters and Ti content on structural and wear properties of MoS_2-Ti coatings," *Wear*, vol. 259, no. 7–12, pp. 814–819, 2005.

[252] X. Qin, P. Ke, A. Wang, and K. H. Kim, "Microstructure, mechanical and tribological behaviors of MoS_2-Ti composite coatings deposited by a hybrid HIPIMS method," *Surf. Coatings Technol.*, vol. 228, pp. 275–281, 2013.

[253] P. Wang, G. Zhang, Z. Lu, W. Yue, and L. Zhu, "Effect of electric currents on tribological behaviors of Ti/MoS_2 composite film sliding against aluminum," *Surf. Topogr. Metrol. Prop.*, vol. 7, no. 2, 2019.

[254] H. Li, X. Li, G. Zhang, L. Wang, and G. Wu, "Exploring the Tribophysics and Tribochemistry of MoS_2 by Sliding MoS_2/Ti Composite Coating Under Different Humidity," *Tribol. Lett.*, vol. 65, no. 2, pp. 1–10, 2017.

[255] F. Gustavsson, M. Bugnet, T. Polcar, A. Cavaleiro, and S. Jacobson, "A High-Resolution TEM/EELS Study of the Effect of Doping Elements on the Sliding Mechanisms of Sputtered WS_2 Coatings," *Tribol. Trans.*, vol. 58, no. 1, pp. 113–118, 2015.

[256] J. Hardell, I. Efeoğlu, and B. Prakash, "Tribological degradation of MoS_2-Ti sputtered coating when exposed to elevated temperatures," *Tribol. - Mater. Surfaces Interfaces*, vol. 4, no. 3, pp. 121–129, 2010.

[257] M. Cao, L. Zhao, L. Wu, and W. Wang, "Tribological properties of new Cu-Al/MoS_2 solid lubricant coatings using magnetron sputter deposition," *Coatings*, vol. 8, no. 4, p.134, 2018.

[258] W. H. Kao and Y. L. Su, "Optimum MoS_2-Cr coating for sliding against copper, steel and ceramic balls," *Mater. Sci. Eng. A*, vol. 368, no. 1–2, pp. 239–248, 2004.

[259] H. Li, G. Zhang, and L. Wang, "The role of tribo-pairs in modifying the tribological behavior of the MoS_2/Ti composite coating," *J. Phys. D. Appl. Phys.*, vol. 49, no. 9, 2016.

[260] Ö. Baran, F. Bidev, H. Çiçek, L. Kara, I. Efeoğlu, and T. Küçükömeroğlu, "Investigation of the friction and wear properties of Ti/TiB_2/MoS_2 graded-composite coatings deposited by CFUBMS under air and vacuum conditions," *Surf. Coatings Technol.*, vol. 260, pp. 310–315, 2014.

[261] R. Gilmore, M. A. Baker, P. N. Gibson, and W. Gissler, "Preparation and characterisation of low-friction TiB_2-based coatings by incorporation of C or MoS_2," *Surf. Coatings Technol.*, vol. 105, no. 1–2, pp. 45–50, 1998.

[262] M. Berger, M. Larsson, and S. Hogmark, "Evaluation of magnetron-sputtered TiB_2 intended for tribological applications," *Surf. Coatings Technol.*, vol. 124, no. 2–3, pp. 253–261, 2000.

[263] S. Prasad, S. Walck, and J. Zabinski, "Microstructural evolution in lubricious ZnO films grown by pulsed laser deposition," *Thin Solid Films*, vol. 360, no. 1–2, pp. 107–117, 2000.

[264] M. Cao, L. Zhao, W. Wang, H. Han, and W. Lang, "Effects of dopants Ti and Al on microstructure, mechanical and tribological behaviors of ZnO/MoS_2 coating deposited by magnetron co-sputtering," *AIP Adv.*, vol. 9, no. 4, p.045105, 2019.

[265] A. A. Voevodin, J. P. O'Neill, and J. S. Zabinski, "Nanocomposite tribological coatings for aerospace applications," *Surf. Coatings Technol.*, vol. 116–119, pp. 36–45, 1999.

[266] S. Mikhailov *et al.*, "Morphology and tribological properties of metal (oxide)-MoS_2 nanostructured multilayer coatings," *Surf. Coatings Technol.*, vol. 105, no. 1–2, pp. 175–183, 1998.

[267] J. S. Zabinski, M. S. Donley, V. J. Dyhouse, and N. T. McDevitt, "Chemical and tribological characterization of PbO-MoS_2 films grown by pulsed laser deposition," *Thin Solid Films*, vol. 214, no. 2, pp. 156–163, 1992.

[268] C. Klenke, "Tribological performance of MoS_2-B_2O_3 compacts," *Tribol. Int*, vol. 32, no. 1, pp. 23–26, 1990.

[269] J. F. Curry, T. F. Babuska, M. T. Brumbach, and N. Argibay, "Temperature-Dependent Friction and Wear of MoS_2/Sb_2O_3/Au Nanocomposites," *Tribol. Lett.*, vol. 64, no. 1, pp. 1–5, 2016.

[270] J. S. Zabinski, M. S. Donley, and N. T. McDevitt, "Mechanistic study of the synergism between Sb_2O_3 and MoS_2 lubricant systems using Raman spectroscopy," *Wear*, vol. 165, no. 1, pp. 103–108, 1993.

[271] J. S. Zabinski, M. S. Donley, S. D. Walck, T. R. Schneider, and N. T. McDevitt, "The Effects of Dopants on the Chemistry and Tribology of Sputter-Deposited MoS_2 Films," *Tribol. Trans.*, vol. 38, no. 4, pp. 894–904, 1995.

[272] M. A. Hamilton *et al.*, "A possible link between macroscopic wear and temperature dependent friction behaviors of MoS_2 coatings," *Tribol. Lett.*, vol. 32, no. 2, pp. 91–98, 2008.

[273] M. R. Hilton, G. Jayaram, and L. D. Marks, "Microstructure of cosputter-deposited metal- and oxide-MoS_2 solid lubricant thin films," *J. Mater. Res.*, vol. 13, no. 4, pp. 1022–1032, 1998.

[274] S. Gangopadhyay, R. Acharya, A. K. Chattopadhyay, and S. Paul, "Composition and structure-property relationship of low friction, wear resistant TiN-MoSx composite coating deposited by pulsed closed-field unbalanced magnetron sputtering," *Surf. Coatings Technol.*, vol. 203, no. 12, pp. 1565–1572, 2009.

[275] P. J. John, S. V. Prasad, A. A. Voevodin, and J. S. Zabinski, "Calcium sulfate as a high temperature solid lubricant," *Wear*, vol. 219, no. 2, pp. 155–161, 1998.

[276] H. Singh, K. C. Mutyala, H. Mohseni, T. W. Scharf, R. D. Evans, and G. L. Doll, "Tribological Performance and Coating Characteristics of Sputter-Deposited Ti-Doped MoS_2 in Rolling and Sliding Contact," *Tribol. Trans.*, vol. 58, no. 5, pp. 767–777, 2015.

[277] X. Z. Ding, X. T. Zeng, X. Y. He, and Z. Chen, "Tribological properties of Cr- and Ti-doped MoS_2 composite coatings under different humidity atmosphere," *Surf. Coatings Technol.*, vol. 205, no. 1, pp. 224–231, 2010.

[278] A. Savan *et al.*, "Effects of temperature on the chemistry and tribology of co-sputtered MoSx-Ti composite thin films," *Thin Solid Films*, vol. 489, no. 1–2, pp. 137–144, 2005.

[279] M. C. Simmonds, A. Savan, H. Van Swygenhoven, E. Pflüger, and S. Mikhailov, "Structural, morphological, chemical and tribological investigations of sputter deposited MoSx/metal multilayer coatings," *Surf. Coatings Technol.*, vol. 108–109, no. 1, pp. 340–344, 1998.

[280] W. D. Sun *et al.*, "Turbulence-like Cu/MoS_2 films: Structure, mechanical and tribological properties," *Surf. Coatings Technol.*, vol. 422, no. 3 , p. 127490, 2021.

[281] Y. Xu *et al.*, "The effect of Si content on the structure and tribological performance of MoS_2/Si coatings," *Surf. Coatings Technol.*, vol. 403, pp. 126–362, 2020.

[282] C. Zeng, J. Pu, H. Wang, S. Zheng, L. Wang, and Q. Xue, "Study on atmospheric tribology performance of MoS_2–W films with self-adaption to temperature," *Ceram. Int.*, vol. 45, no. 13, pp. 15834–15842, 2019.

[283] H. H. Chien, K. J. Ma, S. V. P. Vattikuti, C. H. Kuo, C. B. Huo, and C. L. Chao, "Tribological behaviour of MoS_2/Au coatings," *Thin Solid Films*, vol. 518, no. 24, pp. 7532–7534, 2010.

[284] J. R. Lince, H. I. Kim, P. M. Adams, D. J. Dickrell, and M. T. Dugger, "Nanostructural , electrical , and tribological properties of composite Au–MoS_2 coatings," *Thin Solid Films*, vol. 517, no. 18, pp. 5516–5522, 2009.

[285] J. R. Lince, "Tribology of co-sputtered nanocomposite Au/MoS_2 solid lubricant films over a wide contact stress range," *Tribol. Lett.*, vol. 17, no. 3, pp. 419–428, 2004.

[286] H. Li, G. Zhang, and L. Wang, "Low humidity-sensitivity of MoS_2/Pb nanocomposite coatings," *Wear*, vol. 350–351, pp. 1–9, 2016.

[287] I. L. Wahl, K J, Seitzman, L E, Bolster and R N, Singer, "Low Friction, High Endurance Ion-Beam Deposited Pb-Mo-S Coatings," *Surf. Coatings Technol.*, vol. 73, no. 3, pp. 152–159, 1995.

[288] J. Yi *et al.*, "Enhanced tribological properties of Y/MoS_2 composite coatings prepared by chemical vapor deposition," *Ceram. Int.*, vol. 46, no. 15, pp. 23813–23819, 2020.

[289] J. Nainaparampil, A. R. Phani, J. E. Krzanowski, and J. S. Zabinski, "Pulsed laser-ablated MoS_2-Al films: Friction and wear in humid conditions," *Surf. Coatings Technol.*, vol. 187, no. 2–3, pp. 326–335, 2004.

[290] I. Efeoglu, Ö. Baran, F. Yetim, and S. Altintaş, "Tribological characteristics of MoS_2-Nb solid lubricant film in different tribo-test conditions," *Surf. Coatings Technol.*, vol. 203, no. 5–7, pp. 766–770, 2008.

[291] J. Pimentel, T. Polcar, and A. Cavaleiro, "Structural, mechanical and tribological properties of Mo–S–C solid lubricant coating," *Surf. Coat. Technol.*, vol. 205, pp. 3274–3279, 2011.

[292] J. Xu, L. Chai, L. Qiao, T. He, and P. Wang, "Influence of C dopant on the structure, mechanical and tribological properties of r.f.-sputtered MoS_2/a-C composite films," *Appl. Surf. Sci.*, vol. 364, pp. 249–256, 2016.

[293] L. Gu, P. Ke, Y. Zou, X. Li, and A. Wang, “Amorphous self-lubricant MoS_2-C sputtered coating with high hardness,” *Appl. Surf. Sci.*, vol. 331, pp. 66–71, 2015.

[294] M. Evaristo, T. Polcar, and A. Cavaleiro, “Tribological behaviour of C-alloyed transition metal dichalcogenides (TMD) coatings in different environments,” *Int. J. Mech. Mater. Des.*, vol. 4, no. 2, pp. 137–143, 2008.

[295] V. Y. Fominski, S. N. Grigoriev, J. P. Celis, R. I. Romanov, and V. B. Oshurko, “Structure and mechanical properties of W-Se-C/diamond-like carbon and W-Se/diamond-like carbon bi-layer coatings prepared by pulsed laser deposition,” *Thin Solid Films*, vol. 520, no. 21, pp. 6476–6483, 2012.

[296] L. Li *et al.*, “The superlattice structure and self-adaptive performance of C–Ti/MoS_2 composite coatings,” *Ceram. Int.*, vol. 46, no. 5, pp. 5733–5744, 2020.

[297] A. A. Voevodin and J. S. Zabinski, “Nanocomposite and nanostructured tribological materials for space applications,” *Compos. Sci. Technol.*, vol. 65, no. 5, pp. 741–748, 2005.

[298] J. H. Wu, M. Sanghavi, J. H. Sanders, A. A. Voevodin, J. S. Zabinski, and D. A. Rigney, “Sliding behavior of multifunctional composite coatings based on diamond-like carbon,” *Wear*, vol. 255, no. 7–12, pp. 859–868, 2003.

[299] A. A. Voevodin and J. S. Zabinski, “Supertough wear-resistant coatings with ‘chameleon’ surface adaptation,” *Thin Solid Films*, vol. 370, no. 1, pp. 223–231, 2000.

[300] J. H. Wu, D. A. Rigney, M. L. Falk, J. H. Sanders, A. A. Voevodin, and J. S. Zabinski, “Tribological behavior of WC/DLC/WS_2 nanocomposite coatings,” *Surf. Coatings Technol.*, vol. 188–189, pp. 605–611, 2004.

[301] Z. Duan *et al.*, “Mo-S-Ti-C Nanocomposite Films for Solid-State Lubrication,” *ACS Appl. Nano Mater.*, vol. 2, no. 3, pp. 1302–1312, 2019.

[302] J. Noshiro, S. Watanabe, T. Sakurai, and S. Miyake, “Friction properties of co-sputtered sulfide/DLC solid lubricating films,” *Surf. Coatings Technol.*, vol. 200, no. 20–21, pp. 5849–5854, 2006.

[303] T. Takeno, S. Abe, K. Adachi, H. Miki, and T. Takagi, “Deposition and structural analyses of molybdenum-disulfide (MoS_2)-amorphous hydrogenated carbon (a-C:H) composite coatings,” *Diam. Relat. Mater.*, vol. 19, no. 5–6, pp. 548–552, 2010.

[304] Y. Wu, H. Li, L. Ji, Y. Ye, J. Chen, and H. Zhou, “A long-lifetime MoS_2/a-C:H nanoscale multilayer film with extremely low internal stress,” *Surf. Coatings Technol.*, vol. 236, pp. 438–443, 2013.

[305] J. Xu, T. F. He, L. Q. Chai, L. Qiao, P. Wang, and W. M. Liu, “Growth and characteristics of self-assembled MoS_2/Mo-S-C nanoperiod multilayers for enhanced tribological performance,” *Sci. Rep.*, vol. 6, no. 5, pp. 1–10, 2016.

[306] S. Cai *et al.*, “Friction and Wear Mechanism of MoS_2/C Composite Coatings Under Atmospheric Environment,” *Tribol. Lett.*, vol. 65, no. 3, pp. 1–12, 2017.

[307] Y. Wu *et al.*, “Influences of Space Irradiations on the Structure and Properties of MoS_2/DLC Lubricant Film,” *Tribol. Lett.*, vol. 64, no. 2, pp. 1–10, 2016.

[308] C. Wang, A. Hausberger, P. Nothdurft, J. M. Lackner, and T. Schwarz, “The potential

of tribological application of DLC/MoS_2 coated sealing materials," *Coatings*, vol. 8, no. 8, pp. 1–21, 2018.

[309] T. Polcar, M. Evaristo, and A. Cavaleiro, "Comparative study of the tribological behavior of self-lubricating W-S-C and Mo-Se-C sputtered coatings," *Wear*, vol. 266, no. 3–4, pp. 388–392, 2009.

[310] M. Evaristo, A. Nossa, and A. Cavaleiro, "Tribological behaviour of reactive and co-sputtered W-S-C coatings," *Ciência Tecnol Dos Mater*, vol. 18, pp. 21–26, 2006.

[311] T. Polcar, M. Evaristo, and A. Cavaleiro, "The tribological behavior of W-S-C films in pin-on-disk testing at elevated temperature," *Vacuum*, vol. 81, no. 11–12, pp. 1439–1442, 2007.

[312] T. Polcar, M. Evaristo, and A. Cavaleiro, "Friction of Self-Lubricating W-S-C Sputtered Coatings Sliding Under Increasing Load," *Plasma Process. Polym.*, vol. 4, no. S1, pp. S541–S546, 2007.

[313] T. Polcar, F. Gustavsson, T. Thersleff, S. Jacobson, and A. Cavaleiro, "Complex frictional analysis of self-lubricant W-S-C/Cr coating," *Faraday Discuss.*, vol. 156, pp. 383–401, 2012.

[314] J. V. Pimentel, T. Polcar, M. Evaristo, and A. Cavaleiro, "Examination of the tribolayer formation of a self-lubricant WSC sputtered coating," *Tribol. Int.*, vol. 47, pp. 188–193, 2012.

[315] H. Nyberg *et al.*, "Extreme friction reductions during initial running-in of W-S-C-Ti low-friction coatings," *Wear*, vol. 302, no. 1–2, pp. 987–997, 2013.

[316] C. Tomastik, A. Tomala, A. Pauschitz, and M. Roy, "The influence of carbon content on the microtribological performance of W-S-C films," *Proc. Inst. Mech. Eng. Part J J. Eng. Tribol.*, vol. 228, no. 7, pp. 745–755, 2014.

[317] T. Polcar, M. Evaristo, and A. Cavaleiro, "Self-lubricating W-S-C nanocomposite coatings," *Plasma Process. Polym.*, vol. 6, no. 6–7, pp. 417–424, 2009.

[318] H. Cao, J. T. M. De Hosson, and Y. Pei, "Effect of carbon concentration and argon flow rate on the microstructure and triboperformance of magnetron sputtered WS_2/a-C coatings," *Surf. Coatings Technol.*, vol. 332, pp. 142–152, 2017.

[319] H. Cao, F. Wen, S. Kumar, P. Rudolf, J. T. M. De Hosson, and Y. Pei, "On the S/W stoichiometry and triboperformance of $WS_xC(H)$ coatings deposited by magnetron sputtering," *Surf. Coatings Technol.*, vol. 365, pp. 41–51, 2019.

[320] T. Bin Yaqub, K. Hebbar Kannur, T. Vuchkov, C. Pupier, C. Héau, and A. Cavaleiro, "Molybdenum diselenide coatings as universal dry lubricants for terrestrial and aerospace applications," *Mater. Lett.*, vol. 275, p. 128035, 2020.

[321] F. Gustavsson, S. Jacobson, A. Cavaleiro, and T. Polcar, "Frictional behavior of self-adaptive nanostructural Mo-Se-C coatings in different sliding conditions," *Wear*, vol. 303, no. 1–2, pp. 286–296, 2013.

[322] A. Pauschitz and M. Roy, "Mechanical and friction properties of Mo-Se-C film at low load," *Surf. Coat. Technol.*, vol. 405, p. 126730, 2021.

[323] M. Evaristo, T. Polcar, and A. Cavaleiro, "Synthesis and properties of W-Se-C

coatings deposited by PVD in reactive and non-reactive processes," *Vacuum*, vol. 83, no. 10, pp. 1262–1265, 2009.

[324] X. Zhao, Z. Lu, G. Wu, G. Zhang, L. Wang, and Q. Xue, "Preparation and properties of DLC/MoS_2 multilayer coatings for high humidity tribology," *Mater. Res. Express*, vol. 3, no. 6, pp. 1–11, 2016.

[325] S. Mikhailov *et al.*, "Morphology and tribological properties of metal (oxide)–MoS_2 nanostructured multilayer coatings," *Surf. Coatings Technol.*, vol. 105, no. 1–2, pp. 175–183, 1998.

[326] M. R. Hilton, R. Bauer, S. V. Didziulis, M. T. Dugger, J. M. Keem, and J. Scholhamer, "Structural and tribological studies of MoS_2 solid lubricant films having tailored metal-multilayer nanostructures," *Surf. Coatings Technol.*, vol. 53, no. 1, pp. 13–23, 1992.

[327] G. B. Hopple, J. E. Keem, and S. H. Loewenthal, "Development of fracture resistant, multilayer films for precision ball bearings," *Wear*, vol. 162–164, pp. 919–924, 1993.

[328] G. Jayaram, L. D. Marks, and M. R. Hilton, "Nanostructure of Au-20% Pd layers in MoS_2 multilayer solid lubricant films," *Surf. Coatings Technol.*, vol. 76–77, pp. 393–399, 1995.

[329] M. C. Simmonds, A. Savan, H. Van Swygenhoven, and E. Pflüger, "Characterization of magnetron sputter deposited MoSx/metal multilayers," *Thin Solid Films*, vol. 354, no. 1, pp. 59–65, 1999.

[330] G. Colas, A. Saulot, E. Regis, and Y. Berthier, "Investigation of crystalline and amorphous MoS_2 based coatings: Towards developing new coatings for space applications," *Wear*, vol. 330–331, pp. 448–460, 2015.

[331] S. Xu, Y. Liu, M. Gao, K.-H. Kang, D.-G. Shin, and D.-E. Kim, "Superior lubrication of dense/porous-coupled nanoscale C/WS_2 multilayer coating on ductile substrate," *Appl. Surf. Sci.*, vol. 476, pp. 724–732, 2019.

[332] H. Ju *et al.*, "Improvement on the oxidation resistance and tribological properties of molybdenum disulfide film by doping nitrogen," *Mater. Des.*, vol. 186, p. 108300, 2020.

[333] H. Xiao and S. Liu, "2D nanomaterials as lubricant additive: A review," *Mater. Des.*, vol. 135, pp. 319–332, 2017.

[334] J. Kogovšek and M. Kalin, "Various MoS_2-, WS_2- and C-based micro- and nanoparticles in boundary lubrication," *Tribol. Lett.*, vol. 53, no. 3, pp. 585–597, 2014.

[335] P. Rabaso *et al.*, "Boundary lubrication: Influence of the size and structure of inorganic fullerene-like MoS_2 nanoparticles on friction and wear reduction," *Wear*, vol. 320, no. 1, pp. 161–178, 2014.

[336] M. Kalin, J. Kogovšek, and M. Remškar, "Mechanisms and improvements in the friction and wear behavior using MoS_2 nanotubes as potential oil additives," *Wear*, vol. 280–281, pp. 36–45, 2012.

[337] L. Rapoport, Y. Bilik, Y. Feldman, M. Homyonfer, S. R. Cohen, and R. Tenne, "Hollow nanoparticles of WS_2 as potential solid-state lubricants," *Nature*, vol. 387, no.

6635, pp. 791–793, 1997.

[338] Manish Chhowalla and Gehan A. J. Amaratunga, “Thin films of fullerene-like MoS_2 nanoparticles with ultra-low friction and wear,” *Nature*, vol. 407, no. 14, pp. 164–167, 2000.

[339] X. Hou, C. X. Shan, and K. L. Choy, “Microstructures and tribological properties of PEEK-based nanocomposite coatings incorporating inorganic fullerene-like nanoparticles,” *Surf. Coatings Technol.*, vol. 202, no. 11, pp. 2287–2291, 2008.

[340] L. Joly-Pottuz, F. Dassenoy, M. Belin, B. Vacher, J. M. Martin, and N. Fleischer, “Ultralow-friction and wear properties of IF-WS_2 under boundary lubrication,” *Tribol. Lett.*, vol. 18, no. 4, pp. 477–485, 2005.

[341] Y. Li, H. Lu, Q. Liu, L. Qin, and G. Dong, “A facile method to enhance the tribological performances of $MoSe_2$ nanoparticles as oil additives,” *Tribol. Int.*, vol. 137, pp. 22–29, 2019.

[342] A. Tomala *et al.*, “Synergisms and antagonisms between MoS_2 nanotubes and representative oil additives under various contact conditions,” *Tribol. Int.*, vol. 129, pp. 137–150, 2019.

[343] P. Rabaso *et al.*, “An investigation on the reduced ability of IF-MoS_2 nanoparticles to reduce friction and wear in the presence of dispersants,” *Tribol. Lett.*, vol. 55, no. 3, pp. 503–516, 2014.

[344] J. Dong *et al.*, “Facile synthesis of ultrathin $NbTe_2$ nanosheets for enhanced tribological properties as a lubricant additive,” *Cryst. Res. Technol.*, vol. 51, no. 11, pp. 671–680, 2016.

[345] E. L. K. Chng, Z. Sofer, and M. Pumera, “MoS_2 exhibits stronger toxicity with increased exfoliation,” *Nanoscale*, vol. 6, no. 23, pp. 14412–14418, 2014.

[346] E. Tan, B. L. Li, K. Ariga, C. T. Lim, S. Garaj, and D. T. Leong, “Toxicity of Two-Dimensional Layered Materials and Their Heterostructures,” *Bioconjug. Chem.*, vol. 30, no. 9, pp. 2287–2299, 2019.

[347] W. Z. Teo, E. L. K. Chng, Z. Sofer, and M. Pumera, “Cytotoxicity of exfoliated transition-metal dichalcogenides (MoS_2, WS_2, and WSe_2) is lower than that of graphene and its analogues,” *Chem. - A Eur. J.*, vol. 20, no. 31, pp. 9627–9632, 2014.

[348] S. P. Rodrigues, T. Polcar, S. Carvalho, and A. Cavaleiro, “The wettability and tribological behaviour of thin F-doped WS_2 films deposited by magnetron sputtering,” *Surf. Coatings Technol.*, vol. 378, p. 125033, 2019.

[349] P. E. Hovsepian, P. Mandal, A. P. Ehiasarian, G. Sáfrán, R. Tietema, and D. Doerwald, “Friction and wear behaviour of Mo-W doped carbon-based coating during boundary lubricated sliding,” *Appl. Surf. Sci.*, vol. 366, pp. 260–274, 2016.

[350] F. Zhao, H. Li, L. Ji, Y. Wang, H. Zhou, and J. Chen, “Ti-DLC films with superior friction performance,” *Diam. Relat. Mater.*, vol. 19, no. 4, pp. 342–349, 2010.

[351] S. V. Johnston and S. V. Hainsworth, “Effect of DLC coatings on wear in automotive applications,” *Surf. Eng.*, vol. 21, no. 1, pp. 67–71, 2005.

[352] J. A. Woollam *et al.*, “Diamondlike Carbon Applications in Infrared Optics and

Microelectronics," *Mater. Sci. Forum*, vol. 52–53, pp. 577–608, 1991.

[353] F. Piazza, D. Grambole, D. Schneider, C. Casiraghi, A. C. Ferrari, and J. Robertson, "Protective diamond-like carbon coatings for future optical storage disks," *Diam. Relat. Mater.*, vol. 14, no. 3–7, pp. 994–999, 2005.

[354] M. Sorgato, D. Masato, and G. Lucchetta, "Tribological effects of mold surface coatings during ejection in micro injection molding," *J. Manuf. Process.*, vol. 36, pp. 51–59, 2018.

[355] B. Saha, W. Q. Toh, E. Liu, S. B. Tor, D. E. Hardt, and J. Lee, "A review on the importance of surface coating of micro/nano-mold in micro/nano-molding processes," *J. Micromechanics Microengineering*, vol. 26, no. 1, p. 013002, 2015.

[356] M. Folea, A. Roman, and N. B. Lupulescu, "An overview of DLC coatings on cutting tools performance," *Acad. J. Manuf. Eng.*, vol. 8, no. 3, pp. 30–36, 2010.

[357] M. Dai, K. Zhou, Z. Yuan, Q. Ding, and Z. Fu, "The cutting performance of diamond and DLC-coated cutting tools," *Diam. Relat. Mater.*, vol. 9, no. 9–10, pp. 1753–1757, 2000.

[358] S. Grigoriev, M. Volosova, S. Fyodorov, M. Lyakhovetskiy, and A. Seleznev, "DLC-coating Application to Improve the Durability of Ceramic Tools," *J. Mater. Eng. Perform.*, vol. 28, no. 7, pp. 4415–4426, 2019.

[359] G. Dearnaley and J. H. Arps, "Biomedical applications of diamond-like carbon (DLC) coatings: A review," *Surf. Coatings Technol.*, vol. 200, no. 7, pp. 2518–2524, 2005.

[360] R. Hauert, K. Thorwarth, and G. Thorwarth, "An overview on diamond-like carbon coatings in medical applications," *Surf. Coatings Technol.*, vol. 233, no. 3, pp. 119–130, 2013.

[361] C. A. Love, R. B. Cook, T. J. Harvey, P. A. Dearnley, and R. J. K. Wood, "Diamond like carbon coatings for potential application in biological implants–A review," *Tribol. Int.*, vol. 63, no. 9, pp. 141–150, 2013.

[362] G. Wang and H. Zreiqat, "Functional coatings or films for hard-tissue applications," *Materials (Basel).*, vol. 3, no. 7, pp. 3994–4050, 2010.

[363] B. R. Manu, A. Gupta, and A. H. Jayatissa, "Tribological properties of 2D materials and composites–A review of recent advances," *Materials (Basel).*, vol. 14, no. 7, 2021.

[364] N. Dwivedi, S. Kumar, H. K. Malik, Govind, C. M. S. Rauthan, and O. S. Panwar, "Correlation of sp^3 and sp^2 fraction of carbon with electrical, optical and nano-mechanical properties of argon-diluted diamond-like carbon films," *Appl. Surf. Sci.*, vol. 257, no. 15, pp. 6804–6810, 2011.

[365] J. Robertson, "Diamond-like amorphous carbon," *Mater. Sci. Eng. R Reports*, vol. 37, no. 4–6, pp. 129–281, 2002.

[366] A. Erdemir and C. Donnet, "Tribology of diamond-like carbon films: Recent progress and future prospects," *J. Phys. D. Appl. Phys.*, vol. 39, no. 18, pp. 311–327, 2006.

[367] D. C. Sutton, G. Limbert, D. Stewart, and R. J. K. Wood, "The friction of diamond-like carbon coatings in a water environment," *Friction*, vol. 1, no. 3, pp. 210–221, 2013.

[368] M. Kalin, I. Velkavrh, J. Vižintin, and L. Ožbolt, "Review of boundary lubrication mechanisms of DLC coatings used in mechanical applications," *Meccanica*, vol. 43, no. 6, pp. 623–637, 2008.

[369] A. Erdemir, "The role of hydrogen in tribological properties of diamond-like carbon films," *Surf. Coatings Technol.*, vol. 146–147, pp. 292–297, 2001.

[370] H. Li, T. Xu, C. Wang, J. Chen, H. Zhou, and H. Liu, "Tribochemical effects on the friction and wear behaviors of a-C:H and a-C films in different environment," *Tribol. Int.*, vol. 40, no. 1, pp. 132–138, 2007.

[371] C. Donnet, J. Fontaine, A. Grill, and T. Le Mogne, "The role of hydrogen on the friction mechanism of diamond-like carbon films," *Tribol. Lett.*, vol. 9, no. 3–4, pp. 137–142, 2001.

[372] C. Meunier, P. Alers, L. Marot, J. Stauffer, N. Randall, and S. Mikhailov, "Friction properties of ta-C and a-C:H coatings under high vacuum," *Surf. Coatings Technol.*, vol. 200, no. 5–6, pp. 1976–1981, 2005.

[373] Y. Liu and E. I. Meletis, "Evidence of graphitization of diamond-like carbon films during sliding wear," *J. Mater. Sci.*, vol. 32, no. 13, pp. 3491–3495, 1997.

[374] Q. Zeng, O. Eryilmaz, and A. Erdemir, "Superlubricity of the DLC films-related friction system at elevated temperature," *RSC Adv.*, vol. 5, no. 113, pp. 93147–93154, 2015.

[375] Y. Liu, A. Erdemir, and E. I. Meletis, "A study of the wear mechanism of diamond-like carbon films," *Surf. Coatings Technol.*, vol. 82, no. 1–2, pp. 48–56, 1996.

[376] O. Wilhelmsson *et al.*, "Design of nanocomposite low-friction coatings," *Adv. Funct. Mater.*, vol. 17, no. 10, pp. 1611–1616, 2007.

[377] Y. Liu, A. Erdemir, and E. I. Meletis, "An investigation of the relationship between graphitization and frictional behavior of DLC coatings," *Surf. Coatings Technol.*, vol. 86–87, pp. 564–568, 1996.

[378] C. W. Ong *et al.*, "Thermal stability of pulsed laser deposited diamond-like carbon films," *Thin Solid Films*, vol. 258, no. 1–2, pp. 34–39, 1995.

[379] Z. Sun, J. R. Shi, B. K. Tay, and S. P. Lau, "UV Raman characteristics of nanocrystalline diamond films with different grain size," *Diam. Relat. Mater.*, vol. 9, no. 12, pp. 1979–1983, 2000.

[380] A. C. Ferrari and J. Robertson, "Interpretation of Raman spectra of disordered and amorphous carbon," *Phys. Rev*, vol. 61, no. 20, pp. 14095–14107, 2000.

[381] Y. Tokuta, M. Kawaguchi, A. Shimizu, and S. Sasaki, "Effects of pre-heat treatment on tribological properties of DLC film," *Tribol. Lett.*, vol. 49, no. 2, pp. 341–349, 2013.

[382] M. G. Kim, K. R. Lee, and K. Y. Eun, "Tribological behavior of silicon-incorporated diamond-like carbon films," *Surf. Coatings Technol.*, vol. 112, no. 1–3, pp. 204–209, 1999.

[383] N. K. Manninen, F. Ribeiro, A. Escudeiro, T. Polcar, S. Carvalho, and A. Cavaleiro, "Influence of Ag content on mechanical and tribological behavior of DLC coatings,"

Surf. Coatings Technol., vol. 232, pp. 440–446, 2013.

[384] C. W. Moura e Silva, J. R. T. Branco, and A. Cavaleiro, "How can H content influence the tribological behaviour of W-containing DLC coatings," *Solid State Sci.*, vol. 11, no. 10, pp. 1778–1782, 2009.

[385] O. Wänstrand, M. Larsson, and P. Hedenqvist, "Mechanical and tribological evaluation of PVD WC/C coatings," *Surf. Coatings Technol.*, vol. 111, no. 2–3, pp. 247–254, 1999.

[386] H. Ronkainen, S. Varjus, and K. Holmberg, "Friction and wear properties in dry, water- and oil-lubricated DLC against alumina and DLC against steel contacts," *Wear*, vol. 222, no. 2, pp. 120–128, 1998.

[387] M. I. De Barros *et al.*, "Friction reduction by metal sulfides in boundary lubrication studied by XPS and XANES analyses," *Wear*, vol. 254, no. 9, pp. 863–870, 2003.

[388] A. Morina, A. Neville, M. Priest, and J. H. Green, "ZDDP and MoDTC interactions and their effect on tribological performance–tribofilm characteristics and its evolution," *Tribol. Lett.*, vol. 24, no. 3, pp. 243–256, 2006.

[389] J. Zhang and H. Spikes, "On the Mechanism of ZDDP Antiwear Film Formation," *Tribol. Lett.*, vol. 63, no. 2, pp. 1–15, 2016.

[390] M. I. De Barros'Bouchet, J. M. Martin, T. Le-Mogne, and B. Vacher, "Boundary lubrication mechanisms of carbon coatings by MoDTC and ZDDP additives," *Tribol. Int.*, vol. 38, no. 3, pp. 257–264, 2005.

[391] T. Vuchkov, M. Evaristo, T. Bin Yaqub, T. Polcar, and A. Cavaleiro, "Synthesis, microstructure and mechanical properties of W–S–C self-lubricant thin films deposited by magnetron sputtering," *Tribol. Int.*, vol. 150, no. 5, p. 106363, 2020.

[392] F. Gustavsson, S. Jacobson, A. Cavaleiro, and T. Polcar, "Frictional behavior of self-adaptive nanostructural Mo–Se–C coatings in different sliding conditions," *Wear*, vol. 303, no. 1–2, pp. 286–296, 2013.

[393] A. Czyzniewski, "Preparation and characterisation of a-C and a-C:H coatings deposited by pulsed magnetron sputtering," *Surf. Coatings Technol.*, vol. 203, no. 8, pp. 1027–1033, 2009.

[394] B. Bhushan, "Chemical, mechanical and tribological characterization of ultra-thin and hard amorphous carbon coatings as thin as 3.5 nm: Recent developments," *Diam. Relat. Mater.*, vol. 8, no. 11, pp. 1985–2015, 1999.

[395] T. Asikainen, M. Ritala, and L. Markku, "DLC based coatings prepared by reactive d.c. magnetron sputtering," *Thin Solid Films*, vol. 440, pp. 60–65, 2003.

[396] W. Y. Lee, Y. J. Jang, T. Tokoroyama, M. Murashima, and N. Umehara, "Effect of defects on wear behavior in ta-C coating prepared by filtered cathodic vacuum arc deposition," *Diam. Relat. Mater.*, vol. 105, 2020.

[397] D. Sheeja, B. K. Tay, S. P. Lau, X. Shi, and X. Ding, "Structural and tribological characterization of multilayer ta-C films prepared by filtered cathodic vacuum arc with substrate pulse biasing," *Surf. Coatings Technol.*, vol. 132, no. 2–3, pp. 228–232, 2000.

[398] S. Sattel, J. Robertson, and H. Ehrhardt, “Effects of deposition temperature on the properties of hydrogenated tetrahedral amorphous carbon,” *J. Appl. Phys.*, vol. 82, no. 9, pp. 4566–4576, 1997.

[399] M. Weiler *et al.*, “Preparation and properties of highly tetrahedral hydrogenated amorphous carbon,” *Phys. Rev. B - Condens. Matter Mater. Phys.*, vol. 53, no. 3, pp. 1594–1608, 1996.

[400] J. T. Gudmundsson, “Physics and technology of magnetron sputtering discharges,” *Plasma Sources Sci. Technol.*, vol. 29, no. 11, pp. 1–54, 2020.

[401] K. S. Sree Harsha, *Principles of vapor deposition of thin films*. Elsevier, 2005.

[402] N. K. Jain, M. Sawant, and S. H. Nikam, “Metal Deposition: Plasma-Based Processes,” *Encycl. Plasma Technol.*, pp. 722–740, 2017.

[403] H. Baránková and L. Bárdos, *Handbook of Deposition Technologies for Films and Coatings*. Oxford: Elsevier, 2010.

[404] S. Berg and T. Nyberg, “Fundamental understanding and modeling of reactive sputtering processes,” *Thin Solid Films*, vol. 476, no. 2, pp. 215–230, 2005.

[405] M. Arif and C. Eisenmenger-Sittner, “In situ assessment of target poisoning evolution in magnetron sputtering,” *Surf. Coatings Technol.*, vol. 324, pp. 345–352, 2017.

[406] K. L. Choy, *Chemical Vapour Deposition (CVD), Advances, Technology, and Applications*. Boca Raton: CRC Press, 2019.

[407] B. Vengudusamy, “Behaviour of Lubricant Additives on DLC Coatings,” (Doctoral dissertation, Imperial College London), 2011.

[408] R. L. Boxman, “Recent developments in vacuum arc deposition,” *IEEE Trans. Plasma Sci.*, vol. 29, no. 5 I, pp. 762–767, 2001.

[409] B. K. Tay, Z. W. Zhao, and D. H. C. Chua, “Review of metal oxide films deposited by filtered cathodic vacuum arc technique,” *Materials Science and Engineering R: Reports*, vol. 52, no. 1–3. pp. 1–48, 2006.

[410] W. Song, P. P. Choi, G. Inden, U. Prahl, D. Raabe, and W. Bleck, “On the spheroidized carbide dissolution and elemental partitioning in high carbon bearing steel 100Cr6,” *Metall. Mater. Trans. A Phys. Metall. Mater. Sci.*, vol. 45, no. 2, pp. 595–606, 2014.

[411] F. Fernandes, M. Danek, T. Polcar, and A. Cavaleiro, “Tribological and cutting performance of TiAlCrN films with different Cr contents deposited with multilayered structure,” *Tribol. Int.*, vol. 119, pp. 345–353, 2018.

[412] A. Basu *et al.*, “Laser surface hardening of austempered (bainitic) ball bearing steel,” *Scr. Mater.*, vol. 56, no. 10, pp. 887–890, 2007.

[413] Simply Bearings Ltd, “AISI 52100 Chrome Steel Data Sheet.” [Online]. Available: https://simplybearings.co.uk/shop/files/52100.pdf.

[414] S. Z. Erhan and S. Asadauskas, “Lubricant basestocks from vegetable oils,” *Ind. Crops Prod.*, vol. 11, no. 2–3, pp. 277–282, 2000.

[415] R. Kreivaitis, M. Gumbytė, A. Kupčinskas, and K. Kazancev, “Investigating the

tribological properties of PILs derived from different ammonium cations and long chain carboxylic acid anion," *Tribiology Int.*, vol. 141, p. 105905, 2020.

[416] R. González, J. L. Viesca, A. H. Battez, M. Hadfield, A. Fernández-González, and M. Bartolomé, "Two phosphonium cation-based ionic liquids as lubricant additive to a polyalphaolefin base oil," *J. Mol. Liq.*, vol. 293, p. 111536, 2019.

[417] Phoenix Tribology Ltd, "TE77 HIGH FREQUENCY FRICTION MACHINE." [Online]. Available: http://www.phoenix-tribology.com/at2/leaflet/te77.

[418] J. J. Truhan, J. Qu, and P. J. Blau, "The effect of lubricating oil condition on the friction and wear of piston ring and cylinder liner materials in a reciprocating bench test," *Wear*, vol. 259, no. 7–12, pp. 1048–1055, 2005.

[419] B. B. He, *Two-Dimensional X-Ray Diffraction*. John Wiley & Sons, 2009.

[420] Z. Matej, L. Nichtova, and R. Kužel, "Microstructural characterization of nanocrystalline powders and thin films by x-ray powder diffraction," *NANOCON 2009 - 1st Int. Conf. Conf. Proc.*, pp. 53–60, 2009.

[421] M. Birkholz, *Thin Film Analysis by X-Ray Scattering*. John Wiley & Sons, 2006.

[422] M. Bouroushian and T. Kosanovic, "Characterization of Thin Films by Low Incidence X-Ray Diffraction," *Cryst. Struct. Theory Appl.*, vol. 01, no. 03, pp. 35–39, 2012.

[423] M. Raza, "Oxygen vacancy stabilized zirconia (OVSZ); synthesis and properties," (Doctoral dissertation, University of Mons), 2017.

[424] W. C. Oliver and G. M. Pharr, "An improved technique for determining hardness and elastic modulus using load and displacement sensing indentation experiments," *J. Mater. Res.*, vol. 7, no. 6, pp. 1564–1583, 1992.

[425] N. A. Sakharova, J. V. Fernandes, J. M. Antunes, and M. C. Oliveira, "Comparison between Berkovich, Vickers and conical indentation tests: A three-dimensional numerical simulation study," *Int. J. Solids Struct.*, vol. 46, no. 5, pp. 1095-1104, 2009.

[426] S. Zak, C. O. W. Trost, P. Kreiml, and M. J. Cordill, "Accurate measurement of thin film mechanical properties using nanoindentation," *J. Mater. Res.*, vol. 37, no. 7, pp. 1373–1389, 2022.

[427] S. Chen, L. Liu, and T. Wang, "Investigation of the mechanical properties of thin films by nanoindentation, considering the effects of thickness and different coating-substrate combinations," *Surf. Coatings Technol.*, vol. 191, no. 1, pp. 25–32, 2005.

[428] N. Barbakadze, S. Enders, S. Gorb, and E. Arzt, "Local mechanical properties of the head articulation cuticle in the beetle Pachnoda marginata (Coleoptera, Scarabaeidae)," *J. Exp. Biol.*, vol. 209, no. 4, pp. 722–730, 2006.

[429] W. Oliver and G. Pharr, "An improved technique for determining hardness and elastic modulus using load and displacement-sensing indentation systems," *J. Mater. Res.*, vol. 7, no. 6, pp. 1564–1583, 1992.

[430] Bruker alicona, "Focus-Variation." [Online]. Available: https://www.alicona.com/our-technology/focus-variation/.

[431] D. A. Macdonald, "The application of focus variation microscopy for lithic use-wear

quantification," *J. Archaeol. Sci.*, vol. 48, pp. 26–33, 2014.

[432] Y. Zheng, X. Zhang, S. Wang, Q. Li, H. Qin, and B. Li, "Similarity evaluation of topography measurement results by different optical metrology technologies for additive manufactured parts," *Opt. Lasers Eng.*, vol. 126, pp. 1–21, 2020.

[433] A. Amanov, Y. Pyun, J. Kim, and S. Sasaki, "The usability and preliminary effectiveness of ultrasonic nanocrystalline surface modification technique on surface properties of silicon carbide," *Appl. Surf. Sci.*, vol. 311, pp. 448–460, 2014.

[434] Britannica, "scanning electron microscope." [Online]. Available: https://www.britannica.com/technology/scanning-electron-microscope.

[435] A. Abdullah and A. Mohammed, "Scanning Electron Microscopy (SEM)," *Int. Conf. Hydraul. Pneum.*, vol. 2018, pp. 7–9, 2018.

[436] K. D. Vernon-Parry, "Scanning electron microscopy: an introduction," *III-Vs Rev.*, vol. 13, no. 4, pp. 40–44, 2000.

[437] M. Ezzahmouly *et al.*, "Micro-computed tomographic and SEM study of porous bioceramics using an adaptive method based on the mathematical morphological operations," *Heliyon*, vol. 5, no. 12, p. e02557, 2019.

[438] M. Scimeca, S. Bischetti, H. K. Lamsira, R. Bonfiglio, and E. Bonanno, "Energy dispersive X-ray (EDX) microanalysis: A powerful tool in biomedical research and diagnosis," *Eur. J. Histochem.*, vol. 62, no. 1, pp. 89–99, 2018.

[439] Thermo Fisher, "EDX Analysis with SEM: How Does it Work?" [Online]. Available: https://www.thermofisher.com/blog/microscopy/edx-analysis-with-sem-how-does-it-work/.

[440] T. E. Davies, H. Li, S. Bessette, R. Gauvin, G. S. Patience, and N. F. Dummer, "Experimental methods in chemical engineering: Scanning electron microscopy and X -ray ultra-microscopy—SEM and XuM," *Can. J. Chem. Eng.*, vol. 100, no.11, pp. 3145–3159, 2022.

[441] P. Kuisma-Kursula, "Accuracy, precision and detection limits of SEM-WDS, SEM-EDS and PIXE in the multi-elemental analysis of medieval glass," *X-Ray Spectrom.*, vol. 29, no. 1, pp. 111–118, 2000.

[442] D. E. Newbury, "Mistakes encountered during automatic peak identification of minor and trace constituents in electron-excited energy dispersive X-ray microanalysis," *Scanning*, vol. 31, no. 3, pp. 91–101, 2009.

[443] P. Schlossmacher, D. O. Klenov, B. Freitag, S. Von Harrach, and A. Steinbach, "Nanoscale Chemical Compositional Analysis with an Innovative S/TEM-EDX System," *Microsc. Anal. Nanotechnol. Suppl.*, vol. 24, pp. S5–S8, 2010.

[444] D. C. Bell and A. J. Garratt-Reed, *Energy Dispersive X-ray Analysis in the Electron Microscope*. London: Garland Science, 2003.

[445] A. Kudelski, "Analytical applications of Raman spectroscopy," *Talanta*, vol. 76, no. 1, pp. 1–8, 2008.

[446] A. Cantarero, "Raman Scattering Applied to Materials Science," *Procedia Mater. Sci.*, vol. 9, pp. 113–122, 2015.

[447] R. Panneerselvam *et al.*, “Surface-enhanced Raman spectroscopy: Bottlenecks and future directions,” *Chem. Commun.*, vol. 54, no. 1, pp. 10–25, 2017.

[448] H. Vašková, “A powerful tool for material identification: Raman spectroscopy,” *Int. J. Math. Model. Methods Appl. Sci.*, vol. 5, no. 7, pp. 1205–1212, 2011.

[449] J. V. Pimentel, “Adaptive self-lubricating low-friction coatings,” (Doctoral dissertation, Czech Technical University), 2013.

[450] P. R. Munroe, “The application of focused ion beam microscopy in the material sciences,” *Mater. Charact.*, vol. 60, no. 1, pp. 2–13, 2008.

[451] K. Sloyan, H. Melkonyan, H. Apostoleris, M. S. Dahlem, M. Chiesa, and A. Al Ghaferi, “A review of focused ion beam applications in optical fibers,” *Nanotechnology*, vol. 32, no. 47, p. 472004, 2021.

[452] Jeol, “focused ion-beam milling.” [Online]. Available: https://www.jeol.co.jp/en/words/emterms/search_result.html?keyword=focused ion-beam milling.

[453] L. Reimer, *Transmission Electron Microscopy: Physics of Image Formation and Microanalysis*. Berlin, Heidelberg: Springer, 2013.

[454] Britannica, “transmission electron microscope.” [Online]. Available: https://www.britannica.com/technology/transmission-electron-microscope.

[455] N. Tanaka, “Present status and future prospects of spherical aberration corrected TEM / STEM for study of nanomaterials,” *Sci. Technol. Adv. Mater.*, 2008.

[456] H. Kang, J. H. Kim, J. won Oh, T. S. Back, and H. J. Kim, “Ultra-thin TEM sample preparation with advanced backside FIB milling method,” *Microsc. Microanal.*, vol. 16, no. 2, pp. 6–7, 2010.

[457] D. N. Dunn, L. E. Seitzman, and I. L. Singer, “The origin of an anomalous, low 2θ peak in x-ray diffraction spectra of MoS_2 films grown by ion beam assisted deposition,” *J. Mater. Res.*, vol. 12, no. 5, pp. 1191–1194, 1997.

[458] T. Koch, M. Evaristo, A. Pauschitz, M. Roy, and A. Cavaleiro, “Nanoindentation and nanoscratch behaviour of reactive sputtered deposited W-S-C film,” *Thin Solid Films*, vol. 518, no. 1, pp. 185–193, 2009.

[459] T. Bin Yaqub, A. Al-Rjoub, A. Cavaleiro, and F. Fernandes, “Exploring the industrial implementation of W–S–N coatings: a detailed study of the synthesis, compositional, structural, mechanical and multi-environment lubrication properties,” *J. Mater. Res. Technol.*, vol. 18, pp. 547–563, 2022.

[460] T. Vuchkov, T. Bin Yaqub, M. Evaristo, and A. Cavaleiro, “Synthesis, microstructural and mechanical properties of self-lubricating Mo-Se-C coatings deposited by closed-field unbalanced magnetron sputtering,” *Surf. Coatings Technol.*, vol. 394, p. 125889, 2020.

[461] G. Weise, N. Mattern, H. Hermann, A. Teresiak, I. Ba, and W. Bru, “Preparation, structure and properties of MoS_x films,” *Thin Solid Films*, vol. 298, no. 1–2, pp. 98–106, 1997.

[462] A. V. Bondarev, P. V. Kiryukhantsev-Korneev, A. N. Sheveyko, and D. V. Shtansky,

"Structure, tribological and electrochemical properties of low friction TiAlSiCN/MoSeC coatings," *Appl. Surf. Sci.*, vol. 327, pp. 253–261, 2015.

[463] T. Bin Yaqub, S. Bruyere, J. F. Pierson, T. Vuchkov, and A. Cavaleiro, "Insights into the wear track evolution with sliding cycles of carbon-alloyed transition metal dichalcogenide coatings," *Surf. Coatings Technol.*, vol. 403, p. 126360, 2020.

[464] B. Pilotti *et al.*, "Bi_2S_3 and MoS_2 Soft Coatings: A Comparative Study of Their Frictional Behavior Under Different Humidity Levels, Normal Loads, and Sliding Speeds," *Tribol. Lett.*, vol. 69, no. 3, pp. 1–24, 2021.

[465] A. Nossa and A. Cavaleiro, "Tribological behaviour of N(C)-alloyed W-S films," *Tribol. Lett.*, vol. 28, no. 1, pp. 59–70, 2007.

[466] T. Hudec, T. Roch, M. Gregor, Ľ. Orovčík, M. Mikula, and T. Polcar, "Tribological behaviour of Mo-S-N solid lubricant coatings in vacuum, nitrogen gas and elevated temperatures," *Surf. Coatings Technol.*, vol. 405, no. 34, pp. 1–7, 2021.

[467] T. Hudec *et al.*, "Titanium doped $MoSe_2$ coatings–Synthesis, structure, mechanical and tribological properties investigation," *Appl. Surf. Sci.*, vol. 568, p. 150990, 2021.

[468] T. Bin Yaqub, F. Fernandes, A. Al-Rjoub, and A. Cavaleiro, "Mo-Se-N dry lubricant coatings as a universal solution for protecting surfaces of complex 3D parts," *Mater. Lett.*, vol. 316, p. 131967, 2022.

[469] Y. Yang *et al.*, "Brittle Fracture of 2D $MoSe_2$," *Adv. Mater.*, vol. 29, no. 2, p. 1604201, 2017.

[470] G. Colas, P. Serles, A. Saulot, and T. Filleter, "Strength measurement and rupture mechanisms of a micron thick nanocrystalline MoS_2 coating using AFM based micro-bending tests," *J. Mech. Phys. Solids*, vol. 128, pp. 151–161, 2019.

[471] D. Nam, J. U. Lee, and H. Cheong, "Excitation energy dependent Raman spectrum of $MoSe_2$," *Sci. Rep.*, vol. 5, no. 1, p. 17113, 2015.

[472] T. Vitu, T. Huminiuc, G. Doll, E. Bousser, and T. Polcar, "Tribological properties of Mo-S-C coating deposited by pulsed d.c. magnetron sputtering," *Wear*, vol. 480, pp. 1–10, 2021.

[473] A. Banerji, S. Bhowmick, and A. T. Alpas, "Role of temperature on tribological behaviour of Ti containing MoS_2 coating against aluminum alloys," *Surf. Coatings Technol.*, vol. 314, pp. 2–12, 2017.

[474] A. Goikhman, D. Fominski, M. Gritskevich, R. Romanov, V. Fominski, and N. Smirnov, "Features of pulsed laser ablation of MoS_2 and $MoSe_2$ targets and their influence on the tribological properties of the deposited low friction films," *J. Phys. Conf. Ser.*, vol. 1686, no. 1, p. 012044, 2020.

[475] T. Bin Yaqub, T. Vuchkov, S. Bruyère, J. F. Pierson, and A. Cavaleiro, "A revised interpretation of the mechanisms governing low friction tribolayer formation in alloyed-TMD self-lubricating coatings," *Appl. Surf. Sci.*, vol. 571, p. 151302, 2022.

[476] T. Spalvins, "A review of recent advances in solid film lubrication," *J. Vac. Sci. Technol. A Vacuum, Surfaces, Film.*, vol. 5, no. 2, pp. 212–219, 1987.

[477] T. W. Scharf, P. G. Kotula, and S. V. Prasad, "Friction and wear mechanisms in

MoS_2/Sb_2O_3/Au nanocomposite coatings," *Acta Mater.*, vol. 58, no. 12, pp. 4100–4109, 2010.

[478] J. Xu *et al.*, "Selective-releasing-affected lubricant mechanism of a self-assembled MoS_2/Mo-S-C nanoperiod multilayer film sliding in diverse atmospheres," *Phys. Chem. Chem. Phys.*, vol. 19, no. 12, pp. 8161–8173, 2017.

[479] P. D. Fleischauer and J. R. Lince, "Comparison of oxidation and oxygen substitution in MoS_2 solid film lubricants," *Tribol. Int.*, vol. 32, no. 11, pp. 627–636, 1999.

[480] J. Rao, T. Rose, M. Craig, and J. R. Nicholls, "Wear coatings for high load applications," *Procedia CIRP*, vol. 22, no. 1, pp. 277–280, 2014.

[481] H. Holleck and V. Schier, "Multilayer PVD coatings for wear protection," *Surf. Coatings Technol.*, vol. 76, pp. 328–336, 1995.

[482] I. L. Singer, R. N. Bolster, J. Wegand, S. Fayeulle, and B. C. Stupp, "Hertzian stress contribution to low friction behavior of thin MoS_2 coatings," *Appl. Phys. Lett.*, vol. 57, no. 10, pp. 995–997, 1990.

[483] A. K. Kohli and B. Prakash, "Contact pressure dependency in frictional behavior of burnished molybdenum disulphide coatings," *Tribol. Trans.*, vol. 44, no. 1, pp. 147–151, 2001.

[484] F. Gustavsson, S. Jacobson, A. Cavaleiro, and T. Polcar, "Ultra-low friction W-S-N solid lubricant coating," *Surf. Coatings Technol.*, vol. 232, pp. 541–548, 2013.

[485] J. V. Pimentel, M. Danek, T. Polcar, and A. Cavaleiro, "Effect of rough surface patterning on the tribology of W-S-C-Cr self-lubricant coatings," *Tribol. Int.*, vol. 69, pp. 77–83, 2014.

[486] J. Zekonyte and T. Polcar, "Friction Force Microscopy Analysis of Self-Adaptive W-S-C Coatings: Nanoscale Friction and Wear," *ACS Appl. Mater. Interfaces*, vol. 7, no. 38, pp. 21056–21064, 2015.

[487] Z. Ping *et al.*, "Study on Synthesis and Tribological Properties Characterization of MoS_2-Ti_L/MoS_2-Ti_H Nano Multilayer Coating," in *IOP Conference Series: Materials Science and Engineering*, vol. 423, no. 1, p. 012048, 2018.

[488] N. Kong, B. Wei, D. Li, Y. Zhuang, G. Sun, and B. Wang, "A study on the tribological property of MoS_2/Ti-MoS_2/Si multilayer nanocomposite coating deposited by magnetron sputtering," *RSC Adv.*, vol. 10, no. 16, pp. 9633–9642, 2020.

[489] J. Pu, S. Ren, Z. Lu, and L. Wang, "A feasible multilayer structure design for solid lubricant coatings in a lunar environment," *RSC Adv.*, vol. 6, no. 70, pp. 65504–65517, 2016.

[490] M. Evaristo, T. Polcar, and A. Cavaleiro, "Can W-Se-C coatings be competitive to W-S-C ones?," *Plasma Process. Polym.*, vol. 6, no.1, pp. 92–95, 2009.

[491] B. Vengudusamy, J. H. Green, G. D. Lamb, and H. A. Spikes, "Tribological properties of tribofilms formed from ZDDP in DLC/DLC and DLC/steel contacts," *Tribol. Int.*, vol. 44, no. 2, pp. 165–174, 2011.

[492] M. Kalin, E. Roman, and J. Vižintin, "The effect of temperature on the tribological mechanisms and reactivity of hydrogenated, amorphous diamond-like carbon coatings

under oil-lubricated conditions," *Thin Solid Films*, vol. 515, no. 7–8, pp. 3644–3652, 2007.

[493] M. Kalin, E. Roman, L. Ožbolt, and J. Vižintin, "Metal-doped (Ti, WC) diamond-like-carbon coatings: Reactions with extreme-pressure oil additives under tribological and static conditions," *Thin Solid Films*, vol. 518, no. 15, pp. 4336–4344, 2010.

[494] K. A. H. Al Mahmud, M. Varman, M. A. Kalam, H. H. Masjuki, H. M. Mobarak, and N. W. M. Zulkifli, "Tribological characteristics of amorphous hydrogenated (a-C: H) and tetrahedral (ta-C) diamond-like carbon coating at different test temperatures in the presence of commercial lubricating oil," *Surf. Coatings Technol.*, vol. 245, pp. 133–147, 2014.

[495] L. Wang, L. Bai, Z. Lu, G. Zhang, and Z. Wu, "Influence of Load on the Tribological Behavior of a-C Films: Experiment and Calculation Coupling," *Tribol. Lett.*, vol. 52, no. 3, pp. 469–475, 2013.

[496] A. Li *et al.*, "Investigation of mechanical and tribological properties of super-thick DLC films with different modulation ratios prepared by PECVD," *Mater. Res. Express*, vol. 6, no. 8, pp. 0–13, 2019.

Appendix. A

				1	2	3	4	5
Configuration		Ball		STEEL	STEEL	STEEL	STEEL	STEEL
		Coating		$MoSe_2$	$MoSe_2$	$MoSe_2$	$MoSe_2$	$MoSe_2$
		Lubricant		PAO4	PAO4	PAO4	PAO4	PAO4
Lubricant	Temperature	T	°C	25	25	25	25	25
	Density	ρ15	g/cm3	0.817	0.817	0.817	0.817	0.817
	Kinematic Viscosity	η40	mm2/s	16.8	16.8	16.8	16.8	16.8
		η100	mm2/s	3.9	3.9	3.9	3.9	3.9
Material	Elastic modulus	E1 (Ball)	N/m2 (Pa)	2.07E+11	2.07E+11	2.07E+11	2.07E+11	2.07E+11
		E2 (Disc)	N/m2 (Pa)	2.10E+11	2.10E+11	2.10E+11	2.10E+11	2.10E+11
	Poisson's ratios	V1 (Ball)		0.3	0.3	0.3	0.3	0.3
		V2 (Disc)		0.3	0.3	0.3	0.3	0.3
	Radii	R1x = R1y (Ball)	m	3.000E-03	3.000E-03	3.000E-03	3.000E-03	3.000E-03
		R2x, R2y (Disc)	m	-	-	-	-	-
	ellipticity parameter	k (=R1y/R1x)		1.030E+00	1.030E+00	1.030E+00	1.030E+00	1.030E+00
	Roughness	Ra (Ball)	nm	10	10	10	10	10
		Ra (Disc)	nm	13.53	13.53	13.53	13.53	13.53
	composite surface roughness	σ	nm	17	17	17	17	17
	Entrainment speed	U	m/s	0.2	0.2	0.2	0.2	0.2
		U1	m/s	0	0	0	0	0
		U2	m/s	0.4	0.4	0.4	0.4	0.4
	Load	W	N	5	8	10	12	15
Parameters	Pressure viscosity coefficient	α	m2/N	1.83E-08	1.83E-08	1.83E-08	1.83E-08	1.83E-08
	Dynamic visocosity	η0	Pa・s	2.41E-02	2.41E-02	2.41E-02	2.41E-02	2.41E-02
	Reduced Yong's modulus	E'	N/m2 (Pa)	2.29E+11	2.29E+11	2.29E+11	2.29E+11	2.29E+11
	Reduced Radii	R'x	m	3.00E-03	3.00E-03	3.00E-03	3.00E-03	3.00E-03
		R'	m	1.50E-03	1.50E-03	1.50E-03	1.50E-03	1.50E-03
	Speed parameter	*U*		7.00E-12	7.00E-12	7.00E-12	7.00E-12	7.00E-12
	Materials parameter	*G*		4.18E+03	4.18E+03	4.18E+03	4.18E+03	4.18E+03
	Load parameter	*W*		2.42E-06	3.88E-06	4.85E-06	5.82E-06	7.27E-06
Hertz theory	Contact radius	a	m	4.61E-05	5.40E-05	5.81E-05	6.18E-05	6.65E-05
			μm	46	54	58	62	67
	Maximum contact pressure	Pmax	N/m2 (Pa)	1.12E+09	1.31E+09	1.41E+09	1.50E+09	1.62E+09
			GPa	1.122	1.312	1.413	1.502	1.618
	Average contact pressure	Paverage	N/m2 (Pa)	7.48E+08	8.75E+08	9.42E+08	1.00E+09	1.08E+09
			GPa	0.75	0.87	0.94	1.00	1.08
	Minimum film thickness	h_{min}	m	2.18E-08	2.11E-08	2.07E-08	2.04E-08	2.01E-08
			nm	22	21	21	20	20
	Lambda ratio	λ		1.3	1.3	1.2	1.2	1.2

Figure 6.1: Calculation sheet for maximum Hertzian contact pressures and lambda ratios of $MoSe_2$ coating tested at different loads.

Appendix. B

				1	2	3	4	5
Configuration		Ball		STEEL	STEEL	STEEL	STEEL	STEEL
		Coating		$MoSe_2$	$MoSe_2$	$MoSe_2$	$MoSe_2$	$MoSe_2$
		Lubricant		PAO4	PAO4	PAO4	PAO4	PAO4
Lubricant	Temperature	T	°C	25	40	60	80	100
	Density	ρ15	g/cm3	0.817	0.817	0.817	0.817	0.817
	Kinematic Viscosity	η40	mm2/s	16.8	16.8	16.8	16.8	16.8
		η100	mm2/s	3.9	3.9	3.9	3.9	3.9
Material	Elastic modulus	E1 (Ball)	N/m2 (Pa)	2.07E+11	2.07E+11	2.07E+11	2.07E+11	2.07E+11
		E2 (Disc)	N/m2 (Pa)	2.10E+11	2.10E+11	2.10E+11	2.10E+11	2.10E+11
	Poisson's ratios	V1 (Ball)		0.3	0.3	0.3	0.3	0.3
		V2 (Disc)		0.3	0.3	0.3	0.3	0.3
	Radii	R1x = R1y (Ball)	m	3.000E-03	3.000E-03	3.000E-03	3.000E-03	3.000E-03
		R2x, R2y (Disc)	m	-	-	-	-	-
	ellipticity parameter	k (=R1y/R1x)		1.030E+00	1.030E+00	1.030E+00	1.030E+00	1.030E+00
	Roughness	Ra (Ball)	nm	10	10	10	10	10
		Ra (Disc)	nm	13.53	13.53	13.53	13.53	13.53
	composite surface roughness	σ	nm	17	17	17	17	17
	Entrainment speed	U	m/s	0.2	0.2	0.2	0.2	0.2
		U1	m/s	0	0	0	0	0
		U2	m/s	0.4	0.4	0.4	0.4	0.4
	Load	W	N	5	5	5	5	5
Parameters	Pressure viscosity coefficient	α	m2/N	1.83E-08	1.62E-08	1.40E-08	1.23E-08	1.09E-08
	Dynamic visocosity	η0	Pa · s	2.41E-02	1.35E-02	7.25E-03	4.44E-03	2.97E-03
	Reduced Yong's modulus	E'	N/m2 (Pa)	2.29E+11	2.29E+11	2.29E+11	2.29E+11	2.29E+11
	Reduced Radii	R'x	m	3.00E-03	3.00E-03	3.00E-03	3.00E-03	3.00E-03
		R'	m	1.50E-03	1.50E-03	1.50E-03	1.50E-03	1.50E-03
	Speed parameter	*U*		7.00E-12	3.92E-12	2.11E-12	1.29E-12	8.66E-13
	Materials parameter	*G*		4.18E+03	3.71E+03	3.21E+03	2.81E+03	2.49E+03
	Load parameter	*W*		2.42E-06	2.42E-06	2.42E-06	2.42E-06	2.42E-06
Hertz theory	Contact radius	a	m	4.61E-05	4.61E-05	4.61E-05	4.61E-05	4.61E-05
			µm	46	46	46	46	46
	Maximum contact pressure	Pmax	N/m2 (Pa)	1.12E+09	1.12E+09	1.12E+09	1.12E+09	1.12E+09
			GPa	1.122	1.122	1.122	1.122	1.122
	Average contact pressure	Paverage	N/m2 (Pa)	7.48E+08	7.48E+08	7.48E+08	7.48E+08	7.48E+08
			GPa	0.75	0.75	0.75	0.75	0.75
	Minimum film thickness	h_{min}	m	2.18E-08	1.38E-08	8.47E-09	5.68E-09	4.08E-09
			nm	22	14	8	6	4
	Lambda ratio	λ		1.3	0.8	0.5	0.3	0.2

Figure 6.2: Calculation sheet for maximum Hertzian contact pressures and lambda ratios of $MoSe_2$ coating tested at different temperatures.

Appendix. C

				1	2	3	4	5
Configuration		Ball		STEEL	STEEL	STEEL	STEEL	STEEL
		Coating		$MoSe_2$/DLC-W	$MoSe_2$/DLC-W	$MoSe_2$/DLC-W	$MoSe_2$/DLC-W	$MoSe_2$/DLC-W
		Lubricant		PAO4	PAO4	PAO4	PAO4	PAO4
Lubricant	Temperature	T	°C	25	25	25	25	25
	Density	ρ15	g/cm3	0.817	0.817	0.817	0.817	0.817
	Kinematic Viscosity	η40	mm2/s	16.8	16.8	16.8	16.8	16.8
		η100	mm2/s	3.9	3.9	3.9	3.9	3.9
Material	Elastic modulus	E1 (Ball)	N/m2 (Pa)	2.07E+11	2.07E+11	2.07E+11	2.07E+11	2.07E+11
		E2 (Disc)	N/m2 (Pa)	1.27E+11	1.27E+11	1.27E+11	1.27E+11	1.27E+11
	Poisson's ratios	V1 (Ball)		0.3	0.3	0.3	0.3	0.3
		V2 (Disc)		0.3	0.3	0.3	0.3	0.3
	Radii	R1x = R1y (Ball)	m	3.000E-03	3.000E-03	3.000E-03	3.000E-03	3.000E-03
		R2x, R2y (Disc)	m	-	-	-	-	-
	ellipticity parameter	k (=R1y/R1x)		1.030E+00	1.030E+00	1.030E+00	1.030E+00	1.030E+00
	Roughness	Ra (Ball)	nm	10	10	10	10	10
		Ra (Disc)	nm	12.34	12.34	12.34	12.34	12.34
	composite surface roughness	σ	nm	16	16	16	16	16
	Entrainment speed	U	m/s	0.2	0.2	0.2	0.2	0.2
		U1	m/s	0	0	0	0	0
		U2	m/s	0.4	0.4	0.4	0.4	0.4
	Load	W	N	10	20	30	40	50
Parameters	Pressure viscosity coefficient	α	m2/N	1.83E-08	1.83E-08	1.83E-08	1.83E-08	1.83E-08
	Dynamic visocosity	η0	Pa・s	2.41E-02	2.41E-02	2.41E-02	2.41E-02	2.41E-02
	Reduced Yong's modulus	E'	N/m2 (Pa)	1.73E+11	1.73E+11	1.73E+11	1.73E+11	1.73E+11
	Reduced Radii	R'x	m	3.00E-03	3.00E-03	3.00E-03	3.00E-03	3.00E-03
		R'	m	1.50E-03	1.50E-03	1.50E-03	1.50E-03	1.50E-03
	Speed parameter	*U*		9.27E-12	9.27E-12	9.27E-12	9.27E-12	9.27E-12
	Materials parameter	*G*		3.16E+03	3.16E+03	3.16E+03	3.16E+03	3.16E+03
	Load parameter	*W*		6.42E-06	1.28E-05	1.93E-05	2.57E-05	3.21E-05
Hertz theory	Contact radius	a	m	6.38E-05	8.04E-05	9.21E-05	1.01E-04	1.09E-04
			μm	64	80	92	101	109
	Maximum contact pressure	Pmax	N/m2 (Pa)	1.17E+09	1.48E+09	1.69E+09	1.86E+09	2.00E+09
			GPa	1.172	1.476	1.690	1.860	2.004
	Average contact pressure	Paverage	N/m2 (Pa)	7.81E+08	9.84E+08	1.13E+09	1.24E+09	1.34E+09
			GPa	0.78	0.98	1.13	1.24	1.34
	Minimum film thickness	h_{min}	m	2.14E-08	2.03E-08	1.98E-08	1.93E-08	1.90E-08
			nm	21	20	20	19	19
	Lambda ratio	λ		1.3	1.3	1.2	1.2	1.2

Figure 6.3: Calculation sheet for maximum Hertzian contact pressures and lambda ratios of $MoSe_2$/DLC-W coating tested at different loads.